Finite size and surface effects in bistable molecular nanomaterials

Shiteng Mi

THÈSE

En vue de l'obtention du

DOCTORAT DE L'UNIVERSITÉ DE TOULOUSE

Délivré par l'Université Toulouse 3 - Paul Sabatier

Présentée et soutenue par

Shiteng MI

Le 26 octobre 2023

Effets de taille finie et de surface dans les nanomatériaux moléculaires bistables

---

Ecole doctorale : **SDM - SCIENCES DE LA MATIERE - Toulouse**

Spécialité : **Physique de la Matière**

Unité de recherche :
LCC - Laboratoire de Chimie de Coordination

Thèse dirigée par
Azzedine BOUSSEKSOU et William NICOLAZZI

Jury

M. Volker SCHÜNEMANN, Rapporteur
M. Cristian ENACHESCU, Rapporteur
Mme Marie-Joëlle MENU, Examinatrice
M. Azzedine BOUSSEKSOU, Directeur de thèse

Table of Contents

General introduction

Spin crossover (SCO) compounds are inorganic complexes, which display reversible switching behavior between the so-called high spin (HS) and low spin (LS) states of the central metal ion. The outstanding properties of SCO nanomaterials make them very interesting for several technological applications. Indeed, the spin state switching in SCO materials is accompanied by a dramatic change of various material properties, including magnetic, optical, electrical and mechanical properties, providing scope for applications in electronic, spintronic, photonic and mechanical devices. Motivated by these appealing properties, considerable efforts have been devoted in the past two decades to synthesize SCO materials at reduced size scales (thin films, nanoparticles, nanopatterns, etc.) and to integrate these nano-objects into functional devices. However, as in any material, the phase stability and transformation kinetics are size dependent. Notably, it was shown that in most cases SCO nano-objects display a downshift of the equilibrium temperature, the appearance of an incomplete spin transition as well as the loss of the co-called cooperativity at reduced sizes. To explain these tendencies, it was proposed that surface and interface effects play an increasingly important role in the spin state switching phenomenon at the nanometric scale. In this context, the main objective of this thesis is to try to understand the effects of the presence of surfaces and interfaces on the SCO properties in finite size materials from a theoretical point of view. For this purpose, studies coupling molecular dynamics (MD) simulations and thermodynamics methods have been carried out. In addition to being of fundamental interest, understanding the phenomenon of bistability at the nanometer scale is an essential step towards the rational design and device integration of these switchable nano-objects.

The manuscript is organized as follows:

Chapter I is devoted to the introduction of the molecular spin crossover phenomenon. First, a brief overview of basic ligand-field theoretical and thermodynamical aspects of the phenomenon are provided. Second, the bulk SCO behavior as well as the relevant theoretical models are reviewed. Then, we present different studies concerning the synthesis of SCO nano-objects and the size effects on the SCO properties. In the last section of this chapter, various hypotheses of the origin of finite size effects are discussed.

In **Chapter II** we describe the construction of new force fields for the all-atom MD simulations of SCO materials. It will start with the construction of force fields for the compound [Fe(pyrazine)][Ni(CN)$_4$] in the LS and HS states. The method of extracting the force field parameters from the experimental data will be discussed in detail. Then, we will introduce the so-called "Double-Well" potential to modify these force fields in order to simulate the SCO phenomenon itself. Finally, the validation of the force fields will be made by comparing the results obtained from the MD simulation to the experimental observations in terms of the vibrational properties and the thermally induced spin transition.

In **Chapter III**, based on the newly constructed force field, all-atom MD simulations are preformed to study the HS to LS relaxation process and the associated mechanical deflection in a nanometer thickness bilayer beam, consisting of an SCO active and an inactive layer. First, the interface effects on the nucleation and propagation of LS domains are studied by exploring the spatiotemporal features along the phase transformation. Next, we will analyze how the interface affect the relaxation behavior of the metastable HS fraction. In particular, the deflection behavior of the lattice induced by the HS/LS interface are investigated and compared to a classical thermomechanical model. Finally, the propagation velocity of LS domain boundaries during the relaxation process is discussed using the real-time dynamics provided by the MD simulations.

Chapter IV presents the effects of surface energy and surface stress on the SCO behavior at the nano-scale. For this purpose, a nano-thermodynamic model adapted for the description of the SCO phenomenon at the nano-scale has been built. It highlights the different contributions (surface energy and surface stress) to surface effects on the spin switching behavior of nano-objects. It has thus made it possible to theoretically "design" objects for which the spin transition would be easily adjustable. This theoretical study combines nano-thermodynamics and MD simulations.

The manuscript ends with the general conclusions as well as some perspectives for future works.

Chapter I: Introduction

I. 1 The molecular SCO phenomenon

The spin transition phenomenon can occur in octahedral complexes with metal ions belonging to the first series of transition metals and more particularly having electronic configurations $3d^4$ to $3d^7$, as in the compounds of Fe (III), Fe (II), Co (II) and less frequently in Co (III), Cr (II), Mn (II) and Mn (III). However, the majority of the studied complexes have an iron (II) central ion.

I. 1.1 Crystal field theory

Since spin-transition molecules form complex electronic structures, exact resolution of the Schrödinger equation becomes impossible, whether analytically or numerically. It is then necessary to use simpler models to describe, at least qualitatively, the electronic structure of transition metal complexes. In this context, crystal field theory offers a simple, but powerful means. In this model, the ligands are considered as point charges interacting purely electrostatically with the central metal ion. The charge distribution of the ligands determines the symmetry of the external electrostatic field, which will act on the transition metal and induce a partial lifting of degeneracy [1].

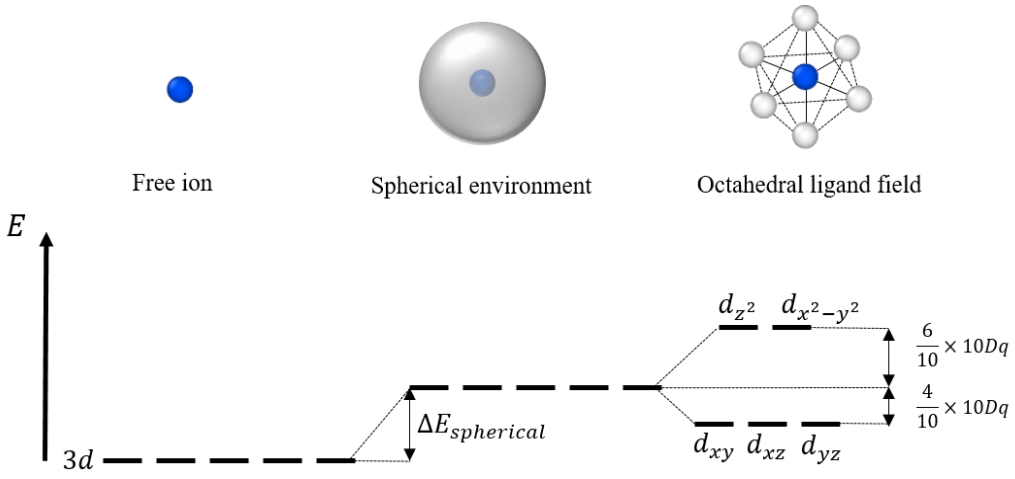

FIG. I. 1: Influence of the crystal field symmetry on metal cation energy levels.

For example, for the Fe (II) cation, the five 3d orbitals are degenerated in the absence of the ligands. If the metal ion is placed in a spherical field, the energy level of the orbitals will be

$$E_{sph} = E_{free} + \Delta E, \quad \text{(I. 1)}$$

where E_{free} is the energy of the free Fe (II) ion. If the positively charged Fe(II) ion is set in a field of perfect octahedral field, formed by six negatively charged ligands, then the electrons in the metal center experience repulsive forces from the ligands. The population of *d* orbitals will then be governed by the minimization of the electrostatic energy. The consequence is a partial lifting of the degeneracy of the energy levels into a low energy level t_{2g}, composed of the three degenerated non-bonding orbitals *dxy, dxz* and *dyz*, and a high energy level e_g, composed of the two degenerate anti-bonding orbitals $d_{z^2}$and $d_{x^2-y^2}$ (shown in **FIG. I. 1**). The energy difference between these molecular orbitals is determined by the strength of the crystal field 10 *Dq*. where *Dq* is a semi-empirical parameter associated with the crystal field strength and dependent on the charge distribution of the metal ion and the metal-ligand distance. The energies of the levels e_g and t_{2g} can be decomposed into two contributions: a spherical field which only has the effect of raising the energy of the electronic levels of the free ion by a value $\Delta E_{spherical}$ and a contribution associated with the lowering of the symmetry leading to the partial lifting of degeneracy. The two energy levels can be expressed as follow:

$$E_{e_g} = E_{free} + \Delta E_{spherical} + \frac{6}{10} \times 10Dq, \quad \text{(I.2)}$$

$$E_{t_{2g}} = E_{free} + \Delta E_{spherical} - \frac{4}{10} \times 10Dq, \quad \text{(I.3)}$$

At the molecular scale, two main effects compete. On one hand, electrons tend to occupy *d* orbitals according to Hund's rule due to the exchange term. On the other hand, they tend to fill the t_{2g} level, which is the lower energy level. Depending on the magnitudes of the ligand field and the electron pairing energy (Π), which is insensitive to the spin state, the consequence of this competition can lead to two possible ground states (see **FIG. I.2**):

If $\Pi > 10Dq$ (weak field), the electrons will occupy the five d orbitals according to Hund's rule, with maximum spin multiplicity as for the free ion. In the case of Fe (II), the total spin is S=2, and this paramagnetic ground state is denominated high spin (HS) state, represented by the spectroscopic term $^5T_{2g}$.

If Π < 10*Dq* (strong crystalline field), the electrons occupy the lowest energy level t_{2g}, in violation of Hund's rule and maximizing the number of paired electrons, with minimum spin multiplicity. In the case of Fe (II), the total spin is S = 0, and this diamagnetic state is called low spin (LS) state, represented by the spectroscopic term $^1A_{1g}$.

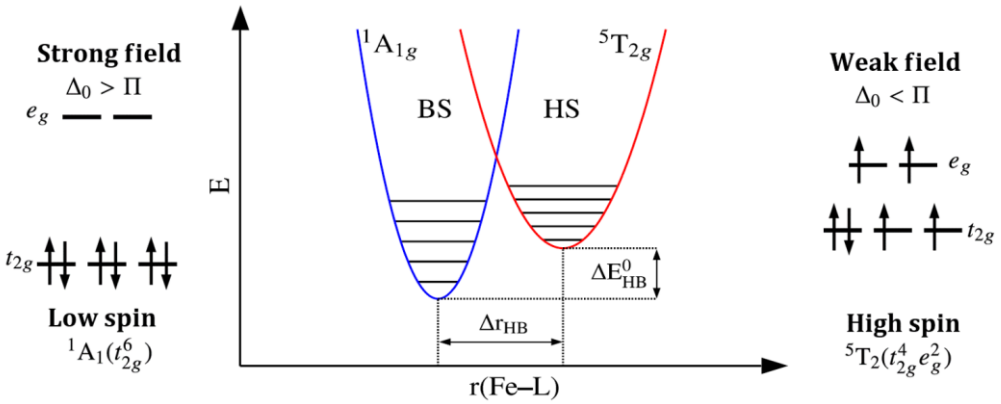

FIG. I.2: Scheme of the electronic configurations for the two possible ground states for iron (II) in an octahedral complex and simplified schematic representation of the configurational diagram of the two molecular spin states (HS and LS) in an SCO complex.

It is important to note that the strength of ligand field strongly depends on the distance (*r*) between the transition metal and the ligand ($1/r^n$, where n = 5, 6) [1]. The ratio of the ligand field strength between the two spin states is given by the equation:

$$\frac{10Dq^{LS}}{10Dq^{HS}} = \left(\frac{r_{HS}}{r_{LS}}\right)^n \qquad \text{(I.4)}$$

where r_{HS} and r_{LS} are the metal-ligand distances in the HS and LS states, respectively. In the case of the most widely investigated Fe(II)N_6 complexes, the typical metal-ligand distances between the two spin states are $r_{HS} \approx 2.2$ Å and $r_{LS} \approx 2$ Å with the change in the metal-ligand distance $\Delta r_{HL} = r_{HS} - r_{LS} \approx 0.2$ Å.

The crystal field theory gives a relatively simple and practical view of the spin transition. However, this theory, based on electrostatic models, can only be applied to the case of charged ligands. To better take into account the case of the uncharged ligands, in particular, the weak covalent bonds of type σ and π between the metal and the ligands, it is necessary to use the ligand field theory. This more general approach gives results similar to those found by crystal field theory [1].

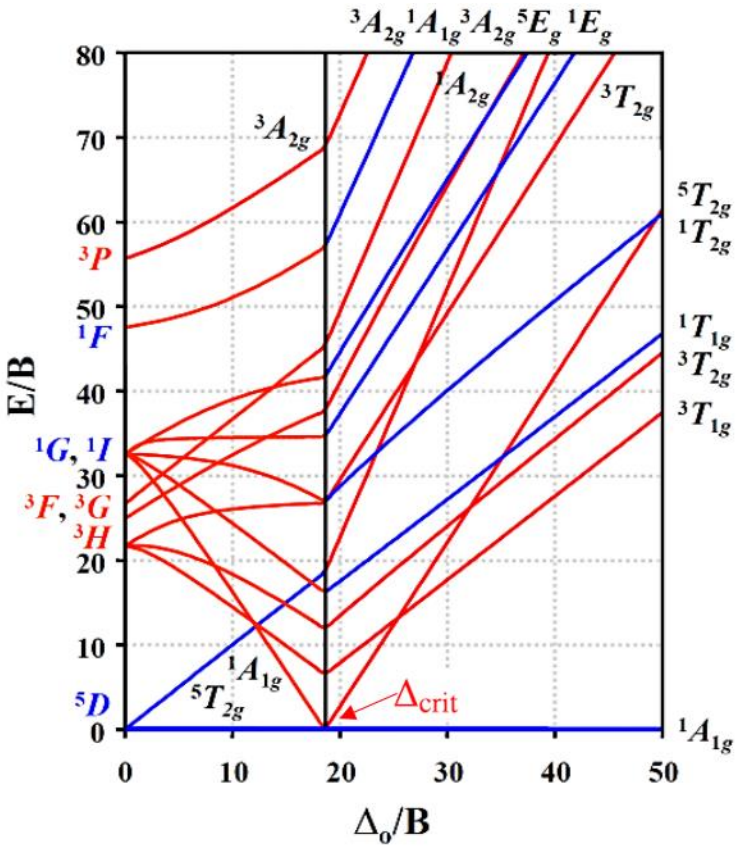

FIG. I.3: Tanabe-Sugano diagram for a transition metal ion with six d electrons in an octahedral ligand field symmetry [2].

The Tanabe-Sugano diagram in **FIG. I.3** represents the energy of the spectroscopic terms of d^6 ions in an octahedral environment, corresponding to ground and excited levels as function of ligand field strength. It can be seen that the ground state is ^{5}D. Under the influence of the ligand field, this state splits into two states, the new ground state $^5T_{2g}$ (HS state) and an excited state ^5E_g. The state $^5T_{2g}$ remains the ground state until $\Delta_0 \approx \Pi$. The critical ligand field value is written as Δ_{crit}. When the value of Δ_0 becomes higher than Δ_{crit}, the $^1A_{1g}$ (LS state) becomes the new ground state [2].

I. 1.2 Thermodynamic aspects of the spin crossover

We first consider the case of a diluted system, i.e., a system made up of a large number of molecules, which interact weakly with each other. The system is in contact with a thermal bath and a volume reservoir, corresponding to the isothermal and isobaric ensemble (N,P,T).

At constant pressure, the spin switching could be viewed as a thermal equilibrium between the two spin states. For such experimental conditions, the relevant state function is the Gibbs energy $G = H - TS$, where H and S represent the system's enthalpy and entropy, respectively. The Gibbs energy difference between the HS and LS phases describes the system's thermodynamic properties:

$$\Delta G = \Delta H - T\Delta S, \tag{I.5}$$

where $\Delta H = H_{HS} - H_{LS}$ is the enthalpy variation and $\Delta S = S_{HS} - S_{LS}$ is the system's entropy variation. We can define the temperature $T_{1/2}$ as the equilibrium temperature at which the proportions of HS and LS molecules are the same, corresponding to $\Delta G = 0$:

$$T_{1/2} = \frac{\Delta H}{\Delta S}, \tag{I.6}$$

According to Eq. I.6, it is possible to summarize the spin transition as follows:

- When $T < T_{1/2}$ ($\Delta H > T\Delta S$), the enthalpy term dominates and the thermodynamic ground state is the LS state ($G_{LS} < G_{HS}$);

- When $T > T_{1/2}$ ($\Delta H < T\Delta S$), the entropic term dominates and the thermodynamic ground state is the HS state ($G_{LS} > G_{HS}$);

- When $T = T_{1/2}$ ($\Delta H = T\Delta S$), the enthalpy and entropy variations are equal and the two spin states are present in the same proportion ($G_{LS} = G_{HS}$).

Thus, in this aspect, the spin switching is regarded as a “entropy-driven phase transformation”.

To give a better understanding of the phase stability, it is essential to detail the contributions to the enthalpy and the entropy. ΔH can be subdivided into two parts: a temperature independent electronic part (ΔH_{el}) and a vibrational part (ΔH_{vib}) [3]. In the same way, it is possible to divide the ΔS into different parts:

$$\Delta S = \Delta S_{el} + \Delta S_{vib} + \Delta S_{trans} + \Delta S_{rot}, \tag{I.7}$$

The last two terms ΔS_{trans} and ΔS_{rot} correspond to the entropy variation of translation and rotation, respectively. These two terms are neglected in most cases because SCO molecules are generally studied in the solid state and translational entropy and rotational entropy in both spin states are very close. The first term $\Delta S_{el} = \Delta S_{orb} + \Delta S_{spin}$ is the electronic entropy variation, which comes from the difference in terms of degeneracy of orbital and spin momenta:

$$\Delta S_{orb} = R\ln\left(\frac{2L_{HS}+1}{2L_{LS}+1}\right), \tag{I.8}$$

$$\Delta S_{spin} = R\ln\left(\frac{2S_{HS}+1}{2S_{LS}+1}\right), \tag{I.9}$$

where R is the ideal gas constant, L and S are the total orbital and total spin momenta, respectively. In the case of the Fe(II) SCO complex with perfect octahedral symmetry, ΔS_{orb} and ΔS_{spin} can be calculated by:

$$\Delta S_{orb} = R\ln(3) = 9.13\ \mathrm{J\cdot mol^{-1}\cdot K^{-1}}, \tag{I.10}$$

$$\Delta S_{spin} = R\ln(5) = 13.38\ \mathrm{J\cdot mol^{-1}\cdot K^{-1}}, \tag{I.11}$$

In most cases, however, the symmetry around the Fe (II) ion is lower and the orbital degeneracy is lifted. Therefore, we have $\Delta S_{el} = \Delta S_{spin} > 0$. Electronic entropy favors the HS state and is constant.

On the other hand, coordination sphere vibrations play a central role in the spin transition mechanism. The difference in entropy of vibrational origin ΔS_{vib} strongly depends on the difference in the modes of vibration within the octahedron between the two spin states. The vibrational entropy is written as:

$$S_{vib}(T) = R\sum_{\lambda}\left(-\ln\left[1-e^{-h\nu_{\lambda}/k_BT}\right] + \frac{h\nu_{\lambda}}{k_BT}\frac{1}{\exp[h\nu_{\lambda}/k_BT]}\right), \tag{I.12}$$

The sum is performed over all vibration modes. In the high temperature or low frequency approximation, $h\nu << k_BT$, Eq. I.12 takes the following form:

$$S_{vib} = R\sum_{\lambda} -\ln(h\nu_{\lambda}/k_BT), \tag{I.13}$$

The difference in vibrational entropy between the two spin states then becomes:

$$\Delta S_{vib} = S_{vib}^{HS} - S_{vib}^{LS} = R\sum_{\lambda}\ln\left(\frac{\nu_{\lambda}^{LS}}{\nu_{\lambda}^{HS}}\right), \tag{I.14}$$

Taking into account the 15 possible distortion modes inside an octahedron, this results in a difference in a temperature independent vibrational entropy:

$$\Delta S_{vib} = 15R\ln\left(\frac{\langle\nu^{LS}\rangle}{\langle\nu^{HS}\rangle}\right), \tag{I.15}$$

By taking the ratio $\frac{\langle\nu^{LS}\rangle}{\langle\nu^{HS}\rangle}$ = 1.3 [4], we get $\Delta S_{vib} \approx 32.7\ \mathrm{J\cdot mol^{-1}\cdot K^{-1}}$. This result tells us two things. On one hand, the vibrational entropy is higher in the HS state ($\Delta S_{vib} > 0$)

and therefore the latter is favored at high temperature. On the other hand, the significant variation of the vibrational entropy shows us the major role it plays in the spin transition. The use of the low frequency approximation gives us an idea of the importance of vibrational properties in spin transition compounds.

Moreover, it is interesting to note that the entropy variation has been estimated by calorimetric measurements [5], typically between 40 and 80 $\mathrm{J \cdot mol^{-1} \cdot K^{-1}}$. These values are clearly higher than the obtained ΔS_{el} above, and the difference between ΔS and ΔS_{el} is attributed to the contribution of the vibrational entropy ΔS_{vib}. The difference of the vibrational entropy is mainly attributed to the difference of the intramolecular vibrational modes (ΔS_{vib}^{intra}) between LS and HS states, which is confirmed by Raman and infrared spectroscopy [6-8].

I.2 Collective behavior

I.2.1 Notion of the cooperativity

I.2.1.1 Introduction to the cooperativity phenomenon

We have only considered, until now, the case of an isolated molecule and then the case of diluted systems. However, in a solid medium, the interactions between the molecules can no longer be neglected. We have seen that the metal-ligand distance increases when the molecule switches from the LS to the HS state, causing an increase in the volume of the octahedron by ~ 25 % and, as a consequence, an expansion of the whole lattice by typically 1-10 %.

For example, if a molecule surrounded by HS molecules switches from the HS to LS state, all the molecules will be under the stress and strain due to the reduction of the volume (**FIG. I.4**), which thus bring to an increase of the elastic energy of the crystal lattice. For strong elastic interactions (intermolecular interaction), the intermediate state between the pure LS and HS states is not stable and the lattice is blocked in its current state until the intake energy is large enough to exceed the energy barrier. These collective phenomena are called cooperativity. They may lead in some cases to a first-order phase transition with an elastically driven memory effect (hysteresis).

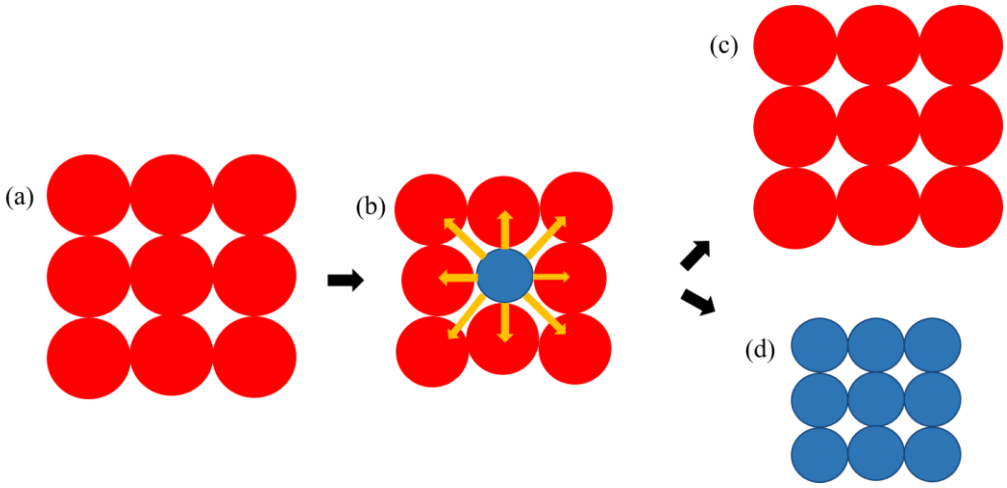

FIG. I.4: Simplified local representation of the collective mechanisms in the case of a strongly cooperative spin-transition compound. (a) A group of molecules are in the HS state. (b) The central molecule switches to the LS state, the volume change implies the deformation of the lattice as well as the appearance of tensile stresses (yellow arrows). As a result, (c) either the molecule returns to the LS state or (d) the neighbors switch towards the HS state.

I.2.1.2 Different spin crossover phenomena

By convention, a thermally induced spin crossover curve plots the average HS fraction (n_{HS}) as a function of the temperature. In a SCO material composed of N molecules, at a given temperature and pressure, there will be N_{HS} molecules in the HS state and N_{LS} in the LS state. n_{HS} is defined as:

$$n_{HS} = \frac{N_{HS}}{N}, \tag{I.16}$$

FIG. I.5 highlights the most frequently observed cases in the SCO materials. Until the 1960s, the observed spin conversions were all gradual [9, 10], as shown in **FIG. I.5** (a). The weak intermolecular interaction in these compounds gives rise to a homogeneous transformation between the HS and the LS phases, following a Boltzmann distribution.

The first abrupt spin transition was observed in 1964 by Baker and Bobonich for the compound $[Fe(phen)_2(NCS)_2]$ [11]. Three years later, in 1967, this observation was confirmed

by König and Madeja [12]. This first-order transition is displayed in **FIG. I.5** (b). This behavior was attributed to the intermolecular interactions and the notion of cooperative system was introduced [13, 14]. For strongly cooperative systems, we notice the appearance of a first-order phase transition accompanied by a hysteresis cycle (**FIG. I.5 (**c)). This type of spin transition is characterized by the temperatures $T_{1/2}^{\uparrow}$ and $T_{1/2}^{\downarrow}$ representing, respectively, the transition temperature (at n_{HS} = 1/2) from the LS to HS state (warming mode) and that from the HS to LS state (cooling mode). The first observation of a hysteresis cycle was reported on the compound [Fe(4,7-$(CH_3)_2$-phen)$_2$$(NCS)_2$] in 1976 by König and Ritter [15]. This strong cooperativity is explained by the strong intermolecular interactions leading to the existence of a metastable state.

Multi-step spin transitions have also been demonstrated (**FIG. I.5 (d**)). The first two-step spin transition was observed in 1987 by Zelentsov for the case of a Fe(III) complex of 2-bromosalicylaldehyde-thiosemicarbazone [16]. These stepped transitions can have various origins. They can appear for example due to the presence of two different crystallographic positions of the metal centers in the lattice. This phenomenon also exists in mono- or poly-nuclear systems where the environment of each metal center is identical. The spin transition of a metal induces local distortions and makes the spin transition of the neighbor metal less favorable [17]. This kind of spin transition is related to the competition between short-range interactions (which tend to favor HS–LS pairs) and long-range interactions (which tend to favor a homogeneous phase) [18, 19].

Incomplete transitions were also reported (**FIG. I.5** (**e**)). This may correspond to the appearance of a residual HS fraction at low temperature and/or a residual LS fraction at high temperature [20]. The appearance of this kind of transition may be due to several reasons. First, this phenomenon may occur because of a kinetic effect at very low temperatures when the HS molecules are trapped by a quenching process [21]. Another reason is related to the existence of defects in the lattice, which prevents locally the formation of LS species (HS fraction) or HS species (LS fraction). Moreover, such incomplete transitions may also appear in SCO systems for which the difference in energy between the HS and LS states is very close; this situation is called equi-energetic scenario [4].

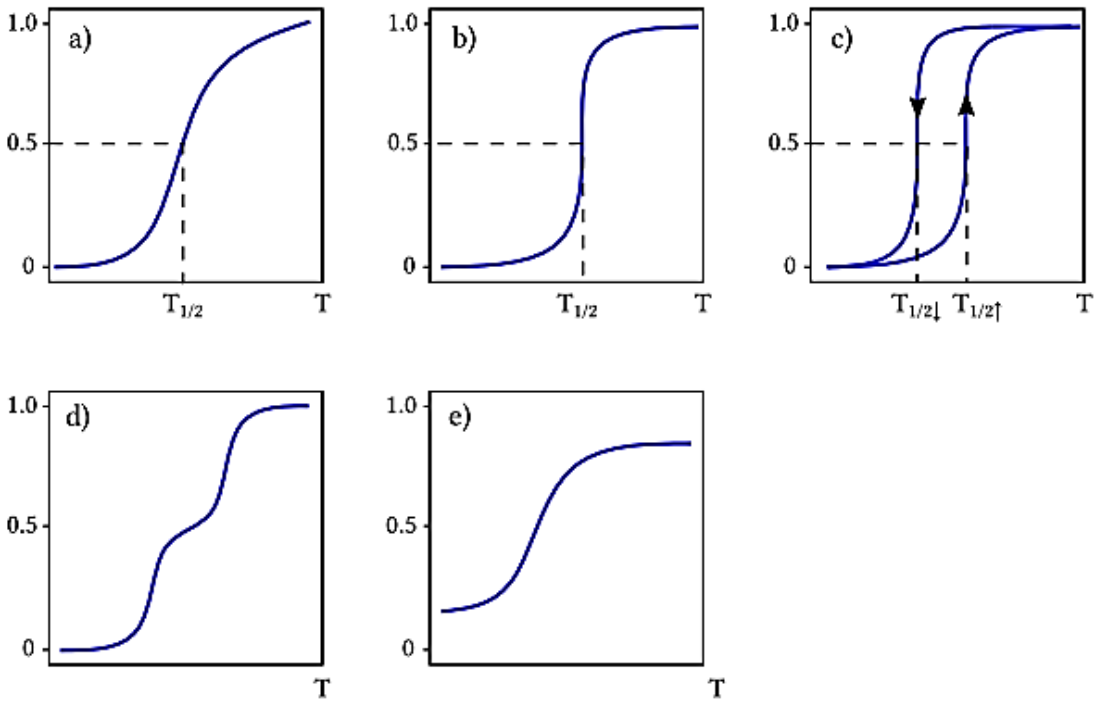

FIG. I.5: Schematic representation of the main thermally induced SCO curves [22]. The spin state change is followed by the thermal evolution of the fraction of molecules in the HS state, the so-called HS fraction (n_{HS}). (a) Gradual spin conversion, (b) abrupt spin transition, (c) abrupt spin transition with hysteresis loop, (d) two-step transition, and (e) incomplete spin conversion.

I.2.2 Macroscopic and mesoscopic approaches

I.2.2.1 Thermodynamic models

Let's consider a SCO material in contact with a pressure and thermal bath, made up of *N* molecules, where the intermolecular forces are negligible. The Gibbs energy of this system can be written as:

$$G = n_{HS}G_{HS} + (1 - n_{HS})G_{LS} - TS_{mix}, \quad \text{(I.17)}$$

where G_{HS} and G_{LS} are the free energy of the HS and LS states, respectively. S_{mix} is the mixing entropy, which corresponds to the loss of statistical information for the system related

to the large number of possibilities to distribute N_{HS} molecules in the HS state among N molecules. According to the Boltzmann's formula, the mixing entropy can be expressed as:

$$S_{mix} = -R[n_{HS}ln(n_{HS}) + (1 - n_{HS})\ln(1 - n_{HS})], \quad \text{(I.18)}$$

The exact stationary solution of the thermodynamic model is found at:

$$\left(\frac{\partial G}{\partial n_{HS}}\right)_{T,P} = 0, \quad \text{(I.19)}$$

Then, it is possible to follow the thermal evolution of the HS fraction (see **FIG. I.6**):

$$T = \frac{\Delta H}{\Delta S + R\ln\left(\frac{1-n_{HS}}{n_{HS}}\right)}, \quad \text{(I.20)}$$

Then the transition temperature $T_{1/2}$ can be obtained from Eq. I.20 through substituting $n_{HS} = 0.5$ as mentioned above.

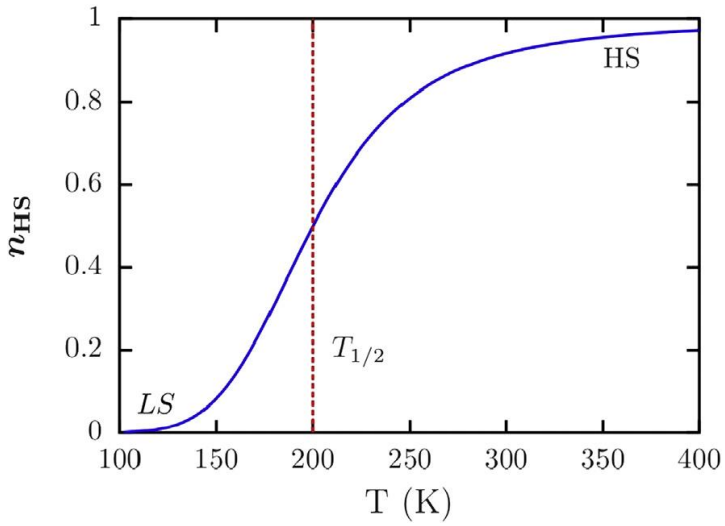

FIG. I.6: Thermal evolution of the HS fraction n_{HS} (blue line) in the case of non-interacting SCO molecules. The equilibrium temperature $T_{1/2}$, where n_{HS} = 0.5 is indicated with a red dashed line.

Cooperative systems

In the thermodynamic approach mentioned above, the molecules do not interact with each other. However, in the solid state, intermolecular interactions can no longer be neglected. The first thermodynamic model considering the intermolecular interactions was introduced by

Slichter and Drickamer in 1972 [23]. In the model, the authors added a nonlinear phenomenological interaction term $\Gamma n_{HS}(1-n_{HS})$ to the total Gibbs free energy (Eq. I.17). The total free energy is then described as:

$$G = n_{HS}G_{HS} + (1-n_{HS})G_{LS} - TS_{mix} + \Gamma n_{HS}(1-n_{HS}), \tag{I.21}$$

where Γ is a phenomenological parameter, which is related to the strength of intermolecular interactions (cooperativity). As before, we can write T as a function of n_{HS}:

$$T = \frac{\Delta H + \Gamma(1-2n_{HS})}{\Delta S + R\ln\left(\frac{1-n_{HS}}{n_{HS}}\right)}, \tag{I.22}$$

It needs to be mentioned that three values of HS fraction can give the same temperature in some cases. This is the signature of the existence of stable, metastable, and unstable states. The stability of the extrema can be verified through the second derivative of Gibbs energy (concave/convex function) around the equilibrium temperature (i.e., n_{HS} = 0.5):

$$\left(\frac{\partial^2 G}{\partial n_{HS}^2}\right)_{T,P,n_{HS}=0.5} = -2\Gamma + 4RT_{1/2}, \tag{I.23}$$

From Eq. I.23, three situations may appear (see **FIG. I. 7**).

When $\Gamma < 2RT_{1/2}$ (weak interaction), $\left(\frac{\partial^2 G}{\partial n_{HS}^2}\right)_{T,P,n_{HS}=0.5} > 0$ and n_{HS} = 0.5 is a minimum point of Gibbs energy. The spin crossover is gradual.

When $\Gamma > 2RT_{1/2}$ (strong interaction), $\left(\frac{\partial^2 G}{\partial n_{HS}^2}\right)_{T,P,n_{HS}=0.5} < 0$ and n_{HS} = 0.5 is a maximum of Gibbs energy. The spin transition is a first order phase transition (abrupt transition) with a hysteresis loop. There are two transition temperatures: $T_{1/2}^{\uparrow}$ (heating process) and $T_{1/2}^{\downarrow}$ (cooling process), which are related to the limit of the metastability. The average $\frac{T_{1/2}^{\uparrow}+T_{1/2}^{\downarrow}}{2}$ is approximately (but not exactly) the equilibrium temperature.

When $\Gamma = 2RT_{1/2}$, the second derivative does not exist. The spin transition is abrupt without hysteresis loop. It is a critical point of the spin transition, associated with the critical temperature $T_C = T_{1/2} = \Gamma/2R$, which gives the limit conditions of the two previous cases.

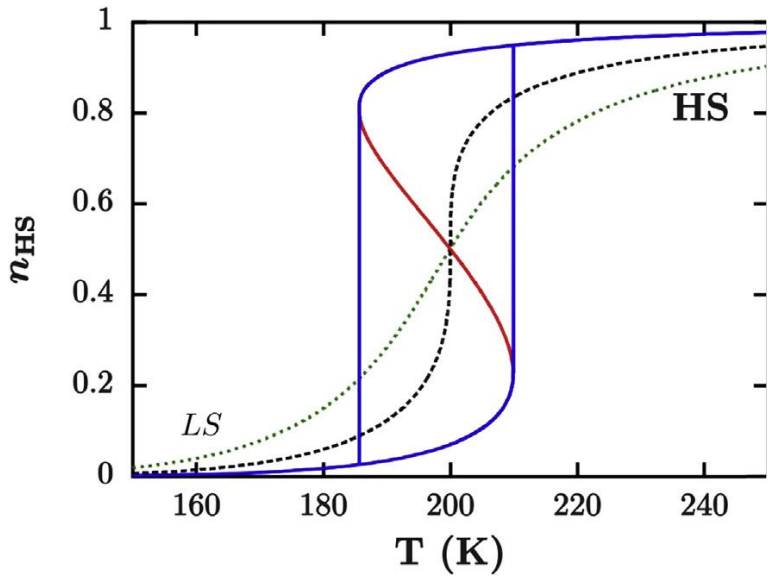

FIG. I.7. Simulation of the thermally induced spin transition by the Slichter and Drickamer model for different interaction strengths. Variations in enthalpy and entropy are, respectively, $\Delta H = 12\ 000\ \mathrm{J \cdot mol^{-1} \cdot K^{-1}}$ and $\Delta S = 60\ \mathrm{J \cdot mol^{-1} \cdot K^{-1}}$. Three different values of Γ have been chosen to illustrate three different situations: the spin conversion (gradual, green dotted line) $2RT_{1/2} > \Gamma = 2\ 000\ \mathrm{J \cdot mol^{-1}}$, the abrupt transition (black dashed line) $2RT_{1/2} = \Gamma = 3\ 324\ \mathrm{J \cdot mol^{-1}}$, and the first-order transition with hysteresis phenomenon (blue full line) $2RT_{1/2} < \Gamma = 5\ 000\ \mathrm{J \cdot mol^{-1}}$. The red curve represents the instable states of the transition (local maxima of Gibbs energy).

In 1974, the existence of spin like-domains, that is, adjacent molecules in the same spin state, has been proposed by Sorai and Seki [5]. To take into account this finding, they considered that the system is divided in N_D clusters in which molecules have the same spin state. The domains do not interact with each other. In this case, the mixing entropy describes the arrangement of domains instead of the distribution of molecules in the material. The total Gibbs energy can be expressed as:

$$G = n_{HS}G_{HS} + (1 - n_{HS})G_{LS} + n_D RT[n_{HS}ln(n_{HS}) + (1 - n_{HS})\ln(1 - n_{HS})], \qquad \text{(I.24)}$$

where n_D is the number of domains per mole. This so called "domain model" is able to simulate the abrupt spin transitions in the limit of large clusters (high cooperativity). However, it cannot reproduce the hysteretic behaviors.

It is worth to mention also that the intermolecular interaction parameter Γ in the Slichter and Drickamer model was modified by Purcell and Edwards [24]:

$$G_{inter} = g_{HS-HS}I_{HS-HS} + g_{HS-LS}I_{HS-LS} + g_{LS-LS}I_{LS-LS}, \quad \text{(I.25)}$$

where $I_{i\text{-}j}$ is the *i-j* pair number and $g_{i\text{-}j}$ is the interaction energy between molecule pairs *i-j*. In this model, the intermolecular interaction depends on the number and the spin state of the molecule pairs. This model successfully improves the fit of the spin transition curves for the $Fe(phen)_2X_2$ (X=NCS^-, $NCSe^-$, and $NCBH_3^-$) compounds. A direct extension of this formulation to the case of the "domain model" was also proposed.

I.2.2.2 Elastic models

Thermodynamic models make it possible to reproduce the behaviors observed experimentally. However, they ignore the origin of the intermolecular interactions since the cooperative term introduced by Slichter and Drickamer is purely phenomenological [23]. In this context, Zimmermann and König proposed a model in 1977, which took into account the spin-orbit coupling, the effect of low-symmetry ligand field as well as the volume change of the elastic medium [25]. The Hamiltonian was solved in the framework of the Bragg-Williams approximation.

Moreover, to explicitly consider the elastic nature associated with the switching of the spin state, models based on the continuum mechanics were developed. From Eshelby's theory, Ohnishi and Sugano developed an elastic model considering the global deformations of the lattice and the local deformations attributed to the change of the metal-ligand distance during the switching of the spin state[13]. Subsequently, Spiering went further, in particular by clarifying the term of intermolecular interaction [14, 26, 27]. To this aim, he rewrote the Gibbs free energy of a set of SCO molecules dispersed in a host matrix in order to identify the different terms. The Gibbs free energy is expressed as:

$$G = n_{HS}(G_{HS} - G_{LS}) - TS_{mix} + \chi\xi n_{HS} - \chi\gamma n_{HS}^2, \quad \text{(I.26)}$$

where $\chi\xi$ is the energy shift due to the matrix, $\chi\gamma$ is the interaction constant and χ is the concentration of SCO molecules in the lattice/medium. In the following, the HS, LS molecules

and the molecules containing a different metal ion *M* are represented by spheres, whose volumes are v_{HS}, v_{LS} and v_m respectively. The misfit of the molecules to the crystal lattice is expressed by $v_\alpha - v_0$, where α =LS, HS, *M*, and the volume v_0 fits to the lattice site, i.e., the volume provided by the lattice for its molecules. In the following, the lattice is assumed to be an isotropic and homogeneous medium. The elastic energy needed to deform the lattice from volume v_0 to that of v_α is then calculated by [27]:

$$e_\alpha = \frac{1}{2}B(\gamma_0 - 1)\frac{(v_\alpha - v_0)^2}{v_0} - \frac{1}{2}B\gamma_0(\gamma_0 - 1)\frac{(v_\alpha - v_0)^2}{V}, \quad \text{(I.27)}$$

where *B* is the bulk modulus, *V* is the total volume of lattice and γ_0 $(0 < \gamma_0 < 3)$ is the Eshelby's constant representing contribution of the local volume change to the global volume change of the lattice. The first term of Eq. I.27 represents the local deformation induced by the molecule. The second term vanishing in an infinite medium ($V \to \infty$) represents the response of the crystal to the surface, which is interpreted as the volume work according to the image pressure on the surface. This pressure is due to the fact that the volume change of the whole lattice is greater than the local volume change ($v_\alpha - v_0$).

Considering the total elastic energy, the phenomenological terms in Eq. I.26 could be identified by [27]:

$$\gamma_{(\chi)} = \frac{\chi}{2}B\gamma_0(\gamma_0 - 1)\frac{(v_{HS} - v_{LS})^2}{v_m}, \quad \text{(I.28)}$$

$$\xi_{(\chi)} = \frac{\chi}{2}B\gamma_0(\gamma_0 - 1)\frac{(v_{HS} - v_{LS})(v_m - v_{LS})}{v_m}, \quad \text{(I.29)}$$

Eq. I.28 and Eq. I.29 demonstrate that the interaction constant depends on the volume misfit between the HS and LS states as well as on the bulk modulus. Thus, the lattice becomes more cooperative as these two ingredients increase. It is possible to rewrite the total Gibbs free energy in the following form:

$$G = n_{HS}(G_{HS} - G_{LS}) - TS_{mix} + (\xi - \gamma)\chi n_{HS} + \chi\gamma n_{HS}(1 - n_{HS}), \quad \text{(I.30)}$$

$$G = n_{HS}(G_{HS} - G_{LS}) - TS_{mix} + Z\chi n_{HS} + \chi\Gamma n_{HS}(1 - n_{HS}), \quad \text{(I.31)}$$

where $\Gamma n_{HS}(1 - n_{HS})$ is the intermolecular interaction. It should be noted that the internal pressures exerted by the SCO molecules and the elastic response of the whole lattice have been taken into account by the constant *Z*. Depending on the volume granted by the host matrix, the term Zxn_{HS} favors one spin state rather than another, which leads to a modification of the

transition temperature (since linear in n_{HS}). This model was subsequently improved by considering the molecules no longer as hard spheres, but as elastic dipoles. However, it is only valid when the concentration of SCO molecules is low. In the opposite case, the bulk modulus of SCO molecules has to be considered.

I.2.3 Microscopic approaches

I.2.3.1 Ising-like model

Four-level model

The first microscopic model for the spin transition was developed by Wajnflasz and Pick in 1970 [28, 29]. This is a four-level model: two electronic levels Γ_{LS} (LS state) and Γ_{HS} (HS state) corresponding to respectively degeneracies g_{LS} and g_{HS} can be divided into two sub-levels associated with ionic radius r_{LS} and r_{HS}. It is therefore possible to have highly improbable states where the electronic configuration is the LS (HS) state with an ionic radius in HS (LS) state. These states would correspond to transient levels of very high energies.

Two-level model

The four-level model was then transformed into a degenerate two-level Ising-type Hamiltonian by Bousseksou et *al* [18]. In this approach, the LS and HS states are modeled by fictitious spins ($\sigma(\mathrm{LS}) = -1;\ \sigma(\mathrm{HS}) = +1$) with a degeneracy $g_{LS} < g_{HS}$. The Hamiltonian of a set of isolated molecules is then written:

$$H_0 = \frac{1}{2}\delta_0 \sum_{i=1}^{N} \sigma_i, \tag{I.32}$$

where N is the number of molecules and $\delta_0 > 0$ is the energy difference between the two spin states. At zero temperature, it is obvious that the LS state will be favored. On the other hand, at high temperature, it is the high spin state which is favored because of its greater degeneracy. It has been shown that this two-level degenerate model is equivalent to a non-degenerate model where a temperature-dependent field is introduced. The Hamiltonian is then written as [30]:

$$H_0 = \frac{1}{2}[\delta_0 - k_B T \ln(g_{HS}/g_{LS})] \sum_{i=1}^{N} \sigma_i, \tag{I.33}$$

This notation has the advantage of clarifying the role of entropy in the spin transition. The ratio of g_{HS}/g_{LS} takes into account not only the degeneracies of electronic origin but also the degeneracies of vibrational origin. To consider intermolecular interactions within the lattice, an interaction term W_{ij} between molecules i and j is expressed as a function of the fictitious spins. The general Taylor development of this function to the second order is:

$$W_{ij} = C + \frac{1}{2}\delta_1(\sigma_i + \sigma_j) + J\sigma_i\sigma_j, \tag{I.34}$$

where C is an energy constant which is chosen to be zero, δ_1 is a contribution of the lattice to the energy difference between the two spin states which is added to δ_0 to form the parameter Δ_0, improperly called "ligand field" and J is the interaction term between two molecules, which describes the collective effects. Therefore, the total Hamiltonian is:

$$H = \frac{1}{2}\Delta_{eff}\sum_{i=1}^{N}\sigma_i - J\sum_{\langle i,j\rangle}\sigma_i\sigma_j, \tag{I.35}$$

with $\Delta_{eff} = \Delta_0 - k_B T \ln(g_{HS}/g_{LS})$ the temperature dependent field. The summation runs over all the pairs of interactions between first neighbors. When J is positive, the interactions favor HS-HS and LS-LS pairs (ferromagnetic-like interactions) and when J is negative, the interactions favor HS-LS pairs (anti-ferromagnetic-like interactions).

The average of the fictitious spins $m = \langle\sigma\rangle$ is expressed as:

$$m = \frac{1}{z}\sum_{\{\sigma\}}\sigma_i e^{\beta E_i} = n_{HS} - n_{LS}, \tag{I.36}$$

with Z the partition function and $\beta = 1/k_B T$. The HS fraction can be deduced by the relation:

$$n_{HS} = \frac{1+m}{2}, \tag{I.37}$$

Ising type models have the advantage of giving a microscopic description of the collective phenomena that appear in spin transition materials. However, the coupling term J is not sufficient to account for both short-range and long-range interactions. Thus, the Hamiltonian have been modified to include long-range interactions [31]:

$$H = \frac{1}{2}\Delta_{eff}\sum_{i=1}^{N}\sigma_i - J\sum_{\langle i,j\rangle}\sigma_i\sigma_j - G_{(\langle\sigma\rangle)}\sum_{\mathrm{i}}\sigma_i\langle\sigma\rangle, \tag{I.38}$$

where $G_{(\langle\sigma\rangle)}$ is the long-range interaction term depending on the mean value of the fictitious spins. This model makes it possible to observe the competitions between short- and long-range

interactions, allowing to reproduce two-step spin transitions [32] and to tune the shape of the hysteresis loop [33].

I.2.3.2 Elastic microscopic models

In order to properly represent the change of lattice shape due to the volume change of each molecule, different kinds of microscopic elastic models have been proposed. The elastic models incorporate the mechanism of the global and inhomogeneous deformation of the lattice, which is responsible for the feature of the elastic long-range intermolecular interactions. In the elastic models, the molecules are linked by "springs", which determine the shift in position of neighbors and subsequently of all molecules in the system. Accordingly, the interaction terms in Eq. I.35 are replaced by the elastic intermolecular potential [34, 35]:

$$H = \frac{1}{2}\Delta_{eff}\sum_{i=1}^{N}\sigma_i + \sum_{\langle i,j\rangle} V_{ij}^{inter}, \tag{I.39}$$

The most widely used expression of the elastic potential is the harmonic potential:

$$\sum_{\langle i,j\rangle} V_{ij}^{inter} = \sum_{i,j}\frac{K_{spring}}{2}\left(\Delta x_{ij}\right)^2, \tag{I.40}$$

where K_{spring} is the force constant and Δx_{ij} is the individual spring elongation between the neighboring molecules in the lattice. Usually, to maintain the topology of the bond network, the first neighbor interactions and the second neighbor interactions should be considered. Therefore, the intermolecular interaction term will be written as:

$$\sum_{\langle i,j\rangle} V_{ij}^{inter} = \frac{K_1}{2}\sum_{i,j}\left[d_{ij} - \left(r_i + r_j\right)\right]^2 + \frac{K_2}{2}\sum_{i,k}\left[d_{ik} - \sqrt{2}(r_i + r_k)\right]^2, \tag{I.41}$$

where K_1 and K_2 are the force constants between the first neighbors (i, j) and the second neighbors (i, k), respectively. d_{ij} and d_{ik} are the distance between the first neighbors and the second neighbors, respectively. r_i, r_j and r_k are the radii of i, j and k molecules, respectively. The model in the above form is the basis of the so-called electro-elastic approach.

In the case of an anharmonic version of this elastic model, the strength of the intermolecular interactions depends on the equilibrium intermolecular distance [35]. Thus, the Hamiltonian of intermolecular interactions becomes:

$$H_{inter} = \sum_{\langle i,j \rangle} \left[J(d_{ij}) \sigma_i \sigma_j + h(d_{ij}) (\sigma_i + \sigma_j) + D(d_{ij}) \right], \quad \text{(I.42)}$$

where J is the coupling term, $h(d_{ij})$ is the intermolecular phonon contribution in the degeneracy ratio between the HS and LS spin states, which creates an additional field in the total Hamiltonian and $D(d_{ij})$ is the mean potential well over the three possible configurations for the intermolecular interactions. As **FIG. I.8** displays, these three terms can be expressed as a function of the Lennard-Jones (LJ) potentials of the three possible bonds with $A_{ij} V_{ij}^{inter}$ with ij = HH, HL, LH or LL:

$$J(d_{ij}) = \frac{A_{HH} V_{HH}^{inter} + A_{LL} V_{LL}^{inter} - 2A_{HL} V_{HL}^{inter}}{4}, \quad \text{(I.43)}$$

$$h(d_{ij}) = \frac{A_{HH} V_{HH}^{inter} - A_{LL} V_{LL}^{inter}}{4}, \quad \text{(I.44)}$$

$$D(d_{ij}) = \frac{A_{HH} V_{HH}^{inter} + A_{LL} V_{LL}^{inter} + 2A_{HL} V_{HL}^{inter}}{4}, \quad \text{(I.45)}$$

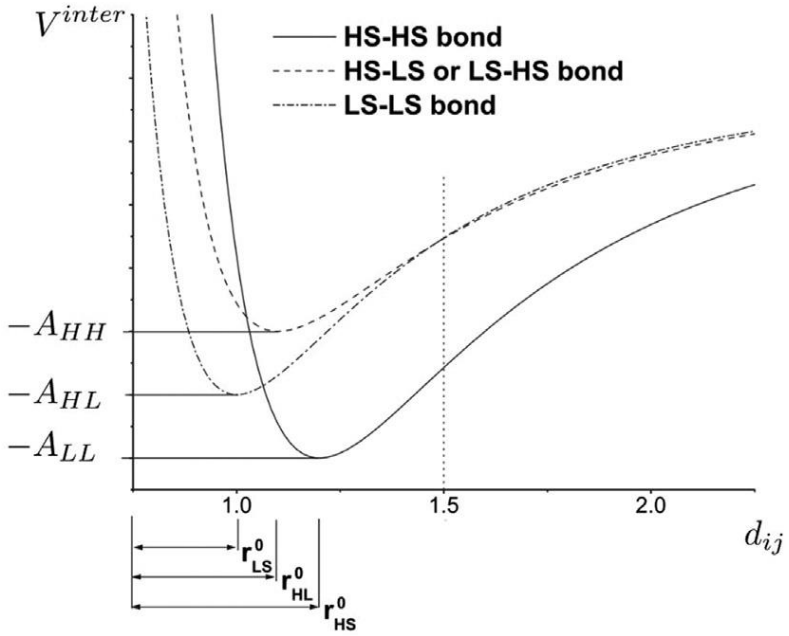

FIG. I.8: Spin-state-dependent Lennard-Jones potential for the anharmonic spin-phonon model. Equilibrium inter-site distances and cohesion energies are dependent on the spin state of the two nearest-neighbour molecules (modelled by Ising fictitious spins) forming the bond.

The so-called two-variable anharmonic model controls the thermal expansion phenomena better than the electro-elastic model. It has been used to simulate X-ray diffraction experiments on

SCO materials, reproducing the crystallographic phase separation (Bragg peak splitting) [36]. The above-mentioned models have been most of the time studied numerically using Monte Carlo (MC) or hybrid MC methods based on the formalism of stochastic equations (master equation).

Another elastic microscopic model, called "atom-phonon model" has been introduced, in which the kinetic energy (*K*) and the potential energy (*V*) have been included in a Hamiltonian as follows [37-40]:

$$H = K + V, \tag{I.46}$$

with:

$$K = \sum_{i=1}^{N} \frac{p_i^2}{2m} + \sum_{i=1}^{N} \frac{P_i^2}{2M}, \tag{I.47}$$

$$V = \sum_{i=1}^{N} V_i^{intra} + \sum_{\langle i,j \rangle} V_{ij}^{inter}, \tag{I.48}$$

where p_i and P_i are the conjugate momenta of the coordinate of the centre x_i and that of the radius r_i, respectively, for the *i*'th molecule. *M* and *m* are the masses of the molecule and the ligand, respectively. As Eq. I.48 shows, the potential energy takes explicitly into account the intra-molecule interaction and the inter-molecule interaction. **FIG. I.9** displays the intra-molecule potential $V^{intra}(x)$ in which the intra-molecular LS potential $y = ax^2$ and the intra-molecular HS one $y = b(x-c)^2 + d$ (broken lines) are mixed by the off-diagonal element *J*, corresponding to higher order spin coupling terms. In the Born-Oppenheimer approximation, the intra-molecular adiabatic potential is given by [41]:

$$V^{intra}(x) = \frac{A}{2}\left(d + b(c-x)^2 - ax^2 - \sqrt{4J^2 + (d + b(c-x)^2 - ax^2)^2}\right), \tag{I.49}$$

More recently, a similar Double-Well potential has been proposed by Nadeem *et al*. to study the light-induced spin-state trapping (LIESST) in SCO materials [42]:

$$V_{intra}(Q) = \frac{V_{\widetilde{HS}}(Q) + V_{\widetilde{LS}}(Q)}{2} - \sqrt{\left(\frac{V_{\widetilde{HS}}(Q) - V_{\widetilde{LS}}(Q)}{2}\right)^2 + \lambda^2}, \tag{I.50}$$

where $V_{\widetilde{HS}}(Q)$ and $V_{\widetilde{LS}}(Q)$ are the potential energy surfaces for the two spin states, λ is the effective coupling and Q is related to the bond length.

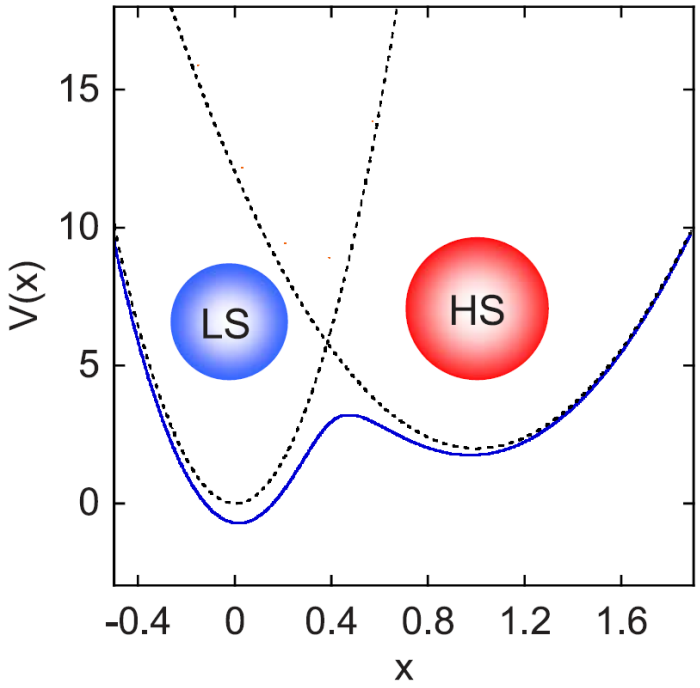

FIG. I.9. Intramolecular interaction energy described by Double-Well potential shown by the blue curve. The dotted curves are the LS and HS potential energy without quantum mixing.

The exponential-type inter-molecular potential is often used with the following expression [37-40]:

$$f(u) = C\left(e^{a'(u-u_0)} + e^{-b'(u-u_0)}\right), \tag{I.51}$$

where C corresponds to the strength of the interaction and a' and b' are model parameters. u_0 is a constant such that the function has the minimum at $u = 0$. When two molecules contact each other, $f(u)$ has a minimum value. The atom-phonon model, usually solved by the molecular dynamics (MD) method [37-40], have been thus carried out to qualitatively study the cooperativity, thermal expansion, clustering mechanism and density of vibrational states. These works allow to qualitatively explain the origin of the cooperativity and the mechanism of the vibrational entropy driven first-order spin transition in SCO materials.

Unlike Monte Carlo methods, the natural ensemble of a MD simulation is the microcanonical ensemble corresponding to conservative systems where all extensive quantities - energy, volume, particle number - are constant. Indeed, MD simulations were initially developed to solve Newton's laws of motion for systems submitted to conservative forces. Therefore, a thermostat and/or barostat has to be modeled. A possible option is the introduction

of a deterministic thermostat such as the so-called Nosé-Hoover thermostat [43, 44]. This implies to consider the degrees of freedom of the thermostat and to couple this latter with the studied system.

Elastic models constitute a step forward for the understanding of the cooperativity of SCO materials. Both the MD and MC approaches are able to describe the different aspects of the spin-transition more precisely than the mean-field or Ising-like models. Besides, they are able to reproduce macroscopic curves as well as microscopic evolutions in bulk materials. They are also able to simulate and explain some aspects of the finite size effects observed in small particles at the nanometer scale as well as nucleation and domain growth mechanisms [40, 45-48]. However, in MC approaches, the time evolution of probability distributions and thermal average quantities are governed by a master equation in which the "real time", i.e. time coming from dynamic fundamental equations, is not considered. The system in the MC simulation is in contact with an ideal pressure and thermal bath, which makes it difficult to simulate thermal diffusion and other transport properties through the definition of local pressure or temperature. In contrast, MD simulations make it possible to study the dynamics of the system in "real time" and to investigate out of thermodynamic equilibrium systems. However, the MD simulations are performed over relatively short times (of the order of the nanosecond) in comparison with the course of the spin transition at the macroscopic level (several hundred milliseconds). In addition, the temperature and pressure are controlled by adding a viscosity/damping term to the system or additional stochastic forces (Andersen thermostat, Langevin dynamics) without any real physical meaning. In order to combine the advantages of each method, several hybrid methods were then developed.

Notably, Nishino combined MC and MD methods to study the HS/LS interface growth in a 2-dimensional interface model [49]. In this hybrid MC/MD method, the elastic model in combination with the MC method was used to control the spin-state switching and the MD method was then employed to control the lattice relaxation. It is well-known that the time scale of the traditional MD simulations ranges from picosecond (ps) to microsecond (μs), while it is from microsecond to millisecond (ms) for MC simulations - provided the time scale of these computational algorithms based on random samplings can be related to the real time (kinetic/diffusive Monte Carlo methods) [50]. In order to control the ratio of two timescales, a simple relation was proposed:

$$\hat{L} = \left(\hat{L}_{latt}\right)^{n}\left(\hat{L}_{spin}\right)^{m}, \tag{I.52}$$

where $\hat{L}_{latt}$ represents the MD time evolution of the molecular positions and $\hat{L}_{spin}$ represents the time evolution of the spin states in the MC simulation. Through tuning parameters *n* and *m*, the relative times scales of the spin switching and lattice relaxation can be changed. In this approach, it is thus essential to find a suitable relative ratio of time scales between two different methods during the simulation.

In another approach, Paesani *et al*. employed a hybrid MC/MD method based on ligand field molecular mechanics (LFMM) to study the thermally induced spin transition in the $[Fe(pyrazine)_2][Pt(CN)_4]$ compound as well as the effects of rotations of pyrazine ligands and guest molecules on the SCO properties [51-53]. Although this method can simulate a realistic structure, it is quite time consuming, which makes it less possible to simulate systems with large sizes.

So far, to our best knowledge, the so-called all-atom MD method, which can describe the evolutions of bond lengths and angles during the spin transition, has not been reported yet. Based on a force field whose parameters can be obtained from experimental data, the all-atom MD method can simulate large systems with an acceptable computational time. More importantly, this method can provide information concerning non-equilibrium states in the real-time, which appear to be essential for the investigation of spatio-temporal dynamics (relaxation kinetics, domain growths, interface propagations).

I. 3 The spin transition at the nano-metric scale

After developing a coordination complex with a spin transition around room temperature, Olivier Kahn's group came up with the idea of applying this type of material to various fields, for example, to create a new type of molecular memory. Kahn was also a pioneer in working towards the potential application of SCO materials in nanoscale devices. Following this innovative idea, considerable efforts have been made over the past 20 years in the development of nanoscale SCO materials. The size of SCO materials can be decreased along either one direction (thin films) or the three axes (nanoparticles). The ability to change the spin state under various external stimuli as well as the possible presence of memory effects make SCO complexes excellent candidates for their integration into new nano-optical, nano-electrical

and/or nano-mechanical devices. However, a relevant question is what happens to the bistability and the phase stability when the size is decreased?

In the following, we present a brief history of the elaboration of SCO nano-objects, in particular, nanoparticles and thin films. The effect of the size reduction on the physical properties of SCO materials is also discussed.

I. 3.1 Nanoparticles

I. 3.1.1 The Fe(II)-triazole family

The first synthesis of SCO nanoparticles was reported by Létard *et al.* in 2004. The authors observed a thermally induced hysteresis loop in 70 nm nanoparticles of the $[Fe(NH_2trz)_3]Br_2$ compound obtained by a reverse micelle technique [54, 55]. In 2007, Coronado *et al.* synthesized nanoparticles of the $[Fe(Htrz)_2(trz)](BF_4)$ compound with a size of ~15 nm [56]. The authors observed the presence of a 43 K wide hysteresis cycle with $T_{\uparrow} = 386$ K and $T_{\downarrow} = 343$ K. Subsequently, in 2010, they succeeded in synthesizing 6 nm nanoparticles [57]. Again, the hysteresis cycle is observed, but with a smaller width (29 K). Moreover, the spin transition is incomplete with a residual HS fraction of 33 % at low temperature. More recently, in 2015, the size reduction effect on the SCO properties for the $[Fe(Htrz)_2(trz)](BF_4)$ nanoparticles was studied again [58]. Importantly, for the different sizes investigated, the SCO nanoparticles preserve the characteristic abruptness of the spin transition, with, however, a decrease in the hysteresis loop width occurs when the size is reduced (see **FIG. I. 10** (b)). Nevertheless, relatively large hysteresis loop is preserved even for 4 nm particles. Meanwhile, other works, such as those of Durand *et al.* [59], show the existence of a hysteresis loop in 3 - 4 nm $[Fe(Htrz)_2(trz)](BF_4)$s nanoparticles synthesized in silica pores.

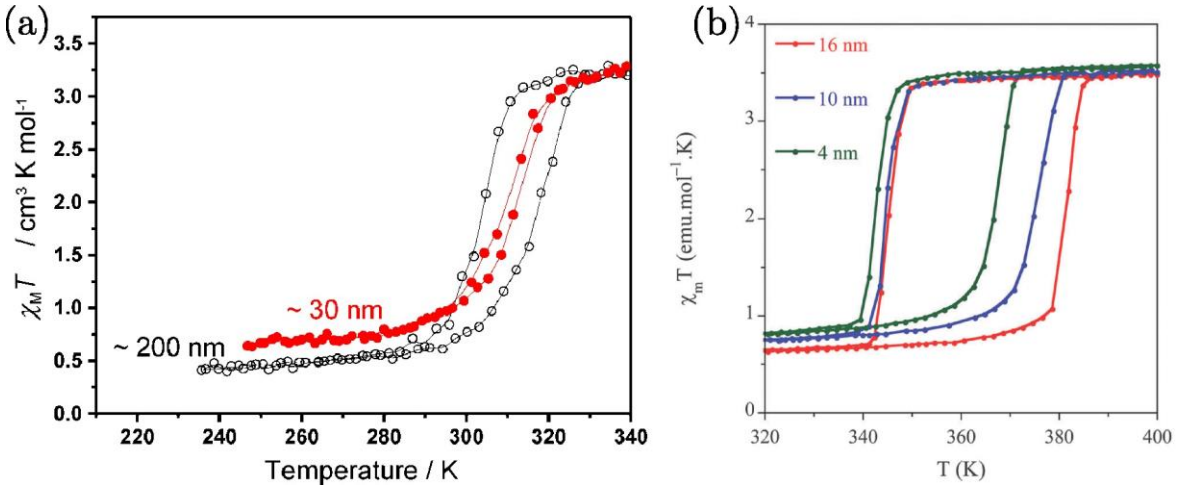

FIG. I. 10. Thermal hysteresis of the magnetic susceptibility (per mole of Fe) for different sizes of nano-particles. (a) In the case of $[Fe(NH_2trz)_3]Br_2$ nanoparticles [60]. (b) In the case of $[Fe(Htrz)_2(trz)](BF_4)$ nanoparticles [56].

In parallel, Létard's team shows the progressive loss of the hysteresis loop as the size of $[Fe(NH_2trz)_3]Br_2$ particles reduces from 200 nm to 30 nm [60, 61] (see **FIG. I.10** (a)). Besides, using temperature-dependent UV-visible absorption measurements, our team reveals that 10 nm particles of $[Fe(NH_2trz)_3](OTs)_2$ exhibit an abrupt spin transition with a hysteresis loop and that only a sharp transition without detectable hysteresis loop was observed for 3-4 nm particles [62-64]. Finally, nanoparticles of the $[Fe(hptrz)_3](OTs)_2$ (hptrz = 4-heptyl-1,2,4-triazole, Ts = para-toluenesulfonyl) compound were obtained through both heterogeneous and homogeneous approaches with or without using different stabilizers [65]. However, in comparison with the bulk sample of $[Fe(hptrz)_3](OTs)_2$, the size reduction effects appear to be rather weak on the SCO properties.

I. 3.1.2 The Hofmann-like clathrates

In 2008, nanoparticles of the Hofmann-like clathrate $[Fe(L)][M(CN)_4]$ (L=bridging ligand as pyrazine (pz), azopyridine (azpy), etc., M=Pt or Ni) for different sizes are synthesized by different groups through different chemical approaches. On one hand, the Real and Mallah teams used the water-in-oil microemulsion technique to prepare different size (8-250 nm)

nanoparticles of the [Fe(pyrazine)][Pt(CN)$_4$] compound [66, 67]. The study of the magnetic properties of the nanoparticles revealed that with size reduction, the nanoparticles display the SCO behavior, which is drastically different from the bulk – in contrast to the Fe(II)-triazole family. Indeed, as shown in **FIG. I.11** (a), there is a loss of the hysteresis cycle, a decrease in the transition temperature and the appearance of the residual HS fraction at low temperatures with the size reduction [67]. Due to the fact that surface/volume ratio is close to the residual HS fraction at low temperature, it has been hypothesized that the residual HS molecules could be located on the surface. On the other hand, the synthesis of ultra-small nanoparticles of the [Fe(pyrazine)][Pt(CN)$_4$] compound has been successfully realized using a chitosan polymeric matrix by Larionova *et al.* [68]. The porous chitosan allows the growth of ~ 4 nm nanoparticles with a narrow size distribution. The authors observed an incomplete spin transition as well as the presence of a hysteresis loop with a width of a few Kelvins (see **FIG. I.11** (b)). Mössbauer spectroscopy reveals that in addition to a residual HS fraction of 34 % at low temperature, there is a residual LS fraction of 38 % at high temperature. Similar observations were also reported by Peng *et al.* [69].

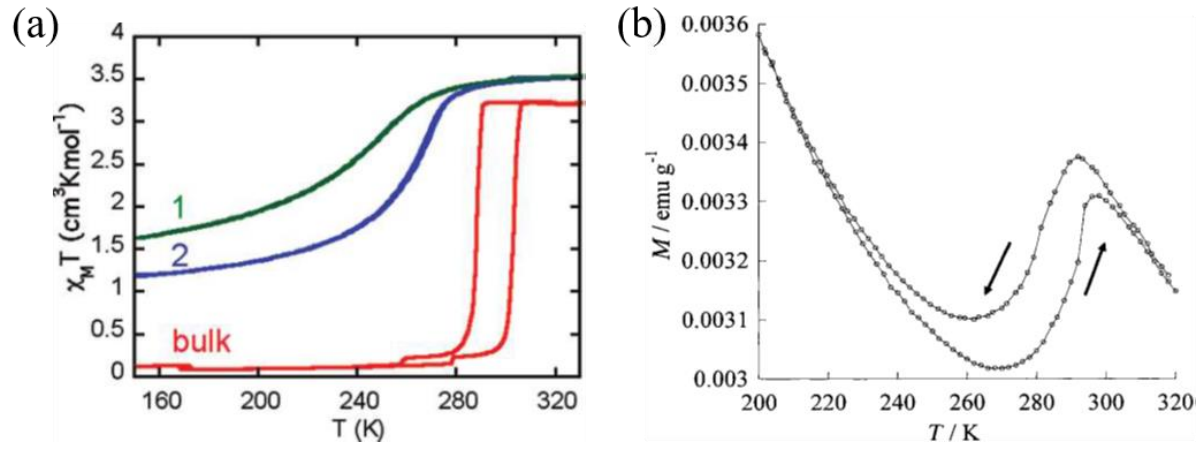

FIG. I.11. (a) Magnetic properties of nanocrystals of [Fe(pyrazine)][Pt(CN)$_4$] of $15 \times 15 \times 5$ and $8 \times 8 \times 3$ nm^3 size compared with that of the bulk [67]. (b) Temperature dependence of the magnetization measured for the 3-4 nm [Fe(pyrazine)][Ni(CN)$_4$] nanoparticles in a chitosan (bio-polymer) matrix [68].

I. 3.1.3 Molecular complexes

There are only a few reported SCO nanoparticles based on molecular complexes and even fewer studies of size effects. It is worth to mention that Tissot *et al.* synthesized $[Fe^{III}(3\text{-MeO-SalEen})_2]PF_6$ SCO nanoparticles of controlled size ranging from 7.5 µm to 18 nm [70]. The 7.5 µm particle shows an abrupt spin transition with the presence of a narrow hysteresis loop. With the size reduction, the loss of the hysteresis loop and an increasingly gradual transition could be noticed. However, regardless of the size, no residual HS fraction is observed at low temperature (see **FIG. I. 12** (a)). Similar results have been obtained for the compound $Fe(phen)_2(NCS)_2$ (see **FIG. I. 12** (b)) [71]. In both cases, an abrupt transition is observed for larger sizes. As the size decreases, the transition becomes more and more gradual. However, it remains complete and without a significant change in the transition temperature.

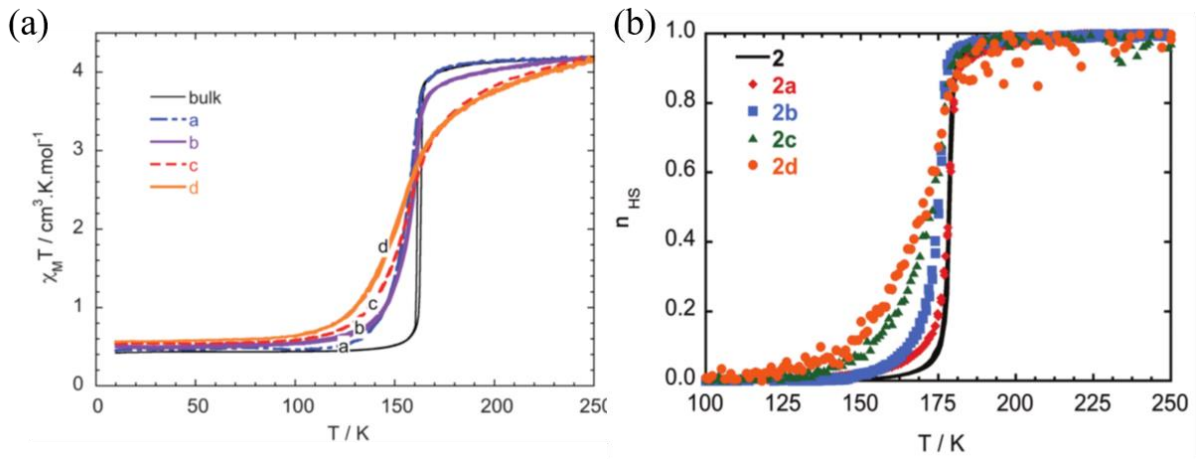

FIG. I. 12. (a) Magnetic properties of $[Fe(III)(3\text{-MeO-SalEen})_2]PF_6$ particles with sizes ranging from **d** = 18 nm to **a** = 8 µm (**b** = 950 nm and **c** = 3.5 µm) [70]. (b) Spin transition curves extracted from magnetic measurements on the $Fe(phen)_2(NCS)_2$ compound with different sizes of 20 nm **(2d),** 29 nm **(2c),** $650^2 \times 175$ nm^3 **(2b),** $1.4^2 \times 0.35$ µm^3 **(2a)** and the pure polycrystalline sample **(2)** [71].

Overall, compared to the Fe(II)-triazole compounds which can retain the bulk-like SCO properties with large hysteresis down to a few nanometers, Hofmann-like clathrates show a more pronounced change of their physical properties with size reduction. In contrast, molecular

complexes appear to keep a complete spin transition and a near-constant equilibrium temperature as the size decreases, but their SCO curves become more and more gradual.

I. 3.2 Thin films

The first approach used for the elaboration of thin films of spin crossover complexes was the Langmuir-Blodgett (LB) technique [72]. This method consists in forming a monolayer of compound on the surface of an aqueous solution through the presence of amphiphilic molecules. By immersion of a solid substrate, it is possible to obtain a film with a monolayer thickness. If several consecutive cycles are applied the final thickness will correspond to the sum of the monolayers. The first fabrication of thin films of SCO compounds using the LB method was reported in 1998 by Soyer et al. [73]. This film was developed using an amphiphilic iron (II) complex $[Fe^{II}L_2(NCS)_2]$, with L a substituted bipyridine. The LB technique can provide very good homogeneity and thickness control of the order of one monolayer, but as a disadvantage requires the presence of specific amphiphilic functional groups in the SCO, and is therefore materials-dependent. Later, growth of SCO thin films on solid surfaces was achieved using the sequential surface assembly approach, spin coating, drop casting, or thermal evaporation techniques.

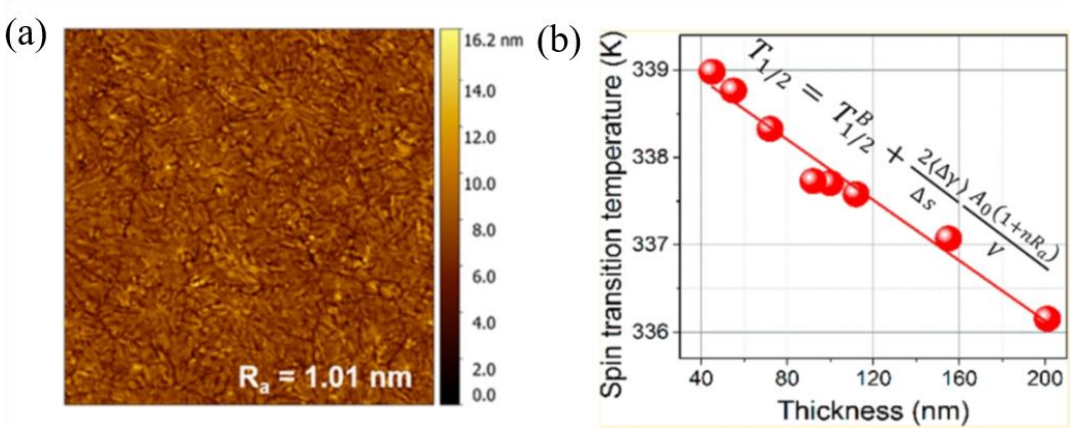

FIG. I. 13. (a) Representative AFM topography image of a 45 nm thick film of $[Fe(HB(tz)_3)_2]$ (b) The transition temperature of the thin film as a function of the thickness. The curve was fitted by a nano-thermodynamic model taking into account the surface properties in a phenomenological way [74].

The thermal evaporation technique makes it possible to obtain thin films with a thickness ranging from nanometer to micrometer. Relying on this method, Shalabaeva et *al.* [74] were able to grow high quality thin films of the $[Fe^{II}(HB(tz)_3)_2]$(tz= 1,2,4-triazol-1-yl) complex (see **FIG. I. 13** (a)). This work highlighted a 3 K increase of the transition temperature when the thickness of the thin layer decreases from 200 nm to 40 nm (see **FIG. I. 13** (b)). This result is important because until now we systematically observed a decrease in the transition temperature with the size reduction. This original behavior was numerically simulated using a nano-thermodynamic model taking into account both the difference of surface energy between the HS and LS states and the strong anisotropy of mechanical properties when the system changes the spin state. On the other hand, the $[Fe^{II}((3,5\text{-}(CH_3)_2Pz)_3BH)_2]$, (Pz = pyrazolyl) ultrathin films grown on different metallic surfaces have been systematically investigated [75-82]. Interestingly, the studies on thermally induced spin transition of these films stressed a residual HS fraction at low temperature, a downshift of transition temperature as well as a loss of cooperativity with the decrease in thickness [83, 84].

Furthermore, thin films of the SCO coordination complexes [Fe(pyrazine)][$M(CN)_4$] (M=Ni, Pd, or Pt) were fabricated by Cobo et al. using the layer-by-layer (LBL) method in 2006 [85]. A gold-coated silicon substrate was first functionalized with a disulfide-based anchoring layer to ensure a quasi-epitaxy between the surface and the material to be deposited. Then, the process comprises a number of deposition cycles, each cycle corresponding to the assembly of the Fe center, the tetracyanometalate unit and the pyrazine ligand. The multilayers obtained revealed a hysteresis loop with a width of 25 K centered around 310 K. This approach has been extended to novel coordination polymers displaying thermal, guest and light-induced SCO phenomena [86-88]. Sakaida studied the thermally induced SCO properties of [$Fe(pyridine)_2$][$Pt(CN)_4$] thin films prepared through the LB method for different thicknesses [89]. The authors found a downshift of transition temperature and they reported that the SCO curve becomes less steep with the occurrence of a residual HS fraction when the thickness of the thin film is reduced. Subsequently, Haraguchi et al. investigated the SCO properties of the heterostructured [Fe(pyrazine)][$Ni(CN)_4$]-[Fe(pyrazine)][$Pt(CN)_4$] thin films fabricated by the LB method, composed of 5 layers of [Fe(pyrazine)][$Ni(CN)_4$] (bottom buffer layer) and 30-90 layers of [Fe(pyrazine)][$Pt(CN)_4$] [90]. They found that the transition temperature of the [Fe(pyrazine)][$Pt(CN)_4$] layer can be controlled in the range of 300-380 K by introducing the

[Fe(pyrazine)][Ni(CN)$_4$] buffer layer, where the smaller lattice parameter of the buffer layer causes a compressive strain to the [Fe(pyrazine)][Pt(CN)$_4$] (see **FIG. I. 14**).

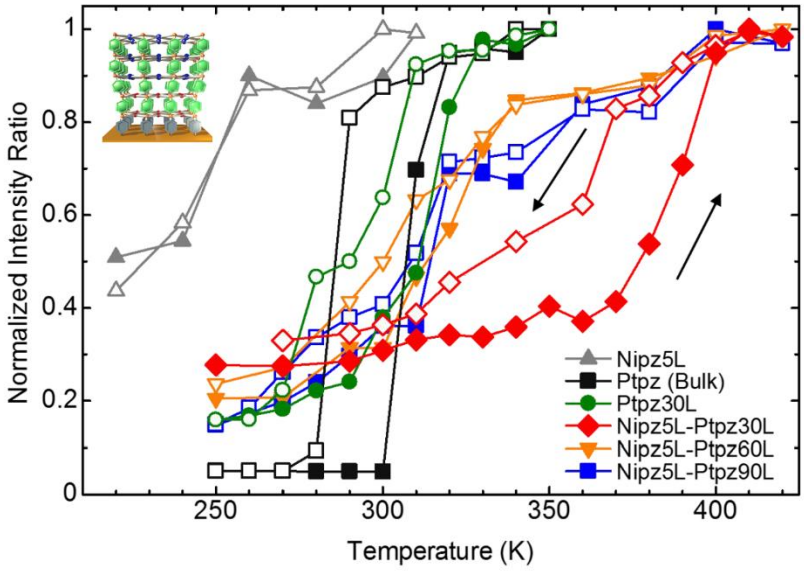

FIG. I.14: Temperature dependence of the normalized Raman intensity ratio (intensity of ν(ring)/intensity of δ(CH)). Filled and open symbols denote heating and cooling processes, respectively [90].

I.4 Mechanism behind the size effects

I.4.1 Atomistic modeling

As mentioned above, experimental observations in some coordination nanoparticles demonstrate that the size reduction results in a downshift of the equilibrium temperature and incomplete spin transitions. Indeed, a number of residual HS molecules remain in the nanoparticles at low temperature and the associated HS fraction increases with the rise in the surface-to-volume ratio suggesting the presence of inactive molecules at the surface. The origin of inactive molecules at the surface with different physical and chemical properties may be attributed to surface chemical reactions, structural disorder and/or the alteration of the ligand by the external environment. This finding has been first considered *ad hoc* by adding specific boundary conditions (e.g. surface molecules fixed in the HS state or by weakening the ligand field at the surface). The investigation of surface effects in squared nanoparticles using the

Ising-like model with such specific boundary conditions (surface molecules fixed in the HS state) has demonstrated that the HS surface sheet acts as a "negative pressure" [91], and pressure effects can be grasped through an effective modification of the ligand field [91]. This leads to a downshift in the equilibrium temperature, which follows an algebraic law with the size (**FIG. I. 15** (a)).

FIG. I.15 (b) shows the investigation of the thermal spin transition of circle-shaped nanoparticles in a core-shell structure, where the shell is simulated by forced HS molecules on the surface, using an electro-elastic model [92]. This work demonstrated that the hysteresis loop shifts to a lower temperature with the reduction of the size of the particle due to the existence of the HS shell which applies a negative stress on the active SCO core and that the presence of a large hysteresis is related to a thin and stiff shell.

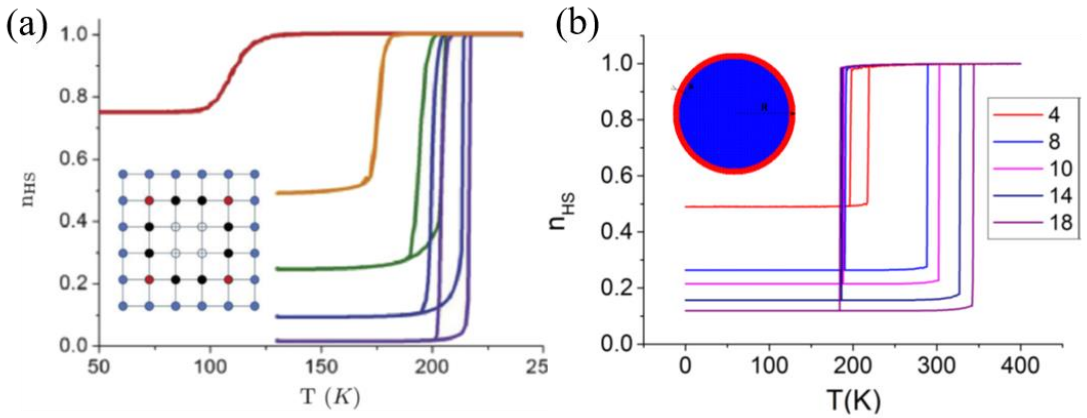

FIG. I.15: Temperature dependence of the HS fraction of (a) square-shaped nanoparticle for different sizes (L) with fixed boundary condition (HS molecules fixed at the surface) simulated using an Ising-like model. From left to right, L = 4, 7, 10, 40, 200 [91]. (b) Spin transition in circle-shaped nanoparticles with different radii with the HS state blocked at the surface, modeled by the so-called electro-elastic model [92].

Mikolasek et *al*. [93] showed that the surface physico-chemical properties could affect all the vibrational properties of nano-objects, modifying the electron-phonon coupling and consequently they play a role in the existence of the bistability phenomenon at the nanometric scale. For this purpose, the study of the effects of surface on the vibrational properties of a cubic-shaped nanoparticle was carried out through calculating the mean square displacement by MC methods. The simulations revealed an inhomogeneous distribution of the root mean

square displacement near the surface and a high value of this quantity near the vertices of the cube (see **FIG. I.16**). In other words, the mechanical (or vibrational) properties of the surface are different from those of the interior of the nanoparticle, because molecules located on the surface are immersed in a different environment than those located in the core of the nano-object (mainly due to a lack of coordination for the molecules located on the surface). Further investigations using the two-variable microscopic Ising-like model stressed the significant contribution of surface relaxations to the transition temperature [94, 95].

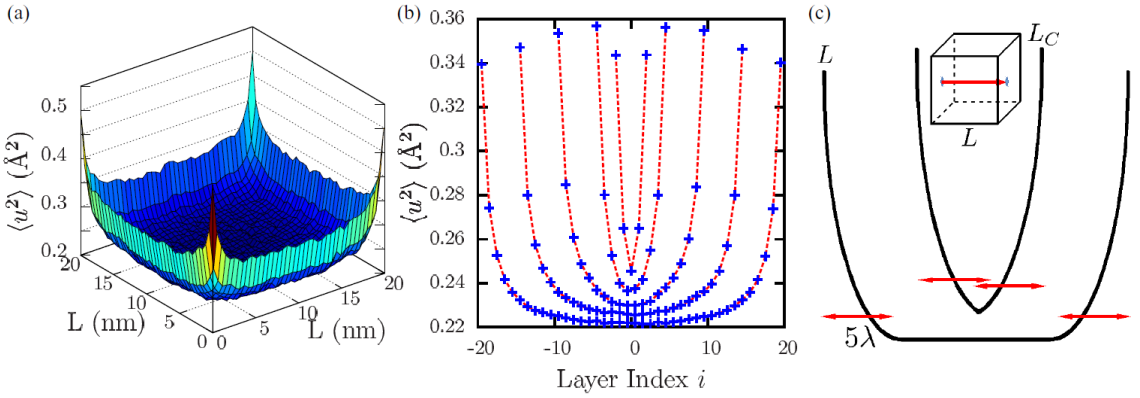

FIG. I.16: (a) Spatial distribution of the local mean-square displacements for a section of a cubic system of size N = 403 with free surfaces. (b) Corresponding averaged profile of local mean-square displacements for different system sizes (N = 53, 103, 203, 303, and 403). The center of the cube is taken as the reference to identify the layers between two opposite surfaces. (c) Schematic representation of the surface effects on the lattice dynamics at the nanometric scale where λ is the characteristic surface thickness. When $L \approx Lc$, the vibrational properties of the system are completely different from the corresponding bulk material ($L \gg Lc$) [93].

To highlight the effects of solid-solid interfaces on the SCO properties of bilayer/multilayer films and core-shell particles, Affes et *al.* [96] used the electro-elastic model to simulate the thermally induced spin transition considering an SCO membrane deposited on a substrate. By tuning the substrate lattice parameter, it is possible to observe a change of the transition temperature of the SCO membrane (**FIG. I. 17** (a)). This means that the phase stability of SCO molecules can be controlled by the mechanical stress (interface energy) at the interfaces. This work underlined also the importance of the elastic deformation generated by the misfit lattice parameters between the HS and LS phases on the propagation velocity of HS/LS phase boundaries. The increase of the lattice mismatch between the two layers leads to

an increase of the interface elastic energy inducing a decrease in the propagation velocity of the boundary, which affects the nucleation dynamics. Furthermore, using the mechano-elastic model, Anastasia et *al.* studied the epitaxial effects experienced by one single monolayer of self-assembled molecules in contact with a substrate which owns a larger lattice parameter [97]. It is found that the increase of the strength of the interaction between substrate and SCO monolayer brings out larger residual HS fractions and a decrease of the transition temperature (**FIG. I. 17** (b)). These phenomena are caused by the shrinking of the layer while molecules switch from larger volume HS to lower volume LS state, which produces larger elastic forces between the SCO layer and the substrate. These forces, directly depending on the value of the elastic constant of the springs linking the SCO molecules to substrate, gradually decrease the HS → LS transition probabilities with every molecule switching from HS to LS state.

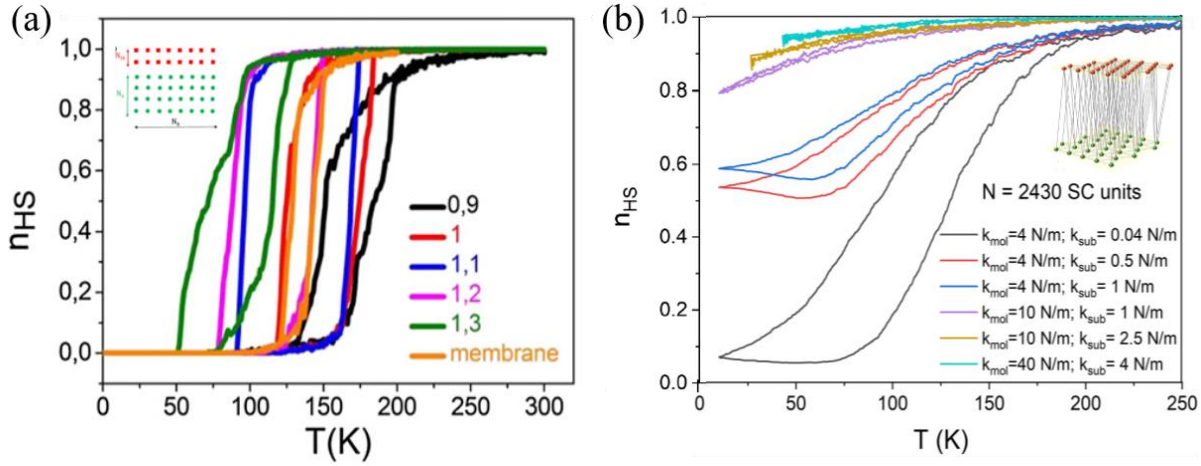

FIG. I. 17. Temperature dependence of HS fraction (a) as a function of the thickness of an SCO membrane, calculated using the electro-elastic model [96]. (b) SCO curves for different spring constants between the SCO layer and the substrate, calculated using the mechano-elastic model [97].

Interface effects also exist in the case of SCO particles embedded in a matrix. In a first approach, Stoleriu considered SCO nanoparticles embedded into a polymer environment [98]. The polymer is represented in this approach as a rigid or flexible shell of non-switching molecules, which interact with the molecules situated at the edge of the lattice by way of springs, with a given elastic constant denoted as k_{pol}. The MC simulation showed that when the HS to LS transition occurs, an increasing negative pressure appears at the edge of the system due to the existence of interface, giving rise to a downshift of transition temperature and a

residual HS fraction (**FIG. I. 18** (a)). Oubouchou *et al*. performed calculations using the electro-vibration model [99] and considering a nanoparticle embedded in a matrix whose elastic properties and structure are similar to the HS phase ("weak" interface). The analysis of the strain and local pressure mappings showed that increasing the thickness of the surrounding medium leads to a release of the elastic strain at the nanoparticle/matrix interface and a decrease in the transition temperature (**FIG. I. 18** (b)). Moreover, Felix *et al*. studied core–shell nanoparticles displaying SCO effect in the shell and/or in the core using a two-variable anharmonic model [100]. It was found that the SCO transition temperature can be controlled by adjusting the width of the shell and the width of the core as well as the misfit between the lattice constants (**FIG. I. 18** (c)).

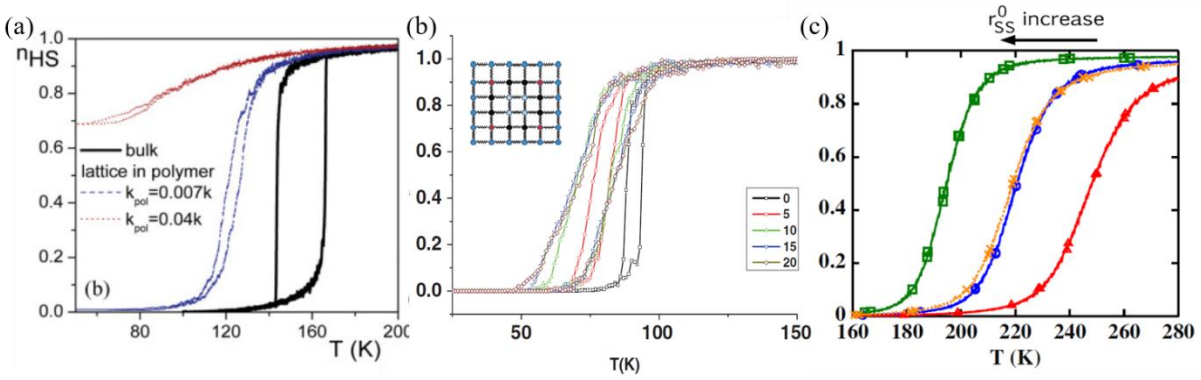

FIG. I. 18. (a)Thermal hysteresis for a bulk SCO system (thick full line) and nanoparticles embedded in a polymer matrix (thin dashed and dotted lines) simulated with the mechano-elastic model [98]. (b) Simulation using the electro-elastic model of the thermal dependence of the HS fraction for square-shaped SCO nanoparticles at constant core size L = 10 surrounded by various numbers of HS shell layers. The hysteresis shifts downwards as a result of the negative elastic pressure induced by the shell [99]. (c) Spin transition curves without (dotted line, cross symbols) and with (solid lines) an inactive shell. Square, circle and triangle symbols represent thermal spin transition curves of core–shell nanoparticles for different shell lattice parameters: r^0_{ss}= 6.83, 6.7, 6.57 Å, respectively. [100].

Furthermore, due to the existence of LS/HS interfaces, mechanical deformations could also appear during the spin state switching in a core-shell system or in a multilayer system, such as an SCO membrane deposited on a rigid substrate (see **FIG. I. 19**) [97, 101]. It is well-known that the bimetallic strip consisting of two kinds of materials is forced to bend under heating or cooling due to the different coefficients of thermal expansion of the materials. Nevertheless,

the potential applications of the traditional bimetallic actuators are greatly limited by the fact that the volume change induced through the thermal expansion is too small to produce large motion. In this regard, the SCO complexes provide a fascinating potential to be integrated into bilayer actuator devices [102-106].

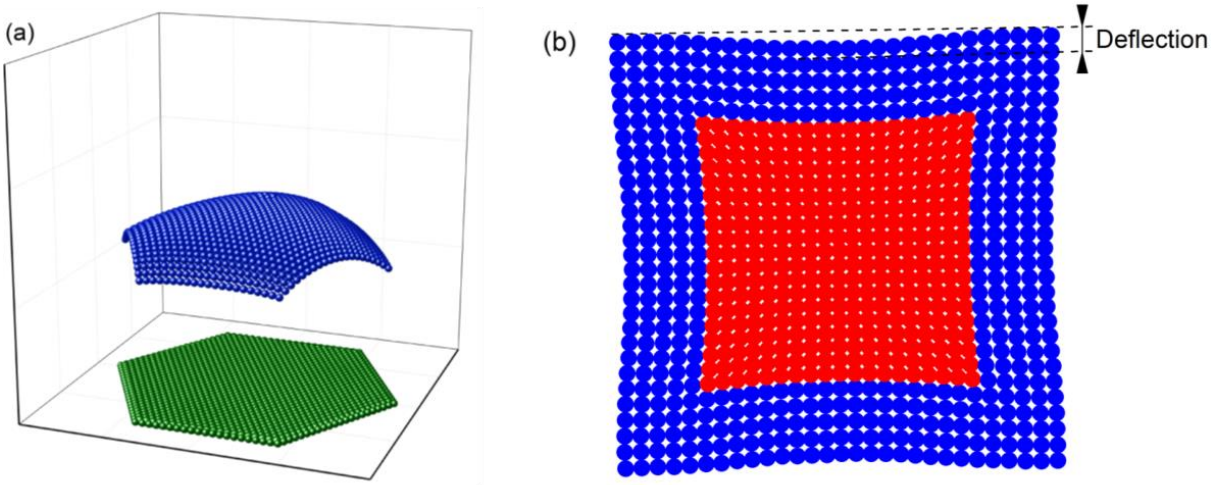

FIG. I. 19. (a) Simulation using the mechano-elastic model of a system constituted of a SCO membrane deposited on a rigid substrate showing large local distortions [97]. (b) Snapshot of the LS core embedded in the HS shell calculated with the electro-elastic model [101].

I.4.2 Nano-thermodynamic modeling

It is well-known that atoms at a surface/interface have a different local environment than the atoms in the bulk. It results in different equilibrium positions and energies of surface/interface atoms in comparison with atoms in the bulk. Properties of the solid which are sensitive to the atomic positions or energies will necessarily be affected at or near a surface. As discussed above, the atomistic simulations have revealed that the physical properties of surfaces/interfaces seem to be one of the driving forces of the spin transition at the nanometric scale. However, it is difficult to relate the experimentally obtained macroscopic quantities (e.g. elastic moduli) to the parameters of atomistic models. In this context, nano-thermodynamics naturally plays an increasingly important role by providing a more direct link with experiments and by explicitly considering the different contributions of surface.

Surface energy effects on the SCO behavior were first studied by Félix *et al.* through a nano-thermodynamic model [107]. In this work, a spherical core-shell model composed of $N = N_c + N_s$ molecules is considered. N_c and N_s are the numbers of molecules in the core and shell, respectively. The number of molecules at the surface is defined by $N_s = A/A_0$, with A the surface area of the nanoparticle and A_0 the unit cell surface area. In the case of a spherical particle, a simple relation exists between the volume and the surface:

$$\frac{A}{V} = \frac{4\pi r^2}{4/3\pi r^3} = \frac{3}{r}, \tag{I.53}$$

The numbers of molecules on the surface and in the core are then written as:

$$N_s = N\frac{3V_0}{rA_0} = N\alpha_s, \tag{I.54}$$

$$N_c = N\left(1 - \frac{3V_0}{rA_0}\right) = N\alpha_c, \tag{I.55}$$

where α_s and α_c are, respectively, the ratios of molecules at the surface and in the core. The total HS fraction is calculated according to the HS fractions on the surface and in the core:

$$n_{HS} = n_{HS}^s\alpha_s + n_{HS}^s\alpha_c, \tag{I.56}$$

The total surface energy depends on the spin state of the surface:

$$\gamma A = \gamma_{LS}A + n_{HS}^s(\gamma_{HS} - \gamma_{LS})A = n_{HS}^s\gamma_{HS}A + (1 - n_{HS}^s)\gamma_{LS}A, \tag{I.57}$$

It is assumed that the surface area does not change during the spin transition.

Since the HS fraction on the surface is not the same than that in the core, it is necessary to rewrite the total mixing entropy:

$$S_{mix} = S_{mix}^s + S_{mix}^c, \tag{I.58}$$

where S_{mix}^s and S_{mix}^c are the mixing entropies on the surface and in the core, respectively, which can be expressed as:

$$S_{mix}^s = -R[n_{HS}^s \ln(n_{HS}^s) + (1 - n_{HS}^s)\ln(1 - n_{HS}^s)], \tag{I.59}$$

$$S_{mix}^c = -R[n_{HS}^c \ln(n_{HS}^c) + (1 - n_{HS}^c)\ln(1 - n_{HS}^c)], \tag{I.60}$$

Compared to the thermodynamical model introduced by Slichter and Drickamer, Félix's model takes account into the variation of the spin state dependence of the elastic intermolecular interactions (Γ). As mentioned above, the intermolecular interactions can be related to the bulk

modulus of the lattice ($\Gamma \propto B$). Considering a linear variation of the bulk modulus with the HS fraction, Γ follows the relation:

$$\Gamma = \Gamma_{LS} + n_{HS}(\Gamma_{HS} - \Gamma_{LS}), \tag{I.61}$$

Finally, considering all the above-mentioned contributions, the total Gibbs free energy of the spherical core-shell model can be expressed as:

$$G = n_{HS}G_{HS} + (1 - n_{HS})G_{LS} + \Gamma n_{HS}(1 - n_{HS}) - T(S^c_{mix} + S^s_{mix}) + [n^s_{HS}\gamma_{HS} + (1 - n^s_{HS})\gamma_{LS}]A, \tag{I.62}$$

The exact stationary solution of the thermodynamic model is found at $\frac{\partial G}{\partial x^b} = 0$ and $\frac{\partial G}{\partial x^s} = 0$, which brings out the following system of two equations:

$$T = \frac{\Delta H + \Gamma(1 - 2\alpha_c n^c_{HS}) + \Delta\Gamma n_{HS}(1 - n_{HS}) - 2\alpha_s \Gamma n^s_{HS}}{R \ln\left(\frac{1 - n^c_{HS}}{n^c_{HS}}\right) + \Delta S}, \tag{I.63}$$

$$T = \frac{\Delta H + \Gamma(1 - 2\alpha_s n^s_{HS}) + \Delta\Gamma n_{HS}(1 - n_{HS}) - 2\alpha_c \Gamma n^c_{HS} + \Delta\gamma A}{R \ln\left(\frac{1 - n^s_{HS}}{n^s_{HS}}\right) + \Delta S}, \tag{I.64}$$

This numerical study shows that the difference of surface energy ($\Delta\gamma$) between the two spin states leads to either a downshift ($\Delta\gamma < 0$) or an upper shift ($\Delta\gamma > 0$) of the transition temperature (see **FIG. I.20**). Besides, if the difference is large enough $\Delta\gamma = -0.1$ J · m^{-2} (resp. $\Delta\gamma = +0.1$ J · m^{-2}), the molecules on the surface will be blocked in the LS (resp. HS) state. As the residual HS fraction has been observed by several experimental approaches, this model predicts that the surface energy of HS state is lower than that of LS state. This prediction can be understood in a simple way by noting that the cohesive energy is lower in the HS state than in the LS state. Thus, the energy cost associated with breaking a bond to create a surface is lower in the HS state than in the LS state.

From a thermodynamic point of view, the surface effect can be described by two important quantities: the surface energy (γ) and the surface stress (σ). As shown in **FIG. I.21**, the surface energy is the work per unit area involved in forming a surface, which exposes new atoms [108-110]. This property describes the irreversible work to form a new surface in the solid state, which is related to cleavage processes. In the solid state, the surface stress is the work per unit area needed to elastically stretch a pre-existing surface. Both surface energy and surface stress have impacts on the phase stability at reduced size, it is therefore necessary to further clarify the role of surface stress in the SCO behavior at the nano-metric scale.

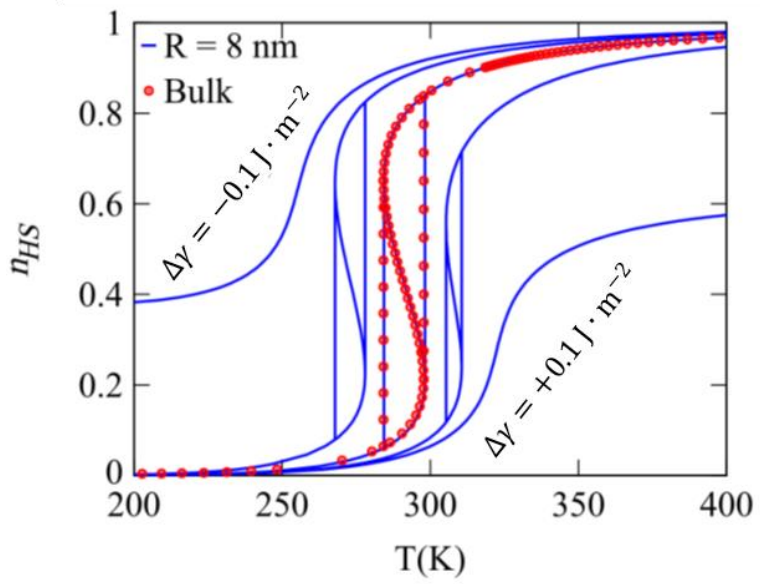

FIG. I. 20: Thermally induced spin transition curves calculated for a bulk SCO material and 8 nm nanoparticles with different values of $\Delta\gamma$ using the nanothermodynamical model [107].

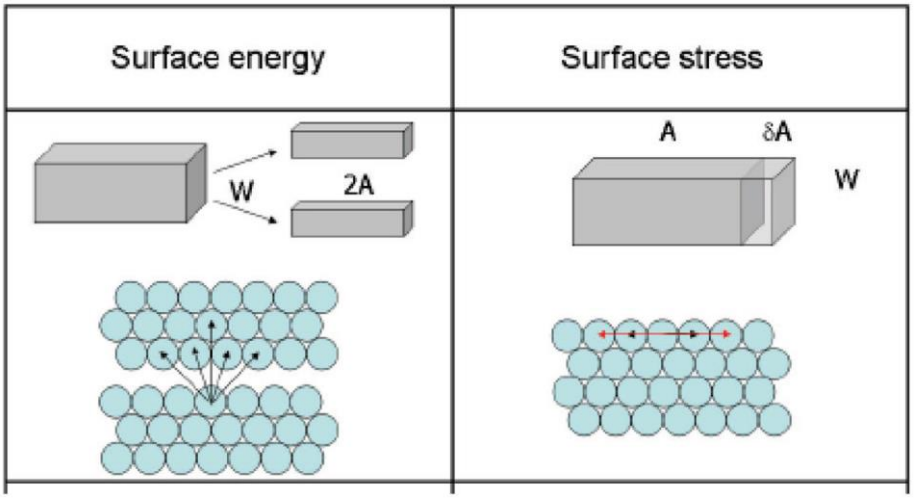

FIG. I.21. Schematic representation of the difference between surface energy and surface stress [109].

In a different approach, an analytical modelling of core-shell nanoparticles with a coherent interface using continuum mechanics theory has been developed by Félix *et al.* [111]. In this model, the total Gibbs energy is written as:

$$G(T, P_{ext}, n_{HS}) = n_{HS}G_{HS} + (1 - n_{HS})G_{LS} - TS_{mix} + \Gamma n_{HS}(1 - n_{HS}) + U_{def}(n_{HS}), \quad \text{(I.65)}$$

where $U_{def}(n_{HS})$ is the spin-state dependence of the elastic deformation energy, which can be derived from the interfacial stress (P_{in}). Therefore, analytical expressions of the interfacial stress (P_{in}) and the interfacial elastic energy density have been derived as a function of the Young's modulus (Y), the Poisson ratio (υ) as well as the size (a, b) of the core (subscript 1) and the shell (subscript 2):

$$P_{in} = \frac{2b^2 a_2 p_{ext} \frac{1-\upsilon_2^2}{Y_2(Y_2 - a_2^2)} + a_1 - a_2}{\frac{a_1}{Y_1}(1+\upsilon_1)(1-2\upsilon_1) + \frac{a_2}{Y_2(b^2 - a_2^2)}\frac{1+\upsilon_2}{}\left[(1-2\upsilon_2)a_2^2 + b^2\right]}, \quad \text{(I.66)}$$

where a_1 and a_2 represent the radius of the core and that of the shell hole, respectively. c represents the radius when the core and hole surfaces are in contact ($a_1 = a_2$) (see **FIG. I. 22**). A quantitative investigation of the impact of the interfacial elastic energy on the phase stability can also be performed to optimize the elastic coupling between the core and the shell. The spin transition of the core-shell nanoparticle can be simulated by injecting the interfacial energy density into a nano-thermodynamic model. It is important to note that the role of the elastic misfit on the collective behavior and the bistability phenomenon cannot be grasped with this model, because the elastic interaction between molecules is not explicitly taken into account in the model and also the elastic interfacial stress cannot be coupled with the distortions occurring during the spin state change.

More recently, Fahs *et al.* [112] proposed a simple thermomechanical model to investigate the contributions of surface energy and interface stress to size effects in SCO thin films. In this model, the equilibrium temperature of a system containing surface and interface can be expressed as:

$$T_{eq} \approx \frac{\Delta H + \Delta G_S + \Delta G_{int}}{\Delta S} = T_{eq}^{b} + \delta T_{eq}^{s} + \delta T_{eq}^{int}, \quad \text{(I.66)}$$

where T_{eq}^{b} is the equilibrium temperature of the bulk material. δT_{eq}^{s} and δT_{eq}^{int} represent the change in transition temperature due to the presence of surfaces and interfaces, respectively. ΔG_S and ΔG_{int} correspond to surface and interface elastic Gibbs free energies, respectively, which can be calculated as follows:

$$\Delta G_S = \gamma_{eff}^{HS}\alpha_S^{HS} - \gamma_{eff}^{LS}\alpha_S^{LS}, \quad \text{(I.67)}$$

$$\Delta G_{int} = \alpha_I\left(\bar{S}_{eff}^{HS} - \bar{S}_{eff}^{LS}\right), \quad \text{(I.68)}$$

where γ_{eff}^{HS} and γ_{eff}^{LS} are the effective surface energies of the HS and LS states, respectively. α_S^{HS} and α_S^{LS} are the elementary surface unit cell areas of the HS and LS states, respectively. α_I is the mean elementary interface area. Finally, $\bar{S}_{eff}^{HS}$ and $\bar{S}_{eff}^{LS}$ are the effective interface stresses of the HS and LS phases, respectively. The surface energy and HS/LS interface stress values have been calculated by means of MD simulations and were then injected into this simple thermomechanical model. This work predicted a ≈10 K downshift of the spin transition temperature with the size reduction. Whereas surface energy favors systematically the HS state, this is not the case for the interface stress. Indeed, it is demonstrated that the LS state is stabilized by the anisotropy of mechanical interface stresses.

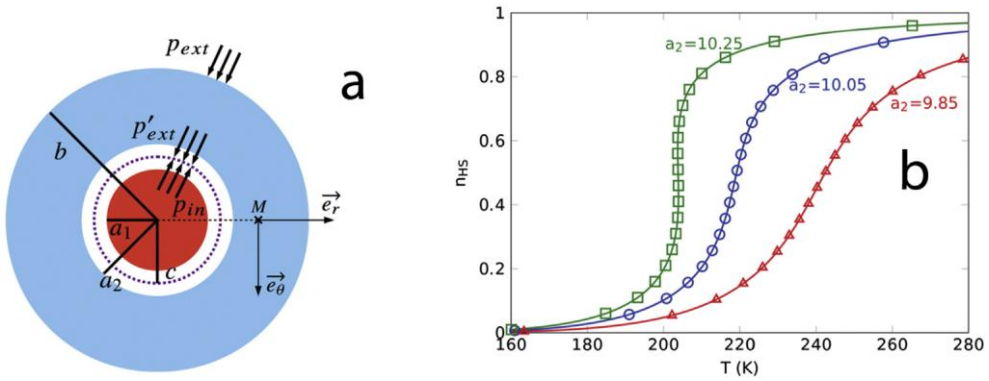

FIG. I. 22: (a) Scheme of an elastic circular core-shell particle. The pressure exerted by the core on the shell is the same as the pressure exerted by the shell on the core, $P_{in} = P'_{ext}$; (b) Spin transition curves of SCO nanoparticles with an inactive shell simulated by a thermodynamic model taking into account the core-shell interfacial elastic energy. When an elastic misfit exists between the core and the shell, the elastic interfacial energy favors either the HS state (green squares) or the LS state (red triangles) depending on the sign of the misfit, whereas the spin transition curve remains unchanged in comparison with an isolated nanoparticle in the absence of misfit (blue circles). [111]

I.4.3 Lattice dynamics

I.4.3.1 Experimental observations

Understanding the lattice dynamical properties of the SCO nanomaterials is of paramount importance in order to design nanomaterials with well-controlled spin-state switching properties. Indeed, the spin transition phenomenon gives rise to a modification of the density of vibrational states (vDOS) with important consequences on different thermodynamic and mechanical properties, such as the vibrational entropy, vibrational enthalpy, elastic constant and stiffness of the lattice. In particular, the vibrational entropy variation between the HS and LS states can be considered as the main driving force of the thermally induced spin transition, while the lattice stiffness plays a crucial role in the cooperative phenomena. Thus, the study of vibrational properties at the nano-scale could offer an exhaustive and quantitative understanding of the physico-chemical phenomena observed in the SCO nanomaterials.

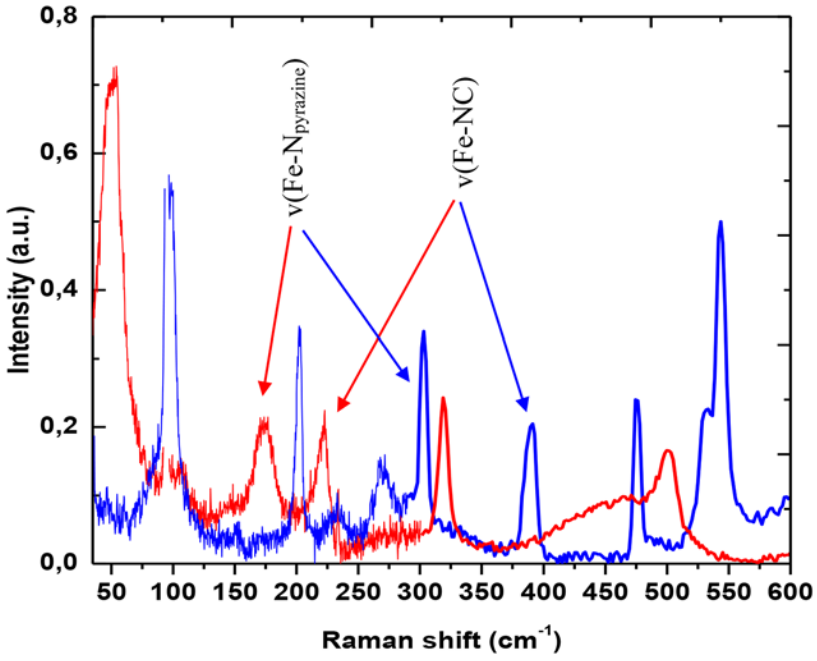

FIG. I. 23. Raman spectra of the [Fe(pyrazine)][Pd(CN)$_4$] compound in the spectral region of the Fe-N vibrations. Red curve: HS state. Blue curve: LS state. [7].

Several studies on the vibrational properties of SCO materials have been carried out in order to understand the spin-state switching process directly related to the thermodynamic properties of the lattice as well as the mechanisms of cooperativity [113-124]. For example, the vibrational modes of the [Fe(pyrazine)][Pd(CN)$_4$] compound were measured by Raman spectroscopy in the range between 50 and 2000 cm^{-1} [7]. Specifically, the low frequencies

between 25 and 600 cm^{-1} are mainly attributed to the metal-ligand vibrations, whereas the high frequencies (> 600 cm^{-1}) are the vibrations of the ligands. One can see from **FIG. I. 23** that the Fe-N stretching modes shift to low frequencies as the molecule switches from the LS to the HS state [7].

In parallel, synchrotron nuclear inelastic scattering (NIS) was used to extract the partial density of vibrational states (vDOS) for different particle sizes. This method, described by Chumakov and Struhahn [125], was employed by Gautier et *al.* [126] to assess the vibrational properties of the [^{57}Fe(pyrazine)Ni(CN)$_4$] compound in the two spin states. Then, Rat et *al.* [127] used the same method to measure the vDOS of the SCO complex [Fe($H_2B(pz)_2)_2$(phen)]. As a rough approximation, the vDOS can be classified into low-energy acoustic modes below ca. 50 cm^{-1} and higher energy optical modes. When switching from the HS to the LS state, the authors detected that the optical modes related to Fe atom displacements shift significantly to higher frequencies, which agrees with Raman spectroscopy measurements [7]. Relying on NIS, Mikolasek et *al.* measured the vDOS of [^{57}Fe (pyrazine)(Ni(CN)$_4$)] SCO nanoparticles at different temperatures and for different particle sizes to study the effects of size reduction on the lattice dynamics [128]. The extracted vibrational energy, which is sensitive to the high-frequency part of the vDOS, does not show a size dependence. On the other hand, the vibrational entropy, which is sensitive to the low-frequency part of the vDOS, exhibits an obvious increase with size reduction. (**FIG. I. 24**).

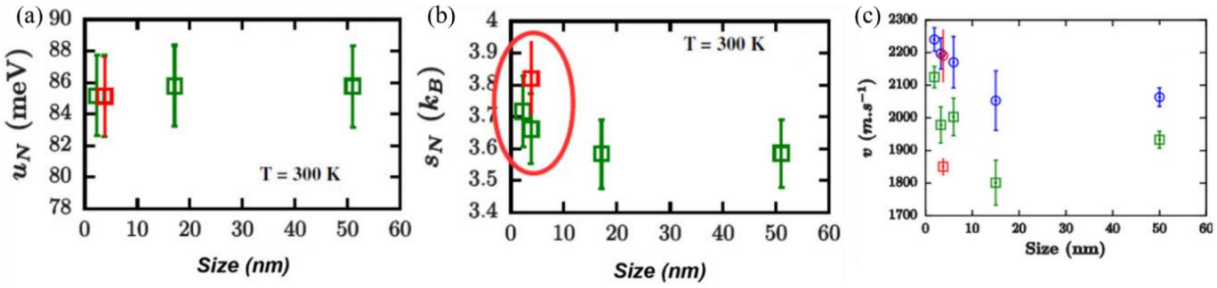

FIG. I. 24. (a) Vibrational energy, (b) vibrational entropy and (c) Debye sound velocity as a function of the particle size for the [^{57}Fe(pyrazine)Ni(CN)$_4$] compound. Circles and squares represent the LS and HS states, respectively. [128]

The size reduction of SCO materials affects not only the thermodynamic quantities, but also the stiffness of the lattice. The studies carried out on [Fe(pz)Ni(CN)$_4$] nanoparticles using Mössbauer spectroscopy reveal that the Debye temperature increases from 170 K to 261 K as

the size of the particle is reduced from 107 to 2 nm [69]. Similar results were obtained by Félix et *al* [107] for the Prussian blue analogue nanoparticles of $Ni_3[Fe(CN)_6]$. As the size decreases, the Debye temperature increases by about 40 K. In both cases, the increase in Debye temperature indicates an increase of the lattice stiffness with the size reduction. Those observations were further confirmed by another independent study conducted on $[Fe(pyrazine)Ni(CN)_4]$ nanoparticles using the NIS technique [128]. This study shows that compared to the bulk material, the Debye sound velocity (i.e., the particle stiffness) of the smallest nanoparticle increases by about 9 %, which will impact the cooperativity of the spin transition (**FIG. I. 24**). The increase of the rigidity of the nanoparticles may be attributed to the sensitivity of the nanoparticles to the external environment [93].

I.4.3.2 Numerical simulations

DFT methods have been successfully employed to simulate the vDOS of SCO Complexes [113, 114, 122-124, 129, 130]. In addition, a combination of force field parametrization through DFT calculations with atomistic molecular dynamics simulations has been employed to investigate time-resolved lattice dynamics of multinuclear chain-like triazole Fe (II) complexes [131, 132]. Although such quantum mechanics calculations can reach a high accuracy, the computational time can quickly be unacceptable. A direct consequence of this technical limitation is that, in general, only zone-center (Γ-point) phonon frequencies are reported and most studies limit their focus to optical modes only. However, acoustic phonons are known to play a critical role in driving collective phenomena (phase transitions) in SCO materials and, generally speaking, low-frequency phonons have key importance in governing the HS/LS phase stability through both entropic and elastic contributions [5]. Hence, in order to fully understand the SCO behavior, contributions from all phonons must be considered, which would imply mapping the entire Brillouin zone. Such detailed investigation of the phonon spectrum, including phonon dispersion curves, remains at present a remarkable challenge on SCO materials with complex structures - both experimentally (inelastic neutron scattering) and computationally (quantum mechanics). In the interim, research has been focused on techniques, which give direct access to the low-frequency phonon DOS without the necessity of measuring full dispersion relations.

In this context, the study of the vibrational properties of SCO nanoparticles was carried out by Mikolasek et *al* [133] using MD simulations. This approach based on the classical mechanics and the statistical physics makes it possible to carry out an initial qualitative analysis of surface effects on the SCO properties. The simulated system is an octahedral patterned cubic lattice, which represents the spin transition complexes in a general and simplified way (**FIG. I.25**). The simulations were performed under both periodic and open boundary conditions to study the size effects. In agreement with the experimental results, the lattice dynamics is size independent down to ~5 nm. In the smallest particles (<5– 10 nm), the main size reduction effect is the quantification of the vibrational states, which brings out the opening of an acoustic gap. This gap makes it impossible to extract the Debye sound velocity in the smallest particles.

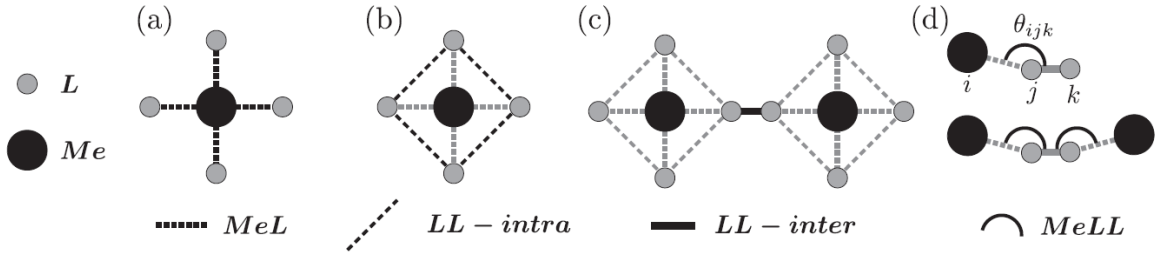

FIG. I.25: 2-dimensional schematic representation of the modeled system with the different interactions between and within the octahedra. [133]

Interestingly, these simulations show a slight decrease of vibrational entropy and an increase of vibrational internal energy (see **FIG. I.26**), which affects both the phase stability and the bistability of the spin transition. However, these results are in discrepancy with the experimental measurements discussed above. The size dependence of the lattice dynamics was then successfully reproduced by Fahs et. al using MD simulations by introducing an anharmonic intermolecular interaction [134]. In particular, the lattice dynamics of SCO materials have been simulated using the so-call *slab method* for different film thicknesses. The authors found that the vDOS of thin films seems to be noisier in comparison with that of the bulk material, a signature of a rarefaction of the number of accessible vibrational modes (see **FIG. I.27**). Moreover, the occurrence of several peaks in the acoustic part of the spectrum, around 5 meV can be observed (upward black arrow on **FIG. I.27**), which significantly contribute to the thermodynamical properties. Therefore, an increase of the vibrational entropy with the size reduction is obtained in good agreement with experimental observations.

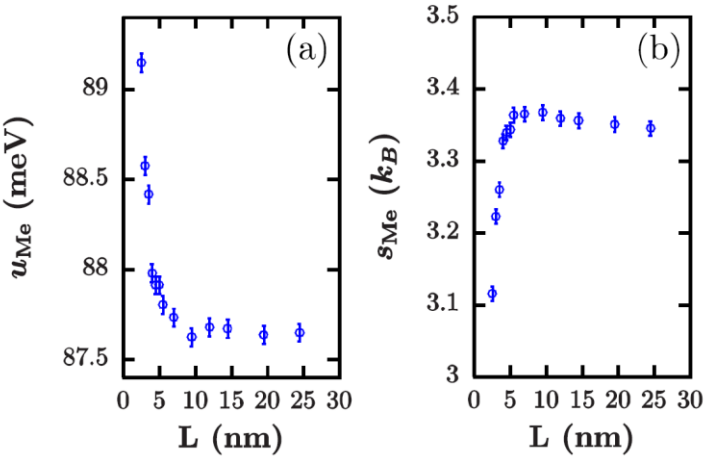

FIG. I.26: (a) Vibrational internal energy per *Me* atom and (b) vibrational entropy per *Me* atom as a function of the particle size from MD simulations on a simple octahedral ML_6 model system [133].

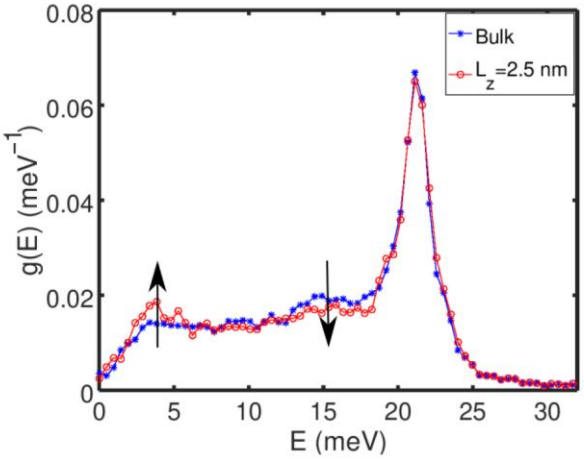

FIG. I.27: Partial vDOS in the HS state for a film of thickness *Lz* = 2.5 nm (red open circles) for the case of a simple octahedral ML_6 model system. The vDOS corresponding to the simulated bulk material is shown for comparison (blue full circles). The arrows indicate the changes in the vDOS [134].

I.5 Objectives

The overall objective of this thesis is to advance the state-of-the-art of numerical simulations of nanoscale SCO materials and thus to achieve a more profound understanding of the mechanisms governing the experimentally observed finite size effects.

As we have seen in this introductive section, there has been a wide array of numerical studies on size effects on SCO materials. Mikolasek *et al* and Fahs *et al* used a simplified octahedral patterned lattice to study the vibrational properties based on MD simulations. However, due to the simplified structure and force field, it remains a challenging task to directly make a comparison between the simulation results and experimental observations. On the other hand, the qualitative "spring-ball" model employed extensively to simulate the spin switching ignore the structural details, which greatly influence different material properties, making it impossible to investigate the interplay between the structure (bonds lengths, angles, …) and the SCO properties. Finally, as presented in Chapter. I.2.3.2, the problems that the MC method and hybrid MC methods are facing, in terms of time scale and thermostat, prevent them to be employed for investigations of dynamical process in "real time" and systems out of thermodynamic equilibrium. To overcome these limitations, in this thesis, we decided to explore possibilities offered by real time, all-atom MD simulation methods, including all the structural information about the material.

From a thermodynamical point of view, a phenomenological parameter Γ including all inter-molecular interactions was used in the nano-thermodynamic model developed by Félix *et al.* [107], which makes it difficult to inject the experimentally accessible physical properties to the model. Moreover, the model used a single parameter, an "effective surface energy", to describe all contributions arising from the presence of surfaces. It appears thus important to develop models, which take into account more explicitly the different contributions (surface energy, surface stress, …).

Accordingly, the first objective of this thesis is the development of force fields for all-atom MD simulations with the aim of building a new elastic model, which is able to describe SCO compounds at the level of chemical bonds. To this aim, new forms of the force field are proposed and the methods to extract the force field parameters from the experimental data (X-ray, Raman and NIS spectroscopic data) are discussed in Chapter II. Then, based on this new force field, the all-atom MD simulations are performed in Chapter III to investigate the spin state switching process in a nanoscale, bimorph beam in order to explore the interface effects on the SCO behavior and the associated mechanical actuation. The last objective is to develop

a nano-thermodynamics model including experimentally accessible physical properties and different contributions of surface (surface energy/surface stress), which is then used to investigate the effects of surface energy/stress on the SCO properties at reduced size scales in Chapter IV.

Chapter II: Construction of the force fields for all-atom Molecular Dynamics simulation

II.1 Introduction

As mentioned in **Chapter I.4.3**, in the field of numerical simulations, DFT methods have been successfully employed to simulate the vDOS of [Fe(pyrazine)][Pt(CN)$_4$] [124, 130]. Although such quantum mechanics calculations can reach a high accuracy, the computational time can be quickly unacceptable. Besides, most studies based on the DFT calculation only focus on the optical modes. In order to catch the contributions from all phonons, the vDOS of simplified model systems was also carried out through MD simulations [133, 134]. However, such model systems just catch the main features of the octahedral coordination of SCO materials - all the more that the parametrization of the force field (FF) is based on experimental data collected for specific compounds.

Moreover, although the Ising-like model solved by MC method successfully reproduced first-order phase transitions with hysteretic behaviors, the cooperative mechanisms are introduced through a phenomenological inter-spin coupling which does not explicitly consider the elastic origin of intermolecular interactions. On the other hand, the atom-phonon model whose description of the intramolecular part is identical to the Ising-like model has been then proposed. However, giving realistic values to these model parameters (e.g extracted for experimental data remains impossible or at least very complicated due to the drastic simplifications involved in these models. In the previous studies, the most widely used "spring-ball" model ignores the intricate details of the framework of the octahedral coordination sphere as well as the structural and crystallographic properties of SCO materials. What is more, the parameters used in these class of "spring-ball" models are mainly obtained by taking order of magnitude and it is hard to reproduce different properties of a specific SCO compound.

In this chapter, a new force field of [Fe(pyrazine)][Ni(CN)$_4$] for the LS and HS states has been constructed from Raman and NIS spectroscopic data. This force field, including simple harmonic and Lennard-Jones type interactions, is thus designed to investigate lattice dynamical properties of bulk [Fe(pyrazine)][Ni(CN)$_4$] in the two spin states. Notably, we show that it can

be used to predict the spin-state dependent values of sound velocity, vibrational entropy and other properties, which stem primarily from the low-frequency part of the vDOS. However, the FFs were built separately for the two spin states, preventing thus the simulation of the spin state switching process. To go further, it becomes necessary to simulate switchable materials by reproducing the effect of the vibronic coupling on the elastic deformation of realistic structures. To this aim, in the present work, inspired by previous reports of Nishino et al. [37-40], we implement a 'vibronic' approach in our recently published FF of the [Fe(pyrazine)][Ni(CN)$_4$] SCO complex, enabling us to model the spin transition process through all-atom MD simulations.

This chapter is organized as follow. First, we discuss the model and methods; in particular, we describe the methodology to extract the parameters of the force field from the experimental data. Then, we show and discuss the numerical results concerning the ability of this force field coupled with all-atom MD techniques to simulate the vibrational properties, the thermally induced spin transition and its impact on the elastic strain of realistic structure.

II.2 The model and method

II.2.1 Force fields for vibrational properties

We study a three-dimensional (3D) network of [Fe(pyrazine)][Ni(CN)$_4$] [51,135]. According to the experimental data [51, 135], the size of the LS and HS tetragonal unit cells is 7.013×7.013×6.776 Å^3 and 7.257×7.257×7.256 Å^3, respectively. As shown in **FIG. II.1** (a), all the atoms are bonded by pair harmonic potentials with different force constants. The bond lengths based on the experimental data [136] and force constants are displayed in **TABLE. II.1**. It should be noted that, the Fe-$N_{N\text{-}C}$ and Fe-N_{cycle} bond lengths are set as 1.944 and 1.973 Å for the LS structure (resp. 2.117 and 2.213 Å for the HS structure). It brings out an increase of about 14.7% of the unit cell volume [136]. For a sake of simplification, all the bond lengths in pyrazine are set to be 1.415 Å.

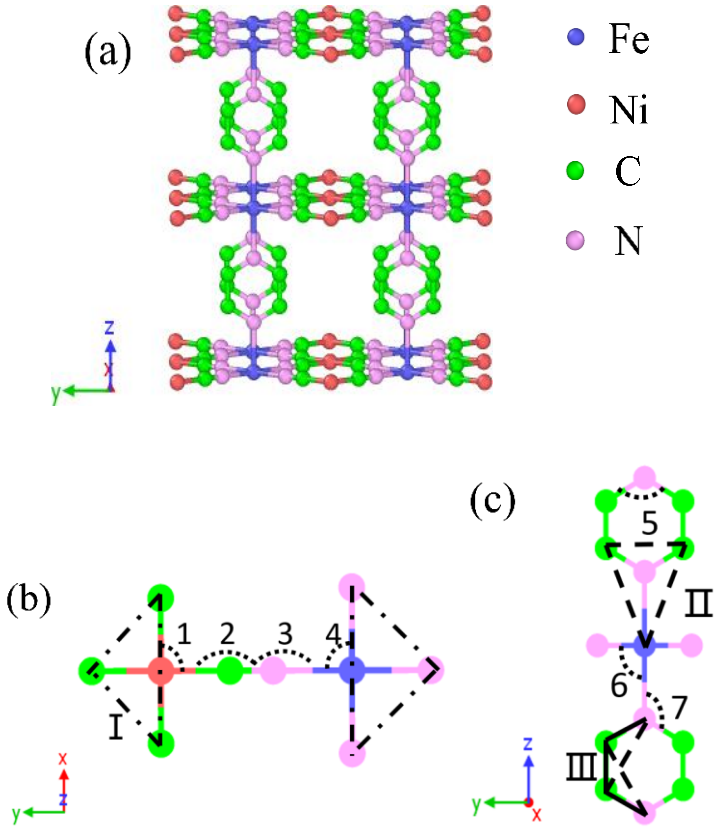

FIG. II.1: (a) Schematic representation of the [Fe(pyrazine)][Ni(CN)$_4$] structure. (b - c) Schematic representation of the force field with the different interactions considered in this work. The lines between two atoms stand for the chemical bonds, which are painted in the color of the corresponding atoms.

TABLE. II.1: Harmonic bond-stretching force constants and bond lengths for the LS and HS states used in the simulations.

Bond	LS		HS	
	Force constants (kcal/mol·Å^2)	Bond lengths (Å)	Force constants (kcal/mol·Å^2)	Bond lengths (Å)
C-N	2512	1.158	2392	1.158
C-Ni	220	1.857	180	1.857
Fe-N_{N-C}	128	1.944	50	2.117
Fe-N_{pz}	96	1.973	28	2.213
C_{pz}-C_{pz}	866	1.415	866	1.415
C_{pz}-N_{pz}	780	1.415	780	1.415

In order to stabilize the structure, as indicated in **FIG. II.1** (b) and (c), 3-body harmonic angular potentials (angles 1, 2 … 7) are introduced in the force field. Based on the crystallographic space group *P4/mmm* [136], angles 1, 4 and 6 are set as 90°; angles 2 and 3 are set as 180°, while angles 5 and 7 are set as 120° for simplification. Furthermore, we also introduce 4-body improper potentials (I and II in **FIG. II.1** (b) and (c)) and a dihedral potential (III in **FIG. II.1** (c)) in order to keep atoms in the same plane. Such 4-body potentials are much weaker than bond potentials and angular potentials, while they play an important role in the low frequency vibrations. The corresponding improper angles I and II are both set as 180°.

According to the above setting, the total potential energy ($E_{potential}$) can be described in the usual way [137] as:

$$E_{potential} = \sum_{bonds}\frac{1}{2}K_b[(b-b_0)^2-(b_c-b_0)^2] + \sum_{angles}\frac{1}{2}K_\theta(\theta-\theta_o)^2 + \sum_{impropers}\frac{1}{2}K_\varphi(\varphi-\varphi_o)^2 + \sum_{dihedrals}\frac{1}{2}K_\emptyset(1-\cos\emptyset) + \epsilon_{ij}\left[\left(\frac{\sigma_{ij}}{r_{ij}}\right)^{12} - 2\left(\frac{\sigma_{ij}}{r_{ij}}\right)^{6}\right], \quad \text{(II.1)}$$

where K_b, K_θ, K_φ and $K_\emptyset$ stand for the force constants of the 2-body bond potential, 3-body angular potential, 4-body improper potential and 4-body dihedral potential, respectively. b, θ, φ and $\emptyset$ are the bond length, angle, improper angle and dihedral angle, respectively, and the subscript 'o' refers to their equilibrium value. The zero-crossing b_c can be roughly estimated by $0.84b_o$ [138]. To describe the non-bonding interaction, a 12-6 Lennard-Jones potential (last term of Eq. II.1) is selected in this work. r_{ij} is the instantaneous distance between atoms i and j, σ_{ij} is the van der Waals bond length and ϵ_{ij} corresponds to the well depth of this anharmonic potential.

We now turn to define the force constants of harmonic potentials and establish relations with experimentally accessible physical quantities. Based on Raman spectroscopy data of [Fe(pyrazine)][Ni(CN)$_4$] [7], the bond potential force constants can be obtained from the harmonic oscillator approximation [139]:

$$K_b = 4\pi^2 c^2 \frac{\mu}{N_o}\omega_e^2, \quad \text{(II.2)}$$

where N_o is the Avogadro number, c is the velocity of light and ω_e is the harmonic frequency from Raman experiment. μ is the reduced mass, defined by:

$$\mu = \frac{m_i m_j}{m_i + m_j}, \quad \text{(II.3)}$$

where m_i and m_j are the masses of atoms *i* and *j*, respectively.

To our best knowledge, there is no effective method in literature to obtain angular, dihedral and improper force constants from experimental data. Thus the harmonic angular force constants of [Fe(pyrazine)][Ni(CN)$_4$] are first estimated by [137]

$$K_\theta = 664.12 \frac{Z_i^* Z_k^*}{r_{ik}^5}\left[3r_{ij}r_{jk}(1-\cos^2\theta_o) - r_{ik}^2\cos\theta_o\right], \quad \text{(II.4)}$$

where Z_i^* and Z_k^* are the effective charges of the atoms *i* and *j*, respectively. r_{ik} is the distance between the atoms *i* and *k*. These force constants are further adjusted to fit the partial vDOS from NIS experiments. The optimized angular, dihedral and improper force constants are summarized in **TABLE. II.2**.

TABLE. II.2: Optimized and estimated harmonic angular, dihedral and improper force constants in the LS and HS states.

Angular	LS-Force constants (kcal/mol·rad^2)		HS-Force constants(kcal/mol·rad^2)	
	Optimized	Estimated	Optimized	Estimated
1.C-Ni-C(90°)	76	100	86	100
2.Ni-C-N(180°)	126	148	114	148
3.Fe-N-C(180°)	-	-	50	87
4.N-Fe-N(90°)	172	155	60	120
5.C-C-N/C-N-C (120°)	222	274	222	274
6.N-FeN_{pz}(90°)	19	152	60	112
7.C-N-Fe(120°)	56	73	46	58
I. Ni-C-C-C/ Fe-N-N-N (180°)	10	-	7	-
II. N-Fe-C-C (180°)	14	-	24	-
III. Dihedral	30	-	30	-

For the non-bonding potential, which models the long-range interaction within the structure, the parameters in reference [137] are directly used in this work. It should be pointed

out that the non-bonding interaction energies are only calculated between atoms separated by more than two bonds to avoid non-physical strong short-range interactions. Indeed, at very short distances, long-range interactions could combine with pairwise harmonic potential, leading to an unphysical increase of the bond rigidity and causing an instability of the structure resulting in its collapse. The parameters of the nonbonding potential are shown in **TABLE. II.3**, wherein σ_{ij} is obtained by:

$$\sigma_{ij} = \sqrt{\sigma_i \times \sigma_j}, \tag{II.5}$$

where σ_i and σ_j are the atomic van der Waals distances of the atoms *i* and *j*, respectively. And ϵ_{ij} is obtained by:

$$\epsilon_{ij} = \sqrt{\epsilon_i \times \epsilon_j}, \tag{II.6}$$

where ϵ_i and ϵ_i are the atomic van der Waals energies of the atoms *i* and *j*, respectively. Finally, π-stacking have not been considered in the force field since the averaged pyrazine-pyrazine distance is approximatively 7 Å, which is large enough to avoid strong interactions between pyrazine rings. Indeed, the interaction energies described by the Lennard-Jones potential are close to zero at such distance.

TABLE. II.3: Parameters for the nonbonding potential used in the simulations.

Element	ε_i (kJ/mol)	σ_i (Å)
Ni	0.015	2.834
Fe	0.013	2.912
C	0.105	3.815
N	0.069	3.660

II.2.2 Force field for thermal spin transition

Starting from the **Section. II.2.1** of this chapter, the total potential energy ($E_{potential}$) of this coordination network can be described by considering the following terms:

$$E_{potential} = E_{bond} + E_{angular} + E_{dihedral} + E_{improper} + E_{non-bonding}$$

$$+E^{(i)}_{cooperativity}, \quad i = 1,2 \tag{II.7}$$

where E_{bond}, $E_{angular}$, $E_{dihedral}$, $E_{improper}$ and $E_{non-bonding}$ are the 2-body bonding potential, the 3-body angular potential, the 4-body dihedral potential, the 4-body improper potential and the long-range non-bonding potential, respectively. In order to reproduce the cooperative effects on the spin-transition behavior of the [Fe(pyrazine)][Ni(CN)$_4$] complex, a cooperative interaction term, $E^{(i)}_{cooperativity}$ ($i = 1,2$), whose origin lies in the lattice distortions, must be added to the initial formula. This term will be further discussed hereafter. Compared to our previous work in **Chapter. II.2.1**, the force constants in Eq. II.7 are only slightly adjusted. Notably, the introduction of a new 4-body improper potential (N-Fe-N-N) appears necessary to stabilize the FeN_6 octahedral structure. The resulting parameters are displayed in **TABLEs. II.4**, **II.5** and **II.6.**

TABLE. II.4: Parameters used (equilibrium angles and force constants) for the angular, dihedral and improper force potentials.

Angular	Force constant (kcal mol^{-1} rad^{-2})
1. C-Ni-C (90°)	86
2. Ni-C-N (180°)	134
3. Fe-N-C (180°)	80
4. N-Fe-N (90°)	54
5. C-C-N (120°)	222
6. N-Fe-N$_{pz}$ (90°)	54
7. C-N-Fe (120°)	50
I. Ni-C-C-C/Fe-N-N-N (180°)	40
II. N-Fe-C-C (180°)	60
III. Dihedral	30
IV. N-Fe-N-N (54.74°)	150

TABLE. II.5: Bond-stretching force constants and corresponding bond lengths. Fe-N bonds are modelled by a double-well potential whose parameters are reported in **TABLE. II.6.**

Bond	Force constant (kcal mol^{-1} Å^{-2})	Bond length (Å)
N-C	2512	1.158
Ni-C	220	1.857
Fe-N (LS)	Double-Well	1.944
Fe-N (HS)	Double-Well	2.211
C_{pz}-C_{pz}	866	1.56
C_{pz}-N_{pz}	780	1.56

In order to include the vibronic coupling in the [Fe(pyrazine)][Ni(CN)$_4$] structure, the harmonic Fe-N interaction used in the previous work is replaced by a Double-Well potential, similar to the ones previously proposed in refs. [37, 41]:

$$E_{bond}^{Double-Well} = \frac{A}{2}\{d + b(c - (r - r_{LS}))^2 + a(r - r_{LS})^2$$

$$-\sqrt{4J^2 + [d + b(c - (r - r_{LS}))^2 + a(r - r_{LS})^2]^2}\}, \quad \text{(II.8)}$$

where r_{LS} stands for the equilibrium Fe-N bond length. Parameters *a* and *b* are associated to the LS and HS force constants, respectively. The bond length and energy differences between the HS and LS states are characterized by the parameters *c* and *d,* respectively. *A* is a coefficient which gives the energy scale of the vibronic coupling and it is set to 2 under the consideration of reducing the number of parameters. *J* is the off-diagonal element, resulting from higher order spin-orbit coupling, which mixes the LS and HS harmonic potentials as shown in **FIG. II. 2**. According to the reported crystallographic data for [Fe(pyrazine)][Ni(CN)$_4$] [136], the equilibrium Fe-N bond lengths in the LS and HS states are set to $r_{LS} = 1.944$ Å and $r_{HS} = 2.212$ Å, respectively, giving rise to $c = r_{HS} - r_{LS} = 0.27$ Å. *a*, *b*, *d* and *J* are then obtained through a fitting procedure according to the following criteria:

$$\begin{cases} E_{Fe-N}^{Double-Well}(r_{HS}) - E_{Fe-N}^{Double-Well}(r_{LS}) = \Delta E_{HS-LS} \\ \left(\frac{d^2 E_{Fe-N}^{Double-Well}}{dr^2}\right)_{r=r_{LS}} = K_{LS} \\ \left(\frac{d^2 E_{Fe-N}^{Double-Well}}{dr^2}\right)_{r=r_{HS}} = K_{HS} \end{cases}, \quad \text{(II.9)}$$

where ΔE_{HS-LS} is the energy gap between the zero-point HS and LS states, K_{LS} and K_{HS} are the force constants of the Fe-N bond in LS and HS states, respectively. Based on Raman spectroscopy data reported for [Fe(pyrazine)][Ni(CN)$_4$] [7], the bond potential force constants can be obtained from the harmonic oscillator approximation [139]. From Eq. II.2 and Eq. II.3, we obtained the force constants K_{LS} = 138 kcal mol^{-1} Å^{-2} and K_{HS} = 31 kcal mol^{-1} Å^{-2}. The energy gap $\Delta E_{HS-LS} = 0.473$ kcal mol^{-1} is crudely estimated from the reported enthalpy variation (ΔH_{exp}) between two spin states by $\frac{\Delta H_{exp}}{6}$ (since each Fe site comprises six Fe-N bonds) [135]. The obtained parameters of the Fe-N double-well potential are listed in **TABLE. II.6**. Accordingly, as shown in **FIG. II. 2**, the unstable point between the two spin states is obtained for a Fe-N bond length of r_c = 2.07 Å.

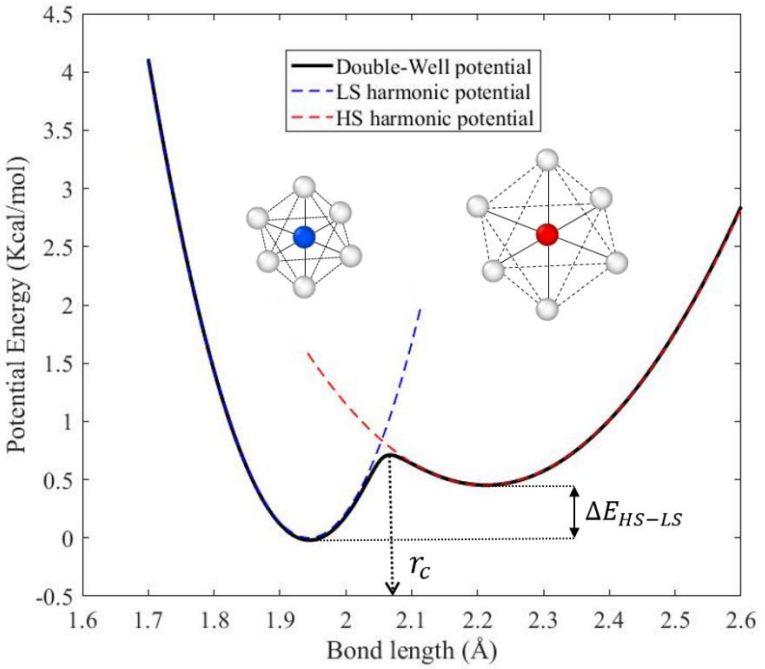

FIG. II. 2: Representation of the double-well potential (full black line) and of the LS (blue dashed line) and HS (red dashed line) harmonic potentials as a function of the Fe-N bond length. Schematic FeN_6 coordination octahedra of the [Fe(pyrazine)][Ni(CN)$_4$] complex are shown in inset, in the LS and HS states.

TABLE. II.6: Parameters used for the intra- and inter-molecular double-well potentials.

Parameter	Value	Parameter	Value
A	2	B	Variable
a (kcal mol^{-1} Å^{-2})	35	a_0 (kcal mol^{-1} Å^{-2})	32
b (kcal mol^{-1} Å^{-2})	8	b_0 (kcal mol^{-1} Å^{-2})	30
c (Å)	0.27	c_0 (Å)	0.49
d (kcal mol^{-1})	0.23	-	-
J (kcal mol^{-1})	0.09	J_0 (kcal mol^{-1})	0.3

In Eq. (1), $E_{cooperativity}$ refers to the potential energy, which arises from the interactions between the coordination octahedra, caused by lattice distortions. For the sake of simplicity, this term is introduced in the form of a two-body potential between the iron centers (see **FIG. 3** (a)). Two different potentials have been tested. First, a monophasic Morse-like potential, similar to the intermolecular potential introduced in ref. [37], has been considered (**Fig. 3** (b)):

$$E^{(1)}_{cooperativity}(R) = D\left(e^{a'(R-R_0)} + e^{-b'(R-R_0)}\right), \quad \text{(II.10)}$$

where $a' = 0.5$ and $b' = 1$. R_0 is a constant such that $E^{(1)}_{cooperativity}(R)$ has the minimum at $R = 0$. D is a tunable parameter which controls the strength of intermolecular interactions. Then, double-well (biphasic) potential using the same format than the Fe-N interaction has been proposed (**FIG. II. 3** (c)):

$$E^{(2)}_{Cooperativity} = \frac{B}{2}\{b_0(c_0 - (R - R_{LS}))^2 + a_0(R - R_{LS})^2$$

$$-\sqrt{4J_0^2 + [b_0(c_0 - (R - R_{LS}))^2 + a_0(R - R_{LS})^2]^2}\}, \quad \text{(II.11)}$$

where R_{LS} is the lattice constant where R_{LS} is the lattice constant of the equilibrium LS state, while B, a_0, b_0 and c_0 are parameters, which control the energy barrier between the HS and LS phases and the concavity of the double-well potential, respectively. J_0 is an off-diagonal element. The term $E^{(2)}_{cooperativity}$ becomes zero in the neat LS and HS states, which means that there is no excess elastic energy (induced by lattice distortion) in the pure LS and HS phases.

The parameter c_0 = 0.49 Å is taken through the variation of lattice constants between the LS and HS forms. $a_0 \approx b_0$ with the same order of magnitude as a was chosen to leave the energy barrier in the middle between the two minima, i. e., the maximum interaction energy appears for HS- LS pairs. J_0 is chosen to be slightly larger than J to give a smooth connection between two harmonic potentials. The corresponding values of the parameters are listed in **TABLE. II.6**.

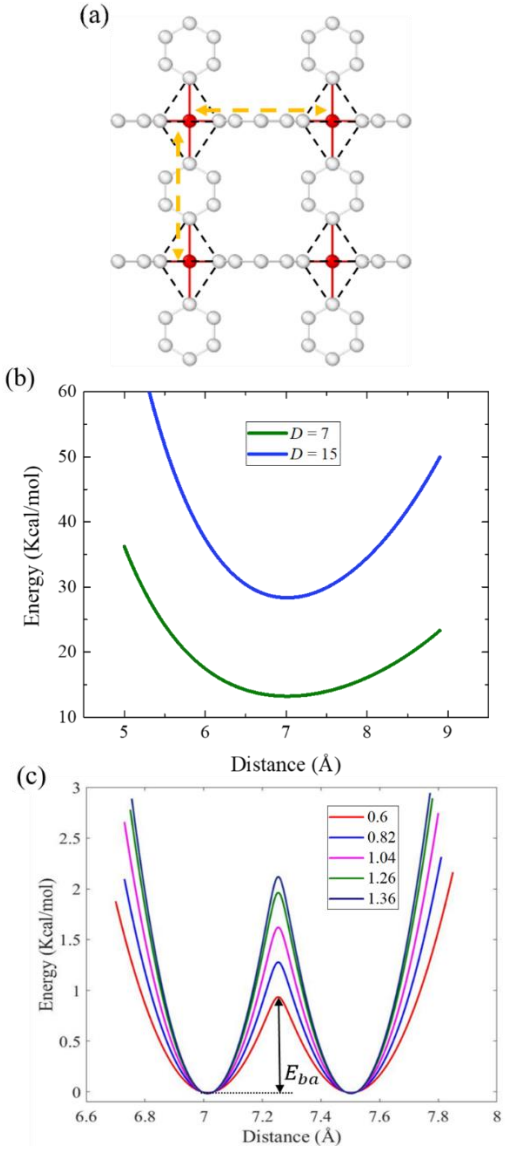

FIG. II. 3: (a) Schematic 2D picture of the [Fe(pyrazine)][Ni(CN)$_4$] structure, showing the Fe-Fe interactions. (b) Potential energies associated with Fe-Fe intermolecular interactions described by the monophasic potential $E^{(1)}_{cooperativy}$, given by Eq. II.9, for different values of the parameter *D*. (c) Potential energies associated with Fe-Fe intermolecular interactions described by the double-well potential $E^{(2)}_{cooperativy}$, given by Eq. II.11, for different values of the parameter *B*.

To identify the molecular spin state, a three-dimensional Voronoi cell was considered for each Fe site [140]. Given a metric space (*M*, *d*) and a discrete set of atomic positions $\{s_1,\ s_2, \dots\} \subset M$, the Voronoi cell $V(s_i)$ associated with an atomic site s_i is the set of all points such that:

$$V(s_i) = \left\{x \in \mathbb{R}^3 \middle| d(x, s_i) \leq d\left(x, s_j\right),\ \forall i \neq j\right\}, \tag{II.12}$$

According to the above description, the shape of the Voronoi cell in the ground LS and HS states is a perfect cube. Here, the Voronoi volume associated with the Fe ions (V_{Fe}) is used as a parameter to identify the molecular spin state: if $V_{Fe} > r_c^3$, then the Fe site is considered to be in the HS state, otherwise it is in the LS state.

II.2.3 Density of vibrational states and extraction of lattice dynamics parameters

In molecular dynamics, the reciprocal space vector information is implicitly contained in the displacements of the atoms. Consider the Fourier transform of the velocity vector of atom *n*:

$$V_n(\omega) = \int_{-\infty}^{+\infty} V_n(t)\, e^{-i\omega t} dt, \tag{II.13}$$

Its modulus is written as

$$|V_n(\omega)|^2 = \int_{-\infty}^{+\infty} \int_{-\infty}^{+\infty} V_n^*(t') V_n(t) e^{-i\omega\left(t-t'\right)}\, dt dt' = \int_{-\infty}^{+\infty} \int_{-\infty}^{+\infty} V_n^*(t') V_n(t' + t'') e^{-i\omega t''}\, dt'' dt', \tag{II.14}$$

with $t'' = (t - t')$.

The components of the displacement vectors $u_j(t)$ can be described as the linear combination of displacements (eigenvectors) associated with the normal modes *s*.

$$u_j(t) = \sum_s Q_{s,j}\, e^{-i\omega_s t}, \tag{II.15}$$

The velocity is deduced such as:

$$v_j(t) = \sum_s Q_{s,j}(i\omega_s)\, e^{-i\omega_s t}, \tag{II.16}$$

By injecting Eq. II.16 into Eq. II.14 and summing over the *N* atoms of the system, we obtain:

$$\sum_{n=1}^{N} |V_n(\omega)|^2 =$$

$$\sum_{j=1}^{3N} \sum_{s} \sum_{s'} \int_{-\infty}^{+\infty} \int_{-\infty}^{+\infty} Q^*_{s',j}\, Q_{s,j}\, \omega_s \omega_{s'} e^{-i(\omega-\omega_s)t''} e^{i(\omega_s-\omega_{s'})t'} dt' dt'' =$$

$$\sum_{j=1}^{3N} \sum_{s} \sum_{s'} \int_{-\infty}^{+\infty} \left(Q^*_{s',j} Q_{s,j} \omega_s \omega_{s'} e^{-i(\omega-\omega_s)t''} dt'' \int_{-\infty}^{+\infty} e^{i(\omega_s-\omega_{s'})t'} dt' \right) =$$

$$\sum_{j=1}^{3N} \sum_{s} \int_{-\infty}^{+\infty} \left|Q_{s,j}\right|^2 \omega_s^2\, e^{-i(\omega-\omega_s)t''} dt'', \tag{II.17}$$

The equipartition theorem leads to:

$$\left|Q_{s,j}\right|^2 \omega_s^2 = k_B T, \tag{II.18}$$

Each mode of vibration therefore has an average total energy equivalent to thermal energy ($k_B T$). Taking this relationship into account, Eq. II.17 can be rewritten as:

$$\sum_{n=1}^{N} |V_n(\omega)|^2 = 3N k_B T \sum_S \delta(\omega - \omega_s), \tag{II.19}$$

where $g(\omega) = \sum_S \delta(\omega - \omega_s)$ is the density of vibrational states.

On the other hand, considering the system in a stationary state, we obtain:

$$\sum_{n=1}^{N} |V_n(\omega)|^2 = \int_{-\infty}^{+\infty} \left(\int_{-\infty}^{+\infty} V_n(t' + t'')\, V_n^*(t') dt' \right) e^{-i\omega t''} dt''$$

$$= \beta \int_{-\infty}^{+\infty} \langle \sum_{n=1}^{N} V_n(t' + t'') V_n^*(t') \rangle_{t'} e^{-i\omega t''} dt'', \tag{II.20}$$

where $\langle \sum_{n=1}^{N} V_n(t' + t'') V_n^*(t') \rangle_{t'}$ is the velocity autocorrelation function of atom *n* and β is a constant.

By combining relations Eq. II.19 and Eq. II.120, it is possible to link the velocity autocorrelation function to the density of vibrational states.

$$g(\omega) = \frac{\beta}{3Nk_BT}\int_{-\infty}^{+\infty}\langle\sum_{n=1}^{N} V_n(t_0+\tau)V_n^*(t_0)\rangle_{t'} e^{-i\omega\tau}d\tau = \text{Cnste}\int_{-\infty}^{+\infty}\gamma(\tau)e^{-i\omega\tau}d\tau, \quad \text{(II.21)}$$

where $\gamma(\tau)$ is the velocity autocorrelation function. The changes of variable $t' \to t_0$ and $t'' \to \tau$ are used to highlight the choice of a reference time t_0 which is often fixed at 0.

Misrecognition of the constant in $\gamma(\tau)$ can be avoided by normalizing the density of vibrational states as follows:

$$\tilde{g}(\omega) = \frac{g(\omega)}{\int_{-\infty}^{+\infty} g(\omega)d\omega}, \quad \text{(II.22)}$$

The vDOS is of fundamental importance for the investigation of lattice dynamics. Its knowledge provides informations on the Debye sound velocity (v_D), the vibrational entropy (s), the mean force constant ($\langle C\rangle$) and the vibrational internal energy (u) [125], according to the following equations, which are mainly related to the area under the vDOS curves. In particular the expression of the Debye sound velocity is:

$$v_D = \lim_{E\to 0}\left(\frac{\tilde{m}}{\rho}\frac{1}{2\pi^2\hbar^3}\frac{E^2}{\tilde{g}(E)}\right)^{1/3}, \quad \text{(II.23)}$$

where $\tilde{m}$ is the average mass of oscillating atoms, $\hbar$ the Planck constant, E the energy, $\tilde{g}(E)$ the density of vibrational states, $\rho = \frac{N\langle M\rangle}{V}$ the mass density, N the number of atoms in the primitive cell, V the volume of the primitive cell, and $\langle M\rangle$ the average mass of the primitive cell atoms. The vibrational entropy can be expressed as:

$$s = 3k_B\int_0^{+\infty}\tilde{g}(E)\left[\frac{\beta E}{2}\frac{e^{\beta E}+1}{e^{\beta E}-1} - ln\left(e^{\frac{\beta E}{2}} - e^{-\frac{\beta E}{2}}\right)\right]dE, \quad \text{(II.24)}$$

where k_B is the Boltzmann constant, T the temperature and $\beta = 1/(k_BT)$. Finally, the mean force constant $\langle C\rangle$ and the vibrational internal energy u can be written as follows:

$$\langle C\rangle = \frac{\tilde{m}}{\hbar^2}\int_0^{\infty}\tilde{g}(E)\,E^2dE, \quad \text{(II.25)}$$

$$u = \frac{3}{2}\int_0^{+\infty}\tilde{g}(E)E\frac{e^{\beta E}+1}{e^{\beta E}-1}dE, \quad \text{(II.26)}$$

II.2.4 Molecular dynamics calculations

MD calculations of [Fe(pyrazine)][Ni(CN)$_4$] were conducted through the well- established software of Large-scale Atomic/Molecular Massively Parallel Simulator package (LAMMPS) [141]. [Fe(pyrazine)][Ni(CN)$_4$] structures with 20×20×20 unit-cells are built in the LS and HS states, which corresponds to simulation box volumes of 140.26×140.26×135.52 Å^3 and 145.15×145.15×145.12 Å^3, respectively. In each simulation, periodic boundary conditions are applied along the *x*, *y* and *z* directions in order to simulate a bulk material and to avoid the contributions of surface effects. Both structures are initially optimized at 0 K through the conjugate gradient method [142]. Then, the temperatures are fixed at 100 K and 300 K for the LS and HS states, respectively, using the deterministic Nose-Hoover thermostat [43, 44]. Each structure is relaxed under canonical ensembles (NVT) for 150000 timesteps and the velocity Verlet algorithm is used to integrate the equations of motion [143]. Finally, the velocity autocorrelation function ($\gamma(\tau)$) is collected during 4000 timesteps and the partial vDOS ($\tilde{g}(E)$) of Fe is derived through a suitable Fourier transformation as described above.

Then, the double-well potentials, given by Eq. II.18 and Eq. II.11, are exported in an appropriate format, which could be identified by LAMMPS, by means of the Python environment. The [Fe(pyrazine)][Ni(CN)$_4$] structure with 10 × 10 × 10 unit cells is built in the LS state, which corresponds to a simulation box size of 70.13 × 70.13 × 70.13 Å^3 containing 16 000 atoms. In each simulation, periodic boundary conditions are applied along the *x*, *y* and *z* directions in order to simulate the bulk material, thus avoiding surface/interface effects. The temperature is controlled by the Nose-Hoover thermostat [43, 44] and a timestep of 1 fs is selected. The structure is initially relaxed at a temperature of T = 50 K for 20 000 MD steps to reach an equilibrium state. Then, the system is warmed up from 50 to 460 K with increments of 10 K and then cooled back to 50 K. 20 000 MD steps are selected for each temperature increment, while 5 000 MD steps are used, after each increment, to stabilize the structure and measure the HS fraction. The isothermal-isobaric (NPT) ensemble is employed to control the total stress by changing the size of the simulation box along three directions. Finally, the Voronoi analysis is conducted through the Voro++ software package [144] to calculate the atomic volume of Fe sites. The spin configurations and atomic positions after the simulations are visualized by means of the Open Visualization Tool (OVITO) software [145].

II.3 Results and discussions

II.3.1 Vibrational properties

The parameters of the force field built in **Section. II.2.1** were obtained by comparison with experimental vibrational spectra of [Fe(pyrazine)][Ni(CN)$_4$] and by empirical methods.

In a first step, the force constants of harmonic bond potentials, as displayed in **TABLE. II.1**, were derived from Raman spectra using Eq. II.2. For this latter, no adjustment of the experimental values has been realized since, within the scope of the present study, the harmonic pairwise potential defined by the first term of Eq. II.1 gives a relevant description of the stretching process of chemical bonds [139]. Obviously, the Fe-N force constants display a huge change at the spin transition, but one can note changes of all force constants related to bonds in the 2D sheet, formed by $[Ni(CN)_4]^{2-}$ and Fe^{2+} ions. Nevertheless, we shall stress that the changes in the force field of the $[Ni(CN)_4]^{2-}$ moiety remain just a work hypothesis as other effects may also account for the Raman frequency shifts (e.g. mode coupling).

The force constants of harmonic angular potential are initially roughly estimated by the method described in **Section. II.2.1** of this chapter. The values are then further adjusted by trial-and-error to fit the partial vDOS from NIS experiment. **TABLE. II.2** displays the optimized force constants as well as the first estimates. As expected, large differences between the LS and HS states can be found for angles related to the FeN_6 octahedra. Yet, for a better match with the experimental vDOS a spin-state dependence of the force-field of the $[Ni(CN)_4]^{2-}$ moiety had to be also implemented. **TABLE. II.2** gathers also the parameters of the dihedral and improper potentials. Generally speaking, the force constants of improper potentials are lower than those of bonding and angular potentials.

The optimized partial vDOS of Fe is compared with the experimental vDOS spectra [126, 128] in **FIG. II.4**. Overall, the shape of the vDOS spectrum in the LS state is substantially different from that of the HS state - primarily due to the structural differences of the FeN_6 octahedra between the two spin states. In comparison with a previous work [134], in which a simple cubic SCO model structure was investigated, the asymmetry of the vDOS curves between the LS and the HS states is retrieved since the anisotropy of the structural changes upon the SCO in the compound [Fe(pyrazine)][Ni(CN)$_4$] is considered in this force field. In **FIG. II.4** (b), several peaks, identified as Fe-ligand stretching vibrational modes can be observed in the optical part of the vDOS spectra, above ca. 20 meV, which are also well recognizable in the experimental vDOS. Notably, an intense, broad peak is observed for the HS structure, located around 35 meV, while several peaks appear in the LS state at 28, 33, 40.5,

42, 54 and 60 meV. Although the vibrational frequency values are not accurate, they are close to the experimental observation (< ± 5 meV). In particular, a blueshift (resp. redshift) of the HS peak (resp. LS peaks) can be denoted, i.e. the effect of the SCO is less marked in the simulations. In addition, the width of these peaks is sharper in the simulated spectra, most likely due to the harmonic character of the pairwise potentials and the lack of disorder and defects (e.g. guest molecules) in the theoretical study.

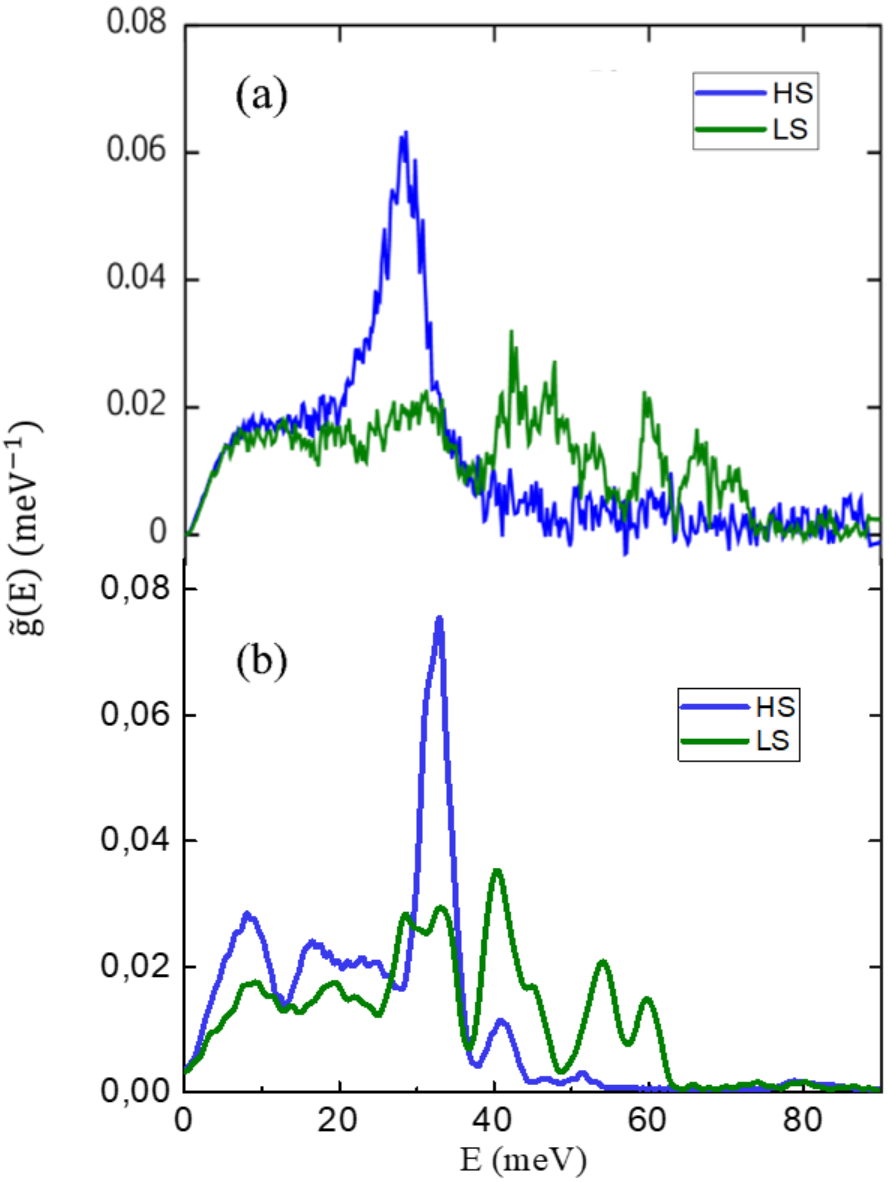

FIG. II.4:. Partial (Fe) densities of vibrational states in the LS and HS states obtained (a) from NIS experiments [128] and (b) from MD simulations performed in this work.

To characterize the lattice rigidity, the Debye sound velocity was extracted from the low frequency part (acoustic modes) of the vDOS, where the conditions for the application of continuum mechanics and linear elastic theory are fulfilled (large wavelength in comparison with lattice parameters). It results in the validity of the Debye approximation [125], which can be inferred from a nearly constant value for the ratio $\tilde{g}(E)/E^2$ at low energies as shown in **FIG. II. 5.** When going from the LS to the HS state, the Debye sound velocity downshifts from 2083 to 1820 *m/s*. The decrease of v_D upon the LS to HS transition indicates that the HS phase is softer than the LS phase, as it can be expected. We note the good match with the experimental observations (**TABLE. II.7**) providing confidence in the parametrization of the force field with respect to the critical region of acoustic modes.

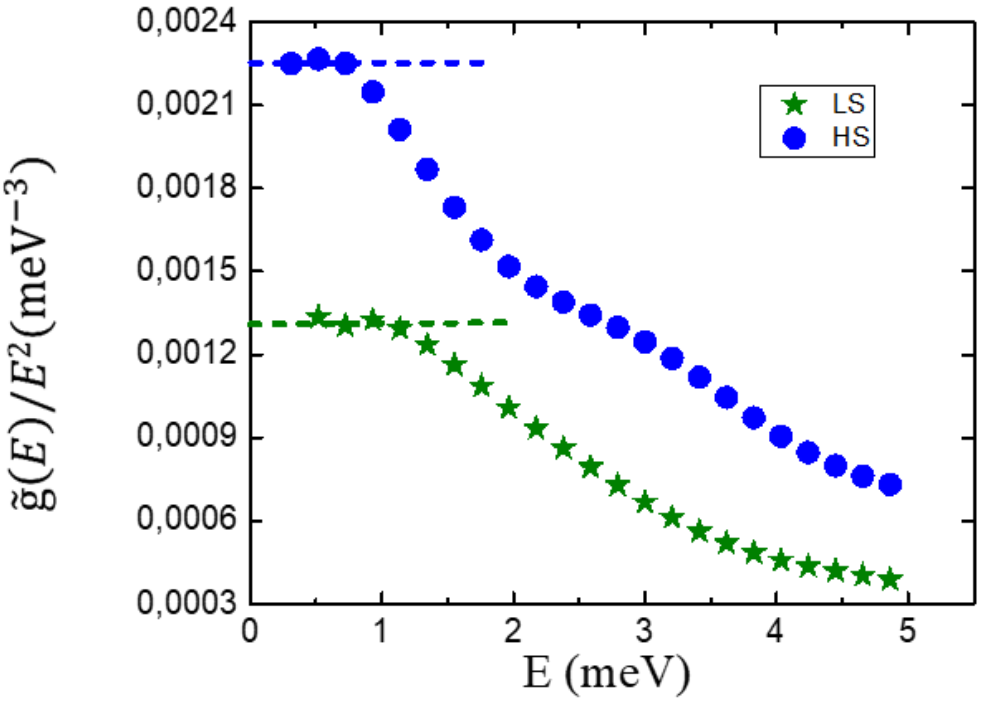

FIG. II. 5: $\tilde{g}(E)/E^2$ as a function of E calculated for the LS and HS states. The dashed lines are the linear fits at lowest energies – showing the validity range of the Debye approximation.

TABLE. II.7: Comparison of Debye sound velocity (v_D), mean force constant ($\langle C \rangle$), vibrational entropy (s) and vibrational internal energy (u) of the LS and HS forms obtained in the present study and from NIS experiments [128].

	LS		HS	
	This work	NIS	This work	NIS
$v_D(m/s)$	2083	2063 ± 27	1820	1933 ± 20
$\langle C \rangle (N/m)$	292	331 ± 10	173	204 ± 10
s (k_B)	0.99	0.90	3.92	3.57
u (meV)	53.3	56.0	84.8	85.8

The vibrational entropy, whose definition takes mainly into account the low frequency part of the spectrum, increases upon a LS to HS transition in coherence with the overall softening of the HS lattice. The numerical and the experimental values of s almost coincide, which reinforces our belief that the force field is able to model the low frequency vDOS of SCO materials. The mean force constant and vibrational internal energy have been also extracted from the vDOS for both spin states. These two quantities characterize the optical modes since according to their definitions, the main contribution to $\langle C \rangle$ and u come from the high-energy part of the vDOS. The extracted values for u match well the experimental observations. However, some discrepancy can be observed for the mean force constants $\langle C \rangle$. The redshift of the calculated optical modes in the LS state may explain the lower numerical value for $\langle C \rangle$ in comparison with experimental results. In the HS state, however, the computed blueshift should result in a stiffening of the local environment of iron. Yet, the vibrational modes located between 5 - 20 meV (corresponding to a complicated combination of inter- and intra-molecular vibrational modes) apparently give non-negligible contributions, leading to a lower numerical value of the mean force constant if compared with the extracted experimental value. Nevertheless, the numerical ratio $\left(\frac{\langle C \rangle_{LS}}{\langle C \rangle_{HS}}\right)_{num} \approx 1.69$ is close to the experimental one $\left(\frac{\langle C \rangle_{LS}}{\langle C \rangle_{HS}}\right)_{exp} \approx 1.62$.

II.3.2 Thermally induced spin transition

Then, MD simulations have been conducted including the monophasic Morse-like potential $E^{(1)}_{cooperativity}$, given by Eq. II. 10, in the FF. The temperature dependence of the Fe atomic volume is plotted in **FIG. II. 7** for different values of the parameter *D*. The increase of the strength of the $E^{(1)}_{cooperativity}$ leads to more gradual transitions, i. e., it is not possible to simulate a first-order transition. This result is rather unexpected, because it contrasts with previous 'spring-ball' models, where first-order spin transitions was successfully modelled either by increasing the elastic constant related to the intermolecular bonds, or by increasing the difference between the elastic constants (or lattice parameters) of the HS and LS structures [35, 37, 146, 147]. Here, it was not possible to simulate first-order transitions by including this spin-state-independent intermolecular potential in the FF.

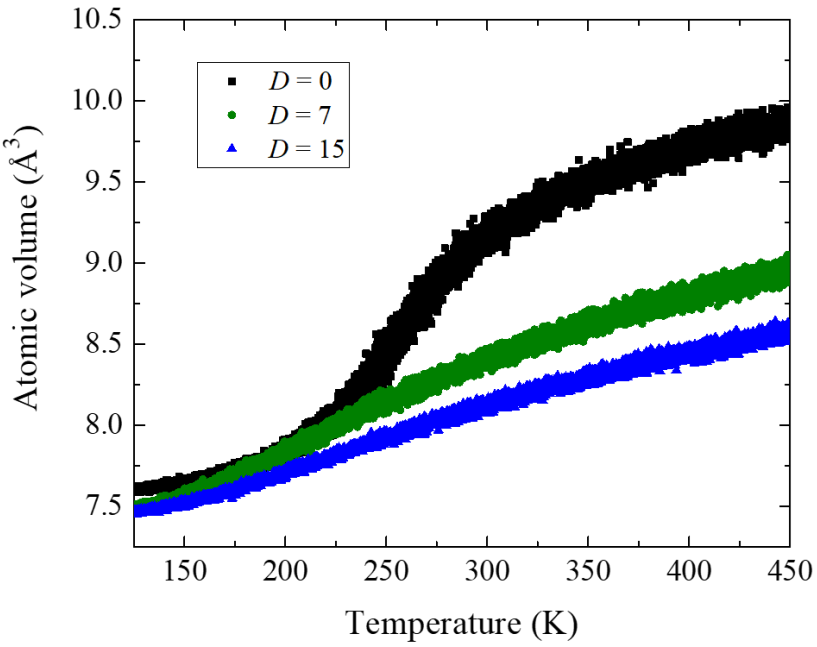

FIG. II. 7: Thermal evolution of the atomic volume of Fe using $E^{(1)}_{cooperativity}$ in the FF and for different values of D.

Unlike spring-ball models, such as electro-elastic, mechano-elastic or anharmonic elastic models, in which the question of the structure stability does not arise and the parameters responsible of cooperative phenomena are fairly well identified, the present model aims to give a more realistic description of the lattice dynamics and elastic properties of the [Fe(pyrazine)][Ni(CN)$_4$] SCO complex. The construction of the FF and its parametrization have been achieved based on the available experimental data, while ensuring the structure stability and preserving the crystallographic properties of the material. Therefore, including the switching capability of SCO molecules into the present FF complicates this initial task. The Morse-like potential, which is simply set between two central Fe atoms, is not able to describe the complexity of inter-molecular interactions that may come from the *N*-body interactions and local distortions in the realistic structure. An alternative way is to introduce a spin-state-dependent intermolecular two-body potential to model the elastic energy barrier that needs to be overcome to change the intermolecular distances (between two consecutive Fe centers) accompanying the spin-state switching. Here, we show that the introduction of this type of spin-state-dependent energy potential, $E^{(2)}_{cooperativity}$ given by Eq. II.11, generates of a local elastic energy barrier, whose effect compensates the weakness of intermolecular interactions in certain crystallographic directions. Using this double-well biphasic potential in the FF, **FIG. II. 8** (a) and **8**(b) display the temperature dependence of the HS fraction (n_{HS}) and of the Fe atomic volume, respectively, upon a heating/cooling cycle, for selected values of the elastic energy barrier given by the parameter *B*. When $B = 0$ (zero energy barrier), the phase transformation is found to be gradual and a perfect overlap is observed for the thermal spin-transition curves in the heating and cooling modes (**FIG. II. 8** (a), black squared dots), as it is expected for a weakly cooperative system. Furthermore, the transition temperature T_{eq}, at which the HS and LS fractions are equal (n_{HS} = 50 %), is found to be $T_{eq}^{MD} \approx 280$ K.

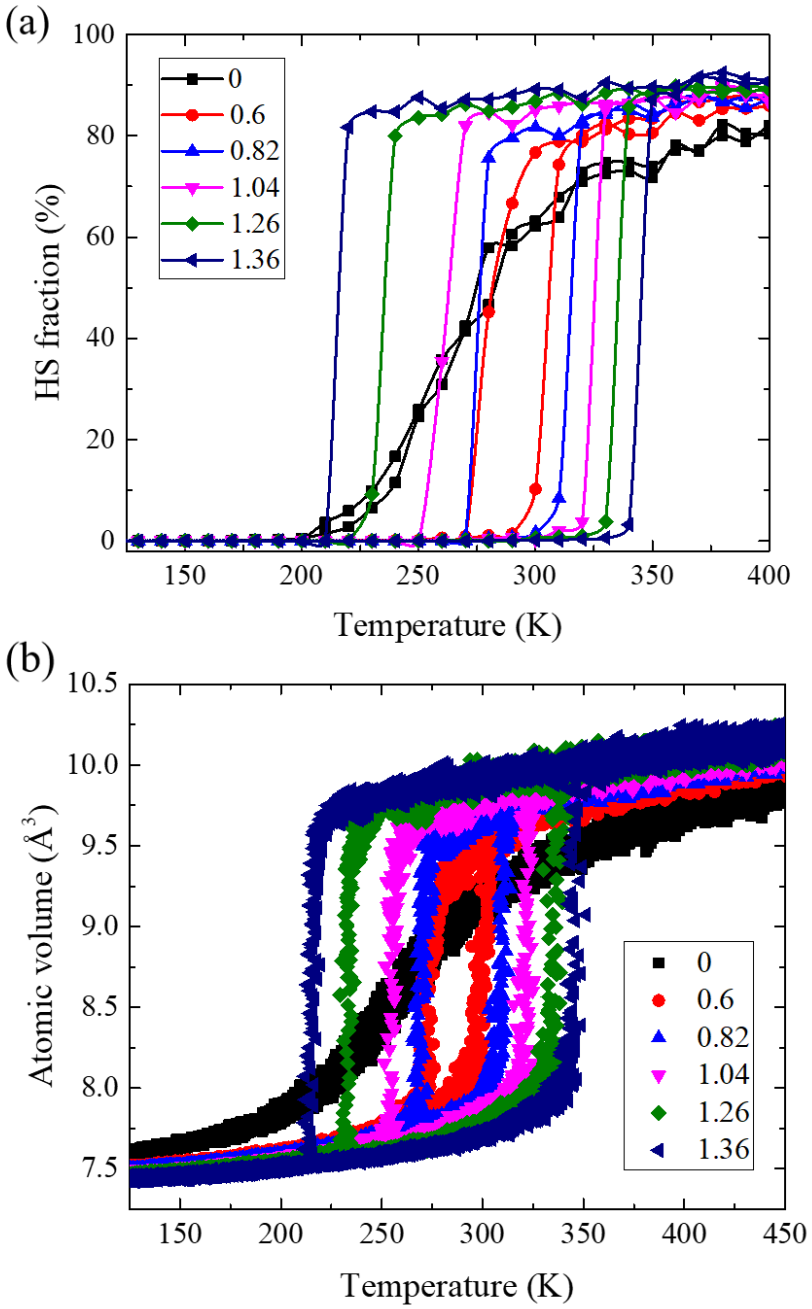

FIG. II. 8: Temperature dependence of (a) the HS fraction and of (b) the atomic volume of Fe ions using the intermolecular potential $E^{(2)}_{cooperativity}$ in the FF for selected values of B (strength of the intermolecular interactions).

At this point, it is interesting to note that the entropy (S) of the system can be expressed as [37]:

$$S = Nk_B\left(1 - \ln\frac{\hbar}{k_B T}\sqrt{\frac{K}{m}}\right), \tag{II.27}$$

where N is the number of Fe-N bonds, k_B is the Boltzmann constant, $\hbar$ is the reduced Planck constant, K is the force constant and m is the atomic mass. Based on this expression, the entropy difference (ΔS) between the HS and LS states is given by:

$$\Delta S = S_{HS} - S_{LS} = Nk_B \ln\sqrt{\frac{K_{LS}}{K_{HS}}}, \tag{II.28}$$

and the transition temperature T_{eq}, is defined by the condition:

$$\Delta G = \Delta H - T_{eq}\Delta S = 0, \tag{II.29}$$

where ΔG and ΔH are the Gibbs free energy difference and the enthalpy difference between the HS and LS states. Thus, the estimated transition temperature, T_{eq}^{est}, is given by:

$$T_{eq}^{est} = \frac{\Delta H}{\Delta S} = \frac{\Delta E_{HS-LS}}{k_B \ln\sqrt{\frac{K_{LS}}{K_{HS}}}}, \tag{II.30}$$

According to our setting of the Fe-N potential (vide supra), the transition temperature $T_{eq}^{est} \approx 320$ K calculated by Eq. II.30 is significantly higher than the value obtained from the MD simulations ($T_{eq}^{MD} \approx 280$ K). This discrepancy is certainly due to the fact that the simple thermodynamical estimation (Eq. II.28) only considers the entropy associated with the stretching vibrational modes of the Fe-N bonds which gives $\Delta S_{est} \approx 6.21N$ J K^{-1} mol^{-1}. Whereas, the entropy variation in the MD simulations estimated by $\Delta S_{MD} \approx \frac{N\Delta E_{HS-LS}}{T_{eq}^{MD}} = 7.07N$ J K^{-1} mol^{-1} is ~12 % larger than ΔS_{est}. According to the literature, the rotation of the pyrazine ligand contributes up to 9 % to the total entropy [53, 148, 149]. The remaining contribution (~3 %) comes most likely from low-frequency vibrational modes.

Remarkably, when increasing the value of B (i.e., the strength of the elastic interactions), we observe the occurrence of more and more abrupt SCO and the opening of a thermal hysteresis loop, characteristic of a system that exhibits a first-order transition (**FIG. II. 8** (a) and (b)). As displayed in **FIG. II. 9**, the transition temperature of the system in the heating mode ($T_{1/2\uparrow}$) is progressively shifted from 280 to 350 K, while $T_{1/2\downarrow}$ (in the cooling mode) is shifted from 280 to 215 K with the increase of B from 0 to 1.4, denoting a sizeable broadening of the hysteresis loop ($\Delta T = T_{1/2\uparrow} - T_{1/2\downarrow}$) from 0 to 135 K. Importantly, we find that the

equilibrium temperature between the LS and HS phases, which can be defined (as a first approximation) as:

$$T_{eq} = \frac{T_{1/2\uparrow} + T_{1/2\downarrow}}{2}, \tag{II.31}$$

remains virtually unchanged, regardless of the value of *B* (see **FIG. II. 9** (a)).

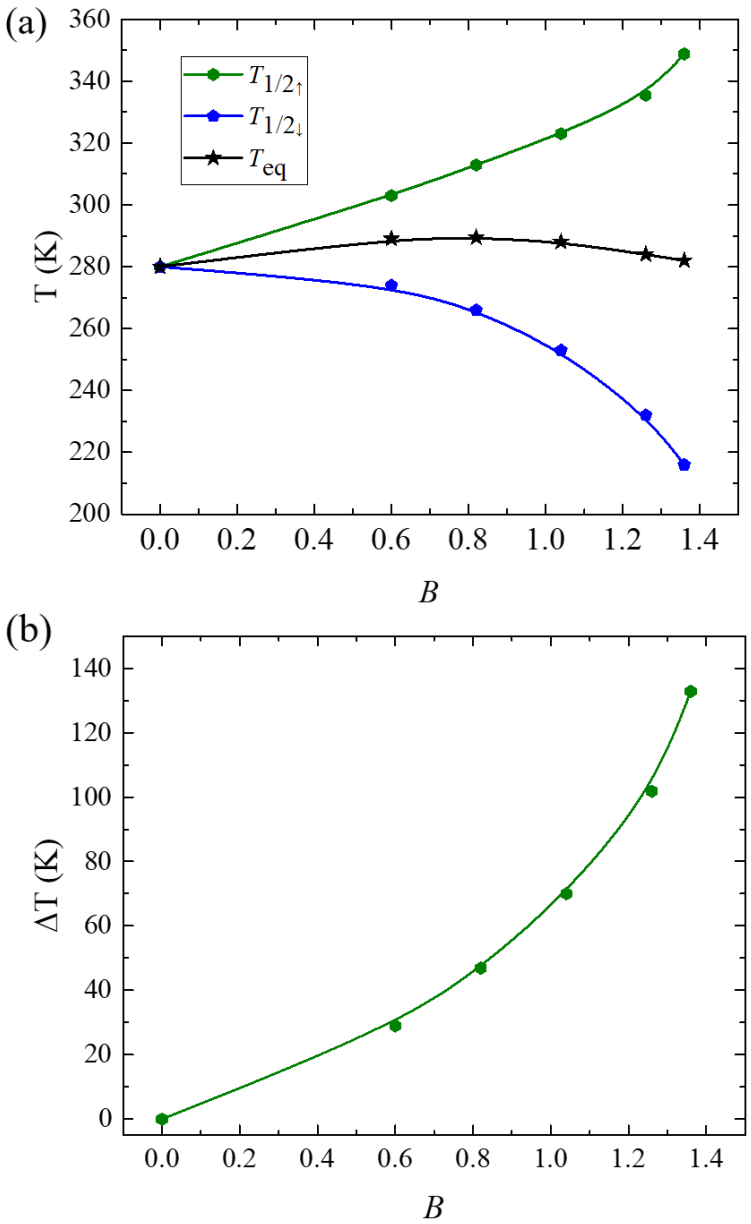

FIG. II. 9: Dependence of (a) $T_{1/2\uparrow}$, $T_{1/2\downarrow}$, T_{eq} and (b) ΔT on *B*.

In addition to controlling the height of the elastic energy barrier, it is important to note that the parameter *B* also has an influence on the stiffness of the crystal lattice. Indeed, as shown in **FIG. II. 8** (b), a progressive decrease of the atomic volume is observed with *B* at low temperature (in the pure LS state), indicating that the lattice is less deformable in the case of higher values of *B*. It is also interesting to notice in **FIG. II. 8** (a) that the residual LS state observed at high temperatures decreases from ~20 % to ~10 % with the increase of *B*. Such an effect indicates that the elastic interaction between two Fe sites tends to stabilize the HS state at high temperature.

It is worth noting that when $B = 0.6$, the transition temperatures upon heating and cooling are $T_{1/2\uparrow} \approx 310$ K and $T_{1/2\downarrow} \approx 280$ K, respectively, giving rise to a 30-K-wide hysteresis loop, close to the experimental hysteresis width observed for the [Fe(pyrazine)][Ni(CN)$_4$] complex (ΔT = 25 K) [135]. In addition, the experimentally observed transition temperature is also well reproduced, showing that our approach is able to simulate experimental SCO behaviors while using a realistic structure and FF.

Recently, Wolny et al. [124, 150] introduced the notion of cooperativity energy (H_{coop}), which reflects how the spin transition of a central molecule is affected by the spin state of its neighboring molecules:

$$H_{coop} = \left[E_{(1HS\_LS)} - E_{(LS)}\right] - \left[E_{(HS)} - E_{(1LS-HS)}\right], \tag{II.32}$$

where $E_{(LS)}$ and $E_{(HS)}$ are the energies of the system in the pure LS and HS phase, while $E_{(1HS-LS)}$ (resp. $E_{(1LS-HS)}$) is the energy of the LS (resp. HS) matrix with one molecule in the HS (resp. LS) state. Trough DFT calculations, the value of H_{coop} for the compound [Fe(pyrazine)][Pt(CN)$_4$] was estimated to be $H_{coop} = 15$ kcal mol^{-1} [124]. In our MD simulations, the influence of neighboring molecules on the spin transition of a central molecule can be roughly estimated by the elastic energy barrier (E_{ba}) induced by inter-molecular interactions (see **FIG. II. 3** (c)). When $B = 0.6$, which corresponds to the experimentally observed SCO behavior, the elastic energy of the central molecule is estimated to be $6 \cdot E_{ba} = 23.5$ kcal mol^{-1}, which is indeed close to the value of $H_{coop} = 15$ kcal mol^{-1}.

A significant advantage of the present model, which is shared with all discrete elastic models based on a deformable lattice, is the possibility to investigate the spatiotemporal aspects of the spin transition at the level of chemical bonds, by monitoring the local molecular spin state and the local structural (strain) changes as well as their time evolution upon the phase

transformation. These simulations are of paramount importance to better understand the couplings between the electronic and elastic degrees of freedom in SCO materials. The present simulations make it possible to follow the temperature evolution of the spatial distribution of the fraction of HS molecules, based on the definition of the Voronoi volume associated with Fe ions. **FIG. II. 10** depicts selected snapshots of the modelled system at different temperatures during both heating and cooling (for B = 0.6). This viewpoint is identical to what can be obtained from other elastic models: lattice deformations are hidden and only the local spin state is visible. In our simulations, only homogeneous phase transformations are observed and no clustering process occurs. This result is coherent with previous theoretical investigations considering infinite systems (without surfaces), where elastic distortion mediates the interactions among local states: spatially uniform configurations are maintained even during the first-order phase transformation [151].

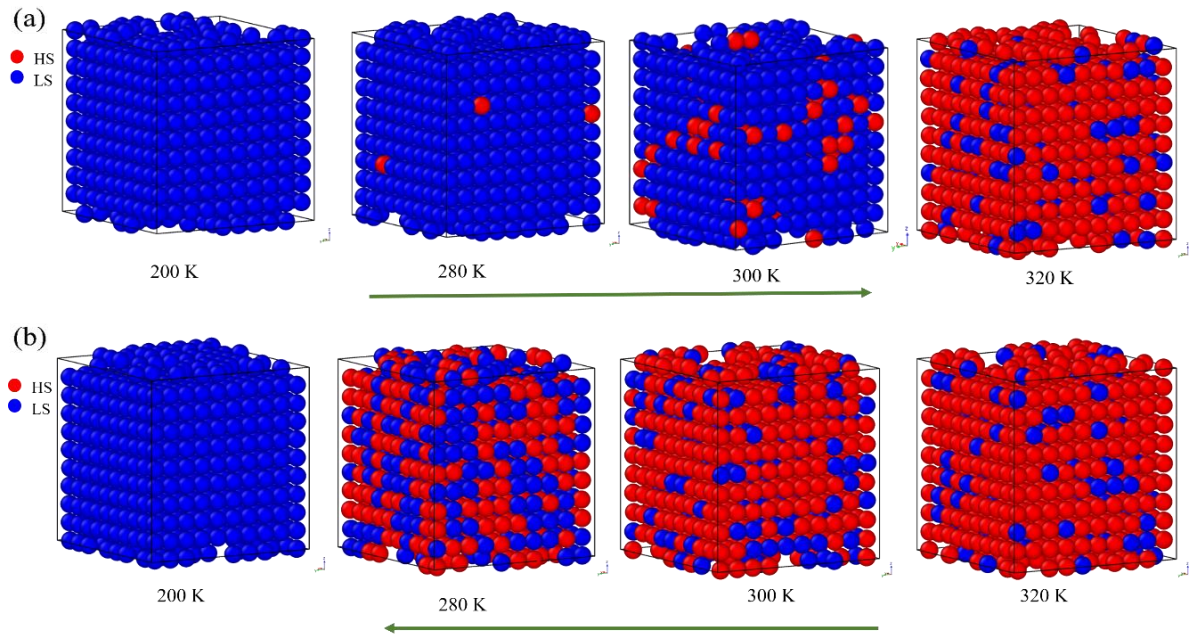

FIG. II. 10: Temperature dependence of the local HS fraction along (a) the heating process (LS-to-HS transition) and (b) the cooling process (HS-to-LS transition) for B = 0.6. In these snapshots, only the molecular spin states are depicted through blue and red balls to represent the LS and HS states, respectively. As a reminder, the transition temperatures in the heating and cooling modes are *ca.* 310 and 280 K, respectively.

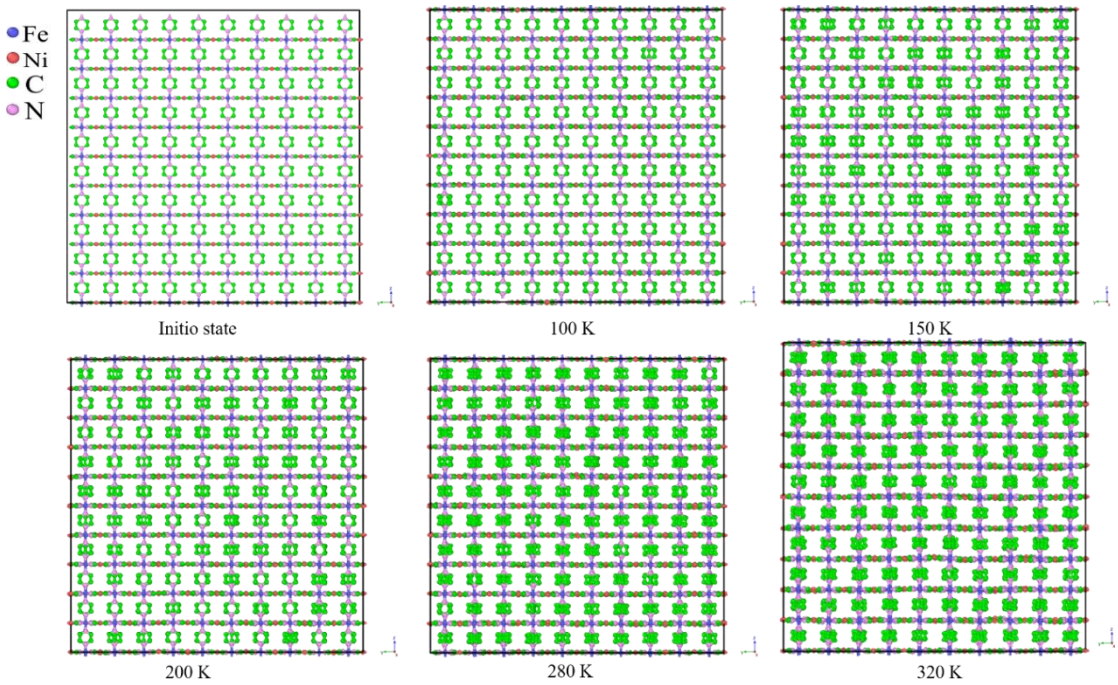

FIG. II. 11: Sectional view in the plane (*yOz*) at the middle of the simulated structure, upon the heating process at different temperatures (for $B = 0.6$). As a reminder, the transition temperature in the heating mode is $T_{1/2\uparrow} \approx 310$ K.

In comparison to previously reported elastic models, an important novelty of our approach is the possibility to simulate the real-time, spatiotemporal dynamics of the spin-state transformation in a SCO system based on a realistic structure. As an example, **FIG. II. 11** shows sectional views of the modeled structure, along the (*yOz*) plane, at selected temperatures during the LS-to-HS transformation. A significant increase of the size of the system is observed concomitantly with the molecular switching, which corroborates the fact that a strong electron-lattice coupling is operating during the spin-state change. This global expansion of the system is mainly attributed to the volume increase of the FeN_6 coordination sphere. Indeed, as depicted in **FIG. II. 12**, an abrupt change (by ~7.5 %) of the averaged Fe-N bond length is observed upon the spin transition, while, in comparison, the Ni-C bond length increases only slightly (relative variation ~0.2 %) in good agreement with X-ray diffraction measurements [136]. Interestingly, the progressive activation of the rotational movement of the pyrazine ligands with the temperature increase (upon the LS-to-HS transition) is also evidenced in our simulations, in good agreement with experimental observations [148]. Overall, our simulations allow to perform an accurate investigation of the local and macroscopic response of a realistic structure

to the electronic switching at the molecular scale, offering appealing perspectives for a deeper understanding of collective behaviors induced by elastic interactions. In particular, the analysis of the macroscopic repercussion (on the lattice) of the molecular volume change induced by the spin-state change of the compound, is essential for the future elaboration of heat-to-motion devices (e.g. actuators) or for the development of more sophisticated structures such as micro-electromechanical systems (MEMS).

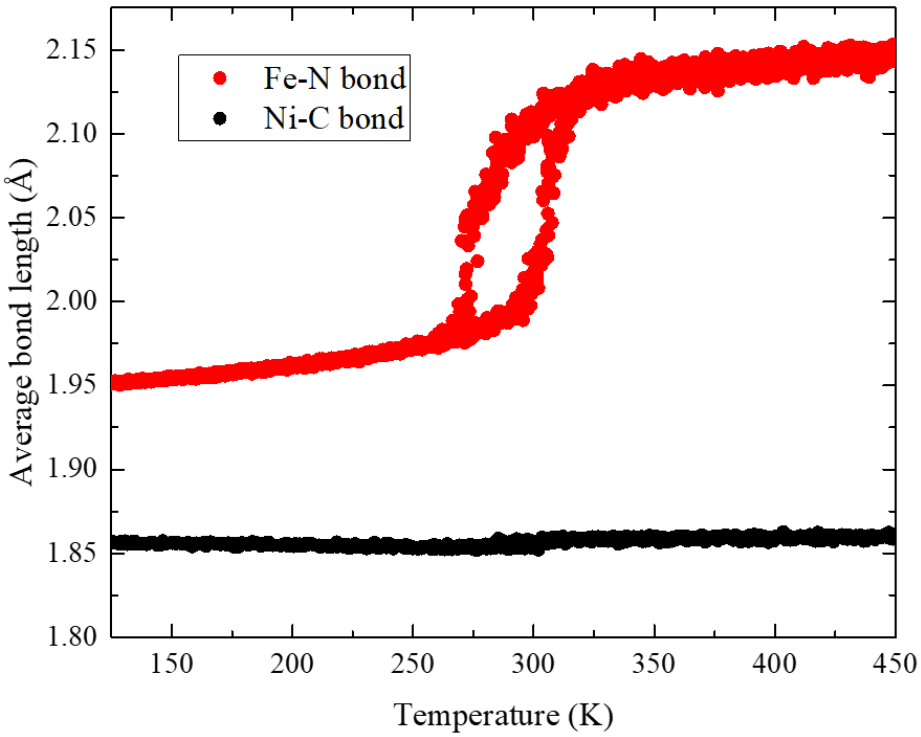

FIG. II. 13: Thermal evolution of the averaged Fe-N bond (red circle) and Ni-C bond (black circle) lengths for $B = 0.6$.

II.4 Conclusions

Compared to *ab initio* simulation, this new force field is quite simplified by the use of harmonic interactions and less heavy in terms of computational implementations and computational times. Nevertheless, it appears to be able to reasonably simulate the whole vDOS spectra, from the low (acoustic) to the high (optical) energies with an acceptable accuracy.

Undoubtedly, the success of the force field parametrization in this work mainly comes from a sufficiently large set of accurate experimental data and a legitime question is how generally applicable is the proposed parametrization. In this context, considerable progress have been achieved in the parametrization of force-field applied to materials where experimental input is less rich than in the present case, based on ab-initio calculations [152]. A very important point is the ability of this approach to quantitatively model the acoustic part of the vDOS, which is not easily accessible with ab initio calculations or experiments. The simulation of the mechanical properties and the collective vibrational modes is essential to grasp cooperative mechanisms at the origin phase transitions in these materials.

Then, based on the force field, a new elastic model of the [Fe(pyrazine)][Ni(CN)$_4$] SCO compound, including both intra- and inter-molecular interactions, has been developed. We demonstrate that this model enables to reproduce the experimental observed thermal SCO phenomenon in [Fe(pyrazine)][Ni(CN)$_4$], through all-atom MD simulations. The inter-molecular elastic energies strongly affect the SCO behavior and a direct correlation is observed between the width of the thermal hysteresis loop and the strength of the inter-molecular elastic interaction. Compared to the widely used "spring-ball" models, the present model is more quantitative since it is constructed on the basis of a realistic structure whose force field has been parametrized using available experimental data. The mechanisms of spin transition and lattice relaxation are combined together during the MD simulation, which effectively avoids any timescale mismatch (that can arise when using two different simulation methods) and ad hoc assumptions in MC simulations. This asset is primordial to investigate the dynamical processes that arise during phase transformations, such as global deformation and interface growth, etc. It should be also pointed out that our approach is transferable to other SCO compounds since the FF can be parametrized by DFT even in the absence of experimental data. In addition, it is easy to open the boundary conditions of the present 3D model, which would offer the possibility to investigate the effect of surfaces/interfaces on the SCO phenomenon and, more specifically, the spatiotemporal development of the nucleation-and-growth process in cooperative SCO solids. These aspects are examined in **Chapter III** for the simulation of the properties of nanoscale actuators based on the compound [Fe(pyrazine)][Ni(CN)$_4$].

Chapter III: Lattice bending and spatiotemporal study of a bimorph actuator

III.1 Introduction

In **Chapter II**, a new FF for the [Fe(pyrazine)][Ni(CN)$_4$] compound has been built in the first part of this work. This FF is based on the consideration of the realistic, all-atom structure of the SCO material and of the different interactions within and between SCO units. Using this FF, MD simulations have been carried out in the isothermal-isobaric ensemble using periodic boundary conditions to simulate the thermally induced spin-state switching in the bulk [Fe(pyrazine)][Ni(CN)$_4$] material. We found that the model reproduces adequately main experimental observations, including the switching temperatures, the thermal hysteresis loop and changes of various structural parameters.

In this chapter, we use this all-atom MD method to investigate how the LS/HS interface affects the spatiotemporal dynamics of the spin-state switching in a bimorph, nanoscale actuator made of the [Fe(pyrazine)][Ni(CN)$_4$] complex and the associated actuating performance of the device. To form a bimorph structure, a few [Fe(pyrazine)][Ni(CN)$_4$] layers have been simply set SCO-inactive. The spin-state configuration and the local strain are calculated in real time together with the deflection of the bimorph cantilever as a function of the thickness of the inactive and active part of the structure. By modulating the strength of the intermolecular interactions, we have also investigated the influence of the cooperativity of the SCO material on the switching dynamics and actuation phenomena.

III.2 The model and calculation method

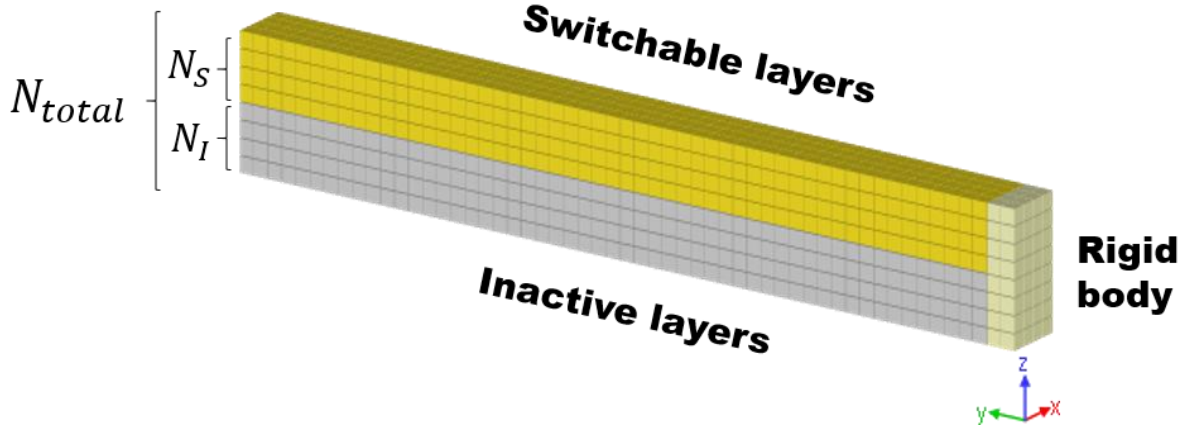

FIG. III. 1: Schematic view of the studied bimorph cantilever system, composed of 4 × 55 × N_{tot} unit cells (along the *x*, *y* and *z* directions, respectively) of the [Fe(pyrazine)][Ni(CN)$_4$] SCO material.

The present MD simulations are performed using the large-scale atomic/molecular massively parallel simulator software package (LAMMPS) [141] using the force field described in **Chapter II.2.2**. As shown in **FIG. III. 1**, the studied structure consists of a parallelepiped cantilever composed of 4 × 55 × N_{tot} ($6 \leq N_{tot} \leq 12$) unit cells (along the *x*, *y* and *z* directions, respectively) of the [Fe(pyrazine)][Ni(CN)$_4$] SCO complex, corresponding to systems with ca. 22 800 – 44 280 atoms. The whole structure is initially prepared in the HS state. One extremity of the cantilever system was considered to be clamped. To do that, two unit-cells along the *y* direction are set as a rigid body, meaning that the displacement of each atom is blocked. Along the *z* direction (i.e. the thickness of the cantilever), N_I [Fe(pyrazine)][Ni(CN)$_4$] layers are set as inactive, which means that the Fe^{II} ions are fixed into the HS state by replacing the Fe-N double-well potential by a simple harmonic potential. Finally, the remaining N_S (= N_{tot} – N_I) [Fe(pyrazine)][Ni(CN)$_4$] layers constitute the active (switchable) part of the system, in which the Fe sites are able to switch between the HS and LS states. For each simulation, the structure is relaxed at 100 K; the temperature and pressure conditions being controlled by the Nose-Hoover method [43, 44]. All calculations were performed under the NVT ensemble and a timestep of 1 fs was used. The Voronoi analysis is conducted through the Voro++ software package [144] to calculate the atomic volume of Fe ions in order to identify the local spin state for each complex. The atomic positions and strain mapping resulting from the simulation are visualized by means of the OVITO software [145]. During the relaxation process, significant structural deformations appear due to the large difference of volume between the LS and HS

states. In order to follow this structural relaxation, the local strain at each Fe atom is derived by considering the relative motion of its neighbors [46, 153, 154]. In detail, the relative position of two neighboring sites, denoted *j* and *k*, before strain, is given by:

$$\Delta \boldsymbol{X}_{jk} = \boldsymbol{X}_k - \boldsymbol{X}_j, \tag{III.1}$$

where $\boldsymbol{X}_k$ and $\boldsymbol{X}_j$ are the position vectors of the atomic sites *k* and *j*, respectively, before strain. Accordingly, the relative position of these two atomic sites after strain is given by:

$$\Delta \boldsymbol{x}_{jk} = \boldsymbol{x}_k - \boldsymbol{x}_j, \tag{III.2}$$

where $\boldsymbol{x}_k$ and $\boldsymbol{x}_j$ are the position vectors of the atomic sites *k* and *j*, respectively, after strain. Eq. (III.1) and Eq. (III.2) can be related through the transformation gradient $\boldsymbol{F}$:

$$\Delta \boldsymbol{x}_{jk} = \boldsymbol{F} \cdot \Delta \boldsymbol{X}_{jk}, \tag{III.3}$$

The strain tensor is then obtained by:

$$\boldsymbol{E} = 1/2\,(\boldsymbol{F}^{\mathrm{T}}\boldsymbol{F} - \mathbf{I}), \tag{III.4}$$

where $\mathbf{I}$ is the identity tensor.

III.3 Results and discussions

III.3.1 Spatiotemporal aspects of the HS-to-LS relaxation process

First, the thickness of the modelled device is set to N_{tot} = 8 unit cells. Along the *y* direction, one extremity of the cantilever is fixed, while the other one is free to move. Two cases are considered: 1) the case of an all-active system (N_I = 0) in which all Fe sites are able to switch between the LS and HS states, and 2) the case of a bimorph system (N_I = 4) composed of four SCO active (at the top) and four inactive (HS) [Fe(pyrazine)][Ni(CN)$_4$] layers (at the bottom). As described in **Chapter II.2.2**, the cooperative phenomena, controlled by the height of the elastic energy barrier, are driven by the value of the parameter *B* in the expression of the potential connecting the SCO-active Fe sites:

$$E_{Cooperativity} = \frac{B}{2}\{b_0(c_0 - (R - R_{LS}))^2 + a_0(R - R_{LS})^2$$

$$-\sqrt{4J_0^2 + [b_0(c_0 - (R - R_{LS}))^2 + a_0(R - R_{LS})^2]^2}\}, \quad \text{(III.5)}$$

where a_0, b_0 and c_0 are parameters that control the concavity of the double-well potential energy. In the following, except otherwise mentioned, we set in the simulations the parameter B to 0.6, which allows to correctly reproduce the first-order spin transition curve with a 30-K-wide thermal hysteresis loop centered at ~290 K, which was experimentally observed for the bulk compound [Fe(pyrazine)][Ni(CN)$_4$] [135] (see **FIG. III. 2**). At this stage, it may be worth to note that in ultrathin SCO films one may expect a modification of SCO properties [74, 83, 84, 89, 90], but these finite size effects will be ignored in the present calculations.

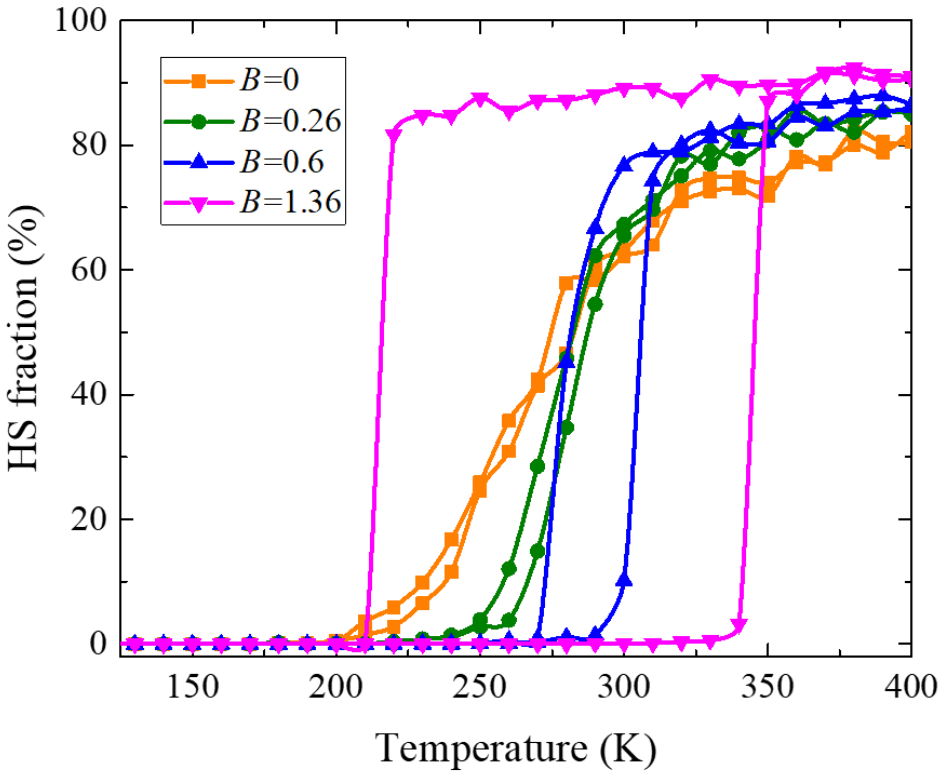

FIG. III. 2: Simulated spin-transition curves of the [Fe(pyrazine)][Ni(CN)$_4$] SCO compound, showing the thermal evolution of the HS fraction for different values of the parameter B, which controls the strength of the elastic interactions.

FIG. III. 3(a) depicts selected snapshots showing the spatial distribution of the spin-state configuration in the all-active system (N_I = 0), during the HS-to-LS relaxation process at 100 K. In these representations, it is worth mentioning that each unit cell of the

[Fe(pyrazine)][Ni(CN)$_4$] compound is simply represented by a red (or a blue) ball, depending on whether the corresponding Fe^{2+} ion is in the HS (or in the LS) state. Nevertheless, in the present work, it is important to remind that a realistic, all-atom structure is always considered in the simulations. In agreement with previous experimental and theoretical observations [40, 48, 155-157], we find that the HS-to-LS relaxation takes place via a heterogeneous phase separation process, characterized by the nucleation and the growth of a stable LS domain within the initial, metastable HS phase. In detail, the nucleation of a LS domain is found to occur at the corner of the system (where no mechanical constraint is applied) at ~21 ps, followed by the propagation of a LS/HS phase boundary throughout the cantilever to reach the opposite rigid border at $t \approx 60$ ps. By comparing the fully relaxed lattice (at $t = 60$ ps) to the initial HS lattice (at $t = 0$), we can note that the complete relaxation of the structure from the HS to the LS state is accompanied by a sizeable contraction of the unit cell, which leads to a visible decrease of the size of the system by ~5 %. For the same time delays, corresponding snapshots of the local strain in the structure, calculated from the simulations, are shown in **FIG. III. 3**(b). As the lattice state at $t = 0$ (full HS state) is taken as the reference in the present simulation, positive and negative values of the local strain correspond to tensile and compressive deformations, respectively. Overall, the simulated strain maps exhibit similar features than the spin-state configuration, indicating a clear correlation between the local spin state and the local strain of the structure. Specifically, as depicted in **FIG. III. 3**(b), a compressive strain region (deep blue color) is observed at the top left corner of the beam at $t = 21$ ps, in accordance with the nucleation of the LS domain. This compressive region then grows all along the cantilever, following the evolution of the spin-state configuration displayed in **FIG. III. 3**(a). At this stage, we shall underline that the typical relaxation times observed in our investigations are of the order of a few tens of ps (depending on the geometry of the system), which is significantly faster than what one would expect for an SCO system at 100 K [158]. This observation is linked to the fact that the intramolecular energy barrier was set in our model to significantly lower values than the experimentally observed ones, in order to 'fit' the relaxation time into the timeframe of the MD simulations. To overcome this drawback, future work may focus on using coarse-grained (CG) or Accelerated MD methods [159, 160].

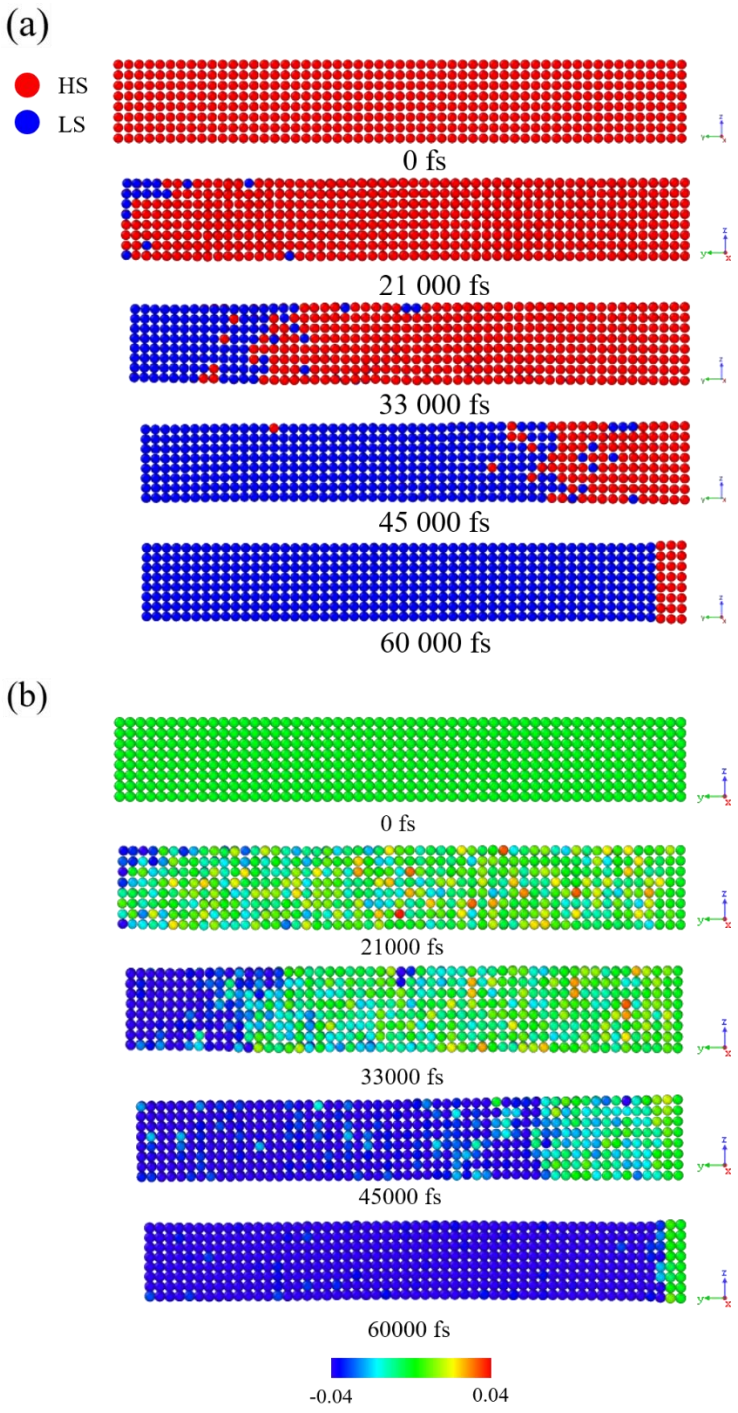

FIG. III. 3: Selected snapshots showing the spatial distribution of (a) the spin-state configuration and (b) the local lattice strain in the all-active system (N_I = 0) at different times during the HS-to-LS relaxation process at 100 K (for B = 0.6). In (a), the red and blue balls represent HS and LS sites, respectively. In (b), the color scale changes from red (tensile) to blue (compressive) strain through green (initial, zero strain) colors.

By comparison, **FIG. III. 4**(a) depicts selected snapshots of the spatial distribution of the local spin state during the relaxation process in the case of the bimorph system (N_I = 4), composed of four active (top) and four inactive (bottom) [Fe(pyrazine)][Ni(CN)$_4$] layers. Again, the left extremity of the bimorph cantilever is kept free to move. We observe that a LS domain appears at the top left corner of the beam at $t \approx 32$ ps, i.e. with a delay compared to the case of the all-active system (**FIG. III. 3**). At this moment, the concentration of these newly formed LS sites is already found to induce a slight bending of the cantilever. Later, at t = 67 ps, as the LS domain grows, a larger macroscopic distortion of the lattice (which results in a significant deflection of the device) is observed, and, interestingly, a second LS domain is formed in the middle of the cantilever. As depicted in the local strain mapping shown in **FIG. III. 4**(b), we can rationalize this observation by the fact that the bending of the lattice generates a compressive stress within the active part, which results in a local negative strain (indicated by an arrow at t = 32 ps), favoring the nucleation of this second LS domain. Finally, from t = 97 ps to t = 232 ps, the two formed LS domains merge and grow until reaching the rigid edge of the cantilever. Interestingly, in the stationary state (at t = 232 ps), we observe that a few SCO sites at the interface between the active and inactive parts of the system remain blocked in the HS state, presumably because they are submitted to a permanent tensile stress coming from the lattice misfit with the inactive (HS) part of the cantilever. Indeed, as displayed in **FIG. III. 4**(b), a detailed observation of the local strain mapping in the final relaxed state (at t = 232 000 fs) shows that strain gradients exist in both the active and the inactive layers of the cantilever. In clear, it appears that the magnitude of compressive strain gradually decreases within the active part when approaching the interface. In the same way, the distribution of strain in the inactive part of the structure shifts from compressive to tensile deformation (from green to red color). Such a gradient of strain within the structure is an obvious consequence of the bending of the cantilever. In addition, due to the existence of the HS/LS interface (between the inactive and active layers), the mismatch between HS and LS lattices gives rise to a compressive (resp. tensile) stress in the material near the interface in the inactive (resp. active) part, indicating competing mechanical effects between the active and inactive parts of the bimorph system.

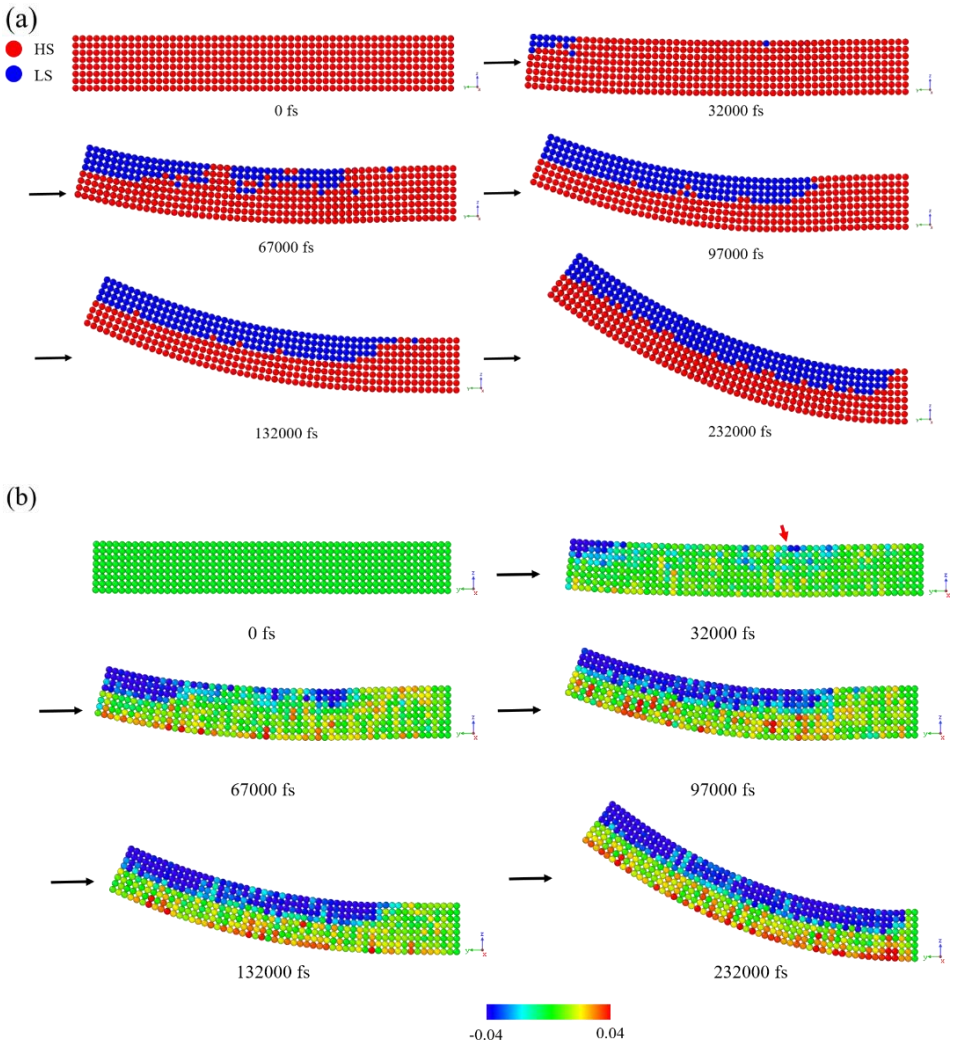

FIG. III. 4: Selected snapshots showing the spatial distribution of (a) the spin-state configuration and (b) the local lattice strain in the bimorph cantilever (N_I = 4), at different times during the HS-to-LS relaxation process at 100 K (for B = 0.6). In (a), the red and blue balls represent HS and LS sites, respectively. In (b), the color scale changes from red (tensile to blue (compressive) strain through green (initial, zero strain) colors.

III.3.2 Relaxation curves of the molecular spin state

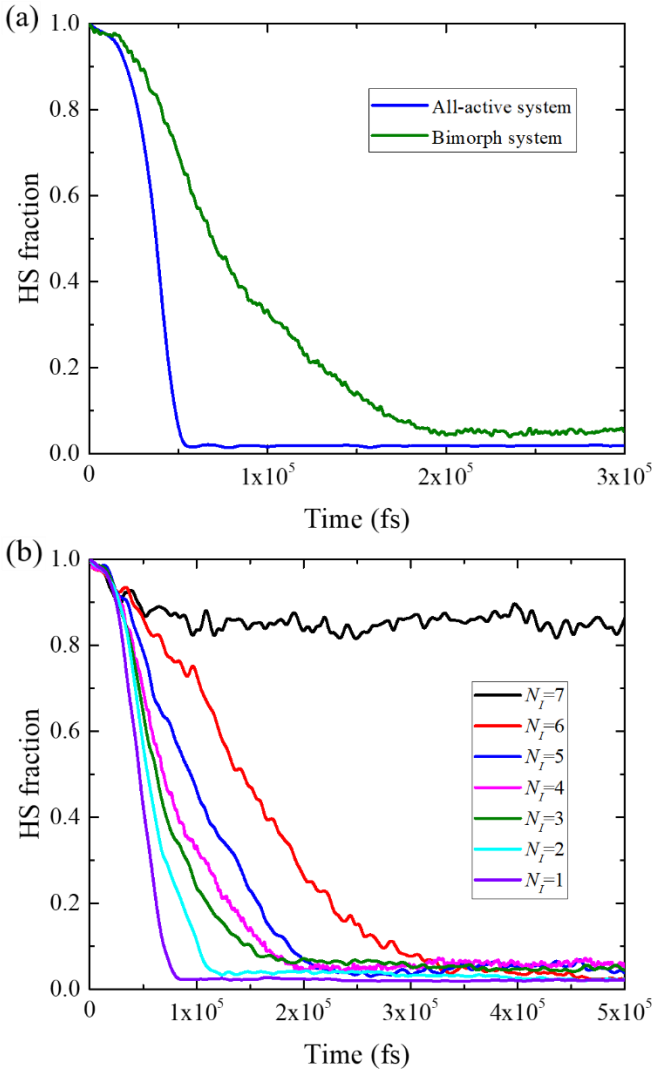

FIG. III. 5: (a) Time evolution of the HS fraction during the relaxation process at T = 100 K (for B = 0.6), in the all-active system (N_I = 0) and in the bimorph system (N_I = 4). (b) Time evolution of the HS fraction during the relaxation process in the bimorph system for different numbers N_I of inactive layers from 1 to 7.

FIG. III. 5(a) compares the thermal relaxation curves, displaying the time evolution of the fraction of HS sites, in the all-active system (N_I = 0) and in the bimorph system (N_I = 4). As shown in **FIG. III. 5**(a), the time needed by the system to reach the relaxed stationary state is considerably extended due to the presence of the inactive layers. Indeed, this inactive part (which remains in the HS state) produces a tensile stress in the active layers, as the latter switch from the HS to the LS state, due to the lattice misfit at the interface. As this tensile stress favors the HS state, the relaxation process is submitted to a law of moderation, resulting in a slowdown of the relaxation kinetics. Interestingly, if both ends of the bimorph are clamped, this effect is

further amplified, because the structure cannot relieve any more part of the tensile stress by the bending movement (see blue curve in **FIG. III. 5(**a)). **FIG. III. 5**(b) depicts the evolution of the HS-to-LS relaxation kinetics in the bimorph system (with N_{tot} = 8) upon varying the number of inactive layers N_I from 1 to 7. Remarkably, a considerable slowdown of the relaxation kinetics can be observed when increasing the thickness of the inactive part of the cantilever. A straightforward explanation is that the increase of the thickness of the inactive (HS) part contributes to generating tensile stress on the active part, whereas the increased stiffness of the structure prevents the release of this stress. These effects result in a longer lifetime of the metastable HS state in the active layers. Interestingly, as shown in **FIG. III. 5**(b) (black curve), in the extreme case where N_I = 7 (i.e. N_S = 1), it appears that only ~15 % of the SCO sites in the active layers switch into the LS form in the stationary state.

Qualitatively comparable results have been obtained from the simulations of the spin-transition properties of SCO monolayers on a substrate (using spring-ball models), or from the simulations of bimorph nanoparticles in which a SCO core is surrounded by an inactive shell [76, 78, 80, 84, 91, 96-101, 111, 161-164]. These different theoretical investigations have the advantage to give a description of the elastic mechanisms involved in the switching process of such hybrid nanomaterials and are in a qualitative good agreement with the different accessible experimental observations.

III.3.3 Deflection behaviors

To investigate the actuating performance of the modelled bimorph system, we focus on the deflection, which is defined as the distance between the instantaneous and initial vertical positions of the free extremity of the cantilever. **FIG. III. 6**(a) shows the time evolution of the deflection in the bimorph actuator (N_{tot} = 8) associated to the HS-to-LS relaxation process for different thicknesses of the inactive part (N_I ranging from 1 to 7 layers). For each simulated system, damped oscillations of the deflection of the cantilever are observed before reaching a stationary mechanical state, defining the equilibrium deflection. It is worth mentioning that these oscillations take place on a longer timescale (~ns) than the relaxation kinetics of the molecular spin state (~100 ps, see **FIG. III. 5**(b)), meaning that the spin-state equilibrium is reached faster than the mechanical equilibrium of the cantilever. This oscillatory movement presumably comes from the fact that the fast switching kinetics of the molecular spin state

initially produces an overshoot of the deflection of the beam, so that the system finally reaches a mechanical equilibrium state by oscillating at its natural bending frequency. It may be worth to mention here that similar damped mechanical oscillations have been recently observed using time-resolved electron microscopy upon pulsed laser excitation of SCO nanoparticles [165]. We can thus suggest that those experimental findings might have the same origin as in the present simulations, i.e. a mismatch between the timescales of the SCO and the natural stretching frequency of the particles.

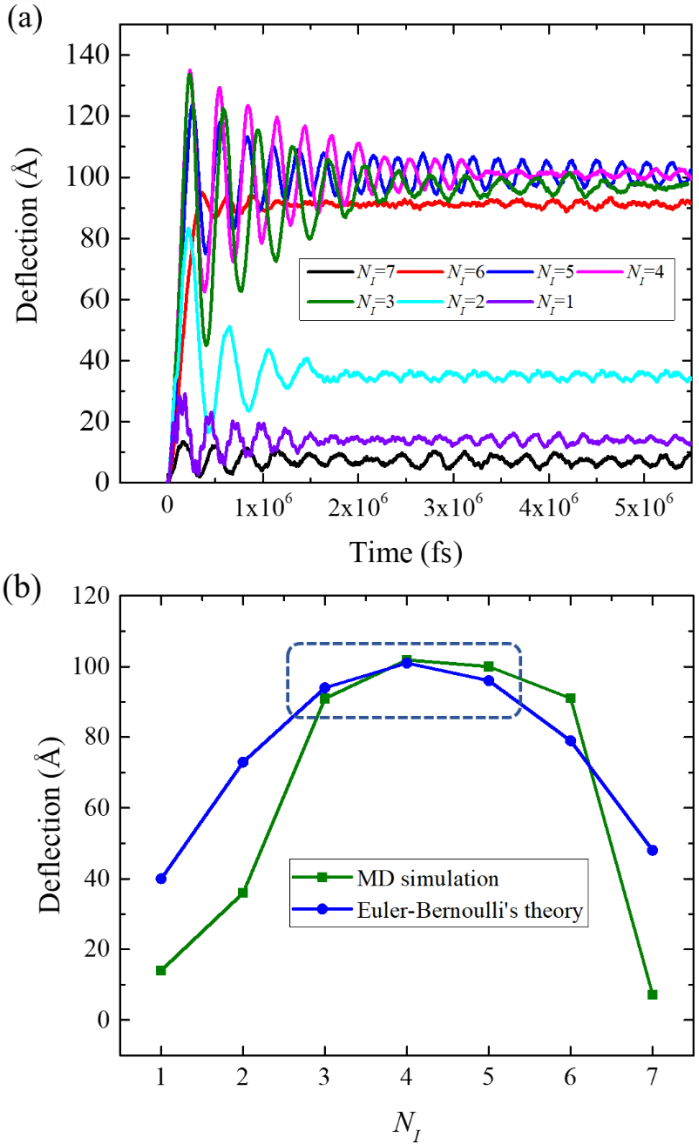

FIG. III. 6: (a) Time evolution of the deflection of the bimorph cantilever (N_{tot} = 8) during the HS-to-LS relaxation process (at 100 K, B = 0.6) for different thicknesses of the inactive part, N_I, ranging from 1 to 7 layers. (b) Equilibrium deflection of the bimorph actuator as a function of N_I deduced from the present MD simulations and from the Euler-Bernoulli's beam theory.

As it can be expected, the equilibrium deflection strongly depends on the number of inactive layers N_I. In particular, the black curve in **FIG. III. 6**(b) shows that the equilibrium deflection exhibits a non-monotonous behavior as a function of N_I and passes through a maximum ($\delta \approx 100$ Å) for $N_I = 4$, i.e., when the thicknesses of the active and inactive regions are equal. Importantly, the atomistic approach used in this work allows to assess macroscopic/mesoscopic quantities, such as mechanical deflections, which can also be inferred from continuum mechanics models. Indeed, according to the Euler-Bernoulli's beam theory [166, 167], the curvature (k) of a bimorph cantilever can be expressed as:

$$k = \frac{6\left(\alpha_i \Delta T + \frac{\Delta L}{L} - \alpha_s \Delta T\right)(1+m)^2}{h\left[3(1+m)^2 + (1+mn)\left(m^2 + \frac{1}{mn}\right)\right]}, \quad \text{(III.5)}$$

$$m = \frac{a_s}{a_i}, \quad \text{(III.6)}$$

$$n = \frac{E_s}{E_i}, \quad \text{(III.7)}$$

$$h = a_s + a_i, \quad \text{(III.8)}$$

where the subscripts *s* and *i* stand for the switchable and inactive parts of the bimorph system, respectively. ΔT is the working temperature range, ΔL is the change of length induced by SCO, α is the coefficient of thermal expansion, E is the Young's modulus and a is the thickness. The deflection δ can be estimated through the following relationship:

$$\delta = \frac{kL^2}{2}, \quad \text{(III.9)}$$

where L is the length of the cantilever. $E_i = 10.4$ Gpa and $E_s = 13.5$ GPa are taken from ref. [126]. It should be noted that the first order HS→LS spin transition causes a spontaneous strain, which is usually ~10^4 times larger than the strain induced by the thermal expansion. Thus, the coefficients of thermal expansion in Eq. 5 are ignored in the present calculation ($\alpha_i = a_i = 0$). By comparison with the result of our MD simulations, the deflections of the various studied systems extracted from the Euler-Bernoulli's theory, are also displayed in **FIG. III. 6**(b). Similar to our MD simulations, the deflection of the bimorph cantilever follows a bell-shape curve as a function of N_I, reaching a maximum for $N_I = 4$. Overall, the deflection values obtained from the two approaches are in good agreement within the range $N_I = 3$–5. As shown in **FIG. III. 6** (b), for lower and higher values of N_I, the results from these two methods show larger deviations. Such a difference can probably arise from the fact that the effective thermomechanical properties are modified when these materials become extremely thin. In

particular, our MD simulations show that only a reduced fraction of SCO complexes can effectively switch into the LS state (in particular in the case $N_I = 7$, as shown in **FIG. III. 5**(b)), which can explain why the deflection is smaller compared to the one extracted from the Euler-Bernoulli's theory.

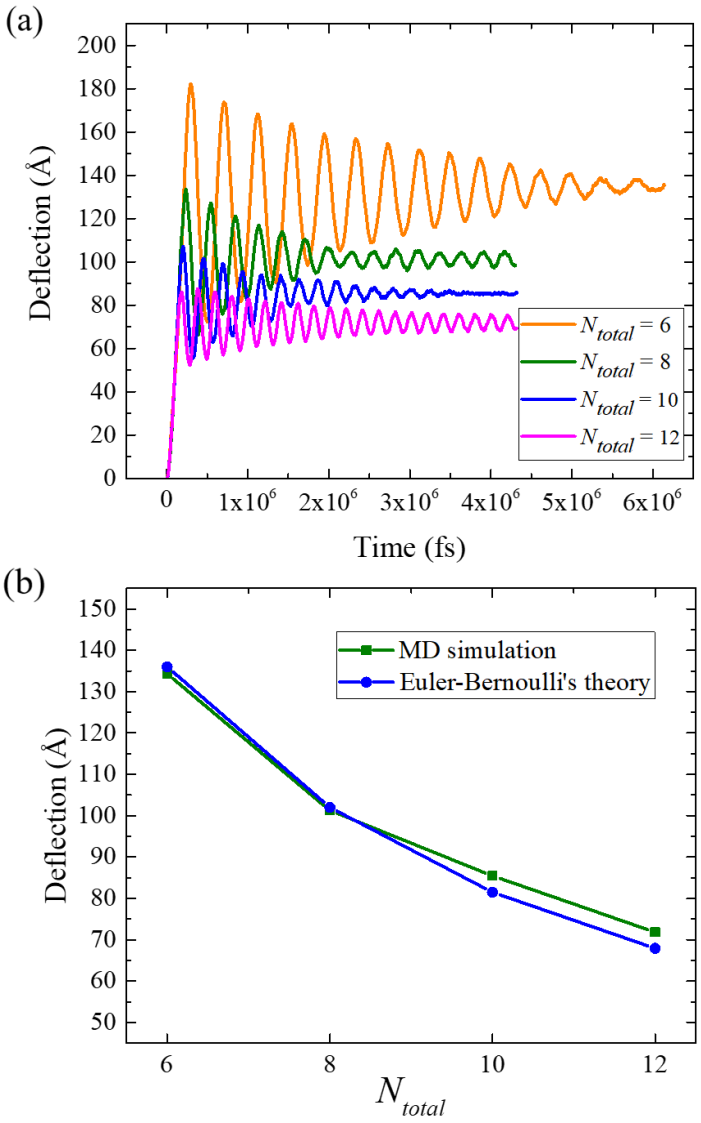

FIG. III. 7: (a) Time dependence of the deflection of the bimorph cantilever for different thicknesses during the HS-to-LS relaxation process (T = 100 K, B = 0.6). (b) Equilibrium deflection of the bimorph cantilever for different thicknesses inferred from the present MD simulations and from the Euler-Bernoulli's beam theory.

We have also investigated the effect of the total thickness (N_{tot}) of the cantilever on the deflection. To this aim, a ratio of $N_I/N_S = 1$ is selected (i.e., equal thicknesses are considered for

the active and inactive parts), which corresponds to the case where the bimorph system exhibits the largest deflection at the thermal and mechanical equilibrium. Bimorph cantilevers with sizes N_{tot} = 6, 8, 10 and 12 (i.e., $N_I = N_S$ = 3, 4, 5 and 6) were analyzed and the time evolution of the deflection of these bimorphs was followed. As shown in **FIG. III. 7**(a), we observe that both the amplitude and the period of the oscillations are reduced when increasing the total thickness of the cantilever, primarily due to the increased bending stiffness of the whole structure. (N.B. The increase of mass acts in the opposite way.) In concomitance, we also observe that the equilibrium deflection is significantly reduced with the increase of the total thickness. Indeed, as depicted in **FIG. III. 7**(b), the deflection at the equilibrium state drops from 134 to 82 Å upon increasing the total thickness of the cantilever from 6 to 12 [Fe(pyrazine)][$Ni(CN)_4$] layers. Besides, as shown in **FIG. III. 7**(b), the equilibrium deflections extracted from the present MD simulations are found to be in good agreement with the values calculated using the Euler-Bernoulli's theory, which further validates our approach.

III.3.4 Effect of the cooperativity

The influence of the cooperativity of the SCO material on the HS-to-LS relaxation process and the actuating performance of the cantilever are investigated by varying the value of the parameter *B*, which drives the strength of the elastic interactions. To this aim, three additional values of *B* (*B* = 0, 0.26 and 1.36) were investigated, which correspond, respectively, to the case of a gradual spin conversion (with no hysteresis loop), a transition with a narrow (~ 5-K-wide) hysteresis loop and a transition with a large (~ 130-K-wide) thermal hysteresis loop, as depicted in **FIG. III. 2**.

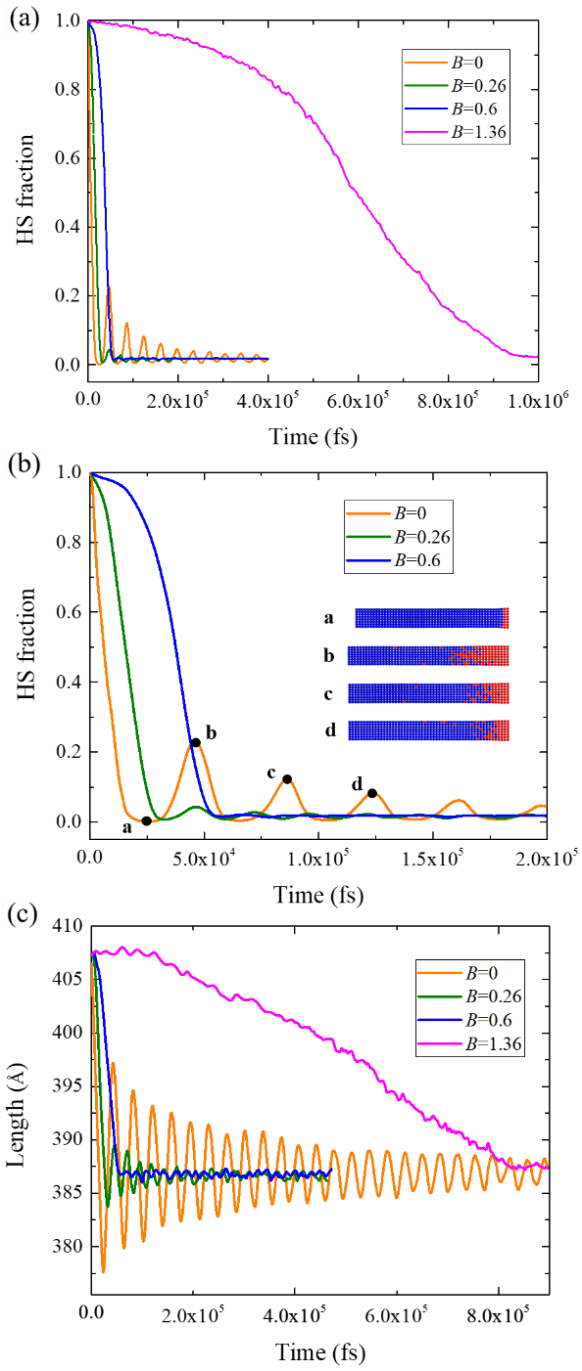

FIG. III. 8: (a) Time evolution of the HS fraction during the HS-to-LS relaxation process at T = 100 K in the all-active system (N_I = 0) for various values of *B*. (b) Zoom showing the time evolution of the HS fraction at short timescales for *B* = 0, 0.26 and 0.6. Inset: Snapshots of the spatial distribution of the spin-state configuration at different times (marked by black dots) in the case *B* = 0. The red and blue balls represent HS and LS sites, respectively. (c) Time evolution of the length of the all-active system (N_I = 0) during the HS-to-LS relaxation process at T = 100 K for various values of *B*.

FIG. III. 8(a) and **8**(b) show the time evolution of the HS fraction in the all-active system (N_I = 0) for different values of *B*. As *B* decreases, the shape of the relaxation curves switches from sigmoidal to exponential (or stretched exponential), which indicates a change from a strongly cooperative behavior to a weakly cooperative behavior [34, 168-170]. This lengthening of the lifetime of the metastable HS state in the 'highly cooperative' case occurs due to the fact that the strong elastic interactions produce a high energy barrier that needs to be overcome in order to relax into the LS state. Interestingly, clear damped oscillations are observed in the time evolution of both the length of the cantilever and of the HS fraction (**FIG. III. 8** (c)). It is found the damped oscillation periods of the spin-state are close to those of the length of the cantilever for each value of *B*. The amplitude and the period of these oscillations appear to be strongly dependent on the cooperative character of the SCO material. Indeed, for low cooperativity (*B* = 0), it appears that the spin-state relaxation time is much faster compared to the period of stretching oscillations of the cantilever ($T_{stretching} \approx 40$ ps), which generates an initial 'overshoot' in the longitudinal deformation of the cantilever. The latter thus releases the excess mechanical energy by oscillating at the natural stretching frequency of the structure. This oscillation frequency is found to depend on the strength of the elastic interactions *B*. Indeed, we observe that the oscillation frequency becomes larger when increasing *B*, which parallels the increasing stiffness of the SCO material. The damped oscillations observed in the temporal evolution of the HS fraction show that the molecular spin state is linked to the global deformation (strain) of the structure, i.e. the oscillation of the beam provokes an oscillation of the HS fraction. However, the amplitude of the oscillations (in terms of HS fraction) are found to be reduced with *B* because the switching kinetics between the LS and HS states becomes slow in comparison with the natural stretching frequency of the cantilever. As an example, for *B* = 1.36, the full relaxation into the LS state is completed in ~1 ns, which is significantly longer than the period of stretching oscillations $T_{stretching}$ of the structure, so that no oscillations are observed at all in this case.

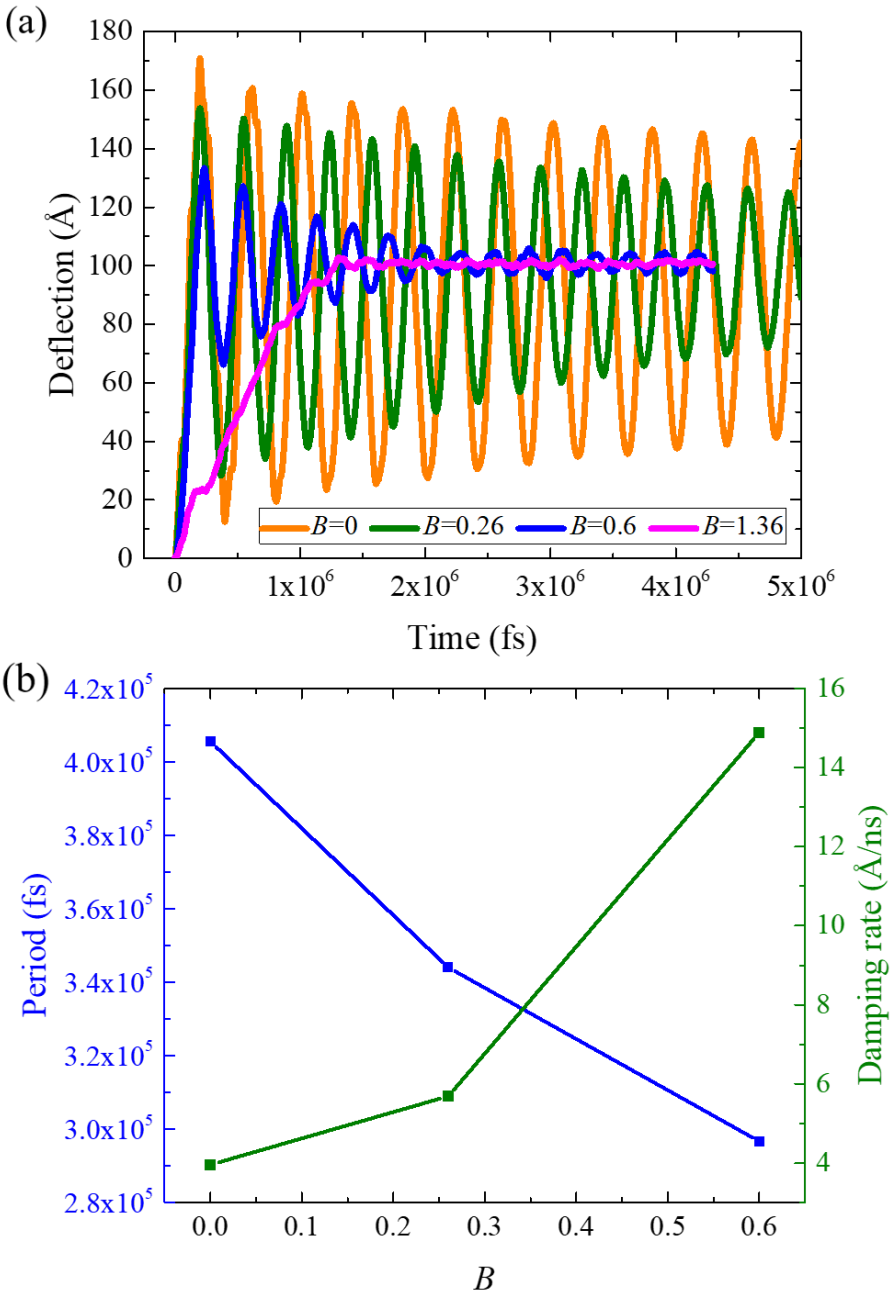

FIG. III. 9: (a) Time evolution of the deflection of the bimorph cantilever (in the case $N_I = N_S = 4$) during the HS-to-LS relaxation process at T = 100 K for various values of *B*. (b) Evolution of the period and damping rate of the deflection oscillations as a function of *B*.

Following this study of the all-active, unimorph cantilever, we have also investigated the effect of cooperativity on the time evolution of the HS fraction and the deflection of the bimorph cantilever. To this aim, we have studied the case $N_I = N_S = 4$, which enables the largest deflection to occur, as discussed previously. The time evolution of the deflection δ of the cantilever during

the HS-to-LS relaxation process is plotted in **FIG. III. 9**(a) for different values of *B*. The first observation is that an identical deflection ($\delta \approx 100$ Å) is obtained at the equilibrium state, independently of the value of *B*. Indeed, since the value of *B* is tuned for both the inactive and the switchable layers of the cantilever, the ratio of the Young's moduli of the two parts (E_s/E_i) remains constant, which implies no change of the equilibrium deflection (see Eq. III.5). However, large damped oscillations of the deflection are observed before reaching the stationary state. These oscillations to reach the mechanical equilibrium state take place at the natural bending frequency of the cantilever. Interestingly, as the cooperativity (*B*) is reduced, both the amplitude and the period of the oscillations are increased (see **FIG. III. 9**(b)). This comes from the fact that the reduction of *B* implies a softening of the lattice, which becomes more deformable, thus allowing larger deflections to occur. In addition, as both the oscillation frequency and the damping rate are proportional to $\sqrt{E}$, we observe that the reduction of *B* leads also to an increase of the bending oscillation period of the bimorph system, going from ~300 ps (~3.33 GHz) to ~400 ps (~2.50 GHz) and a concomitant decrease of the damping rate when the value of *B* is decreased from 0.6 to 0 (**FIG. III. 9**(b)). By comparison, the time evolution of the HS fraction for the different values of *B* is shown in **FIG. III. 10**(a). As already mentioned, the switching kinetics between the LS and HS states is considerably slowed down for large values of *B*. In the case $B = 0$, the HS fraction is found to oscillate with two characteristic periods, $T_{stretching} = 40$ ps and $T_{bend} = 400$ ps, which respectively correspond to the natural stretching period (as it was shown through the study of the all-active system) and the natural bending period of the cantilever. Thus, we find that the time evolution of the HS fraction faithfully follows the (stretching and bending) deformations of the studied bimorph system, clearly showing the interplay between the molecular electronic state and the local stress/strain within the structure. When *B* is increased, the amplitude of the oscillations of the HS fraction is largely reduced (for $B = 0.26$ and 0.6, only the bending oscillations of the cantilever have a visible effect on the HS fraction). Again, this effect arises from the fact that an increase of cooperativity has the effect of progressively slowing down the HS ↔ LS switching kinetics, so that the HS fraction will be first decoupled from the fast stretching oscillations and, in a second time, from the slower bending oscillations of the cantilever. (Note that a slow relaxation kinetics also has the effect of preventing an overshoot effect in the bending or in the longitudinal shrinkage of the cantilever, which could lead to large oscillations.) Finally, as shown in **FIGs. III. 9**(a) and **10**(a), in the case of a highly cooperative SCO material ($B = 1.36$), the full LS state and the equilibrium deflection are reached within ~1.4 ns with no oscillations.

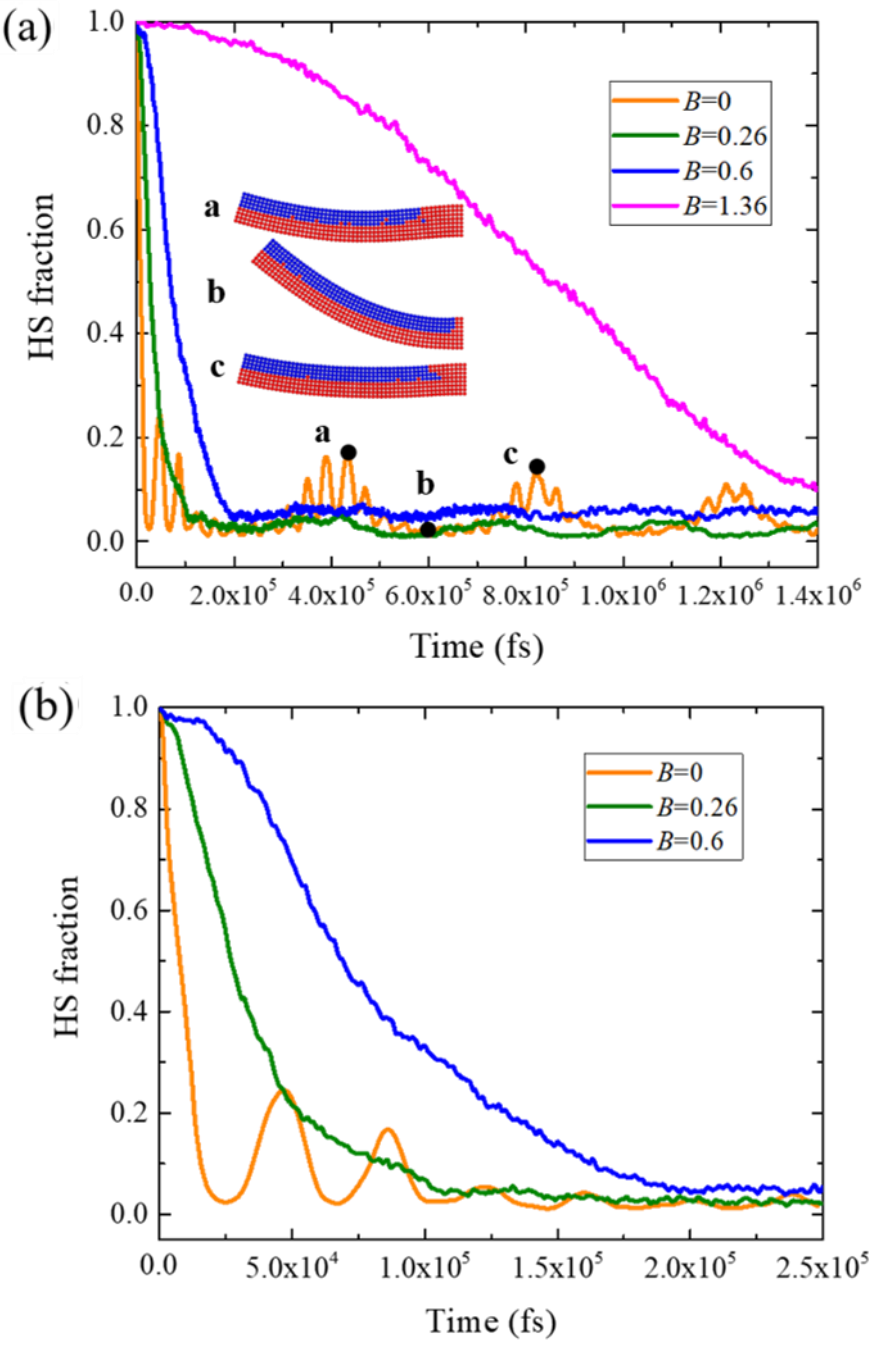

FIG. III. 10: (a) Time evolution of the HS fraction in the bimorph cantilever (in the case N_I = N_S = 4) during the HS-to-LS relaxation process at T = 100 K for various values of B. Inset: Snapshots of the spatial distribution of the spin-state configuration at different times (marked by black dots) in the case B = 0. The red and blue balls represent HS and LS sites, respectively. (b) Zoom showing the time evolution of the HS fraction at short timescales for B = 0, 0.26 and 0.6.

III.3.5 Propagation velocity of the LS/HS phase boundary

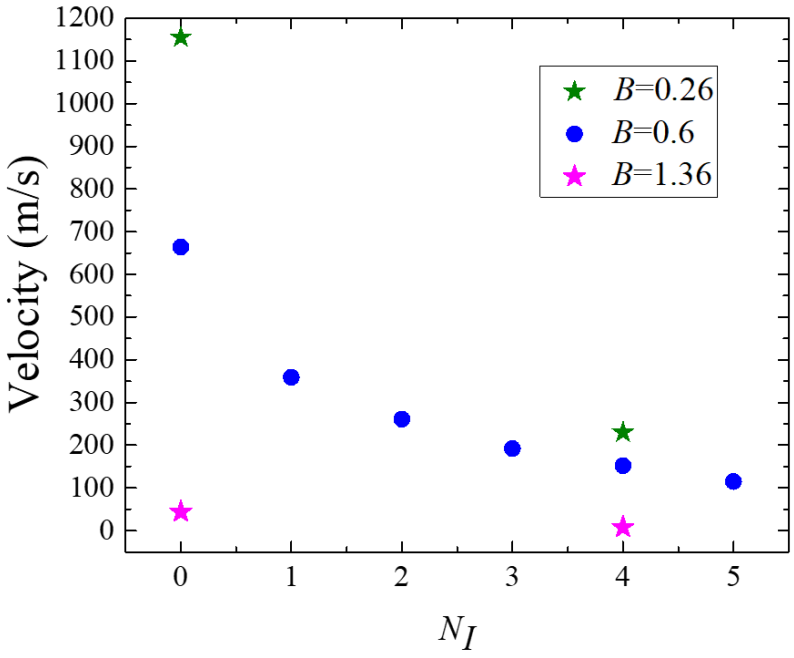

FIG. III. 11: Mean propagation velocity of the HS/LS phase boundary as a function of the number of inactive layers N_I in the bimorph cantilever, during the HS-to-LS relaxation process at T = 100 K.

Our MD simulations provide us also an opportunity to assess the propagation velocities of the HS/LS phase boundary during the relaxation process. This question is of great interest to better understand the mechanistic details of the nucleation and growth process and the switching dynamics of SCO solids exhibiting first-order spin transitions [155]. **FIG. III. 11** displays the evolution of the mean propagation velocity of the HS/LS phase boundary as a function of the number of inactive layers N_I in the bimorph cantilever, during the HS-to-LS relaxation process. We observe clearly that the propagation velocity is considerably lowered when increasing N_I, which can be accounted for to the existence of a tensile stress brought in by the inactive part of the cantilever, which stabilizes the HS phase in the active region. For example, for B = 0.6 (blue dots), the velocity drops from 664 m s^{-1} for the all-active system (N_I = 0) to 115 m s^{-1} in the

presence of five HS inactive layers (N_I = 5). This result agrees with experimental observations in the solid-state grain boundary migration under external strain [171, 172]. In the all-active system (N_I = 0), changing the cooperativity of the SCO material has a huge impact (by more than one order of magnitude) on the propagation velocities of the HS/LS phase boundary, the latter falling from 1155 m s^{-1} for B = 0.26 (weakly cooperative) to 44 m s^{-1} for B = 1.36 (highly cooperative). This change of the velocity presumably comes from the fact that a greater energy barrier has to be overcome (due to stronger elastic interactions) during the growth of the LS phase in highly cooperative materials, which hinders the propagation of the phase boundary.

Overall, propagation velocities of the order of several hundred m s^{-1} are found, which are several orders of magnitude larger than those generally observed in macroscopic SCO single crystals (µm s^{-1} - mm s^{-1}) [155, 173]. This discrepancy can be linked to several factors, such as the extremely different size of the investigated systems, the presence/absence of crystal defects and the use of reduced intermolecular energy barriers in the simulated system. Further work is needed to evaluate the relative importance of these different parameters.

III.4 Conclusions

In conclusion, we have performed a theoretical study to investigate the spin-state relaxation process and the resulting deformation of a bimorph cantilever beam of the [Fe(pyrazine)][$Ni(CN)_4$] SCO material, through all-atom MD simulation based on our recently constructed force field. Spatiotemporal aspects of the spin transition were investigated by visualizing the real-time spin-state configuration and the local strain on each SCO site during the HS-to-LS relaxation process. Interestingly the phase separation process and its dynamics appear to be significantly influenced by the presence of the inactive layers of the actuator, which exert tensile stress on the active layers, while the concomitant bending of the cantilever induces the formation of additional LS domains during the nucleation and growth process. Importantly, the deflection obtained from our simulations at equilibrium is found to be in good agreement with that from the Euler-Bernoulli continuum mechanics model, in particular for sufficiently thick systems. Interestingly, in some cases, clear stretching and bending damped oscillations of the cantilever (at the natural frequencies of the structure) are observed during the switching

process before reaching a mechanical equilibrium state. The amplitude and frequency of these oscillations are found to depend on the total thickness of the cantilever and on the cooperativity (stiffness) of the SCO material. Especially, oscillations with large amplitude are observed in the case of fast spin-state switching (observed for weakly cooperative materials) presumably due to an initial overshoot in the deformation of the structure. Interestingly, damped oscillations were also observed in the time evolution of the HS fraction during the relaxation process, showing the intimate interplay between the deformation state of the cantilever and the molecular spin state.

Chapter IV: Effects of surface energy and surface stress on the spin crossover phenomenon analyzed by a thermodynamic model

IV.1 Introduction

Drastic changes of the SCO properties can appear when the size of the SCO material is reduced to nano-scale, such as the downshift of the equilibrium temperature, the disappearance of hysteresis loop and a residual HS fraction at low temperature. As mentioned above, atomistic simulations solved by MC methods have been extensively used to predict the SCO behaviors at the nano-scale. While these approaches are extremely powerful to uncover the essential physical ingredients, which come into play in the size reduction effects, they remain essentially qualitative due to the oversimplified material structure and the associated difficulties to make a quantitative link between the model parameters and material properties. To conduct a more quantitative analysis using experimentally accessible physical properties of SCO materials, we decided thus to work on an easily solvable nano-thermodynamics model, which could allow predicting the spin-switching behaviors of particular SCO complexes at the nano-scale.

In the solid state, the thermodynamics of surfaces can be expressed by the surface energy (γ) and the surface stress (σ), whose definitions have been given in **Chapter I**. Indeed, several works have highlighted that both the surface energy and the surface stress play important roles in the phase stability of different materials at reduced sizes [174-176] and, as discussed before, the effect of surface stress has already been considered in the context of SCO materials as well [112]. In the present work, we continued the development of the nano-thermodynamical core-shell model proposed by Félix et al. [107]. On one hand side, we replaced the phenomenological interaction term by a continuum mechanical approach, similar to that of Spiering et al. [27], in which the intermolecular elastic interactions are explicitly taken into account by considering the change of the molecular volume during the spin switching. In addition, the spin-state dependent surface stress density has considered for the first time in the field of SCO. Based on

this new model, the consequences of the surface energy/stress on the phase stability of SCO nano-objects were investigated upon size reduction.

First, we will present the new nano-thermodynamic model. Then, we will discuss the effects of surface energy and surface stress on the SCO properties of a 5 nm thick [Fe(pyrazine)][Ni(CN)$_4$] film. Then, based on the surface energies obtained through MD calculation, we will investigate the size reduction effects on [Fe(pyrazine)][Ni(CN)$_4$] thin films. Calculations were also conducted on nanoparticles of [Fe(pyrazine)][Ni(CN)$_4$], which are presented in **Annexes**.

IV.2 Construction of the nano-thermodynamic model

IV.2.1 Bulk material

The total Gibbs free energy (G_{total}) of a SCO system can be expressed as:

$$G_{total} = G - TS_{mix} + G_{elastic} + G_{surface}, \quad \text{(IV.1)}$$

where G, S_{mix}, $G_{elastic}$, and $G_{surface}$ are the contributions of non-interacting molecule Gibbs energy, mixing entropy, elastic interaction and surface energy, respectively. In the following part of this section, each contribution is discussed in details.

First, we consider a bulk SCO system consisting of *N* molecules. The Gibbs energy of non-interacting molecules is:

$$G = N_{\uparrow}G_{\uparrow} + N_{\downarrow}G_{\downarrow} = N_{\uparrow}(G_{\uparrow} - G_{\downarrow}) + NG_{\downarrow}$$

$$= N_{\uparrow}(E_{\uparrow} - E_{\downarrow}) - TN_{\uparrow}(S_{\uparrow} - S_{\downarrow}) + NE_{\downarrow} - TNS_{\downarrow}, \quad \text{(IV.2)}$$

where *E* is the enthalpy, *S* the entropy and *T* the temperature. The subscripts "↑" and "↓" are related to the HS and LS states, respectively. Denoting x the HS fraction, the enthalpy variation (ΔE) and entropy variation (ΔS) between the two states can be written as:

$$x = \frac{N_{\uparrow}}{N}, \quad \text{(IV.3)}$$

$$\Delta E = E_{\uparrow} - E_{\downarrow}, \tag{IV.4}$$

$$\Delta S = S_{\uparrow} - S_{\downarrow}, \tag{IV.5}$$

The total contribution of non-interacting molecules to the Gibbs energy (G) can be then written as:

$$G = Nx(\Delta E - T\Delta S) + N(E_{\downarrow} - TS_{\downarrow}), \tag{IV.6}$$

The mixing entropy indicates a loss of statistical information. Under the thermodynamic limit, it can be expressed as:

$$S_{mix} = -Nk\left[\frac{N_{\uparrow}}{N} ln\left(\frac{N_{\uparrow}}{N}\right) + \frac{N_{\downarrow}}{N}\ln\left(\frac{N_{\downarrow}}{N}\right)\right] = -Nk[xln(x) + (1-x)\ln(1-x)], \tag{IV.7}$$

where *k* is the Boltzmann constant. It should be noted that the mixture is assumed to be uniform and homogenous after the mixing process, i. e., the interface energy between the HS and LS states is not included in the mixing entropy.

We assume that all the molecules of the system have the same minimum volume V_{min} during the spin state switching (**FIG. IV.1**). Accordingly, the elastic interaction energy of the system can be obtained through [27]:

$$G_{elastic} = N_{\uparrow}(\gamma_o - 1)\frac{B_{\uparrow}}{2V_{\uparrow}}(V_{min} - V_{\uparrow})^2 + N_{\downarrow}(\gamma_o - 1)\frac{B_{\downarrow}}{2V_{\downarrow}}(V_{min} - V_{\downarrow})^2, \tag{IV.8}$$

where B is the Bulk modulus, $V_{\uparrow}$ and $V_{\downarrow}$are the equilibrium volumes of the molecules in the HS and LS states, respectively. γ_o is the Eshelby's constant which corresponds to the contribution of local volume change to the global volume change of the whole crystal. It can be estimated through [177]:

$$\gamma_o = 3\frac{1-\nu}{1+\nu}, \tag{IV.9}$$

where ν is the Poisson's ratio. Further, we define the ratio of HS to LS bulk moduli (β) and the mismatch of volumes (m):

$$\beta = \frac{B_{\uparrow}}{B_{\downarrow}}\ , \tag{IV.10}$$

$$m = \frac{V_{\uparrow}}{V_{\downarrow}}\ , \tag{IV.11}$$

The total elastic interaction energy of the bulk system is then written as:

$$G_{elastic} = N(\gamma_o - 1)\frac{B_{\uparrow}V_{\uparrow}}{2}\left[x\left(\frac{V_{min}}{V_{\uparrow}} - 1\right)^2 + (1-x)\frac{m}{\beta}\left(\frac{V_{min}}{V_{\uparrow}} - \frac{1}{m}\right)^2\right], \quad \text{(IV.12)}$$

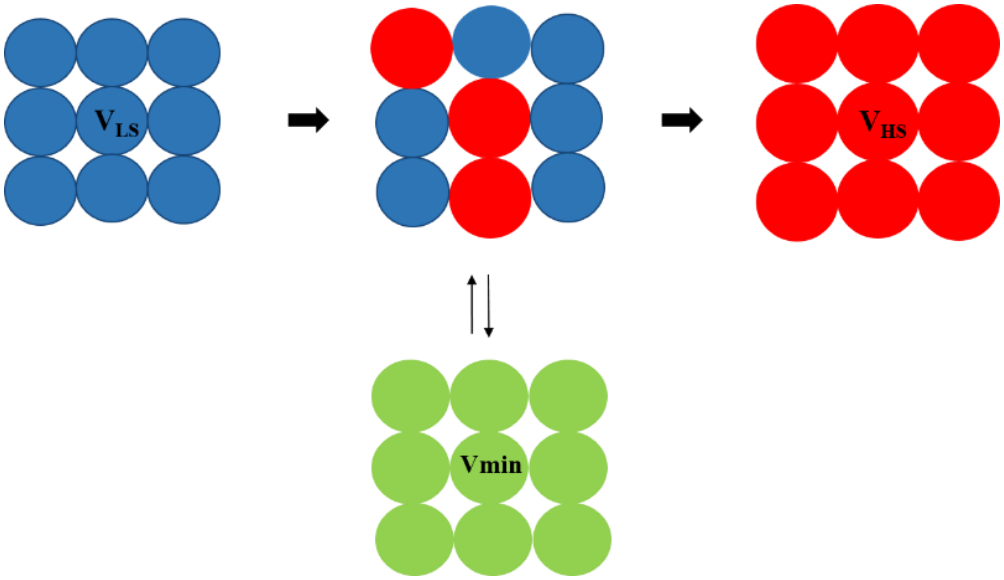

FIG. IV.1: Simplified representations of the SCO molecules during the spin state switching.

As discussed before, the surface energy is the work per unit area involved in forming a surface, while the surface stress is associated with the reversible work per unit area needed to elastically stretch a pre-existing surface. Accordingly, the total surface energy (G^{se}) and the work against surface stress (G^{ss}) in a flat thin film (**FIG. IV.2** (a)) with a surface area *A* can be calculated by:

$$G^{se} = \gamma A, \quad \text{(IV.13)}$$

$$G^{ss} = 2\int \sigma dA, \quad \text{(IV.14)}$$

It should be noted that the surface stress is taken to be isotropic and independent of strain in this study.

Let a^0 be the lattice parameter of the material. N^a and N^b are defined as the number of molecules in the surface and in the core, respectively. The contribution of the surface energy and surface stress to the Gibbs free energy is then written as:

$$G_{surface} = N_{\uparrow}^{a}\left[\frac{V_{\uparrow}}{a_{\uparrow}^{0}}\gamma_{\uparrow} + \left(V_{min}^{2/3} - \frac{V_{\uparrow}}{a_{\uparrow}^{0}}\right)\sigma_{\uparrow}\right] + N_{\downarrow}^{a}\left[\frac{V_{\downarrow}}{a_{\downarrow}^{0}}\gamma_{\downarrow} + \left(V_{min}^{2/3} - \frac{V_{\downarrow}}{a_{\downarrow}^{0}}\right)\sigma_{\downarrow}\right], \quad \text{(IV.15)}$$

On the other hand, for a spherical particle (**FIG. IV.2** (b)) with a volume of V and a surface area of A, according to the Laplace-Young equation [178], the pressure difference (ΔP) between inside and outside the particle is expressed as:

$$\Delta P = \frac{2\sigma A}{3V}, \tag{IV.16}$$

In this case, the work against surface stress (G^{ss}) is derived from the pressure difference:

$$G^{ss} = \Delta P dV = \frac{2\sigma A}{3V} dV, \tag{IV.17}$$

Then the total contribution of the surface is:

$$G_{surface} = N_{\uparrow}^{a} \frac{V_{\uparrow}}{a_{\uparrow}^{0}} \left[\gamma_{\uparrow} + \frac{2}{3}\left(\frac{V_{min}}{V_{\uparrow}} - 1\right)\sigma_{\uparrow}\right] + N_{\downarrow}^{a} \frac{V_{\downarrow}}{a_{\downarrow}^{0}} \left[\gamma_{\downarrow} + \frac{2}{3}\frac{V_{\uparrow}}{V_{\downarrow}}\left(\frac{V_{min}}{V_{\uparrow}} - \frac{1}{m}\right)\sigma_{\downarrow}\right], \tag{IV.18}$$

In Eq. IV.18, $N_{\uparrow}^{a} \frac{V_{\uparrow}}{a_{\uparrow}^{0}} + N_{\downarrow}^{a} \frac{V_{\downarrow}}{a_{\downarrow}^{0}} = 4\pi R^2$ stands for the total surface area of system.

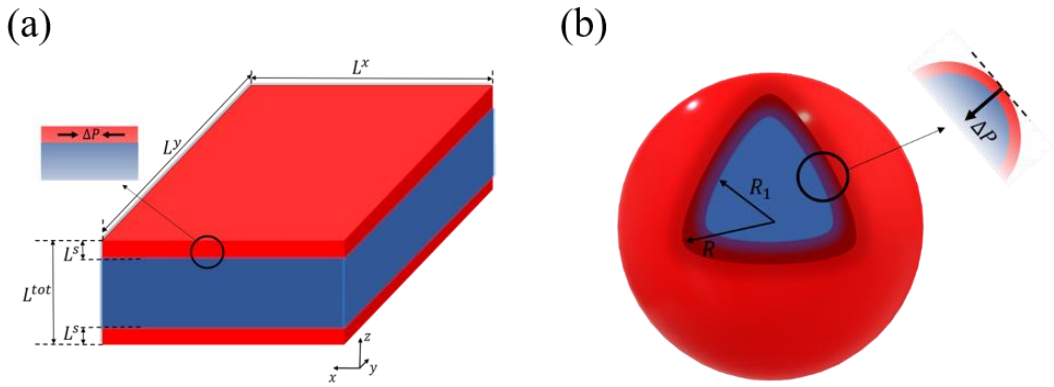

FIG. IV.2. Schematic representations of (a) the thin-film model and (b) the spherical core-shell model. The region in blue color represents the bulk-like core, and the region in red color represents the shell.

IV.2.2 Thin film model

First, we calculate the above contributions in the case of a flat thin film whose dimensions along the x and y directions are L^x and L^y, respectively. The film consists of a bulk-like core with a thickness of L^{tot} and two surfaces with the same thickness of L^s along the z direction, as

shown in **FIG. IV.2** (a). Under the consideration that $L^x(L^y) \gg L^{tot}$ and that all the molecules in the system are in the HS state, the numbers of molecules in the core (N^b) and in the shell (N^s) are:

$$N^b = N\frac{L^{tot}-2L^s}{L^{tot}}, \tag{IV.19}$$

$$N^s = N\frac{2L^s}{L^{tot}}, \tag{IV.20}$$

Assuming that the shell consists of a monolayer, the number of molecules at the surface N^a equals to the number of molecules in the shell N^s. Accordingly, $N_\uparrow^a$ and $N_\downarrow^a$ in Eq. IV.15 can be calculated through:

$$N_\uparrow^a = x^s N^s = x^s N\frac{2L^s}{L^{tot}}, \tag{IV.21}$$

$$N_\downarrow^a = (1-x^s)N^s = (1-x^s)N\frac{2L^s}{L^{tot}}, \tag{IV.22}$$

where x^s is the HS fraction in the shell (surface). Thus, the total Gibbs free energy of the thin-film can be expressed as:

$$G_{total}(V_{min}, x^b, x^s) = N\frac{L^{tot}-2L^s}{L^{tot}}\frac{B_\uparrow V_\uparrow}{2}(\gamma_o - 1)\left[x^b\left(\frac{V_{min}}{V_\uparrow}-1\right)^2 + (1-x^b)\frac{m}{\beta}\left(\frac{V_{min}}{V_\uparrow}-\frac{1}{m}\right)^2\right] +$$

$$N\frac{2L^s}{L^{tot}}\frac{B_\uparrow V_\uparrow}{2}(\gamma_o - 1)\left[x^s\left(\frac{V_{min}}{V_\uparrow}-1\right)^2 + (1-x^s)\frac{m}{\beta}\left(\frac{V_{min}}{V_\uparrow}-\frac{1}{m}\right)^2\right] +$$

$$N\left[x^s\frac{2L^s}{L^{tot}} + x^b\frac{L^{tot}-2L^s}{L^{tot}}\right](\Delta E - T\Delta S) + N(E_\downarrow - TS_\downarrow) +$$

$$NkT\frac{L^{tot}-2L^s}{L^{tot}}[x^b\ln(x^b) + (1-x^b)\ln(1-x^b)] +$$

$$NkT\frac{2L^s}{L^{tot}}[x^s\ln(x^s) + (1-x^s)\ln(1-x^s)] +$$

$$N\frac{L^s}{L^{tot}}\frac{B_\uparrow V_\uparrow R_\gamma}{a_\uparrow^0}\left[x^s+(1-x^s)\frac{a_\uparrow^0\Gamma_\gamma}{a_\downarrow^0 m}\right]+$$

$$N\frac{L^s B_\uparrow R_\sigma}{L^{tot}}V_{min}^{2/3}[x^s+(1-x^s)\alpha]-N\frac{L^s B_\uparrow V_\uparrow R_\sigma}{L^{tot}a_\uparrow^0}\left[x^s+(1-x^s)\frac{a_\uparrow^0\alpha}{a_\downarrow^0 m}\right], \quad \text{(IV.23)}$$

where x^b is the HS fraction in the bulk-like core. In Eq. IV.23, we introduce the LS to HS surface energy ratio $\Gamma_\gamma=\frac{\gamma_\downarrow}{\gamma_\uparrow}$, the LS to HS surface stress ratio $\alpha=\frac{\sigma_\downarrow}{\sigma_\uparrow}$, and the two characteristic lengths $R_\sigma=\frac{2\sigma_\uparrow}{B_\uparrow}$ and $R_\gamma=\frac{2\gamma_\uparrow}{B_\uparrow}$. The exact stationary solution of the model is deduced by solving the following non-linear system of equations:

$$\begin{cases}\frac{\partial G_{total}}{\partial x^b}=0\\ \frac{\partial G_{total}}{\partial x^s}=0,\\ \frac{\partial G_{total}}{\partial V_{min}}=0\end{cases} \quad \text{(IV.24)}$$

which gives:

$$\frac{B_\uparrow V_\uparrow}{2}(\gamma_o-1)\left[\left(\frac{V_{min}}{V_\uparrow}-1\right)^2-\frac{m}{\beta}\left(\frac{V_{min}}{V_\uparrow}-\frac{1}{m}\right)^2\right]+(\Delta E-T\Delta S)+kTln\left(\frac{x^b}{1-x^b}\right)=0, \quad \text{(IV.25)}$$

$$\frac{B_\uparrow V_\uparrow}{2}(\gamma_o-1)\left[\left(\frac{V_{min}}{V_\uparrow}-1\right)^2-\frac{m}{\beta}\left(\frac{V_{min}}{V_\uparrow}-\frac{1}{m}\right)^2\right]+(\Delta E-T\Delta S)+kTln\left(\frac{x^s}{1-x^s}\right)+\frac{B_\uparrow V_\uparrow R_\gamma}{2a_\uparrow^0}\left(1-\frac{a_\uparrow^0\Gamma_\gamma}{a_\downarrow^0 m}\right)+$$
$$\frac{1}{2}B_\uparrow R_\sigma V_{min}^{2/3}[1-\alpha]-\frac{B_\uparrow R_\sigma V_\uparrow}{2a_\uparrow^0}\left[1-\frac{a_\uparrow^0\alpha}{a_\downarrow^0 m}\right]=0, \quad \text{(IV.26)}$$

$$(L^{tot}-2L^s)B_\uparrow(\gamma_o-1)\left[x^b\left(\frac{V_{min}}{V_\uparrow}-1\right)+\left(1-x^b\right)\frac{m}{\beta}\left(\frac{V_{min}}{V_\uparrow}-\frac{1}{m}\right)\right]+2L^sB_\uparrow(\gamma_o-1)\left[x^s\left(\frac{V_{min}}{V_\uparrow}-1\right)+\right.$$
$$\left.(1-x^s)\frac{m}{\beta}\left(\frac{V_{min}}{V_\uparrow}-\frac{1}{m}\right)\right]+\frac{2}{3}L^sB_\uparrow R_\sigma V_{min}^{-1/3}[x^s+(1-x^s)\alpha]=0, \quad \text{(IV.27)}$$

Eq. IV.25, Eq. IV.26 and Eq. IV.27 generate a self-consistent equation set at a given temperature *T*.

IV.2.3 Spherical model

A spherical core-shell model that consists of a bulk-like core with a radius of R_1 and a shell with a thickness of (R-R_1) is then considered, as **FIG. IV.2** (b) shows. Assuming that the system is in HS state and that the shell is made up of a monolayer, we can calculate the volume of the core by $V_b = N_{\uparrow}^{b} V_{\uparrow} = \frac{4\pi R_1^3}{3}$ and the volume of the shell by $V_s = N_{\uparrow}^{s} V_{\uparrow} = NV_{\uparrow} - N_{\uparrow}^{b} V_{\uparrow} = \frac{4\pi R^3}{3} - \frac{4\pi R_1^3}{3}$. Thus, the number of molecules in the core (N^b) and in the shell (N^s) are expressed as:

$$N^b = N\left(\frac{R_1}{R}\right)^3, \tag{IV.28}$$

$$N^s = N\left(1 - \left(\frac{R_1}{R}\right)^3\right), \tag{IV.29}$$

Besides, considering that the all the molecules at the surface are in the HS state, the relation between the surface area of a molecule and the total surface area of the particle is given by:

$$N^a \frac{V_{\uparrow}}{a_o^{\uparrow}} = 4\pi R^2, \tag{IV.30}$$

whereas the relation between the volume of a molecule and the total volume of the particle is:

$$NV_{\uparrow} = \frac{4\pi R^3}{3}, \tag{IV.31}$$

From Eq. IV.30 and Eq. IV.31, the number of molecules at the surface N^a is obtained by:

$$N^a = N\frac{3a_o^{\uparrow}}{R}, \tag{IV.32}$$

The numbers $N_{\uparrow}^{a}$ and $N_{\downarrow}^{a}$ in Eq. IV.18 can be calculated through:

$$N_{\uparrow}^{a} = x^s N^a = x^s N\frac{3a_o^{\uparrow}}{R}, \tag{IV.33}$$

$$N_{\downarrow}^{a} = (1 - x^s)N^a = (1 - x^s)N\frac{3a_o^{\uparrow}}{R}, \tag{IV.34}$$

Considering the shell is made up of a monolayer of molecules ($N^s = N^a$ in this case), the total energy of the spherical system is written as:

$$G_{total}(V_{min}, x^b, x^s) = N\left(\frac{R_1}{R}\right)^3 \frac{B_\uparrow V_\uparrow}{2}(\gamma_o - 1)\left[x^b\left(\frac{V_{min}}{V_\uparrow} - 1\right)^2 + (1 - x^b)\frac{m}{\beta}\left(\frac{V_{min}}{V_\uparrow} - \frac{1}{m}\right)^2\right] +$$

$$N\left(1 - \left(\frac{R_1}{R}\right)^3\right)\frac{B_\uparrow V_\uparrow}{2}(\gamma_o - 1)\left[x^s\left(\frac{V_{min}}{V_\uparrow} - 1\right)^2 + (1 - x^s)\frac{m}{\beta}\left(\frac{V_{min}}{V_\uparrow} - \frac{1}{m}\right)^2\right] +$$

$$N\left[x^s\left(1 - \left(\frac{R_1}{R}\right)^3\right) + x^b\left(\frac{R_1}{R}\right)^3\right](\Delta E - T\Delta S) + N(E_\downarrow - TS_\downarrow) +$$

$$NkT\left(\frac{R_1}{R}\right)^3 [x^b \ln(x^b) + (1 - x^b)\ln(1 - x^b)] +$$

$$NkT\left(1 - \left(\frac{R_1}{R}\right)^3\right)[x^s \ln(x^s) + (1 - x^s)\ln(1 - x^s)] +$$

$$N\frac{3B_\uparrow V_\uparrow R_\gamma}{2R}\left[x^s + (1 - x^s)\frac{a_\uparrow^0 \Gamma_\gamma}{a_\downarrow^0 m}\right] +$$

$$N\frac{B_\uparrow V_\uparrow R_\sigma}{R}\left[x^s\left(\frac{V_{min}}{V_\uparrow} - 1\right) + \alpha\frac{a_\uparrow^0}{a_\downarrow^0}(1 - x^s)\left(\frac{V_{min}}{V_\uparrow} - \frac{1}{m}\right)\right], \quad \text{(IV.35)}$$

The exact stationary solution of the spherical model is found using Eq. IV.24, which brings out the equation set:

$$\frac{B_\uparrow V_\uparrow}{2}(\gamma_o - 1)\left[\left(\frac{V_{min}}{V_\uparrow} - 1\right)^2 - \frac{m}{\beta}\left(\frac{V_{min}}{V_\uparrow} - \frac{1}{m}\right)^2\right] + (\Delta E - T\Delta S) + kTln\left(\frac{x^b}{1 - x^b}\right) = 0, \quad \text{(IV.36)}$$

$$\left(1-\left(\frac{R_1}{R}\right)^3\right)\left[\frac{B_\uparrow V_\uparrow}{2}(\gamma_o-1)\left[\left(\frac{V_{min}}{V_\uparrow}-1\right)^2-\frac{m}{\beta}\left(\frac{V_{min}}{V_\uparrow}-\frac{1}{m}\right)^2\right]+(\Delta E-T\Delta S)+kTln\left(\frac{x^s}{1-x^s}\right)\right]+$$
$$\frac{3B_\uparrow V_\uparrow R_\gamma}{2R}\left(1-\frac{a_\uparrow^0\Gamma_\gamma}{a_\downarrow^0 m}\right)+\frac{B_\uparrow V_\uparrow R_\sigma}{R}\left[\frac{V_{min}}{V_\uparrow}-1-\alpha\frac{a_\uparrow^0}{a_\downarrow^0}\left(\frac{V_{min}}{V_\uparrow}-\frac{1}{m}\right)\right]=0, \quad \text{(IV.37)}$$

$$B_\uparrow\left(\frac{R_1}{R}\right)^3(\gamma_o-1)\left[x^b\left(\frac{V_{min}}{V_\uparrow}-1\right)+(1-x^b)\frac{m}{\beta}\left(\frac{V_{min}}{V_\uparrow}-\frac{1}{m}\right)\right]+B_\uparrow(\gamma_o-1)\left(1-\left(\frac{R_1}{R}\right)^3\right)\left[x^s\left(\frac{V_{min}}{V_\uparrow}-\right.\right.$$
$$\left.\left.1\right)+(1-x^s)\frac{m}{\beta}\left(\frac{V_{min}}{V_\uparrow}-\frac{1}{m}\right)\right]+\frac{B_\uparrow R_\sigma}{R}\left[x^s+\alpha\frac{a_\uparrow^0}{a_\downarrow^0}(1-x^s)\right]=0, \quad \text{(IV.38)}$$

As the equation sets derived from different models are highly non-linear, it seems difficult to solve them analytically. The numerical solutions are obtained at given temperatures T by means of the *vpasolve* solver in MATLAB (MathWorks® Inc. Natick, MA). It should be mentioned that due to the strong coupling between different physical properties as well as the high nonlinearity of the equation set, the investigation of the effects of different parameters on SCO behaviors is a challenging task. Thus, in the next sections, we will first explore the effects of surface energy (resp. surface stress) on the SCO properties of a 5 nm thin [Fe(pyrazine)][Ni(CN)$_4$] film in the case of $\sigma_\uparrow = \sigma_\downarrow = 0\ mJ/m^2$ (resp. $\gamma_\uparrow = \gamma_\downarrow = 0\ mJ/m^2$). Then the values of surface energy and surface stress will be fixed to study the size reduction effects.

IV. 3 Results and discussions

IV.3.1 Bulk material

For our investigation we selected the Hoffmann-like clathrate compound [Fe(pyrazine)][Ni(CN)$_4$], whose physical properties are displayed in **TABLE. IV.1**. This choice was motivated by the fact that the different properties of this compound are relatively well documented and we can also have access to the computational analysis of certain properties thanks to the work reported in **Chapters II-III**. Let us note also that the high symmetry of the

lattice of this compound (P4/mmm) allows us to neglect the effects of anisotropy in a first assumption.

TABLE. IV.1: Physical properties of the [Fe(pyrazine)][Ni(CN)$_4$] compound. [126, 135, 136]

Physical property	Value
$\Delta E \ (J \cdot mol^{-1})$	14500
$\Delta S \ (J \cdot K^{-1} \cdot mol^{-1})$	50
$Y_{\uparrow} \ (GPa)$	10.4
m	1.1
$a_{\uparrow}^{0} \ (nm)$	0.726
β	0.7300
ν	0.33

The isotropic bulk modulus B can be obtained from the isotropic Young's modulus Y as [126]:

$$B = \frac{Y}{3(1-2\nu)}, \tag{IV.39}$$

We calculate first the temperature dependence of the HS fraction for the bulk material, i. e., for $L^{tot} = +\infty$ ($R = +\infty$). As displayed in **FIG. IV.1.3** (a), if we neglect the elastic interactions between the molecules ($G_{elastic} = 0$), a gradual spin conversion is observed, as expected. However, if we include the elastic inter-molecular interaction term, a sharp increase of the HS fraction at $T_{1/2\uparrow} = 303$ K in the heating mode can be seen, whereas a sharp decrease of the HS fraction is found at $T_{1/2\downarrow}$ = 281 K in the cooling process (**FIG. IV.1.3** (a)), giving rise to a hysteresis loop whose width ($\Delta T \approx 22$K) is close to the experimentally observed value of 25 K [135]. The transition temperature in the heating process is about 13 K higher than that of the gradual transition (290 K), which arises due to the extra elastic energy barrier associated with the inter-molecular interactions as shown in **FIG. IV.1.3** (b). It is also interesting to notice in **FIG. IV.1.3** that the LS state residual fraction at high temperature decreases from ~16 % to ~3 % with the participation of the inter-molecular interactions, indicating that the elastic interaction between two molecules tend to stabilize the HS state at high temperature.

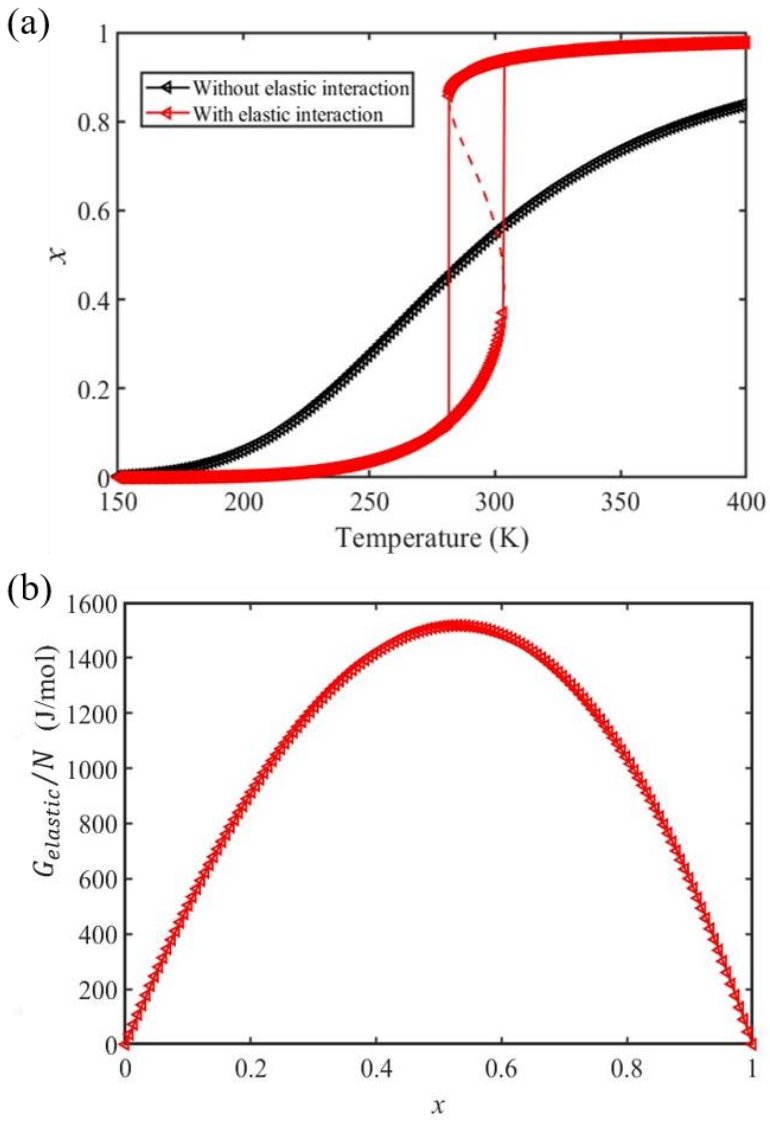

FIG. IV.1.3: (a) Calculated temperature dependence of the HS fraction for the bulk material (red triangles) using the input physical quantities reported in **TABLE. IV.1**. The gradual conversion curve in black, corresponding to the case where no elastic interaction is considered, is represented for comparison. (b) Dependence of the elastic interaction energy density with the HS fraction for the bulk material.

IV.3.2 Surface energy effect

From the simulation of the bulk material, we can conclude that the model is able to reproduce with reasonable accuracy the experimentally observed SCO behavior without using any adjustable, phenomenological parameters. We now turn our attention to investigate the influences of surface energy/stress on the SCO behaviors in finite size systems. It should be mentioned that the results obtained for a thin film of L^{tot} = 5 nm and those obtained for a particle with a radius of R = 5 nm revealed similar conclusions. For this reason, in the following we show only the simulations for the L^{tot} =5 nm thin film of the [Fe(pyrazine)][Ni(CN)$_4$] compound and the results obtained with the spherical model are provided in the **Annexes**.

The temperature dependence of the total HS fraction is first calculated for different values of $\gamma_{\uparrow}$ varying from 10 to 190 mJ/m^2 with an increment of 10 mJ/m^2 under the consideration of $\sigma_{\uparrow} = \sigma_{\downarrow} = 0\ mJ/m^2$. As two typical examples, the cases of $\Gamma_{\gamma} = \frac{\gamma_{\downarrow}}{\gamma_{\uparrow}} = 1.4$ and 2.4 are displayed in **FIG. IV.4**.

In both cases, one can notice an increase of the residual HS fraction at low temperature for increasing values of $\gamma_{\uparrow}$ (indicated by green arrows in **FIG. IV.4**). Interestingly, this residual HS fraction reaches a maximum value of $x = \sim 0.28$, which is close to the proportion of the molecules in the shell $\frac{2L^s}{L^{tot}} = 0.286$. We can thus conclude that the transition temperature of the molecules at the surface is getting reduced and, eventually, they remain trapped in the HS state. Furthermore, as indicated by the red arrows in **FIG. IV.4**, the spin transition shifts gradually to lower temperatures as $\gamma_{\uparrow}$ increases. Due to the existence of elastic intermolecular interactions between the molecules in the shell and core, the molecules in the shell, which switch to the HS state at lower temperatures, force the LS molecules in the core to transit to HS state. Indeed, there is a minimum value of the equilibrium temperature at ~ 266 K with the increase of $\gamma_{\uparrow}$ since the elastic interaction between the shell and core reaches its maximum when all the molecules in the shell switch to the HS state at low temperatures. In other words, the molecules in the shell are fixed in the HS state ($x^s = 1$) when $\gamma_{\uparrow}$ is strong enough, giving rise to the largest misfit between the shell and the bulk-like core.

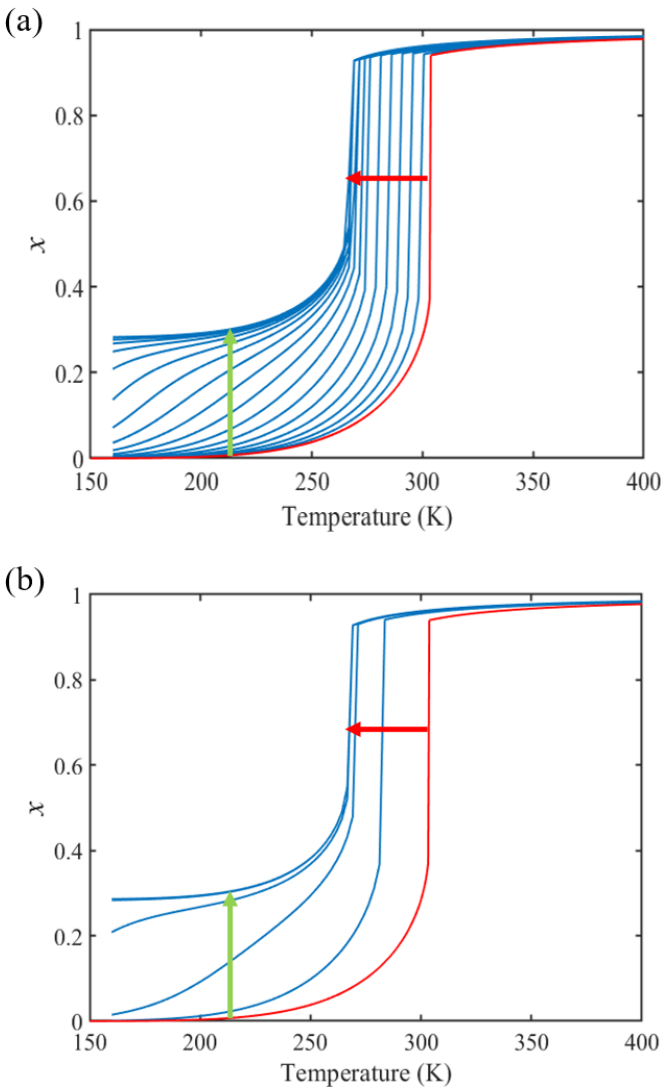

FIG. IV.4. Calculated temperature dependence of the HS fraction (heating mode) for a 5 nm thin film of [Fe(pyrazine)][Ni(CN)$_4$] in the case of (a) $\Gamma_\gamma = \frac{\gamma_\downarrow}{\gamma_\uparrow} = 1.4$ and (b) $\Gamma_\gamma = \frac{\gamma_\downarrow}{\gamma_\uparrow} = 2.4$ for different values of $\gamma_\uparrow$ varying from 10 to 190 mJ/m^2 with an increment of 10 mJ/m^2. The red curve represents the bulk material. Green and red arrows are guides for the eye to follow the evolution the residual HS fraction and the equilibrium temperature, respectively, with the increase of $\gamma_\uparrow$.

As we can see from **FIG. IV.4** (b), for $\Gamma_\gamma = 2.4$ the molecules in the shell completely switch to HS state with lower $\gamma_\uparrow$ in comparison to $\Gamma_\gamma = 1.4$ which means that the effect of surface energy becomes stronger by increasing either the absolute value of the surface energy or the ratio of LS to HS surface energy ratio. Indeed, both of them give rise to the increase of

the surface energy difference between LS and HS states ($\gamma_{\downarrow} - \gamma_{\uparrow}$). This quantity can thus be considered as a driving force of finite size induced effects on the SCO phenomenon.

IV.3.3 Surface stress effect

Different from the surface energy which is always positive, the surface stress could be either positive (tensile stress) or negative (compressive stress), which is associated with the variation of distances between the atoms at surface[108-110]. We have computed the thermally induced spin transition curves of a 5 nm thin film for different values of $\sigma_{\uparrow}$ varying from 10 to 410 mJ/m^2 (-410 to -10 mJ/m^2) with an increment of 20 mJ/m^2. As it is well known that the denser LS phase is usually stiffer than the HS phase, we can make the hypothesis that $\sigma_{\downarrow} > \sigma_{\uparrow}$. To avoid the implication of too much parameters in this study, two ratios of LS to HS surface stress ($\alpha = \frac{\sigma_{\downarrow}}{\sigma_{\uparrow}} = 1.4$ and 2.0) are chosen and the surface energies of both spin states are set to $\gamma_{\uparrow} = \gamma_{\downarrow} = 0$ mJ/m^2 .

FIG. IV.5 (a) and (b) summarize the temperature dependence of the HS fraction calculated through positive surface stress in the cases of $\alpha = \frac{\sigma_{\downarrow}}{\sigma_{\uparrow}} = 1.4$ and 2.0, respectively. As the green arrow indicates in **FIG. IV.5** (a), the increase of $\sigma_{\uparrow}$ brings out an increase of the residual HS fraction at low temperature – similar to the effect of an increasing value of $\gamma_{\uparrow}$ discussed above. Again, the highest residual HS fraction is $x = \sim 0.28$ denoting that the equilibrium temperature of the molecules in the shell is shifted downwards with the increase of $\sigma_{\uparrow}$ until a complete blocking of the shell in the HS state. The existence of the surface stress during the spin switching exerts the stress/pressure to the surface of the material. In terms of the positive surface stress, the two surfaces of the thin film are both under tensile stress, which favors the HS state, leading to a downshift of the transition temperature of the molecules in the shell (surface).

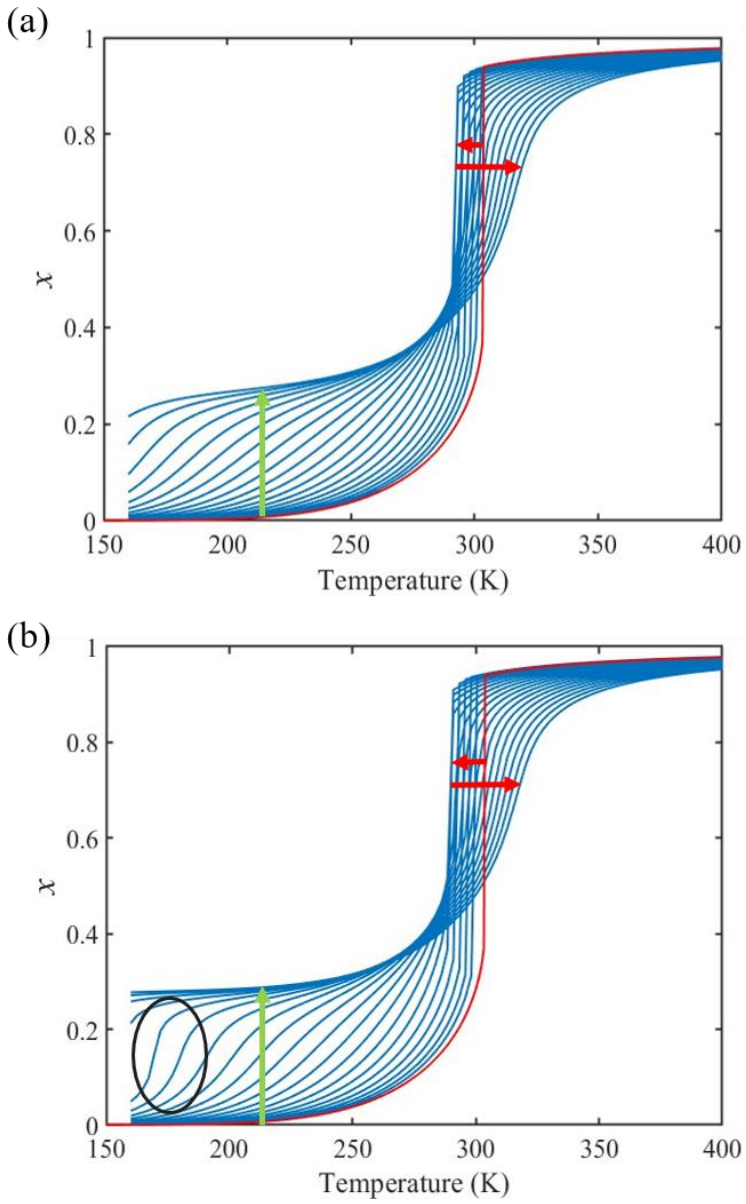

FIG. IV.5. Calculated temperature dependence of the HS fraction (heating mode) for a 5 nm thin film of [Fe(pyrazine)][Ni(CN)$_4$] in the case of (a) $\alpha = \frac{\sigma_\downarrow}{\sigma_\uparrow} = 1.4$ and (b) $\alpha = \frac{\sigma_\downarrow}{\sigma_\uparrow} = 2.0$ for different positive values of $\sigma_\uparrow$ ranging from +10 to +410 mJ/m^2 with an increment of 20 mJ/m^2. The red curve represents the bulk material. Green and red arrows are guides for the eye to follow the evolution the residual HS fraction and the equilibrium temperature, respectively, with the increase of $\sigma_\uparrow$. The black circle highlights an abrupt spin transition in the shell brought into by the tensile stress.

On the other hand, the surface stress must be balanced by volume stress in the bulk-like core since there should be no net force [179, 180]. As a result, we can observe an obvious change of the SCO behavior of the bulk-like core. Indeed, as shown by the red arrows in **FIG. IV.5** (a), the equilibrium temperature first downshifts until it reaches its lowest value (~ 290 K) with increasing $\sigma_{\uparrow}$. Similar to the surface energy effect, this downshift can be attributed to the elastic intermolecular interaction between the HS molecules in the shell and the LS molecules in the bulk-like core. However, the minimum of the equilibrium temperature (~290 K) remains higher when compared to the case of the surface energy effect (~ 266 K) because the molecules in the bulk-like core are under compression, which stabilizes the LS state. In other words, the surface stress induces two competing effects, favoring either the HS or the LS state. However, the stabilization of the HS state is limited by the thickness of the shell. As a result, when the molecules in the shell are fully blocked in the HS state, a further increase of $\sigma_{\uparrow}$ will give rise solely to an increase of the compressive stress in the bulk-like core, which is manifested in **FIG. IV.5** by a clear upshift of the equilibrium temperature. In the case of $\alpha = \frac{\sigma_{\downarrow}}{\sigma_{\uparrow}} = 2.0$, shown on **FIG. IV.5** (b), features in common with the case of $\alpha = \frac{\sigma_{\downarrow}}{\sigma_{\uparrow}} = 1.4$ can be observed, i.e., the downshift of the equilibrium temperature and the increase of the residual HS fraction at low temperature as $\sigma_{\uparrow}$ increases. Interestingly, an abrupt spin transition could be found in the shell as highlighted by the black circles. On the contrary, as $\sigma_{\uparrow}$ increases, the SCO behavior of the bulk-like core changes from abrupt to gradual transition. Such enhancement/loss of the cooperativity in different regions induced by tensile/compressive pressure is well known in the SCO literature, including both theoretical studies as well as experimental observations performed under high pressure [146, 181-186].

FIG. IV.6 (a) displays the thermally induced spin transition for negative (compressive) values of the surface stress in the case of $\alpha = \frac{\sigma_{\downarrow}}{\sigma_{\uparrow}} = 1.4$. Globally, the observed effects "mirror" the case of tensile surface stress, though some differences occur as well.

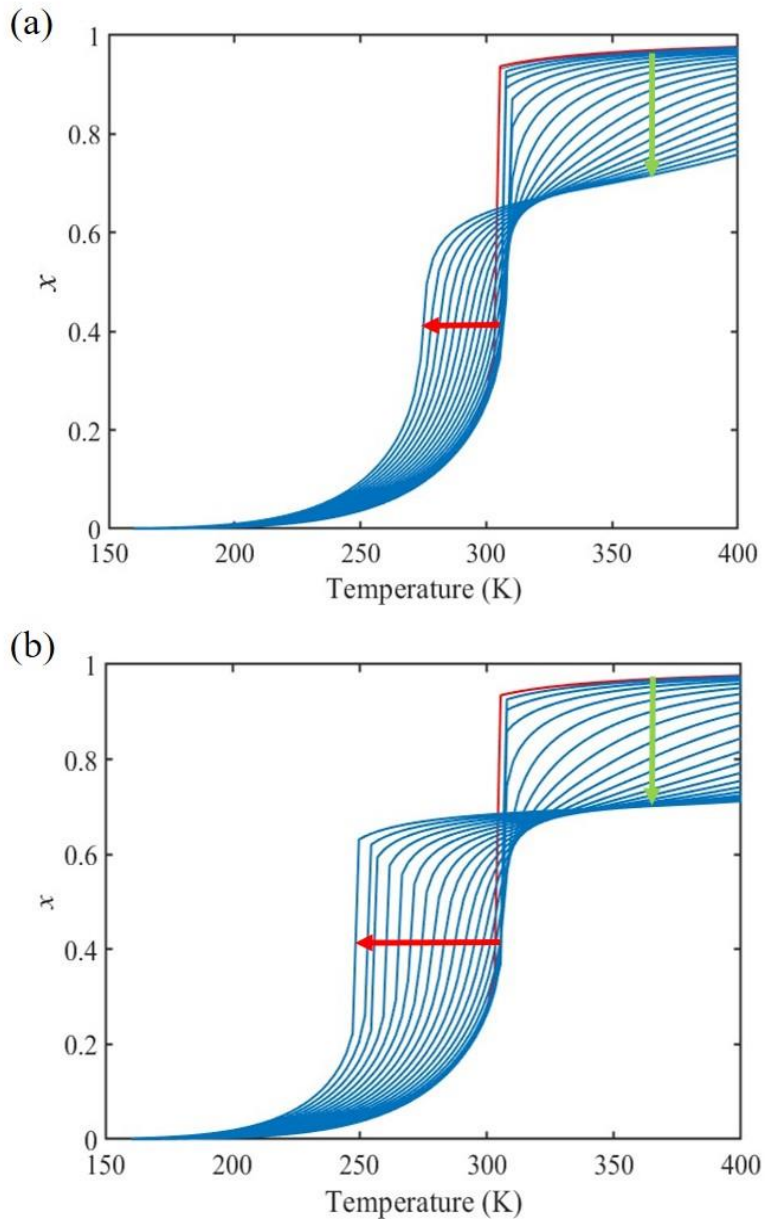

FIG. IV.6. Calculated temperature dependence of the HS fraction (heating mode) for a 5 nm thin film of [Fe(pyrazine)][Ni(CN)$_4$] in the case of (a) $\alpha = \frac{\sigma_\downarrow}{\sigma_\uparrow} = 1.4$ and (b) $\alpha = \frac{\sigma_\downarrow}{\sigma_\uparrow} = 2.0$ for different positive values of $\sigma_\uparrow$ ranging from -410 to -10 mJ/m^2 with an increment of 20 mJ/m^2. The red curve represents the bulk material. Green and red arrows are guides for the eye to follow the evolution the residual LS fraction and the equilibrium temperature, respectively, with the increase of $\sigma_\uparrow$.

On one hand, as indicated by the green arrow in **FIG. IV.6**, an increase of the residual LS fraction at high temperatures can be observed with the increase of the magnitude of $\sigma_\uparrow$. The

residual LS fraction at high temperature peaks at a value of ~ 0.2, indicating that the molecules in the shell are blocked by the compressive stress (i.e. their transition is shifted to high temperatures). We can infer that in the limit $\sigma_{\uparrow} \to -\infty$ ($\alpha \to \infty$), the molecules at the surface are completely blocked in the LS state.

On the other hand, to ensure the mechanical equilibrium, a tensile stress exists in the bulk-like core, balancing the surface stress. Similar to the case of positive surface stress, two competing effects can be noticed. The tensile stress in the core tends to stabilize the HS state, whereas the interaction with the shell tends to stabilize the LS state. As shown in **FIG. IV.6** (a), first a slight increase (~ 3 K) of the equilibrium temperature can be seen when the magnitude of $\sigma_{\uparrow}$ is small. Though the blocked LS molecules in the shell tend to stabilize the LS state in the bulk-like core via elastic intermolecular interactions, the tensile stress, which favors the HS state, becomes quickly dominant as $\sigma_{\uparrow}$ increases, leading to an obvious downshift of the equilibrium temperature (shown by the red arrow). It is thus not surprising to see from **FIG. IV.6** (b) that a clear abrupt spin switching appears in the bulk-like core when the surface stress is strong ($< -310\ mJ/m^2$). It is interesting to remark that this type of surface stress effect might thus contribute to the re-appearance of the hysteresis loop reported in ultra-small nanoparticles of the compound [Fe(pyrazine)][Ni(CN)$_4$] [69]. In previous reports, this phenomenon was attributed to the modification of the surface elastic properties and/or particle-matrix interactions [107, 128], but the present work indicates that the existence of a negative surface stress can also give rise to such effects.

To summarize our findings on the surface energy/stress effects, it is interesting to remark that the experimentally observed incomplete spin transitions in nanoscale objects may be attributed to the double effect of the surface energy and the surface stress. The contribution of surface energy is associated with both electronic and structural surface relaxations, which has been previously discussed in refs. [94, 95, 107, 187]. On the other hand, the contribution of surface stress is related to the mechanical equilibrium, which is the result of the competition of forces acting at the free surface and the bulk-like core during the spin transition. That is to say, a careful modification of the elastic properties of the surface/interface or the chemical nature of the surface could potentially allow one to tune the SCO properties at the nano-scale. The present work provides some general guidelines for this endeavor.

IV.3.4 Size effect

To our best knowledge, there is no reported value of the surface energy or surface stress of any SCO complex. Thus the surface energies of [Fe(pyrazine)][Ni(CN)$_4$] in the LS and HS states were calculated through the MD method described in **Chapter. II** in conjunction with the slab approach discussed in refs. [112]. Firstly, the [Fe(pyrazine)][Ni(CN)$_4$] structure with 20×20×20 unit-cells are built in LS and HS states. The periodic boundary conditions are applied along the *x*, *y* and *z* directions to simulate the bulk model. Secondly, the periodic boundary conditions are applied along the *x*, *y* directions while non-periodic boundary condition is applied along *z* direction, as indicated in **FIG. II. 7**. Each model is relaxed at 300 K and the surface energy (E_{sur}) is calculated by:

$$E_{sur} = \frac{E_{tot} - \sum_i n_i E_{bulk-i}}{2S}, \quad \text{(IV.40)}$$

where *S* is the surface area, E_{tot} the total energy of the surface model, n_i the total number of atom *i* (*i*=Ni, Fe, C and N) in the surface model and E_{bulk-i} the energy of single *i* atom in bulk model.

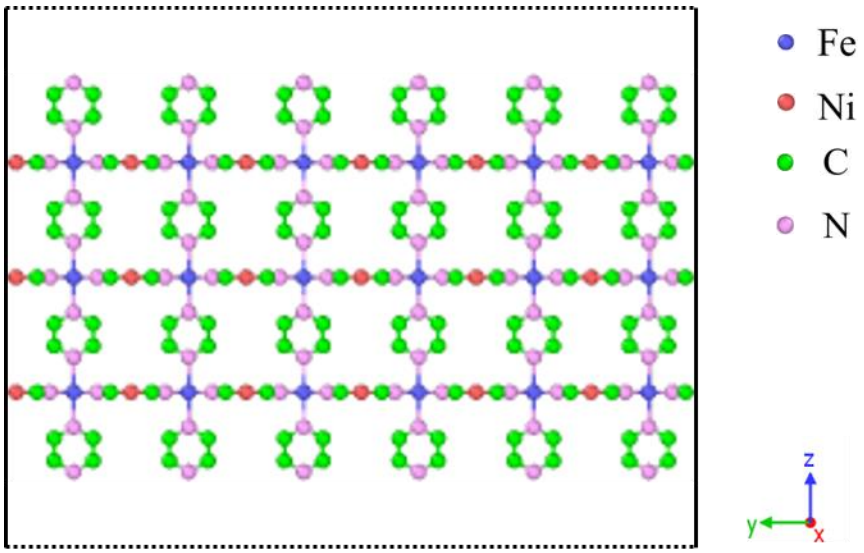

FIG. II. 7: Schematic representation of the 2 dimensional [Fe(pyrazine)][Ni(CN)$_4$] structure.

Through calculation, the obtained surface energies of the LS and HS states are $E_{sur}^{LS} = 48.78\ mJ/m^2$ and $E_{sur}^{HS} = 21.2\ mJ/m^2$, respectively. It is interesting to compare these

numerical values with surface energies of organic and polymeric materials. For example, the surface energies of polymeric materials such as polytetrafluoroethylene (PTFE), poly(methyl methacrylate) (PMMA), and poly(vinyl chloride) (PVC), are respectively 20, 35, and 40 mJ/m^2 at room temperature [188]. The molecular material Boron subphthalocyanine chloride (SubPc) has a surface energy of ~ 48 mJ/m^2. [189] The surface tension or energy is a manifestation of intermolecular forces and is related to other properties derived from intermolecular forces such as the Young's modulus or sound velocity. The Young's moduli of PTFE, PMMA, PVC, and SubPc are respectively 0.5, 2, 3, and 5 GPa. This correspondence of Young's modulus with surface energy is intuitive: the more rigid the material, the higher the surface energy. According to our results above and the experimental observations, the LS state is more rigid than the HS state, which agrees with the relation of surface energies between two spin states ($E_{sur}^{LS} > E_{sur}^{HS}$), further validating the new force fields. Considering the surface stress is related to the elastic deformation, as mentioned above, the ratio $\alpha = \frac{\sigma_\downarrow}{\sigma_\uparrow}$ is set to 1.43, which is close to the ratio of the Young's moduli in the LS and HS states ($\frac{Y_\downarrow}{Y_\uparrow}$) [126]. Moreover, since the size reduction usually leads to a down shift of equilibrium temperature as well as a residual HS fraction at low temperature in the case of compound [Fe(pyrazine)][Ni(CN)$_4$] as mentioned in **Chapter I. 3**, the surface stress of [Fe(pyrazine)][Ni(CN)$_4$] is assumed to negative in the present work. For most solids, the surface stress is generally of the same order of magnitude as the surface energy [110, 174, 175], so that the surface stress in the HS state $\sigma_\uparrow = 100\ mJ/m^2$ is finally fixed arbitrarily for further calculations.

The calculated temperature dependence of the total HS fraction is shown in **FIG. IV.8** for different thicknesses in the case of thin film model (results obtained with the spherical model are provided in the **Annexes**). On the whole, one can clearly see an increase of the residual HS fraction as well as a downshift of the equilibrium temperature with the size reduction, which is in qualitative agreement with experimental observations on different SCO compounds [57, 67-69, 83, 84, 89]. In particular, a gradual spin transition with a transition temperature at ~266 K as well as a residual HS fraction of $x = 0.4$ at 200 K can be found in the 5-layer (~ 3.5 nm) thin film from **FIG. IV.8**. This result can be compared with a recent experimental study on Hoffmann-like clathrates using variable-temperature Raman spectroscopy, which revealed for a 5-layer thick [Fe(pyrazine)][Ni(CN)$_4$] film a gradual SCO curve centered at ~260 K and accompanied by a HS residual fraction of ~ 0.45 at 200 K [90]. Such good agreement between the results from our model and the experimental observations indicates the present model could

predict SCO behaviors at the nano-scale. Nevertheless, it is important to remind that the calculations were based on rough estimates of surface thermodynamical parameters, which should be refined using dedicated experimental and theoretical approaches in order to establish a real predictive capability.

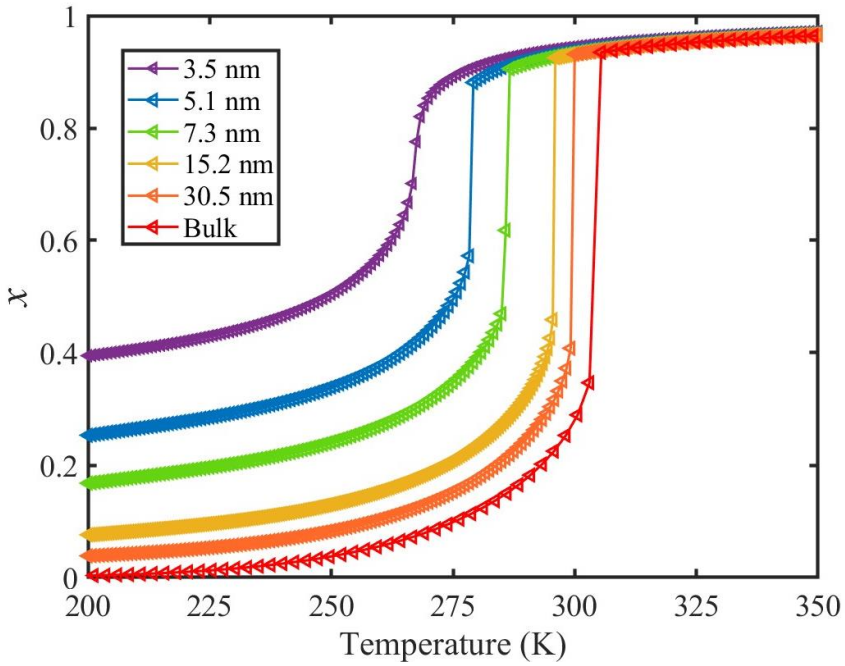

FIG. IV.8: Calculated temperature dependence of total HS fraction for different film thicknesses of the compound [Fe(pyrazine)][Ni(CN)$_4$].

To conclude this study, **FIG. IV.9** (a) displays the computed spin-state equilibrium temperature as a function of the thickness of the [Fe(pyrazine)][Ni(CN)$_4$] films. One can clearly see that the equilibrium temperature, which is close to the transition temperature of the bulk material, downshifts slightly when the film thickness is reduced from 30 to 10 nm, while a more dramatic decrease occurs when $L^{tot} < 10$ nm. Such algebraic decay of the equilibrium temperature with size reduction indicates a stronger surface effect due to the increase of the surface-to-volume ratio. To substantiate the importance of this latter parameter, the blue curve in **FIG. IV.9** (b) shows a linear fit of the equilibrium temperature as a function of $\frac{1}{L^{tot}}$, from which a clear reciprocal relationship can be established between these two quantities:

$$T_{eq}(L^{tot}) \propto \frac{1}{L^{tot}}, \tag{IV.41}$$

It should be noted that the $\frac{1}{L}$ ($\frac{1}{R}$ in the case of the spherical nanoparticle) dependence of the transition temperature with the thickness (radius) is a common finding for various nanoscale materials, which can be ubiquitously linked to the surface-to-volume ratio of the object (e.g. $\frac{A}{V} = \frac{L^x L^y}{L^x L^y L^z} = \frac{1}{L^z}$). In particular, this relationship could be also derived from different atomistic/thermodynamic studies on the size effects in SCO objects [91, 92, 107].

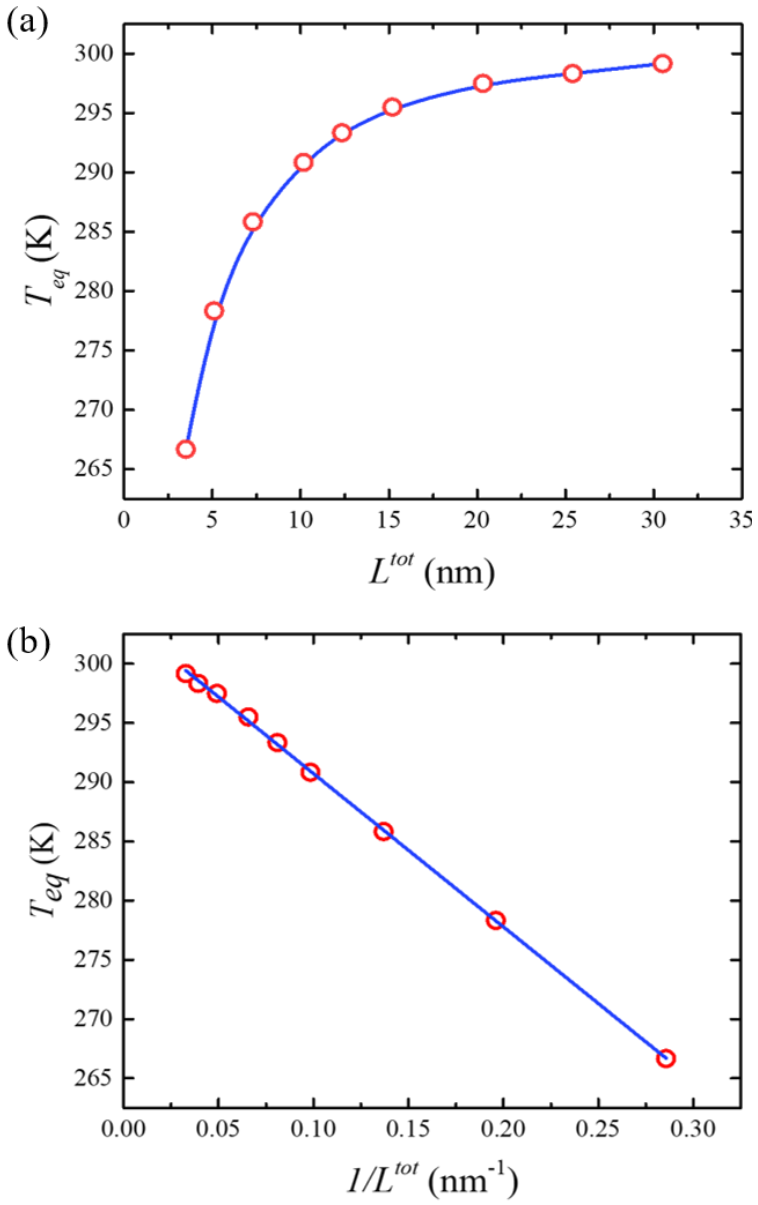

FIG. IV.9: Computed spin-state equilibrium temperature of [Fe(pyrazine)][Ni(CN)$_4$] films as a function of (a) L^{tot} and (b) $1/L^{tot}$.

IV.4 Conclusions

We developed a nano-thermodynamic core-shell model describing the effects of the surface energy/stress on the SCO behaviors in the cases of thin films and spherical particles. The study of the surface energy effect shows a decrease of the equilibrium temperature as well as the occurrence of a residual HS fraction at low temperature, which agrees well with previous experimental reports. Positive or negative surface stresses give rise to a residual HS fraction at low temperature or a residual LS fraction at high temperature, respectively, due to the pressure acting on the shell (surface layer). Remarkably, both the positive and negative surface stresses can lead to either an upshift or to a downshift of the equilibrium temperature, depending on their magnitude. This behavior is a result of the competition between elastic inter-molecular interactions between the core and the shell and the pressure in the core induced by the surface stress. Besides, such competition could bring about the change of the cooperativity, which may further lead to multistep transitions and to the re-opening of hysteresis loops. The present model reveals that the appearance of the incomplete spin transition and the shift of the transition temperature at the nano-scale may be attributed to the double effects of the surface energy (from an energetic point of view) and the surface stress (from a mechanical point of view). With these general conclusions in hand, we conducted a more specific investigation of the size reduction effects on films of the compound [Fe(pyrazine)][Ni(CN)$_4$]. To this aim, we first calculated the surface energies through MD simulations and made a rough estimation of the surface stress in the two spin states. At this stage, the latter quantity appears thus as an adjustable parameter in our model. As such, the good agreement between our computational results and the experimental observations in the literature should not be over interpreted. Nevertheless, the model is already able to grasp the experimentally observed SCO behaviors at the nano-scale and provide physical insights to their origin. The very important point to be stressed is that potentially EACH input parameter of the present model is experimentally accessible. This fact combined by the simple numerical procedure, provides a powerful tool to analyze and even predict SCO behaviors of different compounds at finite sizes.

General conclusions and perspectives

SCO objects show the general trends at reduced size observed in systems exhibiting first order phase transitions such as significant changes in the phase stability, resulting in a shift of the equilibrium temperature, the appearance of the incomplete spin transition as well as alterations of collective behaviors, with, most of the time, a loss of the cooperativity. Such dramatic modifications of the SCO properties are probably a result of the increase of surface-to-volume and the strong interaction between the SCO object and the external environment (matrix effects). In this context, the main purpose of this thesis was to investigate the effects of surface and interface on the SCO properties at the nano-scale. To this aim, all-atom MD simulations and thermodynamics methods were carried out.

The first work reported in this thesis consists in the construction of the empirical force fields of the [Fe(pyrazine)][Ni(CN)$_4$] compound in both spin states. This force field includes simple harmonic and Lennard-Jones type potentials whose parameters were obtained from Raman and NIS spectroscopic data. It appears to be able to reasonably simulate the whole density of vibrational states (vDOS) spectra, from the low (acoustic) to the high (optical) modes with an acceptable accuracy. This numerical approach constitutes thus a good compromise for the investigations of lattice dynamics of SCO materials, between qualitative spring-ball models, providing only general trends, and *ab initio* calculations, providing quantitative vibrational properties of SCO solids only at a very high computational cost and for relatively small systems. A very important point is the ability of this approach to quantitatively model the acoustic part of the vDOS, which is not easily accessible with *ab initio* calculations or experiments.

Then, a Double-Well potential is integrated to the newly constructed force field in order to simulate switchable materials and to reproduce the effect of the vibronic coupling on the elastic deformation of realistic structures. It shows that the thermally induced first order spin transition of [Fe(pyrazine)][Ni(CN)$_4$] compound and associated cooperative mechanisms are successfully grasped by this present forced field. Besides, the all-atom MD method describes the motion of ligands and Fe-N bonds during the spin switching more clearly than the standard spring-ball model, which provides a good starting point for the following study which concerns the HS/LS interface and the lattice distortion.

Based on the force field constructed in **Chapter. II**, the effect of the interface in the [Fe(pyrazine)][Ni(CN)$_4$] bilayer model is investigated by means of the all-atom MD simulation in chapter III. As expected, a significant deflection behavior of the lattice could be observed after introducing the HS/LS interface. The comparison between the deflection of the bilayer model extracted from our simulation and that determined from the classic Euler-Bernoulli's theory illustrates the inapplicability of this latter in the case of the extremely thin layer. Furthermore, through analyzing the evolutions of the local spin configuration and the local strain during the relaxation process, the nucleation of LS domain is detected to appear from the corner and the region under compressive strain, which is in good agreement with experimental observations. Interestingly, in some cases, clear stretching and bending damped oscillations of the cantilever (at the natural frequencies of the structure) are observed during the switching process before reaching a mechanical equilibrium state. Moreover, damped oscillations were also observed in the time evolution of the HS fraction during the relaxation process, showing the intimate interplay between the deformation state of the cantilever and the molecular spin state. Thanks to the real-time provided by MD simulations, the propagation velocities of the LS domain boundary for different models are estimated for the first time. We find that the external tensile strain and the increase of the cooperative of the lattice would largely reduce the propagation velocity of the LS domain boundary, corresponding to a significant increase of the time to return to the steady state observed from the relaxation curves of the HS fraction.

Finally, in order to investigate the surface energy/stress effects on the SCO properties at the nanoscale in a quantitative and precise manner, new core-shell nano-thermodynamics models were developed for SCO thin films and spherical objects. In those models, continuum mechanism approximations were employed to model the intermolecular interactions, considering the spin state dependence of the molecular volume as well as the elastic moduli. Moreover, the spin state dependence of quantities characterizing surface properties, namely the surface energy and the interface stress, have been quantitatively considered for the first time in the field of SCO materials.

A very important advantage of such a model lies in the direct link existing between the input parameters and experimentally accessible physical quantities. The calculated thermally induced SCO curves of the [Fe(pyrazine)][Ni(CN)$_4$] bulk material and thin films are in good agreement with the available experimental results, indicating that this new model has the prerequisite to reproduce and to interpret experimental observations in SCO nanomaterials. The theoretical study of surface energy/stress effects on the SCO properties reveals that the

competition between the pressure induced by the surface stress and the inter-molecular elastic interaction leads to an upper shift or downshift of the equilibrium temperature depending on the magnitude of surface stress, and that both of the surface energy and the surface stress may be the driving forces of the experimentally observed incomplete spin transition at reduced size.

As mentioned in **Chapter II**, the force field is not able to simulate the first order transition by simply introducing the Double-Well intra-molecular interaction to the structure. There is still an open question concerning the different contributions to the cooperativity mechanisms (mechanical properties and volume differences between the HS and LS phases, anisotropic properties and crystallographic properties, etc.). Furthermore, since the system in MC simulations is in an ideal pressure and thermal bath, the study of thermal diffusion processes in SCO materials could be an interesting direction for future MD simulations.

In the study of the spatiotemporal dynamics of the spin transition, it would be interesting to study the nucleation process using the present force field such as estimation of the nucleation energy barrier. Due to the limited size of the simulated system and the absence of structural defects (point defects, dislocations, grain boundaries…), the propagation velocity of domain boundaries observed from simulations varies from 48 m/s to 1150 m/s according to the different models developed in this work. The interface velocity appears to be greater than that deduced from the experiment (around several μm/s) [155, 190]. More importantly, the upper limit of the time-scale of the traditional MD simulation (usually in μs) prevents it from reproducing the experimental observations. As one important perspective, it would further employ the coarse-grained (CG) MD method or the Accelerated MD method [159, 160] to simulate the mesoscopic model including different lattice defects.

In the last chapter of this manuscript, we have stressed and demonstrated many times that both the surface energy and the surface stress may play an important role in nano-sized materials. However, experimental values of surface energy/stress have not been reported in the field of SCO materials, which does not allow a direct comparison of these theoretical investigations with measurements. Nowadays, the only possibility is a comparison with size dependent lattice dynamic experiments and switching properties of SCO nanomaterials. The potential consequences of surface/interface structural, vibrational and mechanical properties on nanosized have been investigated without any experience having made possible to fully characterize surface/interface quantities and their spin state dependence. This pitfall seriously hinders further theoretical investigations. From an experimental point of view, various

techniques can be proposed to extract values of surface energies in both spin states such as contact angle (sessile drop technique), or scanning probe microscopy (Atomic Force Microscopy AFM) as well as instrumented indentation testing (nano-indentation). On the other hand, the so-called “wafer bending” measurements can be performed to extract values of surface stress[110]. In addition, as mentioned in **Chapter I**, the matrix and interface effects resulting in a considerable elastic deformation energy greatly influence the SCO behaviors at nano-metric scale. In this context, it would be interesting to introduce the interface energy/stress contributions into our present thermodynamic model in order to mimic the SCO behaviors of the multilayers or the thin film growth on a substrate.

Bibliography

[1] A. Hauser, Ligand field theoretical considerations, Spin Crossover in Transition Metal Compounds I, (2004) 49-58.

[2] S. Sugano, Y. Tanabe, H. Kamimura, Multiplets of Transition-Metal Ions in Crystals, Academic Press New York1970.

[3] L.F. Lindoy, S.E. Livingstone, Complexes of iron (II), cobalt (II) and nickel (II) with α-diimines and related bidentate ligands, Coordination Chemistry Reviews, 2 (1967) 173-193.

[4] A. Bousseksou, H. Constant-Machado, F. Varret, A simple ising-like model for spin conversion including molecular vibrations, Journal de Physique I, 5 (1995) 747-760.

[5] M. Sorai, S. Seki, Phonon coupled cooperative low-spin 1A1high-spin 5T2 transition in [Fe (phen) 2 (NCS) 2] and [Fe (phen) 2 (NCSe) 2] crystals, Journal of Physics and Chemistry of Solids, 35 (1974) 555-570.

[6] A. Bousseksou, J.J. McGarvey, F. Varret, J.A. Real, J.-P. Tuchagues, A.C. Dennis, M.L. Boillot, Raman spectroscopy of the high-and low-spin states of the spin crossover complex Fe (phen) 2 (NCS) 2: an initial approach to estimation of vibrational contributions to the associated entropy change, Chemical Physics Letters, 318 (2000) 409-416.

[7] G. Molnár, V. Niel, A.B. Gaspar, J.-A. Real, A. Zwick, A. Bousseksou, J.J. McGarvey, Vibrational spectroscopy of cyanide-bridged, iron (ii) spin-crossover coordination polymers: Estimation of vibrational contributions to the entropy change associated with the spin transition, The Journal of Physical Chemistry B, 106 (2002) 9701-9707.

[8] N. Moliner, L. Salmon, L. Capes, M.C. Munoz, J.-F. Létard, A. Bousseksou, J.-P. Tuchagues, J.J. McGarvey, A.C. Dennis, M. Castro, Thermal and optical switching of molecular spin states in the {[FeL [H2B (pz) 2] 2} spin-crossover system (L= bpy, phen), The Journal of Physical Chemistry B, 106 (2002) 4276-4283.

[9] R.C. Stoufer, D.H. Busch, W.B. Hadley, UNUSUAL MAGNETIC PROPERTIES OF SOME SIX-COÖRDINATE COBALT (II) COMPLEXES1—ELECTRONIC ISOMERS, Journal of the American Chemical Society, 83 (1961) 3732-3734.

[10] J. Sams, J. Scott, T. Tsin, Tris [2-(2′-pyridyl) benzimidazole] iron (II) complexes. Some new examples of 5T2—1A1 spin equilibria, Chemical Physics Letters, 18 (1973) 451-453.

[11] W. Baker Jr, H. Bobonich, Magnetic properties of some high-spin complexes of iron (II), Inorganic Chemistry, 3 (1964) 1184-1188.

[12] E. Koenig, K. Madeja, 5T2-1A1 Equilibriums in some iron (II)-bis (1, 10-phenanthroline) complexes, Inorganic Chemistry, 6 (1967) 48-55.
[13] S. Ohnishi, S. Sugano, Strain interaction effects on the high-spin-low-spin transition of transition-metal compounds, Journal of Physics C: Solid State Physics, 14 (1981) 39.
[14] H. Spiering, E. Meissner, H. Köppen, E. Müller, P. Gütlich, The effect of the lattice expansion on high spin⇌ low spin transitions, Chemical Physics, 68 (1982) 65-71.
[15] E. König, G. Ritter, Hysteresis effects at a cooperative high-spin (5T2)⇌ low-spin (1A1) transition in dithiocyanatobis (4, 7-dimethyl-1, 10-phenanthroline) iron (II), Solid State Communications, 18 (1976) 279-282.
[16] V. V, Zelentsov, Soviet Scientific Reviews Series, Section B, 10 (1987) 485.
[17] J.A. Real, H. Bolvin, A. Bousseksou, A. Dworkin, O. Kahn, F. Varret, J. Zarembowitch, Two-step spin crossover in the new dinuclear compound [Fe (bt)(NCS) 2] 2bpym, with bt= 2, 2'-bi-2-thiazoline and bpym= 2, 2'-bipyrimidine: experimental investigation and theoretical approach, Journal of the American Chemical Society, 114 (1992) 4650-4658.
[18] A. Bousseksou, J. Nasser, J. Linares, K. Boukheddaden, F. Varret, Ising-like model for the two-step spin-crossover, Journal de Physique I, 2 (1992) 1381-1403.
[19] A. Bousseksou, F. Varret, J. Nasser, Ising-like model for the two step spin-crossover of binuclear molecules, Journal de Physique I, 3 (1993) 1463-1473.
[20] A. Ewald, R. Martin, I. Ross, A. White, Anomalous behaviour at the 6 A 1-2 T 2 crossover in iron (III) complexes, Proceedings of the Royal Society of London. Series A. Mathematical and Physical Sciences, 280 (1964) 235-257.
[21] P. Gütlich, H.A. Goodwin, Spin crossover in transition metal compounds I, Springer Science & Business Media2004.
[22] P. Gütlich, H.A. Goodwin, Spin crossover—an overall perspective, Spin Crossover in Transition Metal Compounds I, DOI (2004) 1-47.
[23] C. Slichter, H. Drickamer, Pressure-induced electronic changes in compounds of iron, The Journal of Chemical Physics, 56 (1972) 2142-2160.
[24] K.F. Purcell, M.P. Edwards, Cooperativity in thermally induced intersystem crossing in solids: Fe (phen) 2 (NCR) 2, R= BH3, BPh3, S, Se, Inorganic Chemistry, 23 (1984) 2620-2625.
[25] R. Zimmermann, E. König, A model for high-spin/low-spin transitions in solids including the effect of lattice vibrations, Journal of Physics and Chemistry of Solids, 38 (1977) 779-788.

[26] N. Willenbacher, H. Spiering, The elastic interaction of high-spin and low-spin complex molecules in spin-crossover compounds, Journal of Physics C: Solid State Physics, 21 (1988) 1423.
[27] H. Spiering, K. Boukheddaden, J. Linares, F. Varret, Total free energy of a spin-crossover molecular system, Physical Review B, 70 (2004) 184106.
[28] J. Wajnflasz, Etude de la transition „Low Spin" -„High Spin" dans les complexes octaédriques d'ion de transition, Physica Status Solidi (b), 40 (1970) 537-545.
[29] J. Wajnflasz, R. Pick, Transitions «Low spin»-«High spin» dans les complexes de Fe2+, Journal de Physique Colloques, 32 (1971) C1-91-C91-92.
[30] Y. Konishi, H. Tokoro, M. Nishino, S. Miyashita, Magnetic Properties and Metastable States in Spin-Crossover Transition of Co–Fe Prussian Blue Analogues, Journal of the Physical Society of Japan, 75 (2006) 114603-114603.
[31] J. Linares, H. Spiering, F. Varret, Analytical solution of 1D Ising-like systems modified by weak long range interaction: Application to spin crossover compounds, The European Physical Journal B-Condensed Matter and Complex Systems, 10 (1999) 271-275.
[32] D. Chiruta, J. Linares, Y. Garcia, M. Dimian, P.R. Dahoo, Analysis of multi-step transitions in spin crossover nanochains, Physica B: Condensed Matter, 434 (2014) 134-138.
[33] J. Linares, C. Enachescu, K. Boukheddaden, F. Varret, Monte Carlo entropic sampling applied to spin crossover solids: the squareness of the thermal hysteresis loop, Polyhedron, 22 (2003) 2453-2456.
[34] C. Enachescu, L. Stoleriu, A. Stancu, A. Hauser, Model for elastic relaxation phenomena in finite 2D hexagonal molecular lattices, Physical Review Letters, 102 (2009) 257204.
[35] W. Nicolazzi, S. Pillet, C. Lecomte, Two-variable anharmonic model for spin-crossover solids: A like-spin domains interpretation, Physical Review B, 78 (2008) 174401.
[36] W. Nicolazzi, S. Pillet, C. Lecomte, Photoinduced phase separation in spin-crossover materials: Numerical simulation of a dynamic photocrystallographic experiment, Physical Review B, 80 (2009) 132102.
[37] M. Nishino, K. Boukheddaden, Y. Konishi, S. Miyashita, Simple two-dimensional model for the elastic origin of cooperativity among spin states of spin-crossover complexes, Physical Review Letters, 98 (2007) 247203.
[38] M. Nishino, K. Boukheddaden, S. Miyashita, Molecular dynamics study of thermal expansion and compression in spin-crossover solids using a microscopic model of elastic interactions, Physical Review B, 79 (2009) 012409.

[39] K. Boukheddaden, M. Nishino, S. Miyashita, Molecular dynamics and transfer integral investigations of an elastic anharmonic model for phonon-induced spin crossover, Physical Review Letters, 100 (2008) 177206.
[40] M. Nishino, C. Enachescu, S. Miyashita, K. Boukheddaden, F. Varret, Intrinsic effects of the boundary condition on switching processes in effective long-range interactions originating from local structural change, Physical Review B, 82 (2010) 020409.
[41] K. Boukheddaden, Anharmonic model for phonon-induced first-order transition in 1-D spin-crossover solids, Progress of Theoretical Physics, 112 (2004) 205-217.
[42] M. Nadeem, J. Cruddas, G. Ruzzi, B.J. Powell, Toward high-temperature light-induced spin-state trapping in spin-crossover materials: The interplay of collective and molecular effects, Journal of the American Chemical Society, 144 (2022) 9138-9148.
[43] S. Nosé, A unified formulation of the constant temperature molecular dynamics methods, The Journal of Chemical Physics, 81 (1984) 511-519.
[44] W.G. Hoover, Canonical dynamics: Equilibrium phase-space distributions, Physical Review A, 31 (1985) 1695.
[45] M. Nishino, C. Enachescu, S. Miyashita, P.A. Rikvold, K. Boukheddaden, F. Varret, Macroscopic nucleation phenomena in continuum media with long-range interactions, Scientific Reports, 1 (2011) 1-5.
[46] W. Nicolazzi, S. Pillet, Structural aspects of the relaxation process in spin crossover solids: phase separation, mapping of lattice strain, and domain wall structure, Physical Review B, 85 (2012) 094101.
[47] C. Enachescu, M. Nishino, S. Miyashita, L. Stoleriu, A. Stancu, Monte Carlo Metropolis study of cluster evolution in spin-crossover solids within the framework of a mechanoelastic model, Physical Review B, 86 (2012) 054114.
[48] N. Di Scala, N.E.I. Belmouri, M.A.P. Espejo, K. Boukheddaden, Three-dimensional electroelastic modeling of the nucleation and propagation of the spin domains in spin-crossover materials, Physical Review B, 106 (2022) 014422.
[49] M. Nishino, T. Nakada, C. Enachescu, K. Boukheddaden, S. Miyashita, Crossover of the roughness exponent for interface growth in systems with long-range interactions due to lattice distortion, Physical Review B, 88 (2013) 094303.
[50] B. Gajdics, J.J. Tomán, Z. Erdélyi, An effective method to calculate atomic movements in 3D objects with tuneable stochasticity (3DO-SKMF), Computer Physics Communications, 258 (2021) 107609.

[51] G. Massasso, J.r.m. Long, J. Haines, S. Devautour-Vinot, G. Maurin, A.s. Grandjean, B. Onida, B. Donnadieu, J. Larionova, C. Guérin, Iodine Capture by Hofmann-Type Clathrate NiII (pz)[NiII (CN) 4], Inorganic Chemistry, 53 (2014) 4269-4271.
[52] C.H. Pham, J. Cirera, F. Paesani, Molecular mechanisms of spin crossover in the {Fe (pz)[Pt (CN) 4]} metal–organic framework upon water adsorption, Journal of the American Chemical Society, 138 (2016) 6123-6126.
[53] C.H. Pham, F. Paesani, Spin crossover in the {Fe (pz)[Pt (CN) 4]} metal–organic framework upon pyrazine adsorption, The Journal of Physical Chemistry Letters, 7 (2016) 4022-4026.
[54] T. Forestier, S. Mornet, N. Daro, T. Nishihara, S.-i. Mouri, K. Tanaka, O. Fouché, E. Freysz, J.-F. Létard, Nanoparticles of iron (II) spin-crossover, Chemical Communications (Cambridge, United Kingdom), DOI (2008) 4327-4329.
[55] J.-F. Létard, P. Guionneau, L. Goux-Capes, Towards spin crossover applications, Spin Crossover in Transition Metal Compounds III2004.
[56] E. Coronado, J.R. Galán-Mascarós, M. Monrabal-Capilla, J. García-Martínez, P. Pardo-Ibáñez, Bistable spin-crossover nanoparticles showing magnetic thermal hysteresis near room temperature, Advanced Materials, 19 (2007) 1359-1361.
[57] J.R. Galán-Mascarós, E. Coronado, A. Forment-Aliaga, M. Monrabal-Capilla, E. Pinilla-Cienfuegos, M. Ceolin, Tuning size and thermal hysteresis in bistable spin crossover nanoparticles, Inorganic Chemistry, 49 (2010) 5706-5714.
[58] M. Giménez-Marqués, M.L.G.-S. de Larrea, E. Coronado, Unravelling the chemical design of spin-crossover nanoparticles based on iron (II)–triazole coordination polymers: towards a control of the spin transition, Journal of Materials Chemistry C, 3 (2015) 7946-7953.
[59] P. Durand, S. Pillet, E.-E. Bendeif, C. Carteret, M. Bouazaoui, H. El Hamzaoui, B. Capoen, L. Salmon, S. Hébert, J. Ghanbaja, Room temperature bistability with wide thermal hysteresis in a spin crossover silica nanocomposite, Journal of Materials Chemistry C, 1 (2013) 1933-1942.
[60] T. Forestier, A. Kaiba, S. Pechev, D. Denux, P. Guionneau, C. Etrillard, N. Daro, E. Freysz, J.F. Létard, Nanoparticles of [Fe (NH2-trz) 3] Br2 · 3 H2O (NH2-trz= 2-Amino-1, 2, 4-triazole) Prepared by the Reverse Micelle Technique: Influence of Particle and Coherent Domain Sizes on Spin-Crossover Properties, Chemistry–A European Journal, 15 (2009) 6122-6130.
[61] A. Rotaru, F. Varret, A. Gindulescu, J. Linares, A. Stancu, J.-F. Létard, T. Forestier, C. Etrillard, Size effect in spin-crossover systems investigated by FORC measurements, for

surfacted [Fe (NH 2-trz) 3](Br) 2· 3H 2 O nanoparticles: reversible contributions and critical size, The European Physical Journal B, 84 (2011) 439-449.
[62] A. Tokarev, L. Salmon, Y. Guari, W. Nicolazzi, G. Molnár, A. Bousseksou, Cooperative spin crossover phenomena in [Fe (NH 2 trz) 3](tosylate) 2 nanoparticles, Chemical Communications (Cambridge, United Kingdom), 46 (2010) 8011-8013.
[63] L. Salmon, G. Molnár, D. Zitouni, C. Quintero, C. Bergaud, J.-C. Micheau, A. Bousseksou, A novel approach for fluorescent thermometry and thermal imaging purposes using spin crossover nanoparticles, Journal of Materials Chemistry, 20 (2010) 5499-5503.
[64] A. Tokarev, L. Salmon, Y. Guari, G. Molnár, A. Bousseksou, Synthesis of spin crossover nano-objects with different morphologies and properties, New Journal of Chemistry, 35 (2011) 2081-2088.
[65] I.y.A. Gural'skiy, C.M. Quintero, G. Molnár, I.O. Fritsky, L. Salmon, A. Bousseksou, Synthesis of Spin-Crossover Nano-and Micro-objects in Homogeneous Media, Chemistry–A European Journal, 18 (2012) 9946-9954.
[66] I. Boldog, A.B. Gaspar, V. Martínez, P. Pardo-Ibañez, V. Ksenofontov, A. Bhattacharjee, P. Gütlich, J.A. Real, Spin-crossover nanocrystals with magnetic, optical, and structural bistability near room temperature, Angewandte Chemie International Edition, 47 (2008) 6433-6437.
[67] F. Volatron, L. Catala, E. Rivière, A. Gloter, O. Stéphan, T. Mallah, Spin-crossover coordination nanoparticles, Inorganic Chemistry, 47 (2008) 6584-6586.
[68] J. Larionova, L. Salmon, Y. Guari, A. Tokarev, K. Molvinger, G. Molnár, A. Bousseksou, Towards the ultimate size limit of the memory effect in spin-crossover solids, Angewandte Chemie International Edition, 47 (2008) 8236-8240.
[69] H. Peng, S. Tricard, G. Félix, G. Molnár, W. Nicolazzi, L. Salmon, A. Bousseksou, Re-appearance of cooperativity in ultra-small spin-crossover [Fe (pz){Ni (CN) 4}] nanoparticles, Angewandte Chemie, 126 (2014) 11074-11078.
[70] A. Tissot, L. Rechignat, A. Bousseksou, M.-L. Boillot, Micro-and nanocrystals of the iron (iii) spin-transition material [Fe III (3-MeO-SalEen) 2] PF 6, Journal of Materials Chemistry, 22 (2012) 3411-3419.
[71] J. Laisney, A. Tissot, G. Molnár, L. Rechignat, E. Rivière, F. Brisset, A. Bousseksou, M.-L. Boillot, Nanocrystals of Fe (phen) 2 (NCS) 2 and the size-dependent spin-crossover characteristics, Dalton Transactions, 44 (2015) 17302-17311.

[72] J. Daen, Insoluble monolayers at liquid-gas interfaces, Journal of Colloid and Interface Science, 22 (1966) 309.
[73] H. Soyer, C. Mingotaud, M.-L. Boillot, P. Delhaes, Spin crossover of a langmuir− blodgett film based on an amphiphilic iron (II) complex, Langmuir, 14 (1998) 5890-5895.
[74] V. Shalabaeva, M. Mikolasek, M.D. Manrique-Juarez, A.-C. Bas, S. Rat, L. Salmon, W. Nicolazzi, G.b. Molnár, A. Bousseksou, Unprecedented size effect on the phase stability of molecular thin films displaying a spin transition, The Journal of Physical Chemistry C, 121 (2017) 25617-25621.
[75] K. Bairagi, O. Iasco, A. Bellec, A. Kartsev, D. Li, J. Lagoute, C. Chacon, Y. Girard, S. Rousset, F. Miserque, Y J. Dappe, A. Smogunov, C. Barreteau, M-L. Boillot, T. Mallah, V. Repain Molecular-scale dynamics of light-induced spin cross-over in a two-dimensional layer, Nature Communications, 7 (2016) 12212.
[76] M. Kelai, B. Cahier, M. Atanasov, F. Neese, Y. Tong, L. Zhang, A. Bellec, O. Iasco, E. Rivière, R. Guillot, C. Chacon, Y. Girard,a J. Lagoute, S. Rousset, V. Repain, E. Otero, M-A. Arrio, P. Sainctavit, A-L. Barra, M-L. Boillot, T. Mallah, Robust magnetic anisotropy of a monolayer of hexacoordinate Fe (ii) complexes assembled on Cu (111), Inorganic Chemistry Frontiers, 8 (2021) 2395-2404.
[77] K. Bairagi, A. Bellec, C. Fourmental, O. Iasco, J. Lagoute, C. Chacon, Y. Girard, S. Rousset, F. Choueikani, E. Otero, P. Ohresser, P. Sainctavit, M-L. Boillot, T. Mallah, V, Repain, Temperature-, light-, and soft X-ray-induced spin crossover in a single layer of FeII-pyrazolylborate molecules in direct contact with gold, The Journal of Physical Chemistry C, 122 (2018) 727-731.
[78] C. Fourmental, S. Mondal, R. Banerjee, A. Bellec, Y. Garreau, A. Coati, C. Chacon, Y. Girard, J. Lagoute, S. Rousset, M-L. Boillot, T. Mallah, C. Enachescu, C. Barreteau, Y J. Dappe, A. Smogunov, S. Narasimhan, V. Repain, Importance of epitaxial strain at a spin-crossover molecule–metal interface, The Journal of Physical Chemistry Letters, 10 (2019) 4103-4109.
[79] D. Li, Y. Tong, K. Bairagi, M. Kelai, Y.J. Dappe, J. Lagoute, Y. Girard, S. Rousset, V. Repain, C. Barreteau, M. Brandbyge, A. Smogunov, A. Bellec, Negative Differential Resistance in Spin-Crossover Molecular Devices, The Journal of Physical Chemistry Letters, 13 (2022) 7514-7520.
[80] Y. Tong, M. Kelaï, K. Bairagi, V. Repain, J. Lagoute, Y. Girard, S. Rousset, M.-L. Boillot, T. Mallah, C. Enachescu, A. Bellec, Voltage-induced bistability of single spin-crossover

molecules in a two-dimensional monolayer, The Journal of Physical Chemistry Letters, 12 (2021) 11029-11034.
[81] A. Bellec, J. Lagoute, V. Repain, Molecular electronics: Scanning tunneling microscopy and single-molecule devices, Comptes Rendus Chimie, 21 (2018) 1287-1299.
[82] L. Zhang, Y. Tong, M. Kelai, A. Bellec, J. Lagoute, C. Chacon, Y. Girard, S. Rousset, M.L. Boillot, E. Rivière, Prof. Talal Mallah, E. Otero, M-A Arrio, P. Sainctavit, V. Repain, Anomalous light-induced spin-state switching for iron (II) spin-crossover molecules in direct contact with metal surfaces, Angewandte Chemie International Edition, 59 (2020) 13341-13346.
[83] M. Kelai, A. Tauzin, A. Railean, V. Repain, J. Lagoute, Y. Girard, S. Rousset, E. Otero, T. Mallah, M.-L. Boillot, C. Enachescu, A. Bellec, Interface versus Bulk Light-Induced Switching in Spin-Crossover Molecular Ultrathin Films Adsorbed on a Metallic Surface, The Journal of Physical Chemistry Letters, 14 (2023) 1949-1954.
[84] M. Kelai, V. Repain, A. Tauzin, W. Li, Y. Girard, J. Lagoute, S. Rousset, E. Otero, P. Sainctavit, M.-A. Arrio, M-L. Boillot, T. Mallah, C. Enachescu, A. Bellec, Thermal bistability of an ultrathin film of iron (II) spin-crossover molecules directly adsorbed on a metal surface, The Journal of Physical Chemistry Letters, 12 (2021) 6152-6158.
[85] S. Cobo, G. Molnár, J.A. Real, A. Bousseksou, Multilayer sequential assembly of thin films that display room-temperature spin crossover with hysteresis, Angewandte Chemie, 118 (2006) 5918-5921.
[86] C. Bartual-Murgui, L. Salmon, A. Akou, C. Thibault, G. Molnár, T. Mahfoud, Z. Sekkat, J.A. Real, A. Bousseksou, High quality nano-patterned thin films of the coordination compound {Fe (pyrazine)[Pt (CN) 4]} deposited layer-by-layer, New Journal of Chemistry, 35 (2011) 2089-2094.
[87] G. Agusti, S. Cobo, A.B. Gaspar, G. Molnar, N.O. Moussa, P.A. Szilagyi, V. Pálfi, C. Vieu, M. Carmen Muñoz, J.A. Real, Thermal and light-induced spin crossover phenomena in new 3D Hofmann-like microporous metalorganic frameworks produced as bulk materials and nanopatterned thin films, Chemistry of Materials, 20 (2008) 6721-6732.
[88] C. Bartual-Murgui, A. Akou, L. Salmon, G. Molnár, C. Thibault, J.A. Real, A. Bousseksou, Guest effect on nanopatterned spin-crossover thin films, Small, 7 (2011) 3385-3391.
[89] S. Sakaida, K. Otsubo, M. Maesato, H. Kitagawa, Crystal Size Effect on the Spin-Crossover Behavior of {Fe (py) 2 [Pt (CN) 4]}(py= Pyridine) Monitored by Raman Spectroscopy, Inorganic Chemistry, 59 (2020) 16819-16823.

[90] T. Haraguchi, K. Otsubo, O. Sakata, A. Fujiwara, H. Kitagawa, Strain-Controlled Spin Transition in Heterostructured Metal–Organic Framework Thin Film, Journal of the American Chemical Society, 143 (2021) 16128-16135.
[91] A. Muraoka, K. Boukheddaden, J. Linares, F. Varret, Two-dimensional Ising-like model with specific edge effects for spin-crossover nanoparticles: A Monte Carlo study, Physical Review B, 84 (2011) 054119.
[92] A. Slimani, K. Boukheddaden, K. Yamashita, Thermal spin transition of circularly shaped nanoparticles in a core-shell structure investigated with an electroelastic model, Physical Review B, 89 (2014) 214109.
[93] M. Mikolasek, G. Félix, G. Molnár, F. Terki, W. Nicolazzi, A. Bousseksou, Role of surface vibrational properties on cooperative phenomena in spin-crossover nanomaterials, Physical Review B, 90 (2014) 075402.
[94] M. Mikolasek, W. Nicolazzi, F. Terki, G. Molnár, A. Bousseksou, Investigation of surface energies in spin crossover nanomaterials: the role of surface relaxations, Physical Chemistry Chemical Physics, 19 (2017) 12276-12281.
[95] M. Mikolasek, W. Nicolazzi, F. Terki, G. Molnár, A. Bousseksou, Surface transition in spin crossover nanoparticles, Chemical Physics Letters, 678 (2017) 107-111.
[96] K. Affes, A. Slimani, Y. Singh, A. Maalej, K. Boukheddaden, Magneto-elastic properties of a spin crossover membrane deposited on a deformable substrate, Journal of Physics: Condensed Matter, 32 (2020) 255402.
[97] A. Railean, M. Kelai, A. Bellec, V. Repain, M.-L. Boillot, T. Mallah, L. Stoleriu, C. Enachescu, Mechanoelastic simulations of monolayer lattices of spin crossover molecules on a substrate, Physical Review B, 107 (2023) 014304.
[98] L. Stoleriu, P. Chakraborty, A. Hauser, A. Stancu, C. Enachescu, Thermal hysteresis in spin-crossover compounds studied within the mechanoelastic model and its potential application to nanoparticles, Physical Review B, 84 (2011) 134102.
[99] H. Oubouchou, A. Slimani, K. Boukheddaden, Interplay between elastic interactions in a core-shell model for spin-crossover nanoparticles, Physical Review B, 87 (2013) 104104.
[100] G. Félix, M. Mikolasek, G. Molnár, W. Nicolazzi, A. Bousseksou, Tuning the spin crossover in nano-objects: From hollow to core–shell particles, Chemical Physics Letters, 607 (2014) 10-14.

[101] A. Slimani, H. Khemakhem, K. Boukheddaden, Structural synergy in a core-shell spin crossover nanoparticle investigated by an electroelastic model, Physical Review B, 95 (2017) 174104.
[102] M.D. Manrique-Juárez, F. Mathieu, A. Laborde, S. Rat, V. Shalabaeva, P. Demont, O. Thomas, L. Salmon, T. Leichle, L. Nicu, Micromachining-Compatible, Facile Fabrication of Polymer Nanocomposite Spin Crossover Actuators, Advanced Functional Materials, 28 (2018) 1801970.
[103] M.D. Manrique-Juarez, S. Rat, F. Mathieu, D. Saya, I. Séguy, T. Leïchlé, L. Nicu, L. Salmon, G. Molnár, A. Bousseksou, Microelectromechanical systems integrating molecular spin crossover actuators, Applied Physics Letters, 109 (2016) 061903.
[104] M.D. Manrique-Juarez, S. Rat, L. Salmon, G. Molnár, C.M. Quintero, L. Nicu, H.J. Shepherd, A. Bousseksou, Switchable molecule-based materials for micro-and nanoscale actuating applications: Achievements and prospects, Coordination Chemistry Reviews, 308 (2016) 395-408.
[105] M. Piedrahita-Bello, J.E. Angulo-Cervera, A. Enriquez-Cabrera, G. Molnár, B. Tondu, L. Salmon, A. Bousseksou, Colossal expansion and fast motion in spin-crossover@ polymer actuators, Materials Horizons, 8 (2021) 3055-3062.
[106] H.J. Shepherd, I.y.A. Gural'skiy, C.M. Quintero, S. Tricard, L. Salmon, G. Molnár, A. Bousseksou, Molecular actuators driven by cooperative spin-state switching, Nature Communications, 4 (2013) 2607.
[107] G. Félix, W. Nicolazzi, L. Salmon, G. Molnár, M. Perrier, G. Maurin, J. Larionova, J. Long, Y. Guari, A. Bousseksou, Enhanced cooperative interactions at the nanoscale in spin-crossover materials with a first-order phase transition, Physical Review Letters, 110 (2013) 235701.
[108] P. Müller, A. Saúl, Elastic effects on surface physics, Surface Science Reports, 54 (2004) 157-258.
[109] P. Müller, A. Saùl, F. Leroy, Simple views on surface stress and surface energy concepts, Advances in Natural Sciences: Nanoscience and Nanotechnology, 5 (2013) 013002.
[110] R.C. Cammarata, K. Sieradzki, Surface and interface stresses, Annual Review of Materials Science, 24 (1994) 215-234.
[111] G. Félix, M. Mikolasek, G. Molnár, W. Nicolazzi, A. Bousseksou, Control of the Phase Stability in Spin-Crossover Core–Shell Nanoparticles through the Elastic Interface Energy, European Journal of Inorganic Chemistry, 2018 (2018) 435-442.

[112] A. Fahs, S. Mi, W. Nicolazzi, G. Molnár, A. Bousseksou, Disentangling Surface Energy and Surface/Interface Stress Effects in Spin Crossover Nanomaterials, Advanced Physics Research, DOI (2023).
[113] K.L. Ronayne, H. Paulsen, A. Höfer, A.C. Dennis, J.A. Wolny, A.I. Chumakov, V. Schünemann, H. Winkler, H. Spiering, A. Bousseksou, Vibrational spectrum of the spin crossover complex [Fe (phen) 2 (NCS) 2] studied by IR and Raman spectroscopy, nuclear inelastic scattering and DFT calculations, Physical Chemistry Chemical Physics, 8 (2006) 4685-4693.
[114] J.A. Wolny, S. Rackwitz, K. Achterhold, Y. Garcia, K. Muffler, A.D. Naik, V. Schünemann, Vibrational properties of the trinuclear spin crossover complex [Fe 3 (4-(2′-hydroxy-ethyl)-1, 2, 4-triazole) 6 (H 2 O) 6](CF 3 SO 3) 6: a nuclear inelastic scattering, IR, Raman and DFT study, Physical Chemistry Chemical Physics, 12 (2010) 14782-14788.
[115] S. Rackwitz, J.A. Wolny, K. Muffler, K. Achterhold, R. Rüffer, Y. Garcia, R. Diller, V. Schünemann, Vibrational properties of the polymeric spin crossover (SCO) Fe (ii) complexes [{Fe (4-amino-1, 2, 4-triazole) 3} X 2] n: a nuclear inelastic scattering (NIS), Raman and DFT study, Physical Chemistry Chemical Physics, 14 (2012) 14650-14660.
[116] J.A. Wolny, R. Diller, V. Schünemann, Vibrational Spectroscopy of Mono-and Polynuclear Spin-Crossover Systems, European Journal of Inorganic Chemistry, 2012 (2012) 2635-2648.
[117] J.A. Wolny, H. Paulsen, A.X. Trautwein, V. Schünemann, Density functional theory calculations and vibrational spectroscopy on iron spin-crossover compounds, Coordination Chemistry Reviews, 253 (2009) 2423-2431.
[118] J.A. Wolny, V. Schünemann, Z. Németh, G. Vankó, Spectroscopic techniques to characterize the spin state: Vibrational, optical, Mössbauer, NMR, and X-ray spectroscopy, Comptes Rendus Chimie, 21 (2018) 1152-1169.
[119] J.A. Wolny, S. Rackwitz, K. Achterhold, K. Muffler, V. Schünemann, Nuclear inelastic scattering of 1D polymeric Fe (II) complexes of 1, 2, 4-aminotriazole in their high-spin and low-spin state, Hyperfine Interactions, 204 (2012) 129-132.
[120] G.S. Matouzenko, S.A. Borshch, V. Schünemann, J.A. Wolny, Ligand strain and conformations in a family of Fe (II) spin crossover hexadentate complexes involving the 2-pyridylmethyl-amino moiety: DFT modelling, Physical Chemistry Chemical Physics, 15 (2013) 7411-7419.

[121] H. Paulsen, V. Schünemann, J.A. Wolny, Progress in electronic structure calculations on spin-crossover complexes, European Journal of Inorganic Chemistry, 2013 (2013) 628-641.
[122] J.A. Wolny, I. Faus, J. Marx, R. Rüffer, A.I. Chumakov, K. Schlage, H.-C. Wille, V. Schünemann, Vibrational Coupling of Nearest Neighbors in 1-D Spin Crossover Polymers of Rigid Bridging Ligands. A Nuclear Inelastic Scattering and DFT Study, Magnetochemistry, 2 (2016) 19.
[123] K. Jenni, L. Scherthan, I. Faus, J. Marx, C. Strohm, M. Herlitschke, H.-C. Wille, P. Würtz, V. Schünemann, J.A. Wolny, Nuclear inelastic scattering and density functional theory studies of a one-dimensional spin crossover [Fe (1, 2, 4-triazole) 2 (1, 2, 4-triazolato)](BF 4) molecular chain, Physical Chemistry Chemical Physics, 19 (2017) 18880-18889.
[124] T. Hochdörffer, A.I. Chumakov, H.-C. Wille, V. Schünemann, J.A. Wolny, Vibrational properties and cooperativity of the 3D spin crossover network [Fe (pyrazine)][Pt (CN) 4], Dalton Transactions, 48 (2019) 15625-15634.
[125] A. Chumakov, W. Sturhahn, Experimental aspects of inelastic nuclear resonance scattering, Hyperfine Interactions, 123 (1999) 781-808.
[126] G. Félix, M. Mikolasek, H. Peng, W. Nicolazzi, G. Molnár, A.I. Chumakov, L. Salmon, A. Bousseksou, Lattice dynamics in spin-crossover nanoparticles through nuclear inelastic scattering, Physical Review B, 91 (2015) 024422.
[127] S. Rat, M. Mikolasek, J.S. Costá, A.I. Chumakov, W. Nicolazzi, G. Molnár, L. Salmon, A. Bousseksou, Raman and nuclear inelastic scattering study of the lattice dynamics of the [Fe (H2B (pz) 2) 2 (phen)] spin crossover complex, Chemical Physics Letters, 653 (2016) 131-136.
[128] M. Mikolasek, G. Félix, H. Peng, S. Rat, F. Terki, A.I. Chumakov, L. Salmon, G. Molnár, W. Nicolazzi, A. Bousseksou, Finite-size effects on the lattice dynamics in spin crossover nanomaterials. I. Nuclear inelastic scattering investigation, Physical Review B, 96 (2017) 035426.
[129] L.H. Böttger, A.I. Chumakov, C.M. Grunert, P. Gütlich, J. Kusz, H. Paulsen, U. Ponkratz, V. Rusanov, A.X. Trautwein, J.A. Wolny, Spin-and phase transition in the spin crossover complex [Fe (ptz) 6](BF4) 2 studied by nuclear inelastic scattering of synchrotron radiation and by DFT calculations, Chemical Physics Letters, 429 (2006) 189-193.
[130] Á. Fernández-Blanco, L. Piñeiro-López, M. Jiménez-Ruiz, S. Rols, J.A. Real, J.A. Rodríguez-Velamazán, R. Poloni, Probing the SO2 Adsorption Mechanism in Hofmann Clathrates via Inelastic Neutron Scattering and Density Functional Theory Calculations, The Journal of Physical Chemistry C, 126 (2022) 8090-8099.

[131] R. Meyer, C. Mücksch, J.A. Wolny, V. Schünemann, H.M. Urbassek, Atomistic simulations of spin-switch dynamics in multinuclear chain-like triazole spin-crossover molecules, Chemical Physics Letters, 733 (2019) 136666.
[132] J. Herz, R. Meyer, J.A. Wolny, V. Schünemann, H.M. Urbassek, Crystal effects in the vibrational spectra of one-dimensional molecular spin crossover crystals using molecular dynamics simulations, Applied Physics A, 129 (2023) 345.
[133] M. Mikolasek, W. Nicolazzi, F. Terki, G. Molnár, A. Bousseksou, Finite-size effects on the lattice dynamics in spin crossover nanomaterials. II. Molecular dynamics simulations, Physical Review B, 96 (2017) 035427.
[134] A. Fahs, W. Nicolazzi, G. Molnár, A. Bousseksou, Role of Surface Effects in the Vibrational Density of States and the Vibrational Entropy in Spin Crossover Nanomaterials: A Molecular Dynamics Investigation, Magnetochemistry, 7 (2021) 27.
[135] V. Niel, J.M. Martinez-Agudo, M.C. Munoz, A.B. Gaspar, J.A. Real, Cooperative spin crossover behavior in cyanide-bridged Fe (II)− M (II) bimetallic 3D Hofmann-like networks (M= Ni, Pd, and Pt), Inorganic Chemistry, 40 (2001) 3838-3839.
[136] P.D. Southon, L. Liu, E.A. Fellows, D.J. Price, G.J. Halder, K.W. Chapman, B. Moubaraki, K.S. Murray, J.-F. Létard, C.J. Kepert, Dynamic interplay between spin-crossover and host− guest function in a nanoporous metal− organic framework material, Journal of the American Chemical Society, 131 (2009) 10998-11009.
[137] A.K. Rappé, C.J. Casewit, K. Colwell, W.A. Goddard III, W.M. Skiff, UFF, a full periodic table force field for molecular mechanics and molecular dynamics simulations, Journal of the American Chemical Society, 114 (1992) 10024-10035.
[138] F. Taubert, S. Schwalbe, J. Seidel, R. Hüttl, T. Gruber, R. Janot, M. Bobnar, R. Gumeniuk, F. Mertens, J. Kortus, Thermodynamic characterization of lithium monosilicide (LiSi) by means of calorimetry and DFT-calculations, International Journal of Materials Research, 108 (2017) 942-958.
[139] V. Morozov, V. Belokopytov, G. Zegzhda, V. Moiseenko, Force constants and vibration frequencies and forms of the coordination center of cysteine-containing chromium (III) trischelates, Foundations of Physics Letters, 15 (2002) 508-513.
[140] G. Voronoi, Nouvelles applications des paramètres continus à la théorie des formes quadratiques. Deuxième mémoire. Recherches sur les parallélloèdres primitifs, Journal für die reine und angewandte Mathematik (Crelles Journal), 1908 (1908) 198-287.

[141] S. Plimpton, Fast parallel algorithms for short-range molecular dynamics, Journal of Computational Physics, 117 (1995) 1-19.
[142] R. Fletcher, C.M. Reeves, Function minimization by conjugate gradients, The computer journal, 7 (1964) 149-154.
[143] L. Verlet, Computer" experiments" on classical fluids. I. Thermodynamical properties of Lennard-Jones molecules, Physical Review, 159 (1967) 98.
[144] C. Rycroft, Voro++: A three-dimensional Voronoi cell library in C++, Lawrence Berkeley National Lab.(LBNL), Berkeley, CA (United States), 2009.
[145] A. Stukowski, Visualization and analysis of atomistic simulation data with OVITO–the Open Visualization Tool, Modelling and Simulation in Materials Science and Engineering, 18 (2009) 015012.
[146] Y. Konishi, H. Tokoro, M. Nishino, S. Miyashita, Monte Carlo simulation of pressure-induced phase transitions in spin-crossover materials, Physical Review Letters, 100 (2008) 067206.
[147] C. Cantin, J. Kliava, A. Marbeuf, D. Mikaïlitchenko, Cooperativity in a spin transition ferrous polymer: Interacting domain model, thermodynamic, optical and EPR study, The European Physical Journal B, 12 (1999) 525-540.
[148] J.A. Rodríguez-Velamazán, M.A. González, J.A. Real, M. Castro, M.C. Muñoz, A.B. Gaspar, R. Ohtani, M. Ohba, K. Yoneda, Y. Hijikata, A switchable molecular rotator: neutron spectroscopy study on a polymeric spin-crossover compound, Journal of the American Chemical Society, 134 (2012) 5083-5089.
[149] J. Cirera, V. Babin, F. Paesani, Theoretical modeling of spin crossover in metal–organic frameworks:[Fe (pz) 2Pt (CN) 4] as a case study, Inorganic Chemistry, 53 (2014) 11020-11028.
[150] S. Rackwitz, W. Klopper, V. Schünemann, J.A. Wolny, Quantification of intramolecular cooperativity in polynuclear spin crossover Fe (II) complexes by density functional theory calculations, Physical Chemistry Chemical Physics, 15 (2013) 15450-15458.
[151] S. Miyashita, Y. Konishi, M. Nishino, H. Tokoro, P.A. Rikvold, Realization of the mean-field universality class in spin-crossover materials, Physical Review B, 77 (2008) 014105.
[152] S. Sami, M.F. Menger, S. Faraji, R. Broer, R.W. Havenith, Q-Force: Quantum mechanically augmented molecular force fields, Journal of Chemical Theory and Computation, 17 (2021) 4946-4960.
[153] F. Shimizu, S. Ogata, J. Li, Theory of shear banding in metallic glasses and molecular dynamics calculations, Materials Transactions, 48 (2007) 2923-2927.

[154] P. Gullett, M. Horstemeyer, M. Baskes, H. Fang, A deformation gradient tensor and strain tensors for atomistic simulations, Modelling and Simulation in Materials Science and Engineering, 16 (2007) 015001.
[155] K. Ridier, G. Molnár, L. Salmon, W. Nicolazzi, A. Bousseksou, Hysteresis, nucleation and growth phenomena in spin-crossover solids, Solid State Sciences, 74 (2017) A1-A22.
[156] A. Slimani, K. Boukheddaden, F. Varret, H. Oubouchou, M. Nishino, S. Miyashita, Microscopic spin-distortion model for switchable molecular solids: Spatiotemporal study of the deformation field and local stress at the thermal spin transition, Physical Review B, 87 (2013) 014111.
[157] R. Traiche, M. Sy, H. Oubouchou, G. Bouchez, F.o. Varret, K. Boukheddaden, Spatiotemporal observation and modeling of remarkable temperature scan rate effects on the thermal hysteresis in a spin-crossover single crystal, The Journal of Physical Chemistry C, 121 (2017) 11700-11708.
[158] A. Hauser, C. Enachescu, M.L. Daku, A. Vargas, N. Amstutz, Low-temperature lifetimes of metastable high-spin states in spin-crossover and in low-spin iron (II) compounds: The rule and exceptions to the rule, Coordination Chemistry Reviews, 250 (2006) 1642-1652.
[159] D. Hamelberg, J. Mongan, J.A. McCammon, Accelerated molecular dynamics: a promising and efficient simulation method for biomolecules, The Journal of Chemical Physics, 120 (2004) 11919-11929.
[160] S. Takada, Coarse-grained molecular simulations of large biomolecules, Current Opinion in Structural Biology, 22 (2012) 130-137.
[161] L. Stoleriu, A. Stancu, P. Chakraborty, A. Hauser, C. Enachescu, Analysis of first order reversal curves in the thermal hysteresis of spin-crossover nanoparticles within the mechanoelastic model, Journal of Applied Physics, 117 (2015).
[162] Y. Singh, H. Oubouchou, M. Nishino, S. Miyashita, K. Boukheddaden, Elastic-frustration-driven unusual magnetoelastic properties in a switchable core-shell spin-crossover nanostructure, Physical Review B, 101 (2020) 054105.
[163] C. Enachescu, R. Tanasa, A. Stancu, A. Tissot, J. Laisney, M.-L. Boillot, Matrix-assisted relaxation in Fe (phen) 2 (NCS) 2 spin-crossover microparticles, experimental and theoretical investigations, Applied Physics Letters, 109 (2016) 031908.
[164] A. Atitoaie, R. Tanasa, C. Enachescu, Size dependent thermal hysteresis in spin crossover nanoparticles reflected within a Monte Carlo based Ising-like model, Journal of Magnetism and Magnetic Materials, 324 (2012) 1596-1600.

[165] Y. Hu, M. Picher, M. Palluel, N. Daro, E. Freysz, L. Stoleriu, C. Enachescu, G. Chastanet, F. Banhart, Laser-Driven Transient Phase Oscillations in Individual Spin Crossover Particles, Small, DOI (2023) 2303701.
[166] Y. Zan, M. Piedrahita-Bello, S.E. Alavi, G. Molnár, B. Tondu, L. Salmon, A. Bousseksou, Soft Actuators Based on Spin-Crossover Particles Embedded in Thermoplastic Polyurethane, Advanced Intelligent Systems, DOI (2023) 2200432.
[167] S. Timoshenko, Analysis of bi-metal thermostats, Journal of the Optical Society of America, 11 (1925) 233-255.
[168] K. Boukheddaden, J. Linares, H. Spiering, F. Varret, One-dimensional Ising-like systems: An analytical investigation of the static and dynamic properties, applied to spin-crossover relaxation, The European Physical Journal B, 15 (2000) 317-326.
[169] K. Boukheddaden, I. Shteto, B. Hôo, F. Varret, Dynamical model for spin-crossover solids. I. Relaxation effects in the mean-field approach, Physical Review B, 62 (2000) 14796.
[170] I. Shteto, K. Boukheddaden, F. Varret, Metastable states of an Ising-like thermally bistable system, Physical Review E, 60 (1999) 5139.
[171] H. Zhang, M. Mendelev, D. Srolovitz, Computer simulation of the elastically driven migration of a flat grain boundary, Acta Materialia, 52 (2004) 2569-2576.
[172] S. Bhattacharyya, T.W. Heo, K. Chang, L.-Q. Chen, A phase-field model of stress effect on grain boundary migration, Modelling and Simulation in Materials Science and Engineering, 19 (2011) 035002.
[173] M.A. Halcrow, Spin-crossover materials: properties and applications, John Wiley & Sons2013.
[174] Q. Jiang, J. Li, M. Zhao, Thermodynamic consideration on solid transition of CdSe nanocrystals induced by pressure, The Journal of Physical Chemistry B, 107 (2003) 13769-13771.
[175] C. Yang, S. Li, J. Armellin, Size and temperature dependence of phase stability in nanocrystalline pentacene thin films, The Journal of Physical Chemistry C, 111 (2007) 17512-17515.
[176] S. Sood, P. Gouma, Polymorphic phase transitions in nanocrystalline binary metal oxides, Journal of the American Ceramic Society, 96 (2013) 351-354.
[177] J. Eshelby, The continuum theory of lattice defects, Solid state physics, Elsevier1956, pp. 79-144.

[178] J. Weissmüller, J.W. Cahn, Mean stresses in microstructures due to interface stresses: A generalization of a capillary equation for solids, Acta Materialia, 45 (1997) 1899-1906.
[179] R. Shuttleworth, The surface tension of solids, Proceedings of the Physical Society. Section A, 63 (1950) 444.
[180] F.H. Streitz, R.C. Cammarata, K. Sieradzki, Surface-stress effects on elastic properties. I. Thin metal films, Physical Review B, 49 (1994) 10699.
[181] P. Gütlich, A.B. Gaspar, V. Ksenofontov, Y. Garcia, Pressure effect studies in molecular magnetism, Journal of Physics: Condensed Matter, 16 (2004) S1087.
[182] D. Papanikolaou, W. Kosaka, S. Margadonna, H. Kagi, S.-i. Ohkoshi, K. Prassides, Piezomagnetic behavior of the spin crossover prussian blue analogue CsFe [Cr (CN) 6], The Journal of Physical Chemistry C, 111 (2007) 8086-8091.
[183] A.B. Gaspar, G. Molnár, A. Rotaru, H.J. Shepherd, Pressure effect investigations on spin-crossover coordination compounds, Comptes Rendus Chimie, 21 (2018) 1095-1120.
[184] R. Li, G. Levchenko, F.J. Valverde-Muñoz, A.B. Gaspar, V.V. Ivashko, Q. Li, B. Liu, M. Yuan, H. Fylymonov, J.A. Real, Pressure tunable electronic bistability in Fe (II) hofmann-like two-dimensional coordination polymer [Fe (fpz) 2Pt (CN) 4]: A comprehensive experimental and theoretical study, Inorganic Chemistry, 60 (2021) 16016-16028.
[185] R. Li, G. Levchenko, F.J. Valverde-Muñoz, A.B. Gaspar, V.V. Ivashko, Q. Li, W. Xu, H. Fylymonov, B. Liu, J.A. Real, The joint effect of elasticity, interaction energy and entropy on behavior of pressure-and temperature-induced electronic bistability in a family of two-dimensional Hofman-like coordination polymers, Journal of Materials Chemistry C, 10 (2022) 11388-11400.
[186] A. Rotaru, J. Linares, F. Varret, E. Codjovi, A. Slimani, R. Tanasa, C. Enachescu, A. Stancu, J. Haasnoot, Pressure effect investigated with first-order reversal-curve method on the spin-transition compounds [Fe x Zn 1− x (btr) 2 (NCS) 2]· H 2 O (x= 0. 6, 1), Physical Review B, 83 (2011) 224107.
[187] G. Félix, W. Nicolazzi, M. Mikolasek, G. Molnár, A. Bousseksou, Non-extensivity of thermodynamics at the nanoscale in molecular spin crossover materials: a balance between surface and volume, Physical Chemistry Chemical Physics, 16 (2014) 7358-7367.
[188] D.K. Owens, R. Wendt, Estimation of the surface free energy of polymers, Journal of Applied Polymer Science, 13 (1969) 1741-1747.

[189] O. Shalev, S. Biswas, Y. Yang, T. Eddir, O. Ahanotu, W. Lu, R. Clarke, M. Shtein, Growth and modelling of spherical crystalline morphologies of molecular materials, Nature Communications, 5 (2014) 5204.
[190] A. Slimani, F. Varret, K. Boukheddaden, D. Garrot, H. Oubouchou, S. Kaizaki, Velocity of the high-spin low-spin interface inside the thermal hysteresis loop of a spin-crossover crystal, via photothermal control of the interface motion, Physical Review Letters, 110 (2013) 087208.

Annexes

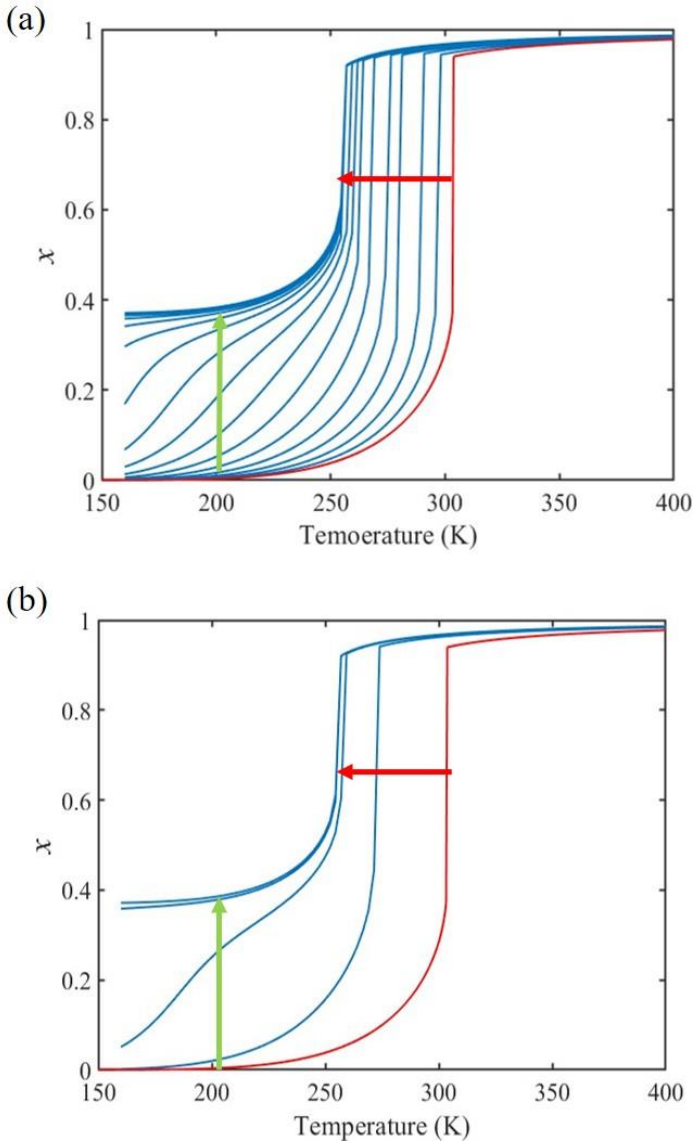

FIG. A.1. Calculated temperature dependence of the HS fraction (heating mode) for a 5 nm spherical particle of [Fe(pyrazine)][Ni(CN)$_4$] in the case of (a) $\Gamma_\gamma = \frac{\gamma_\downarrow}{\gamma_\uparrow} = 1.4$ and (b) $\Gamma_\gamma = \frac{\gamma_\downarrow}{\gamma_\uparrow} = 2.4$ for different values of $\gamma_\uparrow$ varying from 10 to 190 mJ/m^2 with an increment of 10 mJ/m^2. The red curve represents the bulk material. Green and red arrows are guides for the eye to follow the evolution the residual HS fraction and the equilibrium temperature, respectively, with the increase of $\gamma_\uparrow$.

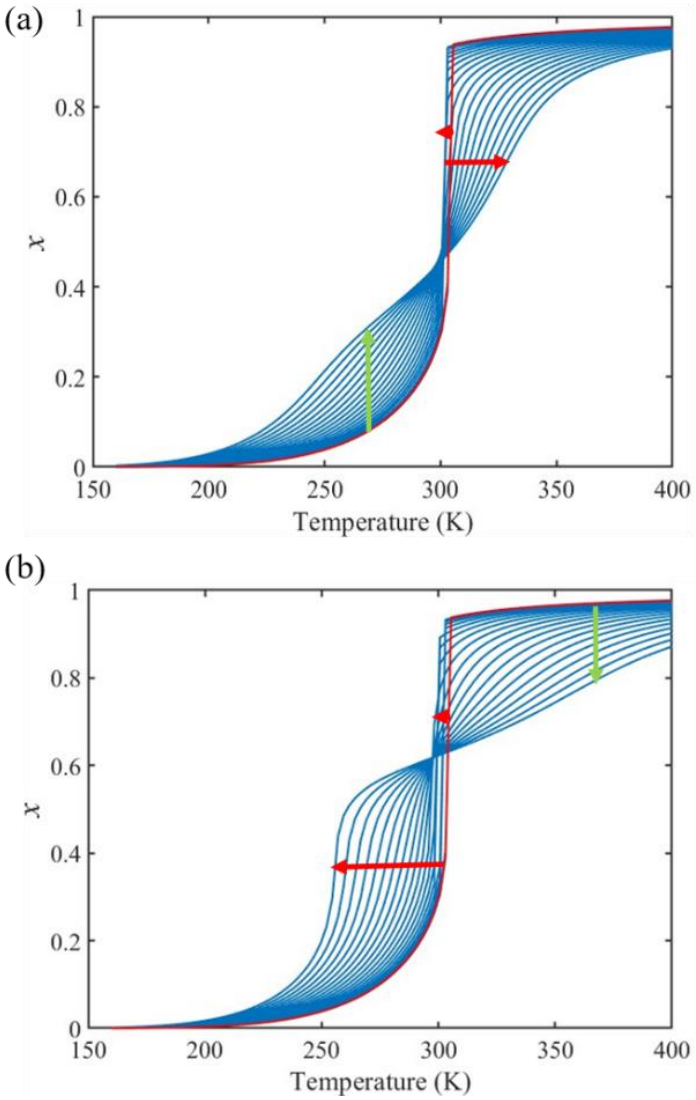

FIG. A.2. Calculated temperature dependence of the HS fraction (heating mode) for a 5 nm spherical particle of [Fe(pyrazine)][Ni(CN)$_4$] in the case of $\alpha = \frac{\sigma_\downarrow}{\sigma_\uparrow} = 1.4$ for different values of $\sigma_\uparrow$ ranging from (a) 10 to -410 mJ/m^2 and (b) -410 to -10 mJ/m^2 with an increment of 20 mJ/m^2. The red curve represents the bulk material. Green and red arrows are guides for the eye to follow the evolution the residual LS fraction and the equilibrium temperature, respectively, with the increase of $\sigma_\uparrow$.

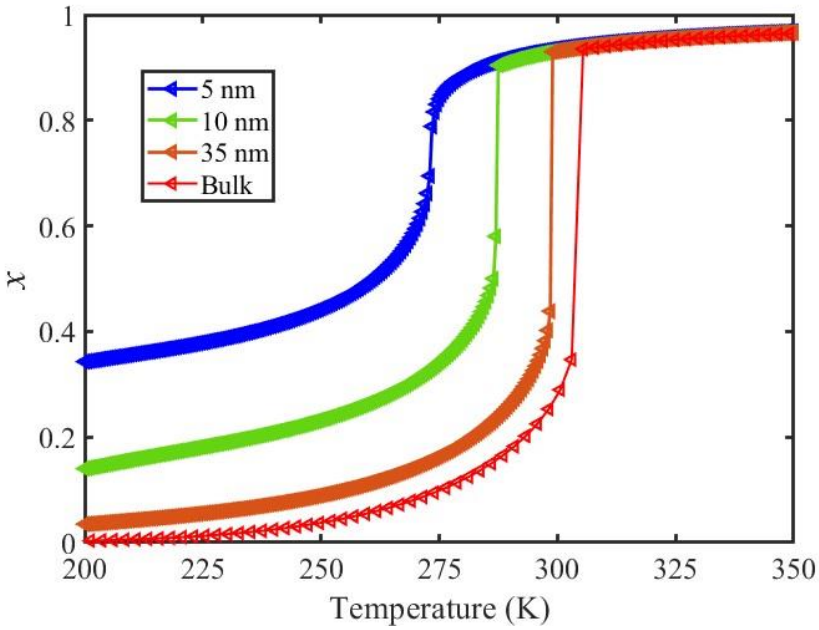

FIG. A.3. Calculated temperature dependence of total HS fraction for different particle radii of the compound [Fe(pyrazine)][Ni(CN)$_4$].

Résumé de la thèse en français

Les composés à transition de spin (TS) sont des complexes inorganiques, qui peuvent commuter de manière réversible entre les états dits haut spin (HS) et bas spin (BS) du cation métallique central. Les propriétés exceptionnelles des nanomatériaux à TS les rendent très intéressants pour plusieurs applications technologiques. En effet, la commutation moléculaire de ces matériaux s'accompagne d'un changement radical de nombreuses propriétés physiques, notamment les propriétés magnétiques, optiques, électriques et mécaniques, offrant des possibilités d'applications dans des dispositifs électroniques, spintroniques, photoniques et mécaniques. Motivés par ces propriétés séduisantes, des efforts considérables ont été consacrés au cours des deux dernières décennies à la fabrication de matériaux à TS à des échelles de taille réduite (films minces, nanoparticules, nanomotifs, etc.) afin d'intégrer ces derniers dans des dispositifs fonctionnels. Cependant, comme dans de nombreux matériaux affichant une allotropie, un polymorphisme ou pouvant changer d'état, la stabilité des phases et la cinétique de transformation dépendent de la taille. Notamment, il a été montré que dans la plupart des cas, les nano-objets à TS présentent une diminution de la température d'équilibre, l'apparition d'une transition de spin incomplète ainsi que d'une perte de l'effet mémoire (disparition du cycle d'hystérésis) dans le cas des matériaux dit coopératifs. Pour expliquer ces observations expérimentales, il a été proposé que les effets de surface et d'interface jouent un rôle de plus en plus important dans le phénomène de changement d'état de spin à l'échelle nanométrique. Dans ce contexte, l'objectif principal de cette thèse est d'essayer de comprendre d'un point de vue théorique les effets de surfaces et d'interfaces sur les propriétés à TS à l'échelle nanométrique. Pour cela, des études couplant des simulations de dynamique moléculaire (MD) et des méthodes de thermodynamique ont été menées. En plus d'être d'un intérêt fondamental, la compréhension du phénomène de bistabilité à l'échelle du nanomètre est une étape essentielle vers la conception rationnelle et l'intégration de ces nano-objets commutables dans dispositifs pour des applications sociétales. Le manuscrit est organisé de la manière suivante :

Le **chapitre I** est consacré à l'introduction du phénomène de croisement de spin (spin crossover en Anglais) à l'échelle de la molécule. Tout d'abord, un bref aperçu des aspects théoriques et thermodynamiques du phénomène basé sur la théorie du champ de ligands est exposé. Ensuite, les différents comportements et phénomènes observés dans les matériaux à TS massifs ainsi que les modèles théoriques pertinents pour les modéliser sont passés en revue de

manière non-exhaustive. Enfin, nous présentons les différentes études qui ont été menés concernant la synthèse, la conception et l'élaboration de nano-objets à TD et les observations expérimentales concernant les effets de taille sur les propriétés de la transition de spin. Dans la dernière section de ce chapitre, diverses hypothèses sur l'origine des effets de la réduction de la taille sont discutées.

Dans le **chapitre II**, nous décrivons la construction de nouveaux champs de force pour les simulations MD tout-atome appliquées aux matériaux à TS. Ce chapitre débute par la construction des champs de force du composé [Fe(pyrazine)][Ni(CN)4] dans les états BS et HS. La méthode d'extraction des paramètres de champ de force à partir des données expérimentales est discutée en détail. Ensuite, nous introduisons le « double puits » de potentiel (« double-well » potential en Anglais) pour modifier ces champs de force afin de simuler le phénomène de la transition de spin lui-même. Enfin, la validation des champs de force est faite en comparant les résultats obtenus à partir de la simulation MD aux données expérimentales (mesures des propriétés vibrationnelles et de commutation moléculaire thermo-induite.)

Dans le **chapitre III**, basé sur le champ de force nouvellement construit, des simulations MD tout-atome sont réalisées pour étudier le processus de relaxation HS à BS et les déformations mécaniques dans une bicouche d'épaisseur nanométrique, constitué d'une couche contenant un composé à transition de spin et d'une autre couche « inerte » d'un point de vue de la transition de spin. Tout d'abord, les effets d'interface sur la nucléation et la propagation des domaines BS sont étudiés en explorant la dynamique spatio-temporelle au cours de la transformation de phase. Ensuite, nous analysons comment l'interface et les contraintes externes affectent le comportement de la relaxation de l'état métastable HS vers l'état le plus stable BS. En particulier, les propriétés de déflexion de la bicouche induite par l'interface HS/BS sont étudiées et comparées à un modèle thermomécanique classique, i.e. un modèle basé sur une approche issue de la mécanique des milieux continus. Enfin, la vitesse de propagation de l'interface HS/BS durant le processus de relaxation est discutée en utilisant la dynamique en temps réel fournie par les simulations MD.

Le **chapitre IV** présente les effets de l'énergie de surface et de la contrainte de surface sur le comportement des matériaux à TS à l'échelle nanométrique. A cet effet, un modèle nano-thermodynamique adapté à la description du phénomène SCO à l'échelle nanométrique a été développé. Il prend en compte les différentes contributions (énergie de surface et contrainte de surface) aux effets de surface sur le comportement de commutation des nano-objets à TS. Ce

modèle permet de « concevoir » théoriquement des objets pour lesquels la transition de spin serait facilement ajustable. Cette étude théorique combine la nano-thermodynamique et les simulations MD.

Le manuscrit se termine par les conclusions générales ainsi que quelques perspectives pour les travaux futurs.

Chapitre I : Introduction

Le phénomène de transition de spin peut se produire dans des complexes octaédriques avec des ions métalliques appartenant à la première série des métaux de transition et plus particulièrement ayant des configurations électroniques $3d^4$ à $3d^7$, comme dans les composés de Fe(III), Fe(II), Co(II) et moins fréquemment dans Co (III), Cr (II), Mn (II) et Mn (III). Cependant, la majorité des complexes étudiés possèdent un ion central de fer (II).

La théorie du champ cristallin peut être employée afin de comprendre l'origine du phénomène de la transition de spin. L'exemple le plus souvent utilisé est celui de l'ion Fe(II) libre dont les niveaux d'énergie électronique de ses cinq orbitales 3d sont dégénérés. L'ion Fe(II) est placé dans un champ électrostatique possédant une géométrie octaédrique parfaite, formé par six ligands chargés négativement. Les électrons du centre métallique subissent des forces répulsives de la part des ligands. La conséquence est une levée de dégénérescence partielle des niveaux d'énergie en un niveau de basse énergie t_{2g} composé des trois orbitales non-liantes dégénérées et un niveau de plus haute énergie eg composé des deux orbitales anti-liantes dégénérées (**FIG. 1.1**). L'écart d'énergie entre ces deux niveaux est déterminé par la force du champ de ligands (10Dq). Au sein de la molécule, deux effets principaux entrent en compétition. D'une part, les électrons tendent à occuper les orbitales d selon la règle de Hund en fonction de l'énergie d'appariement des électrons Π. D'autre part, ils tendent à remplir le niveau t_{2g}, de plus basse énergie. Cette compétition a pour conséquence l'existence possible de deux états fondamentaux : l'état Bas-Spin (BS) diamagnétique $t_{2g}^6e_g^0$ avec un spin S = 0 et l'état haut spin (HS) $t_{2g}^4e_g^2$ paramagnétique S = 2.

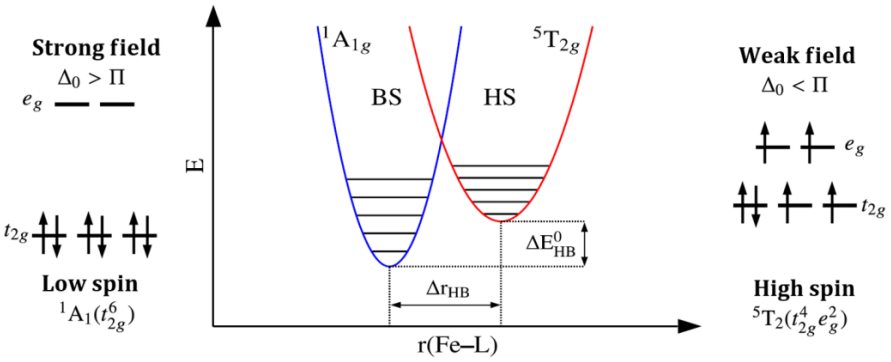

FIG. 1.1: Schéma des configurations électroniques pour les deux états fondamentaux possibles pour le fer (II) dans un complexe octaédrique et représentation schématique simplifiée du diagramme de configuration des deux états de spin moléculaire (HS et BS) dans un complexe SCO.

La taille des matériaux SCO peut être diminuée dans une direction (films minces) ou dans les trois axes (nanoparticules). La possibilité de changer l'état de spin sous divers stimuli externes ainsi que la présence éventuelle d'effets mémoire font des complexes SCO d'excellents candidats pour leur intégration dans de nouveaux dispositifs nano-optiques, nano-électriques et/ou nano-mécaniques. Cependant, il a été montré que dans la plupart des cas les nano-objets SCO présentent une diminution de la température d'équilibre, l'apparition d'une transition de spin incomplète ainsi que la perte de l'effet mémoire (disparition du cycle d'hystérésis) dans le cas des matériaux dits fortement coopératifs (voir **FIG. 1.2**).

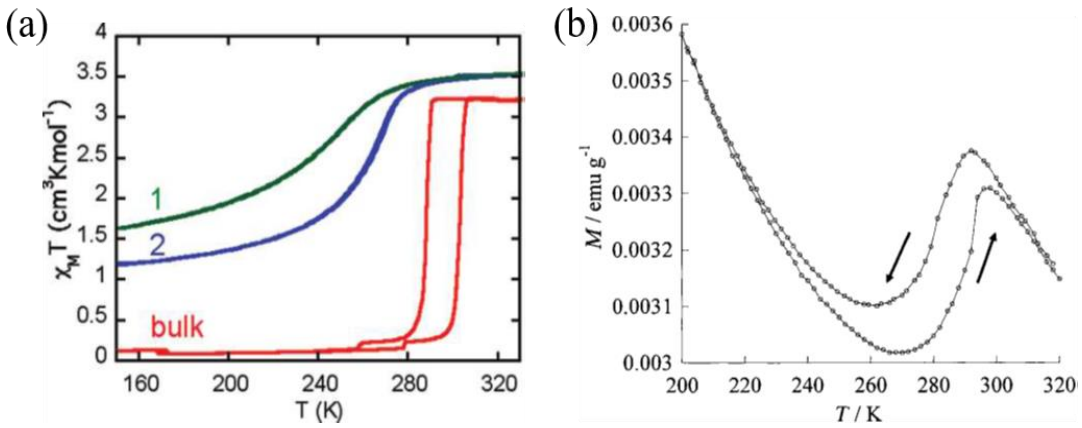

FIG. 1.2: (a) Propriétés magnétiques de nanocristaux de [Fe(pyrazine)][$Pt(CN)_4$] de tailles 15×15×5 et 8×8×3 nm^3 comparées au matériau massif. (b) Dépendance avec la température de l'aimantation de nanoparticules [Fe(pyrazine)][$Ni(CN)_4$] de 3-4 nm intégrées dans une matrice de chitosane (bio-polymère).

Il semble que les effets de surface et d'interface jouent un rôle de plus en plus important sur les propriétés de commutation des matériaux à transition, au fur et à mesure que la taille de ces objets bistables est réduite. En effet, un certain nombre de molécules restent « figé » dans l'état HS à basse température ; on observe que la fraction HS associée augmente avec l'augmentation du rapport surface sur volume suggérant la présence de molécules inactives en surface. L'origine de molécules inactives peut être attribuée à des réactions chimiques de surface, à un désordre structural et/ou à l'altération du ligand par le milieu extérieur. D'un point de vue théorique, cette hypothèse a d'abord été considérée de manière ad hoc en ajoutant des conditions aux limites spécifiques (par exemple, des molécules de surface fixées dans l'état HS ou en affaiblissant le champ de ligand à la surface). L'étude des effets de surface dans des nanoparticules carrées à l'aide de modèles de type Ising avec de telles conditions aux limites spécifiques (molécules de surface fixées dans l'état HS) a démontré que la surface HS exerce une « pression négative » sur le cœur de la nanoparticule. Ces effets de pression peuvent être appréhendés au travers d'une modification locale du champ de ligand effectif. Ces effets conduisent à une diminution de la température d'équilibre avec la réduction de la taille. Un comportement algébrique de la température de transition avec la taille est alors constaté (**FIG. 1.3**).

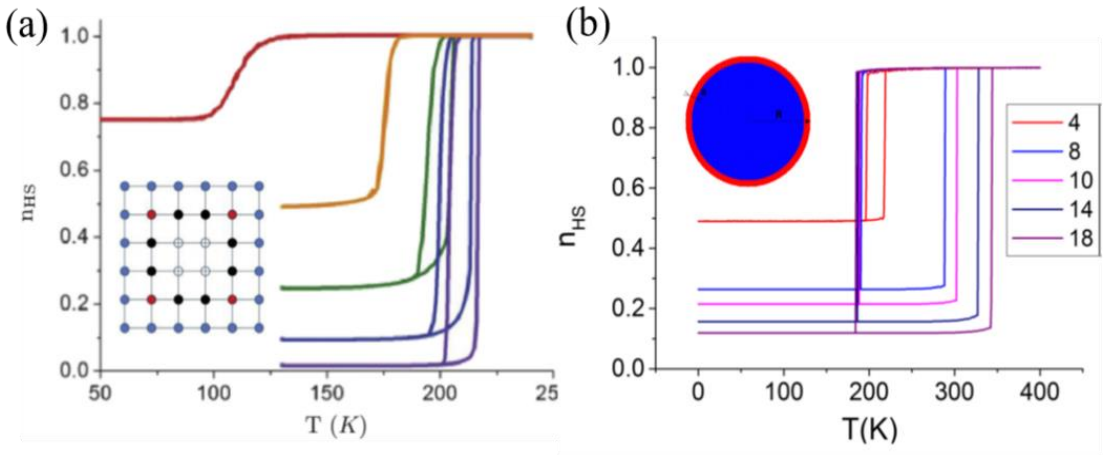

FIG. 1.3: Dépendance en température de la fraction HS de (a) nanoparticules carrées de différentes tailles possédant des conditions aux limites fixes (molécules HS fixées à la surface), simulées à l'aide d'un modèle de type Ising. De gauche à droite, L = 4, 7, 10, 40, 200. (b) Transitions de spin dans de nanoparticules circulaires possédant différents rayons avec l'état HS bloqué en surface, modélisées par le modèle dit électro-élastique.

Comprendre les propriétés dynamiques du réseau des nanomatériaux SCO est également d'une importance primordiale afin de concevoir des nanomatériaux avec des propriétés de commutation d'état de spin bien contrôlées. En effet, le phénomène de transition de spin donne lieu à une modification de la densité d'états vibrationnels (vDOS) avec des conséquences importantes sur les différentes propriétés thermodynamiques et mécaniques, telles que l'entropie vibrationnelle, l'enthalpie vibrationnelle, la constante élastique et la rigidité du réseau (**FIG. 1.4**). En particulier, la variation d'entropie vibrationnelle entre les états HS et BS peut être considérée comme la principale force motrice de la transition de spin induite thermiquement, tandis que la rigidité du réseau joue un rôle crucial dans les phénomènes coopératifs.

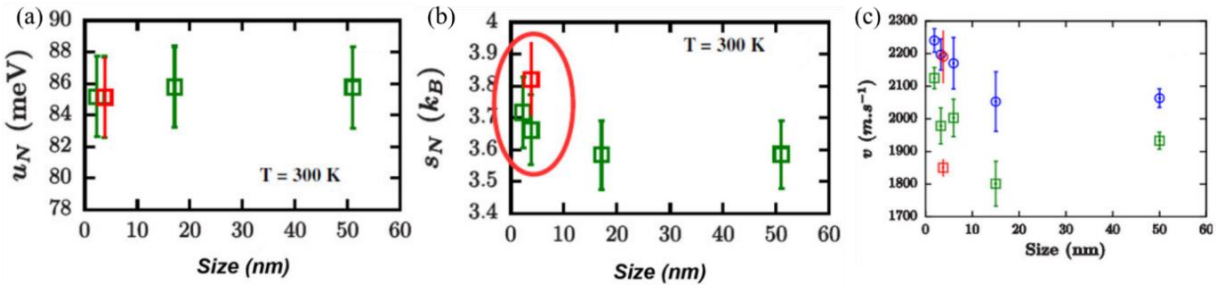

FIG. 1.4. (a) Énergie vibrationnelle, (b) entropie vibrationnelle et (c) Vitesse du son de Debye en fonction de la taille des particules pour le composé [^{57}Fe(pyrazine)Ni(CN)$_4$]. Les cercles et les carrés représentent respectivement les états BS et HS.

Chapitre II : Construction des champs de force pour la simulation de dynamique moléculaire tout atome

Dans ce chapitre, un nouveau champ de force de [Fe(pyrazine)][Ni(CN)$_4$] pour la simulation de dynamique moléculaire tout-atome a été construit à partir de données spectroscopiques Raman et NIS dans les états BS et HS. Comme le montre la **FIG. 2.1** (a), tous les atomes sont liés par des potentiels harmoniques de paires avec des constantes de force différentes. Afin de stabiliser la structure, comme indiqué à la **FIG. 2.1** (b) et (c), des potentiels angulaires harmoniques à 3 corps (angles 1, 2 … 7) sont introduits dans le champ de force. De plus, nous introduisons également des potentiels impropres à 4 corps (I et II sur la **FIG. 2.1** (b) et (c)) et un potentiel dièdre (III sur la **FIG. 2.1** (c)) afin de maintenir les atomes dans le même plan.

L'énergie potentielle totale s'exprime de la manière suivante :

$$E_{potential} = \sum_{bonds} \frac{1}{2} K_b[(b - b_0)^2 - (b_c - b_0)^2] + \sum_{angles} \frac{1}{2} K_\theta (\theta - \theta_o)^2 + \sum_{impropers} \frac{1}{2} K_\varphi (\varphi - \varphi_o)^2 + \sum_{dihedrals} \frac{1}{2} K_\emptyset (1 - \cos \emptyset) + \epsilon_{ij} \left[\left(\frac{\sigma_{ij}}{r_{ij}} \right)^{12} - 2 \left(\frac{\sigma_{ij}}{r_{ij}} \right)^{6} \right], \quad (2.1)$$

où K_b, K_θ, K_φ et $K_\emptyset$ représentent les constantes de force du potentiel de liaison à 2 corps, du potentiel angulaire à 3 corps, du potentiel de torsion dihédrale impropre à 4 corps et du potentiel de torsion dihédrale propre à 4 corps, respectivement. b, θ, φ et $\emptyset$ sont respectivement la longueur de liaison, l'angle, l'angle impropre et l'angle dièdre, et l'indice « o » fait référence à leur valeur d'équilibre. Pour décrire les interactions non covalentes de type Van Der Walls, un potentiel de Lennard-Jones 12-6 est sélectionné dans ce travail. Les constantes de force des potentielles de paires peuvent être obtenues à partir des données de spectroscopie Raman du composée [Fe(pyrazine)][Ni(CN)$_4$]. En revanche, les constantes de force des potentiels à 3 et 4 corps sont ajustées pour reproduire au mieux les courbes vDOS partielles obtenues expérimentalement par diffusion inélastique nucléaire (NIS).

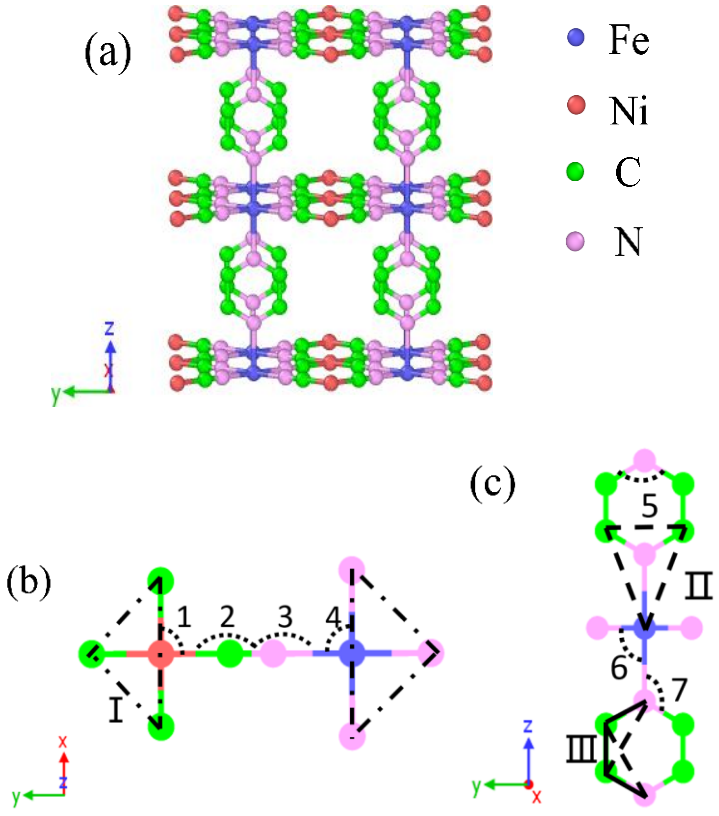

FIG : 2.1: (a) Représentation schématique de la structure [Fe(pyrazine)][Ni(CN)$_4$]. (b-c) Représentation schématique du champ de force avec les différentes interactions considérées dans ce travail. Les lignes entre deux atomes représentent les liaisons chimiques.

Afin d'inclure le couplage vibronique dans la structure [Fe(pyrazine)][Ni(CN)$_4$], le potentiel harmonique Fe-N utilisée dans les travaux précédents est remplacée par un potentiel Double-Well (**FIG. 2.2**), afin de prendre en compte le couplage vibronique dans la structure [Fe(pyrazine)][Ni(CN)$_4$], l'interaction harmonique Fe-N utilisée dans les travaux précédents est remplacée donc par un double puits de potentiel :

$$E_{bond}^{Double-Well} = \frac{A}{2}\{d + b(c - (r - r_{LS}))^2 + a(r - r_{LS})^2$$

$$-\sqrt{4J^2 + [d + b(c - (r - r_{LS}))^2 + a(r - r_{LS})^2]^2}\}, \qquad (2.2)$$

où r_{LS} représente la longueur de la liaison Fe-N à l'équilibre. Les paramètres *a* et *b* sont respectivement associés aux constantes de force BS et HS. La longueur de liaison et les différences d'énergie entre les états HS et BS sont caractérisées par les paramètres *c* et *d*, respectivement. *A* est un coefficient qui donne l'échelle d'énergie du couplage vibronique. *J* est l'élément hors diagonale, résultant du couplage spin-orbite d'ordre supérieur, qui mélange les potentiels harmoniques BS et HS.

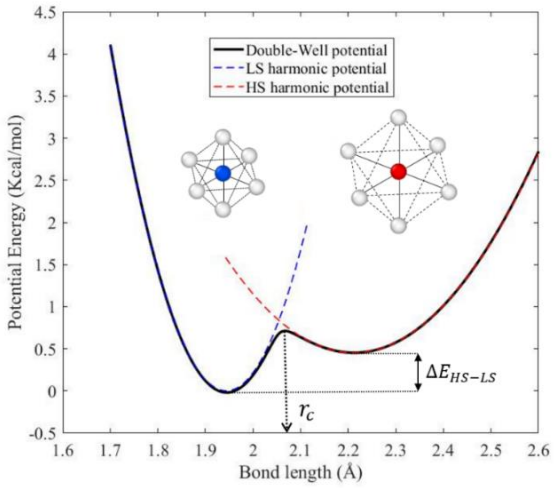

FIG. 2.2: Représentation du double puits de potentiel (ligne continue noire), des potentiels harmoniques BS (ligne pointillée bleue) et HS (ligne pointillée rouge) en fonction de la longueur de la liaison Fe-N. Les structures octaédriques Fe-N_6 dans l'état BS et l'état HS pour le complexe [Fe(pyrazine)] [Ni(CN)$_4$] sont également représentées.

Un potentiel intermoléculaire à deux corps dépendant de l'état de spin est ensuite introduit pour modéliser la barrière d'énergie élastique qui doit être surmontée pour modifier les distances

intermoléculaires (entre deux atomes de fer consécutifs) accompagnant la commutation d'état de spin. Ici, nous montrons que l'introduction de ce type de potentiel énergétique dépendant de l'état de spin, $E_{Cooperativity}$ donnée par l'Eq. 2.3, génère une barrière d'énergie élastique locale, dont l'effet compense la faiblesse des interactions intermoléculaires dans certaines directions cristallographiques.

$$E_{Cooperativity} = \frac{B}{2}\{b_0(c_0 - (R - R_{LS}))^2 + a_0(R - R_{LS})^2$$

$$-\sqrt{4J_0^2 + [b_0(c_0 - (R - R_{LS}))^2 + a_0(R - R_{LS})^2]^2}\}, \quad (2.3)$$

où R_{LS} est la distance intermoléculaire d'équilibre dans l'état BS, tandis que *B*, a_0, b_0 et c_0 sont des paramètres qui contrôlent la barrière d'énergie entre les phases HS et BS et la concavité du double puits de potentiel, respectivement. J_0 est un élément hors diagonale.

Les vDOS partiels de Fe dans les états BS et HS sont calculés par des simulations de dynamique moléculaire. Le vDOS partiel optimisé du Fe est comparé aux spectres vDOS expérimentaux. Sur la **FIG. 2.3** (b), plusieurs pics, identifiés comme des modes vibrationnels d'élongation des liaisons Fe-ligand peuvent être observés dans la partie optique des spectres vDOS, au-dessus d'env. 20 meV. Ils sont également reconnaissables dans le vDOS expérimental. Notamment, un pic intense et large est observé pour la structure HS, situé autour de 35 meV, tandis que plusieurs pics apparaissent dans l'état BS à 28, 33, 40,5, 42, 54 et 60 meV. Bien que les valeurs de fréquence vibrationnelle ne soient pas précises, elles sont proches de l'observation expérimentale (< ± 5 meV).

L'entropie vibrationnelle, la constante de force moyenne et l'énergie interne vibrationnelle ont été extraites du vDOS pour les deux états de spin. Comme on peut le voir dans **TABLE.2.1**, ces valeurs sont toutes en bon accord avec les observations expérimentales du NIS. Pour caractériser la rigidité du réseau, la vitesse du son Debye a été extraite de la partie basse fréquence (modes acoustiques) du vDOS. La diminution de v_D lors de la transition BS vers HS indique que la phase HS est plus douce que la phase BS, comme on peut s'y attendre. On note la bonne concordance avec les observations expérimentales (**TABLE.2.1**) donnant confiance dans la paramétrisation du champ de force par rapport à la région critique des modes acoustiques.

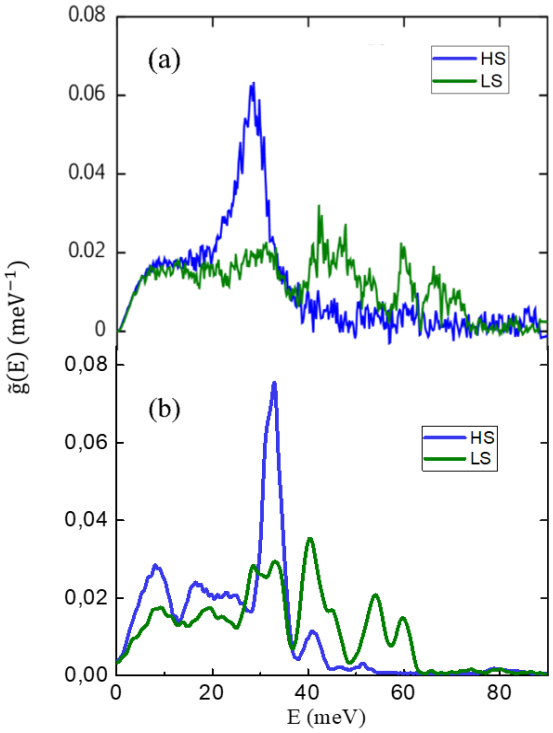

FIG. 2.3: Spectres (vDOS) partiels du matériau massif dans l'état HS et BS obtenus (a) à partir d'expériences NIS et (b) à partir de simulations MD réalisées dans ce travail.

TABLE. 2.1: Comparaison de la vitesse du son Debye (v_D), de la constante de force moyenne ($\langle C \rangle$), de l'entropie vibrationnelle (s) et de l'énergie interne vibrationnelle (u) des formes BS et HS obtenues dans la présente étude et à partir d'expériences NIS.

	BS		HS	
	This work	NIS	This work	NIS
$v_D(m/s)$	2083	2063 ± 27	1820	1933 ± 20
$\langle C \rangle(N/m)$	292	331 ± 10	173	204 ± 10
s (k_B)	0.99	0.90	3.92	3.57
u (meV)	53.3	56.0	84.8	85.8

En nous appuyant sur la simulation MD tout-atome, nous avons ensuite étudié la transition de spin induite thermiquement du complexe [Fe(pyrazine)][Ni(CN)$_4$]. **FIG. 2.4** (a) et (b) montrent la dépendance en température de la fraction HS (n_{HS}) et du volume atomique Fe, respectivement, sur un cycle de chauffage/refroidissement, pour des valeurs sélectionnées de la

barrière d'énergie élastique donnée par le paramètre *B*. Lorsque *B* = 0 (barrière d'énergie nulle), la transformation de phase s'avère être graduelle et un recouvrement parfait est observé pour les courbes thermiques de transition de spin dans les modes chauffage et refroidissement (**FIG. 2.4** (a), carrés noirs), comme on peut s'y attendre pour un système faiblement coopératif. De plus, la température de transition T_{eq}, à laquelle les fractions HS et BS sont égales (n_{HS} = 50 %), s'avère être $T_{eq}^{MD} \approx 280$ K. De manière remarquable, en augmentant la valeur de *B* (c'est-à-dire la force des interactions), on observe l'apparition d'une transition de plus en plus abrupte et de l'ouverture d'une boucle d'hystérésis thermique, caractéristique d'un système présentant une transition de phase du premier ordre (**FIG. 2.4** (a) et (b)).

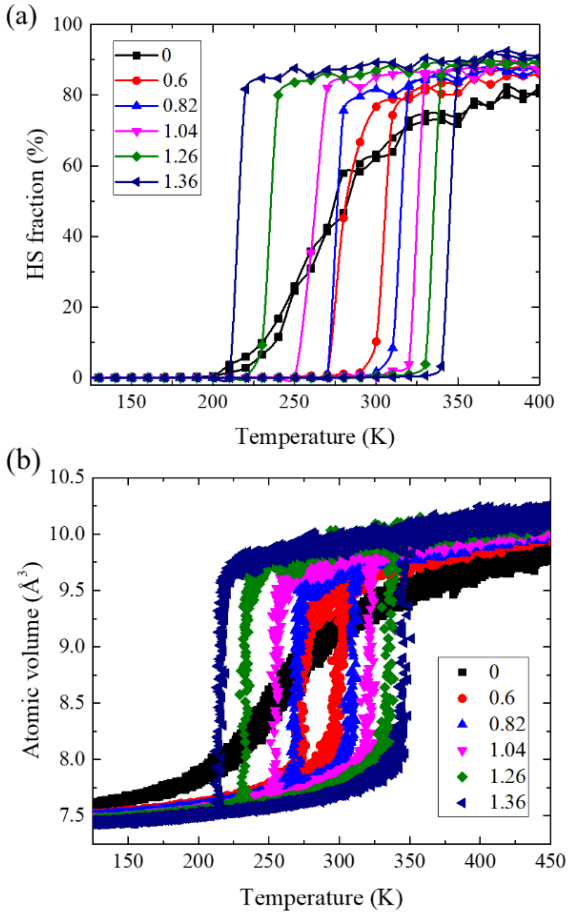

FIG. 2.4: Dépendance en température de (a) la fraction HS et (b) du volume atomique de Fe pour les différentes valeurs de *B*.

Chapitre III: étude numérique de la flexion et des aspects spatio-temporels d'un système bimorphe à transition de spin

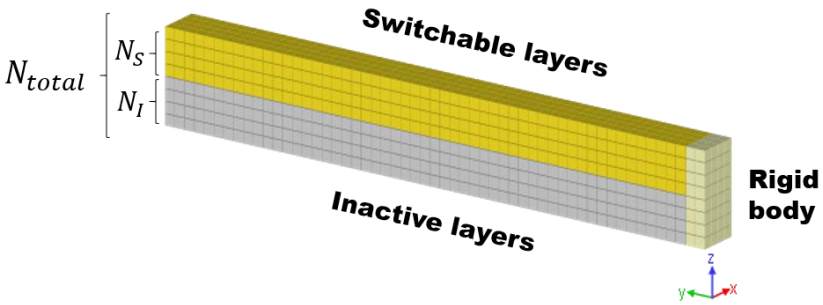

FIG. 3.1: Représentation schématique d'un système bimorphe de type levier, composé de 4 × 55 × N_{tot} mailles élémentaires (respectivement le long des directions *x*, *y* et *z*) du composé à TS [Fe (pyrazine)] [Ni(CN)$_4$].

Dans ce chapitre, nous utilisons la méthode MD tout-atome pour étudier comment l'interface BS/HS affecte la dynamique spatio-temporelle de la commutation de l'état de spin dans un actionneur bimorphe de taille nanométrique constitué de [Fe(pyrazine)][Ni(CN)$_4$] complexe et les performances d'actionnement associées à ce dispositif. Comme le montre la **Fig. 3.1**, la structure étudiée est constituée d'un parallélépipède composé de 4 × 55 × N_{tot} ($6 \leq N_{tot} \leq 12$) mailles élémentaires (suivant respectivement les directions *x*, *y* et *z*) du complexe [Fe(pyrazine)][Ni(CN)$_4$]. Les systèmes sont ensuite relaxés à 100 K.

FIG. 3.2 (a) représente une sélection de configurations instantanées de la distribution spatiale locale de l'état de spin prise au cours du processus de relaxation dans le cas du système bimorphe (N_I = 4), composé de quatre couches actives (en haut) et de quatre autres inactives (en bas). L'extrémité gauche de l'actionneur est maintenue libre de se déplacer. Nous observons qu'un domaine BS apparaît dans le coin supérieur gauche du faisceau à $t \approx 32$ ps. Ce domaine BS induit une légère flexion de l'actionneur. Plus tard, à t = 67 ps, au fur et à mesure que le domaine BS grandit, une distorsion macroscopique plus importante du réseau (qui se traduit par une déflexion significative du dispositif) est observée et un deuxième domaine BS se forme au milieu du levier. Comme illustré sur la cartographie des contraintes locales illustrée à la **Fig. 3.2** (b), on peut rationaliser cette observation par le fait que la flexion du levier génère une contrainte de compression au sein de la partie active, qui se traduit par une déformation locale négative (indiquée par une flèche à t = 32 ps). Celle-ci favorise la nucléation de ce second domaine BS. Enfin, de t = 97 ps à t = 232 ps, les deux domaines BS formés coalescent et grandissent jusqu'à atteindre le bord rigide de l'actionneur. A l'état stationnaire (à t = 232 ps), nous observons que quelques sites SCO à l'interface entre les parties actives et inactives du

système restent bloqués à l'état HS, vraisemblablement parce qu'ils sont soumis à une contrainte de traction permanente exercée par la partie inactive (HS) du levier. En effet, comme le montre la **Fig. 3.2** (b), une observation détaillée de la cartographie des déformations locales dans l'état relaxé final (à t = 232 000 fs) montre que des gradients de déformation existent à la fois dans les couches active et inactive du levier. Il apparaît que l'amplitude de la déformation en compression diminue progressivement au sein de la partie active à l'approche de l'interface. De la même manière, la répartition des déformations dans la partie inactive de la structure passe d'une déformation en compression à une déformation en traction (du vert au rouge). Un tel gradient de déformation au sein de la structure est une conséquence évidente de la flexion du levier.

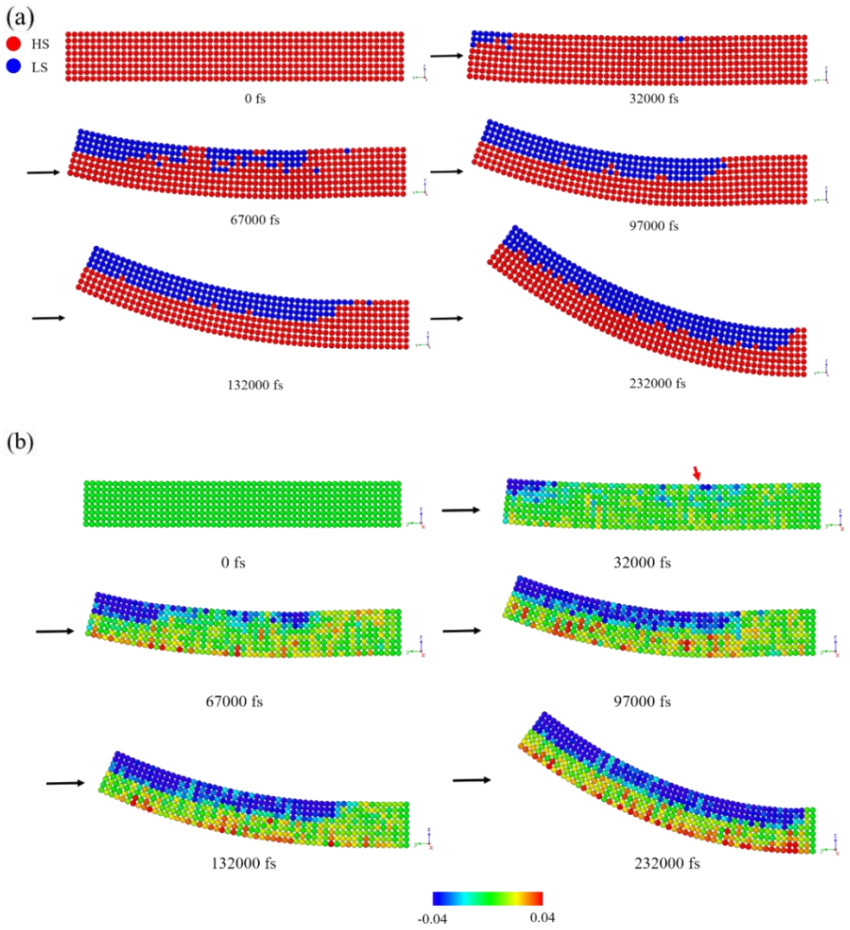

Fig. 3.2: Sélection de configurations instantanées montrant la distribution spatiale de (a) de l'état de spin et (b) de la déformation locale du réseau dans le levier bimorphe (N_I = 4), à différent instants au cours du processus de relaxation HS à BS à 100 K (pour B = 0,6). En (a), les cercles rouges et bleues représentent respectivement les sites HS et BS. En (b), l'échelle de couleurs passe du rouge (traction) au bleu (compression) en passant par les couleurs orange (tension initiale, nulle).

Pour étudier les performances d'actionnement du système bimorphe modélisé, nous nous concentrons sur la déflexion, qui est définie comme la distance entre les positions verticales instantanée et celles de l'extrémité libre du levier. **FIG. 3.3** (a) montre l'évolution temporelle de la déflexion dans l'actionneur bimorphe (N_{tot} = 8) associée au processus de relaxation HS-to-BS pour différentes épaisseurs de la partie inactive (NI allant de 1 à 7 couches). Pour chaque système simulé, des oscillations amorties de la pointe du levier sont observées avant d'atteindre un état mécanique stationnaire, définissant la position d'équilibre. Ce mouvement oscillatoire provient vraisemblablement du fait que la cinétique de commutation rapide de l'état de spin moléculaire produit initialement un « overshoot » de la déviation du faisceau, de sorte que le système atteint finalement un état d'équilibre mécanique en oscillant à sa fréquence de flexion naturelle.

Comme on pouvait s'y attendre, la déflexion d'équilibre dépend fortement du nombre de couches inactives N_I. En particulier, les courbes de la **Fig. 3.3** (b) montrent que la déflexion à l'équilibre présente un comportement non monotone en fonction de N_I et passe par un maximum ($\delta \approx 100$ Å) pour $N_I = 4$, c'est-à-dire lorsque les épaisseurs des régions actives et inactives sont égales. Il est important de noter que l'approche atomistique utilisée dans ce travail permet d'évaluer des quantités macroscopiques/mésoscopiques, telles que les déflexions mécaniques, qui peuvent également être déduites des modèles issu de la mécanique des milieux continus. Par comparaison avec le résultat de nos simulations MD, les déviations des différents systèmes étudiés extraites de la théorie d'Euler-Bernoulli, sont également représentées sur la **Fig. 3.3** (b). Semblable à nos simulations MD, la déflexion du levier bimorphe suit une courbe en forme de cloche en fonction de N_I, atteignant un maximum pour N_I = 4. Globalement, les valeurs de déflexion obtenues à partir des deux approches sont en bon accord dans la plage N_I = 3–5. Comme le montre la **FIG. 3.3** (b), pour des valeurs inférieures et supérieures de N_I, les résultats de ces deux méthodes montrent des écarts plus importants. Une telle différence peut probablement provenir du fait que les propriétés thermomécaniques effectives sont modifiées lorsque ces matériaux deviennent extrêmement minces.

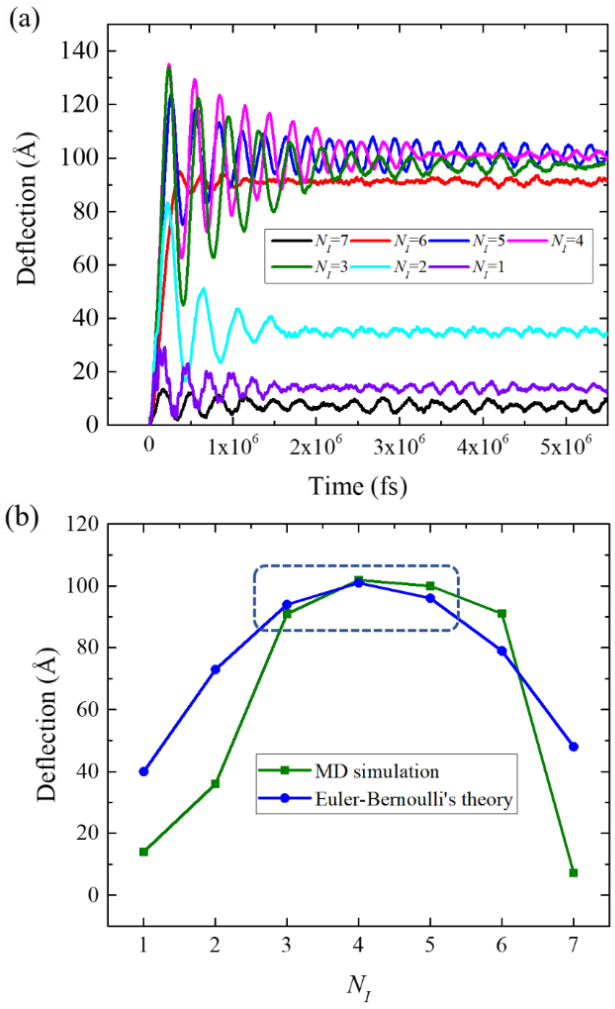

FIG. 3.3: (a) Évolution temporelle de la déflexion de l'actionneur bimorphe (N_{tot} = 8) au cours du processus de relaxation de l'état HS à l'état BS (à 100 K, B = 0,6) pour différentes épaisseurs de la partie inactive, N_I, allant de 1 à 7 couches. (b) Déflexion d'équilibre de l'actionneur bimorphe en fonction de N_I déduite des simulations MD (en vert) et de la théorie des poutres d'Euler-Bernoulli (en bleu).

Nous avons également étudié l'effet de la coopérativité sur l'évolution temporelle de la fraction HS et de la déviation du levier bimorphe. Dans ce but, nous avons étudié le cas $N_I = N_S = 4$, qui permet d'obtenir la plus grande déviation. L'évolution dans le temps de la déflexion δ du levier pendant le processus de relaxation HS à BS est tracée à la **Fig. 3.4** (a) pour différentes valeurs de B. La première observation est qu'une déviation identique ($\delta \approx 100$ Å) est obtenue à l'état d'équilibre, indépendamment de la valeur de B. En effet, puisque la valeur de B est accordée à la fois pour les couches inactives et commutables de l'actionneur, le rapport des modules d'Young des deux parties (E_s/E_i) reste constant. Cependant, de grandes oscillations

amorties de la déviation sont observées avant d'atteindre l'état stationnaire. Ces oscillations pour atteindre l'état d'équilibre mécanique ont lieu à la fréquence de flexion naturelle du levier. Fait intéressant, au fur et à mesure que la coopérativité (*B*) est réduite, l'amplitude et la période des oscillations sont augmentées (voir la **FIG. 3.4** (b)). Cela vient du fait que la réduction de *B* implique un ramollissement du réseau, qui devient plus déformable, permettant ainsi à des déflexions plus importantes de se produire. De plus, comme la fréquence d'oscillation et le taux d'amortissement sont proportionnels à $\sqrt{E}$, nous observons que la réduction de B conduit également à une augmentation de la période d'oscillation de flexion du système bimorphe, passant de ~300 ps (~3,33 GHz) à ~400 ps (~2,50 GHz) et une diminution concomitante du taux d'amortissement lorsque la valeur de B passe de 0,6 à 0 (**FIG. 3.4** (b)).

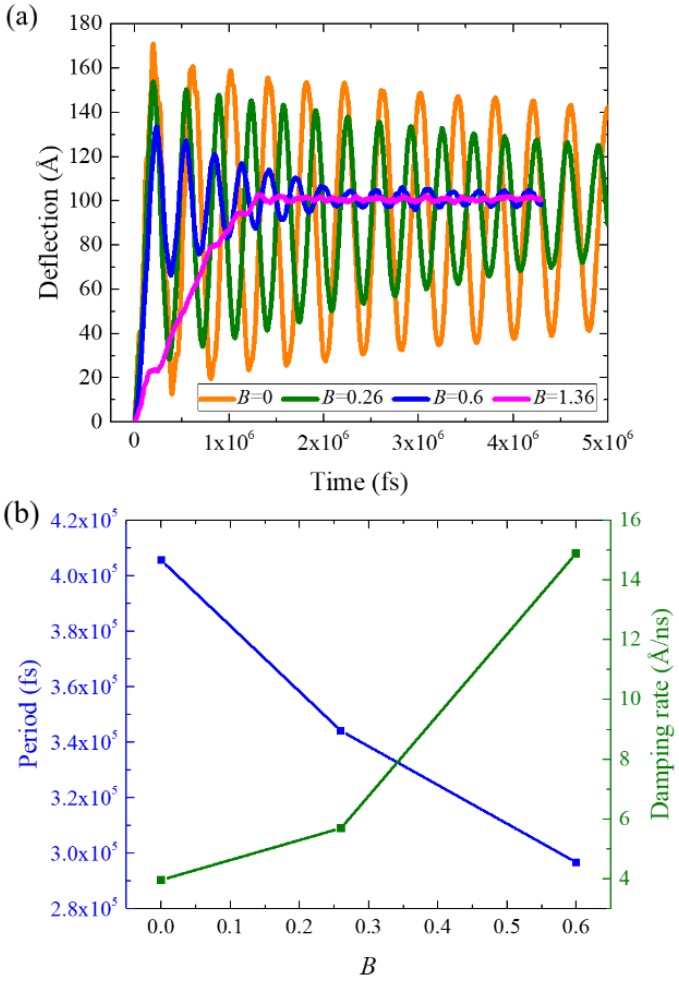

FIG. 3.4: (a) Évolution temporelle de la déflexion du levier bimorphe (dans le cas $N_I = N_S = 4$) au cours du processus de relaxation de l'état HS à l'état BS à T = 100 K pour différentes valeurs de *B*. (b) Évolution de la période et de vitesse d'amortissement des oscillations de déflexion en fonction de *B*.

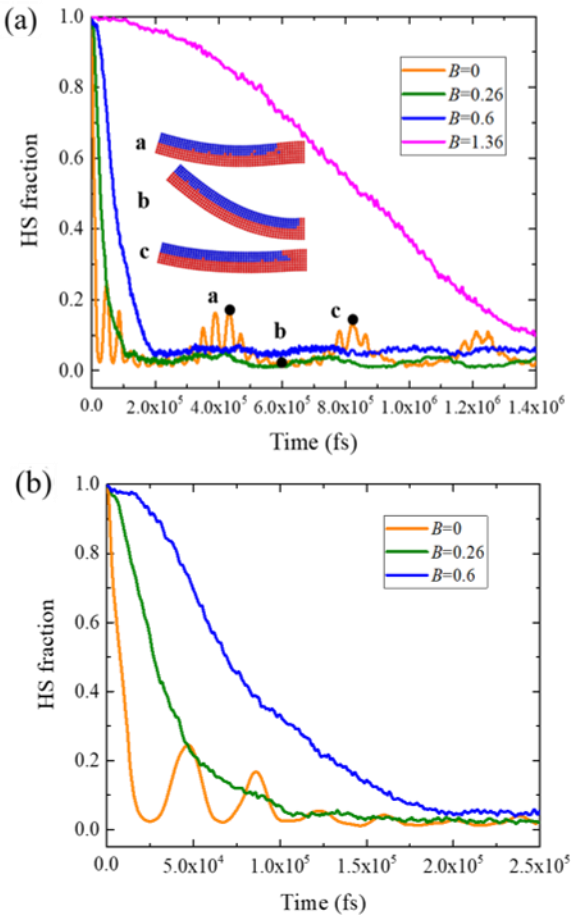

FIG. 3.5: (a) Évolution temporelle de la fraction HS dans le levier bimorphe (dans le cas N_I = N_S = 4) au cours du processus de relaxation de l'état HS à l'état BS à T = 100 K pour différentes valeurs de *B*. Insert : configurations instantanées de la distribution spatiale de l'état de spin à différents instants (repérés par des points noirs) dans le cas *B* = 0. Les cercles rouges et bleues représentent respectivement les sites HS et BS. (b) Zoom montrant l'évolution temporelle de la fraction HS à des échelles de temps courtes pour *B* = 0, 0,26 et 0,6.

Par comparaison, l'évolution temporelle de la fraction HS pour les différentes valeurs de B est représentée sur la **FIG. 3.5** (a). Comme déjà mentionné, la cinétique de commutation entre les états BS et HS est considérablement ralentie pour les grandes valeurs de *B*. Dans le cas *B* = 0, la fraction HS oscille avec deux périodes caractéristiques, $T_{stretching}$ = 40 ps et T_{bend} = 400 ps, qui correspondent respectivement à la période d'élongation naturelle et à la période de flexion naturelle du levier. Ainsi, nous constatons que l'évolution temporelle de la fraction HS suit fidèlement les déformations (élongation et flexion) du système bimorphe, montrant clairement l'interaction entre l'état électronique moléculaire et la contrainte/déformation locale au sein de

la structure. Lorsque le paramètre *B* est augmenté, l'amplitude des oscillations de la fraction HS est largement réduite (pour *B* = 0,26 et 0,6, seules les oscillations de flexion du levier ont un effet visible sur la fraction HS). Là encore, cet effet provient du fait qu'une augmentation de la coopérativité a pour effet de ralentir progressivement la cinétique de commutation HS ↔ BS, de sorte que la fraction HS sera d'abord découplée des oscillations à allongement rapide et, dans un second temps, des oscillations de flexion plus lentes du levier. Enfin, comme le montrent les **Fig. 3.4** (a) et **3.5** (a), dans le cas d'un matériau SCO hautement coopératif (*B* = 1,36), l'état BS complet et la déflexion d'équilibre sont atteints en ~1,4 ns sans oscillation.

Chapitre IV : Effets de l'énergie et des contraintes de surface sur le phénomène de la transition de spin étudiés par une approche thermodynamique.

Dans ce travail, nous avons poursuivi le développement du modèle nano-thermodynamique cœur-coque proposé par Félix et al. D'une part, nous avons remplacé le terme d'interaction phénoménologique par une approche issue de la mécanique des milieux continus, similaire à celle proposée par Spiering et al., où les interactions intermoléculaires d'origine élastiques sont explicitement prises en compte en considérant le changement de volume moléculaire lors de la commutation de spin. De plus, la densité de contraintes de surface dépendant de l'état de spin a été prise en compte pour la première fois dans le domaine du SCO. Sur la base de ce nouveau modèle, les conséquences de l'énergie/contrainte de surface sur la stabilité de phase des nano-objets SCO ont été étudiées lors de la réduction de taille. L'énergie libre totale de Gibbs (G_{total}) d'un système SCO peut être exprimée comme suit :

$$G_{total} = G - TS_{mix} + G_{elastic} + G_{surface}, \quad (4.1)$$

où G, S_{mix}, $G_{elastic}$,et $G_{surface}$ sont les contributions de l'énergie de Gibbs de la molécule sans interaction, mélangeant respectivement l'entropie, l'interaction élastique et l'énergie de surface.

Tout d'abord, nous calculons les contributions ci-dessus dans le cas d'un film mince plat dont les dimensions le long des directions *x* et *y* sont respectivement L^x et L^y. Ensuite, un modèle coeur-coquille sphérique qui consiste en un coeur avec un rayon de R_1 et une coquille avec une épaisseur de (R-R_1), comme la **Fig. 4.1** le montre.

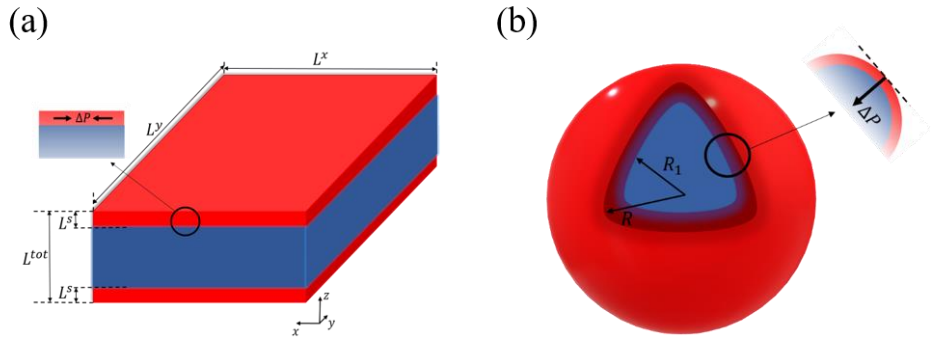

FIG. 4.1: Représentations schématiques (a) du modèle de type couche mince et (b) du modèle sphérique cœur-coquille. La région de couleur bleue représente le cœur et la région de couleur rouge représente la coquille.

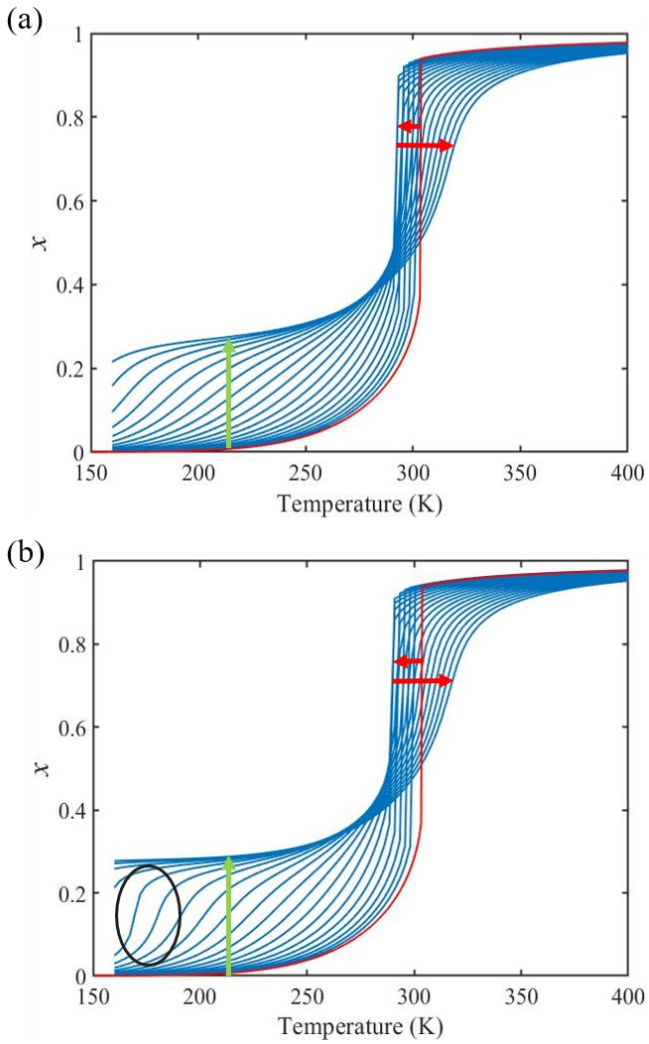

FIG. 4.2: Dépendance en température de la fraction HS pour le film mince de 5 nm d'épaisseur dans le cas de (a) $\alpha = \frac{\sigma_\downarrow}{\sigma_\uparrow} = 1.4$ et (b) $\alpha = \frac{\sigma_\downarrow}{\sigma_\uparrow} = 2.0$ pour différentes valeurs positives de $\sigma_\uparrow$. La courbe rouge représente le matériau massif correspondant.

FIG. 4.2 (a) et (b) résument la dépendance avec la température de la fraction HS dans un film mince de 5 nm calculée pour une contrainte de surface positive dans les cas d'un rapport de contrainte de surface BS/HS $\alpha = \frac{\sigma_{\downarrow}}{\sigma_{\uparrow}}$ =1,4 et 2,0, respectivement. Comme l'indique la flèche verte sur la **Fig. 4.2** (a), l'augmentation de $\sigma_{\uparrow}$ fait apparaître une augmentation de la fraction HS résiduelle à basse température. Encore une fois, la fraction HS résiduelle la plus élevée est $x = \sim 0.28$ indiquant que la température d'équilibre des molécules dans la coquille diminue avec l'augmentation de $\sigma_{\uparrow}$ jusqu'à un blocage complet de la coquille dans l'état HS**.** L'existence de la contrainte de surface lors de la commutation de spin exerce une contrainte/pression sur la surface du matériau. En termes de contrainte de surface positive, les deux surfaces du film mince sont toutes les deux soumises à des contraintes en traction, ce qui favorise l'état HS, entraînant une baisse de la température de transition des molécules dans la coquille.

Nous pouvons observer un changement évident du comportement SCO dans le cœur du nano-objet. En effet, comme le montrent les flèches rouges sur la **Fig. 4.2** (a), la température d'équilibre diminue d'abord jusqu'à ce qu'elle atteigne sa valeur la plus basse (~ 290 K) avec l'augmentation de $\sigma_{\uparrow}$. Semblable à l'effet d'énergie de surface, ce ralentissement peut être attribué à l'interaction intermoléculaire élastique entre les molécules HS dans la coquille et les molécules BS dans le coeur. Cependant, le minimum de la température d'équilibre (~ 290 K) reste plus élevé par rapport au cas de l'effet d'énergie de surface (~ 266 K) car les molécules du coeur sont sous compression, ce qui stabilise l'état BS. En d'autres termes, la contrainte de surface induit deux effets antagonites, favorisant soit l'état HS, soit l'état BS. Cependant, la stabilisation de l'état HS est limitée par l'épaisseur de la coque. Par conséquent, lorsque les molécules de l'enveloppe sont totalement bloquées à l'état HS, une augmentation supplémentaire de $\sigma_{\uparrow}$ entraînera uniquement une augmentation de la contrainte de compression dans le coeur, ce qui se manifeste sur la **Fig. 4.2** par une nette élévation de la température d'équilibre. Dans le cas $\alpha = \frac{\sigma_{\downarrow}}{\sigma_{\uparrow}} = 2.0$, représenté sur la **Fig. 4.2** (b), des caractéristiques communes avec le cas $\alpha = \frac{\sigma_{\downarrow}}{\sigma_{\uparrow}} = 1.4$ peuvent être observées, comme la diminution de la température d'équilibre et l'augmentation de la fraction résiduelle HS à basse température lorsque $\sigma_{\uparrow}$ augmente. Fait intéressant, une transition de spin abrupte a pu être trouvée dans la coque, comme le soulignent les cercles noirs. Au contraire, au fur et à mesure que $\sigma_{\uparrow}$ augmente, le changement d'état de spin du coeur passe d'une transition abrupte à une transition progressive.

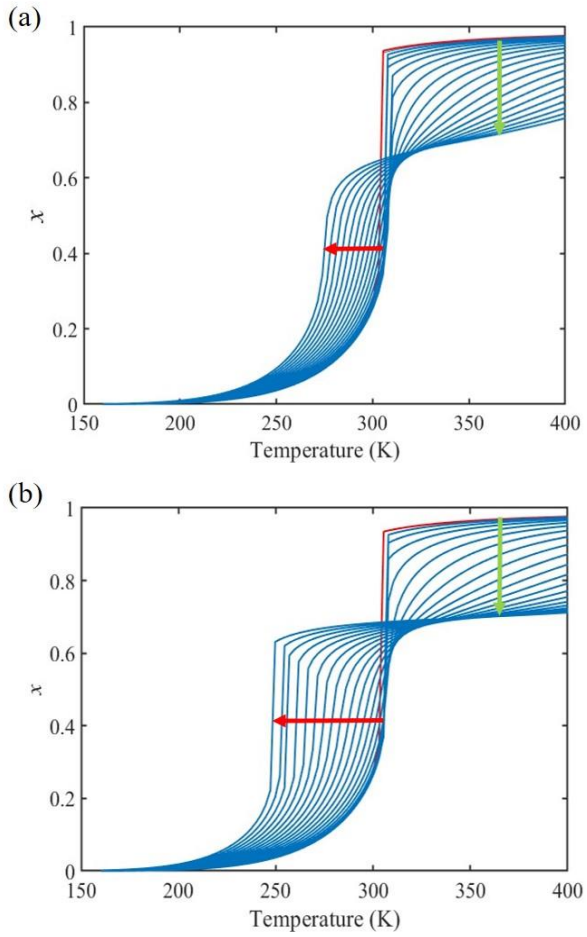

FIG. 4.3: Dépendance en température de la fraction HS pour le film mince de 5 nm dans le cas de (a) $\alpha = \frac{\sigma_{\downarrow}}{\sigma_{\uparrow}} = 1.4$ et (b) $\alpha = \frac{\sigma_{\downarrow}}{\sigma_{\uparrow}} = 2.0$ pour différentes valeurs négatives de $\sigma_{\uparrow}$. La courbe rouge représente le matériau massif.

FIG. 4.3 (a) montre la transition de spin induite thermiquement dans un film mince de 5 nm pour des valeurs négatives (de compression) de la contrainte de surface dans le cas de $\alpha = \frac{\sigma_{\downarrow}}{\sigma_{\uparrow}} =$ 1,4. Globalement, les effets observés sont « en miroir » du cas de la contrainte superficielle en traction, bien que certaines différences se produisent également. D'une part, comme indiquée par la flèche verte sur la **Fig. 4.3**, une augmentation de la fraction BS résiduelle à haute température peut être observée avec l'augmentation de la magnitude de $\sigma_{\uparrow}$. La fraction BS résiduelle à haute température culmine à une valeur de ~ 0,2, indiquant que les molécules de la coquille sont bloquées par la contrainte de compression (c'est-à-dire que leur transition est décalée vers les hautes températures). On peut en déduire qu'à la limite $\sigma_{\uparrow} \to -\infty$ ($\alpha \to \infty$), les molécules à la surface sont complètement bloquées dans l'état BS. D'autre part, pour assurer

l'équilibre mécanique, une contrainte de traction existe dans le coeur, s'équilibrant avec la contrainte de surface. Comme dans le cas d'une contrainte de surface positive, deux effets antagonistes peuvent être observés. La contrainte de traction dans le noyau tend à stabiliser l'état HS, tandis que l'interaction avec la coquille tend à stabiliser l'état BS. Comme le montre la **Fig. 4.3** (a), on observe tout d'abord une légère augmentation (~ 3 K) de la température d'équilibre lorsque l'amplitude de $\sigma_{\uparrow}$ est faible. Bien que les molécules BS bloquées dans la coquille aient tendance à stabiliser l'état BS dans le noyau via des interactions intermoléculaires élastiques, la contrainte en traction, qui favorise l'état HS, devient rapidement dominante au fur et à mesure que $\sigma_{\uparrow}$ augmente, conduisant à une diminution de la température d'équilibre (indiquée par la flèche rouge).

Il n'est donc pas surprenant de voir sur la **Fig. 4.3** (b) qu'une commutation de spin abrupte apparaît dans le noyau massif lorsque la contrainte de surface est forte ($< -310\ mJ/m^2$). Il est intéressant de remarquer que ce type d'effet de contrainte de surface pourrait ainsi contribuer à la réapparition de la boucle d'hystérésis rapportée dans certaines nanoparticules ultra-petites du composé [Fe(pyrazine)][Ni(CN)$_4$]. Dans des rapports antérieurs, ce phénomène était attribué à la modification des propriétés élastiques de surface et/ou des interactions particule-matrice, mais le présent travail indique que l'existence d'une contrainte de surface négative peut également donner lieu à de tels effets.

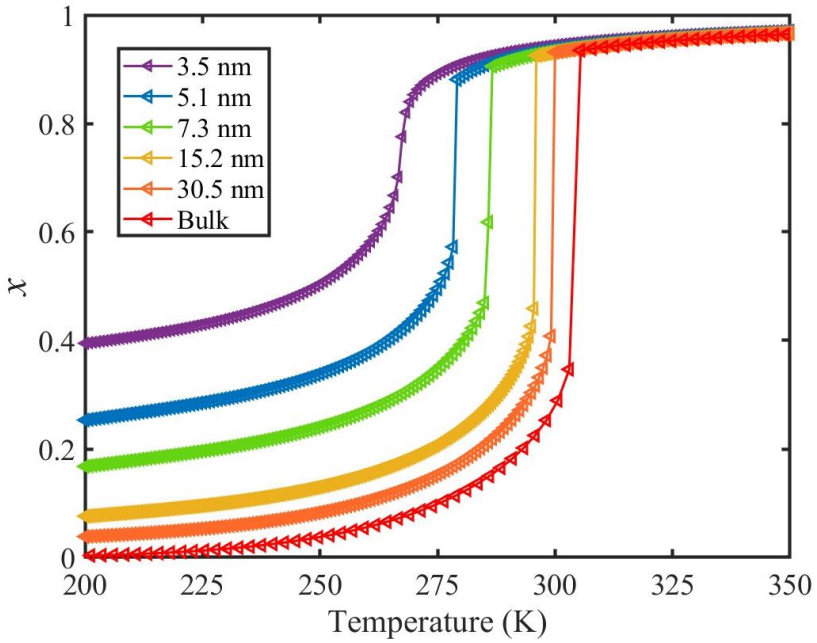

FIG. 4.4: Dépendance en température de la fraction HS totale pour différentes épaisseurs.

La dépendance en température calculée de la fraction HS totale est représentée sur la **Fig. 4.4** pour différentes épaisseurs dans le cas d'un modèle à couche mince. Dans l'ensemble, on peut clairement voir une augmentation de la fraction HS résiduelle ainsi qu'une baisse de la température d'équilibre avec la réduction de taille, ce qui est en accord qualitatif avec les observations expérimentales sur différents composés SCO notamment, une transition de spin graduelle avec une transition température à ~ 266 K ainsi qu'une fraction HS résiduelle de x = 0,4 à 200 K peuvent être trouvées dans le film mince à 5 couches (~ 3,5 nm) de la **Fig. 4.4.** Ce résultat peut être comparé à une étude expérimentale récente effectuée sur les clathrates de type Hoffmann utilisant la spectroscopie Raman à température variable, qui a révélé pour un film de [Fe(pyrazine)][Ni(CN)$_4$] d'épaisseur 5 couches une courbe SCO graduelle centrée sur ~ 260 K, accompagné d'une fraction résiduelle HS de ~ 0,45 à 200 K. Un tel bon accord entre les résultats de notre modèle et les observations expérimentales indique que le modèle actuel pourrait prédire les comportements SCO à l'échelle nanométrique. Néanmoins, il est important de rappeler que les calculs étaient basés sur des estimations grossières des paramètres thermodynamiques de surface, qu'il convient d'affiner à l'aide d'approches expérimentales et théoriques afin d'établir une réelle capacité prédictive.

Conclusion générale et perspectives

Avec la réduction de la taille, les matériaux à TS montrent les mêmes effets de tailles finies que bon nombre de systèmes présentant des transitions de phase du premier ordre telles que des changements importants dans la stabilité de phase, se traduisant par un déplacement de la température d'équilibre, l'apparition d’une transition incomplète ainsi que des altérations des comportements collectifs, avec, la plupart du temps, une perte de la coopérativité et des effets mémoires. Ces modifications spectaculaires des propriétés des matériaux à TS sont probablement le résultat de l'augmentation du rapport surface sur volume et de la forte interaction entre l'objet SCO et l'environnement extérieur (effets de matrice). Dans ce contexte, l'objectif principal de cette thèse était d'étudier les effets de la surface et de l'interface sur les propriétés du SCO à l'échelle nanométrique. Dans ce but, des simulations MD tout-atome et des méthodes thermodynamiques ont été réalisées.

Le premier travail rapporté dans cette thèse consiste en la construction des champs de force empiriques du composé [Fe(pyrazine)][Ni(CN)$_4$] dans les deux états de spin. Ce champ de force comprend des potentiels harmoniques simples et de type Lennard-Jones dont les paramètres ont été obtenus à partir de données spectroscopiques Raman et NIS. Il semble être

capable de simuler raisonnablement l'ensemble des spectres de densité d'états vibrationnels (vDOS), des modes basses fréquences (acoustique) aux modes hautes fréquences (optique) avec une précision acceptable. Cette approche numérique constitue donc un bon compromis pour les investigations de la dynamique de réseau des matériaux à TS, entre les modèles qualitatifs de type masse-ressort, ne fournissant que des tendances générales, et les calculs *ab initio*, ne fournissant des propriétés vibrationnelles quantitatives de ces solides qu'à un coût de calcul très élevé et pour des systèmes relativement petits. Un point très important est la capacité de cette approche à modéliser quantitativement la partie acoustique du vDOS. Cette dernière n'est pas facilement accessible avec des calculs *ab initio* ou avec des mesures expérimentales.

Ensuite, un potentiel de type double-puits est intégré au champ de force nouvellement construit afin de simuler des matériaux commutables et de reproduire l'effet du couplage vibronique sur la déformation élastique du réseau cristallin. L'introduction de ce potentiel couplé au nouveau champ de force permet de reproduire la transition de spin du premier ordre induite thermiquement du composé [Fe(pyrazine)][Ni(CN)$_4$] ainsi que les mécanismes coopératifs associés. En outre, la méthode MD tout-atome décrit de manière plus explicite le mouvement des ligands et des liaisons Fe-N lors de la commutation de spin que les modèles de type masse-ressort, ce qui fournit un bon point de départ pour l'étude suivante qui concerne l'interface HS/BS et les distorsions du réseau présents au cours du changement de l'état de spin.

Basé sur le champ de force construit au **chapitre. II**, l'effet de l'interface dans un modèle bicouche [Fe(pyrazine)][Ni(CN)$_4$] est étudié au moyen de simulations MD tout atome au **chapitre III**. Comme prévu, le phénomène de déflexion de la structure a pu être observé après l'introduction de l'interface HS/BS. La comparaison entre la déflexion du modèle bicouche extrait de notre simulation et celle déterminée à partir de la théorie classique d'Euler-Bernoulli illustre l'inapplicabilité de cette dernière dans le cas de couches extrêmement minces. De plus, en analysant les évolutions de la configuration de spin locale et de la déformation locale au cours du processus de relaxation thermique, la nucléation du domaine BS est détectée au niveau de la surface, dans des régions soumises à une contrainte en compression, ce qui est en bon accord avec les observations expérimentales. Dans certains cas, des oscillations amorties par étirement et flexion de l'actionneur (aux fréquences naturelles de la structure) sont observées pendant le processus de commutation avant le retour à l'équilibre mécanique. De plus, des oscillations amorties ont également été observées dans l'évolution temporelle de la fraction HS au cours du processus de relaxation, démontrant le couplage entre l'état de déformation du levier et l'état de spin moléculaire du fait de la présence du potentiel double-puits dans le champ de

force. Grâce au temps réel inhérent aux simulations MD, les vitesses de propagation de la paroi de domaine BS pour différents modèles sont estimées pour la première fois. Nous constatons que la présence de contrainte en traction et l'augmentation de la coopérative du réseau réduiraient largement la vitesse de propagation de la frontière du domaine BS, correspondant à une augmentation significative du temps de retour à l'état stationnaire observé à partir des courbes de relaxation du HS fraction.

Enfin, afin d'étudier les effets de l'énergie de surface/contrainte sur les propriétés des matériaux à TS à l'échelle nanométrique de manière quantitative et précise, de nouveaux modèles de nano-thermodynamiques de type cœur-coquille ont été développés pour les couches minces et les nano-objets sphériques du SCO. Dans ces modèles, des approches issues de mécanique des milieux continus ont été utilisées pour modéliser les interactions intermoléculaires, en tenant compte de la dépendance de l'état de spin du volume moléculaire ainsi que des modules élastiques. De plus, la dépendance à l'état de spin des grandeurs caractérisant les propriétés de surface, à savoir l'énergie de surface et la contrainte d'interface, a été considérée quantitativement pour la première fois dans le domaine des matériaux SCO.

Un avantage très important d'un tel modèle réside dans le lien direct existant entre les paramètres d'entrée et les grandeurs physiques accessibles expérimentalement. Les courbes de transition de spin induites thermiquement calculées à partir du matériau massif [Fe(pyrazine)][Ni(CN)$_4$] et des films minces sont en bon accord avec les résultats expérimentaux disponibles, indiquant que ce nouveau modèle possède la condition préalable pour reproduire et interpréter les résultats expérimentaux observées dans les nanomatériaux à TS. L'étude théorique des effets de l'énergie de surface/contrainte sur les propriétés du SCO révèle que la compétition entre la pression induite par la contrainte de surface et l'interaction élastique intermoléculaire conduit à un décalage vers le haut ou vers le bas de la température d'équilibre en fonction de l'amplitude de la contrainte de surface. L'énergie de surface et la contrainte de surface peuvent être les forces motrices de la transition de spin incomplète observée expérimentalement à taille réduite.

Ce travail de thèse offre de nombreuses perspectives. En particulier, on constate que le champ de force n'est pas capable de simuler la transition du premier ordre en introduisant simplement l'interaction intramoléculaire de type double puits dans la structure. Il reste donc une question ouverte et non élucidée concernant les différentes contributions aux mécanismes

de coopérativité (propriétés mécaniques et différences de volume entre les phases HS et BS, propriétés anisotropes et propriétés cristallographiques, etc.).

De plus, étant donné que le système étudié par méthode Monte Carlo est dans un bain thermique et de pression idéal, l'étude des processus de diffusion thermique dans les matériaux à TS pourrait être une direction intéressante pour de futures études théoriques par simulations MD.

Dans l'étude de la dynamique spatio-temporelle de la transition de spin, il serait intéressant d'analyser le processus de nucléation en utilisant le champ de force actuel en estimant, par exemple, la barrière d'énergie de nucléation. Du fait de la taille limitée du système simulé et de l'absence de défauts structuraux (défauts ponctuels, dislocations, joints de grains…), la vitesse de propagation des parois de domaine observée à partir des simulations varie de 48 m/s à 1150 m/s selon les différents modèles développés dans ce travail. La vitesse d'interface apparaît supérieure à celle déduite de l'expérience (de l'ordre de quelques µm/s). Plus important encore, la limite supérieure de l'échelle de temps de la simulation MD traditionnelle (généralement de l'ordre de la centaine de microsecondes) empêche de reproduire les observations expérimentales. Une perspective importante serait d'utiliser la méthode MD à grains grossiers (coarsed-grained MD) ou des méthodes MD accélérées pour simuler des systèmes mésoscopiques comprenant différents défauts de réseau.

Dans le dernier chapitre de ce manuscrit, nous avons souligné et démontré à plusieurs reprises que l'énergie de surface et la contrainte de surface peuvent jouer un rôle important dans les nanomatériaux. Cependant, les valeurs expérimentales de l'énergie/contrainte de surface n'ont pas encore été rapportées dans le domaine des matériaux à TS, ce qui ne permet pas une comparaison directe de ces investigations théoriques avec des données expérimentales. De nos jours, la seule possibilité est une comparaison avec les expériences de dynamique de réseau et les propriétés de commutation des nanomatériaux SCO. Les conséquences potentielles des propriétés structurales, vibrationnelles et mécaniques de surface/interface sur des nanoparticules ont été étudiées sans qu'aucune expérience n'ait permis de caractériser complètement les grandeurs surface/interface et leur dépendance avec l'état de spin. Cet écueil entrave sérieusement la poursuite des investigations théoriques. D'un point de vue expérimental, diverses techniques peuvent être proposées pour extraire des valeurs d'énergies de surface dans les deux états de spin telles que la mesure de l'angle de contact (technique de la goutte sessile), ou les techniques de sonde locale (Atomic Force Microscopy AFM) ainsi que les tests

d'indentation instrumentés (nano-indentation). D'autre part, les mesures dites de « wafer bending » peuvent être réalisées pour extraire des valeurs de contrainte de surface. Enfin, comme mentionné au **chapitre I**, les effets de matrice et d'interface, entraînant une énergie de déformation élastique considérable, influencent fortement les comportements des matériaux à TS à l'échelle nanométrique. Dans ce contexte, cela introduirait en outre les contributions de l'énergie et de la contrainte d'interface à notre modèle thermodynamique actuel simulant les comportements des films multicouches ou la croissance de couches minces à TS sur un substrat.

French and English summary

In the last decade, the investigation of phase transitions at the nanometer scale has become an essential element in the field of nanoscience. The fundamental understanding and, eventually, the precise control of the physical and chemical properties of "smart" nanomaterials, exhibiting phase transitions are of paramount importance for their integration in new generation of photonic/electronic nano-devices. Decreasing the size to the nanometer scale usually leads to drastic modifications of the switching properties and gives rise to new phenomena with respect to collective behaviors and phase stability. Such changes are directly correlated to the increase of surface-to-volume ratio with the size reduction and the predominance of the external environment (interface effects). In this context, this thesis work focuses on molecular spin crossover (SCO) nanomaterials which exhibit first order phase transitions between a low spin (LS) and a high spin (HS) state having different electronic configurations and displaying markedly different physical properties (magnetic, electric, elastic, optical etc.). The aim of this work is to develop ambitious multiphysics theoretical investigations to analyze finite size effects on phase change molecular nanomaterials with the prospect of establishing predictive quantitative models and, eventually, bringing out universal laws for phase transitions at the nanoscale. In particular, the force fields of [Fe(pyrazine)][Ni(CN)$_4$] compound are constructed for all-atom Molecular Dynamics (MD) simulations, which describes the vibrational properties and the thermally induced SCO behavior in a quantitative way. Subsequently, the relaxation process of bilayer model is studied using the MD method, illustrating the interface effect (matrix effect) on the lattice distortion and the phase stability. Finally, a new model based on the nano-thermodynamic method is introduced to investigate the SCO phenomenon in nano-objects. Taking into account the physical parameters from experiments and numerical simulations in the nano-thermodynamic model, the different contributions of surface energy and surface stress to the surface effect are clarified for the first time.

Keywords: Spin transition, Size effect, Molecular Dynamics, Nano-Thermodynamics

Au cours de la dernière décennie, l'étude des transitions de phase à l'échelle du nanomètre est devenue un élément incontournable dans le domaine des nanosciences. La compréhension fondamentale et la perspective d'un contrôle précis des propriétés physiques et chimiques de ces nanomatériaux « intelligents », présentant des transitions de phase, sont d'une importance primordiale pour leur intégration dans la nouvelle génération de nanodispositifs photoniques/électroniques. La diminution de la taille à l'échelle du nanomètre conduit généralement à des modifications drastiques des propriétés de commutation et fait apparaître de nouveaux phénomènes quant aux comportements collectifs et à la stabilité de phase. De tels changements sont directement corrélés à l'augmentation du rapport surface/volume lorsque la taille des nano-objets est diminuée et entraînent, en général, une prédominance des propriétés de l'environnement extérieur (effets d'interface). C'est dans ce contexte que se situe ce travail de thèse. En effet, on s'intéresse tout particulièrement aux composés à transition de spin (TS) qui possèdent la capacité de commuter d'un état bas spin (BS) à un état haut spin (HS). Ces deux états moléculaires possèdent des configurations électroniques différentes et présentent des propriétés physiques (magnétiques, électrique, élastique, optique etc.) drastiquement différentes. L'objectif de ce travail est de développer des approches théoriques multiphysiques ambitieuses pour analyser les effets de taille finie sur les nanomatériaux moléculaires à transition de spin dans la perspective d'établir des modèles quantitatifs prédictifs et, à terme, de faire émerger des lois universelles pour les transitions de phase à l'échelle nanométrique. En particulier, un champs de force est construit pour le composé [Fe(pyrazine)][Ni(CN)$_4$] afin de réaliser des simulations de dynamique moléculaire (MD) de type « all-atom », capable de décrire les propriétés vibrationnelles de manière quantitative et de modéliser la transition de spin induite par la température. Ensuite, le processus de relaxation d'un modèle bicouche est analysé à l'aide de la méthode MD, illustrant l'effet d'une interface (ou effet de matrice) sur la distorsion du réseau et mettant en évidence les conséquences sur la stabilité de phase. Enfin, un nouveau modèle nano-thermodynamique est introduit pour étudier le phénomène de la TS dans les nano-objets. Les paramètres de ce modèle thermodynamique possèdent l'avantage d'être facilement, voire directement, reliés à des quantités physiques mesurables ou, le cas échéant, obtenus à l'aide de simulations numériques MD. En particulier, les différentes contributions de l'énergie de surface et de la contrainte de surface à l'effet de surface sont discutées et, pour la première fois, clarifiées.

Mots clés : Transition de spin, Effet de taille, Dynamique moléculaire, Nano-thermodynamique